UiO : University of Oslo

Ivar Thokle Hovden

Structural and functional tracking in longitudinal magnetic resonance imaging of glioblastoma

Thesis submitted for the degree of Philosophiae Doctor

Department of Physics

Faculty of Mathematics and Natural Sciences

Department of Physics and Computational Radiology

Oslo University Hospital

2022

Series of dissertations submitted to the
Faculty of Mathematics and Natural Sciences, University of Oslo
No. 2602

ISSN 1501-7710

Cover: UiO.
Print production: Graphics Center, University of Oslo.

Preface

This thesis is submitted in partial fulfillment of the requirements for the degree of *Philosophiae Doctor* at the University of Oslo. The research presented here was conducted at the University of Oslo and at Oslo University Hospital, under the supervision of Kyrre E. Emblem and professor Eirik Malinen.

This work was supported by the European Research Council ERC through grant 758657, the Norwegian Research Council through grant 261984 and the South-Eastern Norway Regional Health Authority through grant 2017073.

The thesis is a collection of three papers, presented in chronological order of writing. The common theme to them is structural and functional tracking of magnetic resonance imaging data of patients with glioblastoma, with the objective to improve the diagnostic and prognostic accuracy of the disease. It presents multidisciplinary work involving medical physicists, medical doctors, and computer scientists. The candidate has a background from technical cybernetics. The papers are preceded by an introductory, aims, background, material and methods chapter that relate them to each other and provides background information and motivation for the work.

The first paper is joint work with Oliver M. Geier, Ingrid Digernes, Elies Fuster-Garcia, Grethe Løvland, Einar Vik-Mo, Torstein R. Meling and Kyrre E. Emblem, the second paper joint work with Elies Fuster-Garcia, Siri F. Svensson, Christopher Larsson, Jonas Vardal, Atle Bjørnerud and Kyrre E. Emblem, and the third paper joint work with Elies Fuster-Garcia, Jingpeng Li, Atle Bjørnerud, Christopher Larsson, Siri F. Svensson and Kyrre E. Emblem. I am the first and corresponding author of the first and third paper, and second author of the second paper.

Acknowledgements

I acknowledge my main supervisor Kyrre E. Emblem for kickstarting my journey into research. This has not only involved extensive project and grant writing prior to my time at Oslo University Hospital, but also substantial efforts to assure clinically relevant results.

Associate professor Elies Fuster-Garcia offered much of his time at Oslo University Hospital to teach me medical physics as a fresh doctoral candidate and has been an invaluable resource for bridging the gap between computational methods and clinical research, both theoretical and practical. Siri F. Svensson, that started her doctoral period at about the same time as me and in the same research group, has been a great partner to share experiences and challenges.

Through professor Atle Bjørnerud and his computational radiology and artificial intelligence research group additional collaborators were formed that have been valuable in shaping the technical aspect of my work, enabling me to gain practical experience in hardware and software systems and maintenance for research, and generally keeping me motivated as a doctoral candidate. Some of them were the doctoral candidates Jingpeng Li, Jon Andre Ottesen and Lidia Luque, software engineers Jon Nesvold and Martin Rørvang.

Ivar Thokle Hovden

Oslo, December 2022

List of papers

1. Hovden, I.T., Geier, O.M., Digernes, I., Fuster-Garcia, E., Løvland, G., Vik-Mo, E., Meling, T.R., Emblem, K.E., 2020. The impact of EPI-based distortion correction of dynamic susceptibility contrast MRI on cerebral blood volume estimation in patients with glioblastoma. European Journal of Radiology 132, 109278. https://doi.org/10.1016/j.ejrad.2020.109278
2. Fuster-Garcia, E., Thokle Hovden, I., Fløgstad Svensson, S., Larsson, C., Vardal, J., Bjørnerud, A., Emblem, K.E., 2022. Quantification of Tissue Compression Identifies High-Grade Glioma Patients with Reduced Survival. Cancers 14, 1725. https://doi.org/10.3390/cancers14071725
3. Thokle Hovden, I., Fuster-Garcia, E., Li, J., Bjørnerud, A., Larsson, C., Fløgstad Svensson, S., Emblem, K.E., 2022. A Parametric Evaluation of Deformable Image Registration Methods for Assessing Glioblastoma Growth. Submitted to Journal.

Summary

Glioblastoma is a deadly type of brain cancer. It is difficult to treat and has a poor prognosis, with most adult patients surviving only 12-15 months after diagnosis. Magnetic resonance imaging (MRI) scans are essential for diagnosing and treating this disease, but it can be challenging to ensure that the scans provide accurate, clinically useful information.

In this thesis, we investigate methods for improving the accuracy of MRI scans in brain cancer treatment. MRI scans use high-resolution structural images to show doctors the location and size of a tumor, and they can also be used to track how well a person is responding to treatment. In addition, functional MRI techniques, such as measuring cerebral blood volume, can provide additional clinical information.

However, it is not easy to ensure that these imaging modalities, along with advanced postprocessing techniques, correctly present the information that doctors need. For example, it is important to have anatomically correct and consistent values for assessing the blood supply to a tumor, and to be able to track changes in the tumor over time.

In this thesis, we focus on tracking image intensity and displacement, which we call "voxel tracking". This allows us to extract the most anatomically and physiologically correct information from MRI scans. We correct for errors in blood perfusion scans, create prognostic tissue markers, and create a model of how cancer grows and affects the brain.

Our research lays the foundation for more advanced studies of brain cancer, and it has the potential to lead to more personalized treatment plans for patients with glioblastoma. By understanding the details of how the disease progresses, doctors may be able to develop tailored treatment plans that are more effective and have better outcomes for patients.

Sammendrag

Glioblastom er en dødelig type hjernesvulst. Den er vanskelig å behandle og har dårlig prognose, med en median overlevelse på 12-15 måneder etter diagnose for voksne. Magnetresonanstomografi (MR)-skanninger er viktige for å diagnostisere og behandle denne sykdommen, men det kan være utfordrende å sikre at skanningene gir nøyaktige og klinisk nyttige opplysninger.

I denne avhandlingen undersøker vi metoder for å forbedre nøyaktigheten av MR-skanninger i behandling av hjernesvulst. MR-skanninger bruker høyoppløselige bilder for å vise legene plasseringen og størrelsen på en svulst, og de kan også brukes for å spore hvordan en person responderer på behandlingen. I tillegg kan funksjonelle MR-teknikker, som måling av hjernens blodvolum, gi tilleggsinformasjon.

Det er imidlertid ikke en enkel oppgave å forsikre at disse avbildnings- og postprosesseringsteknikkene presenterer den informasjonen legene trenger. Noen eksempler på dette er anatomisk korrekte og konsistente verdier for å evaluere en tumors blodforsyning, eller å kunne spore endringer i tumor over tid.

I avhandlingen fokuseres det på å spore intensiteter og forflytninger i bilde, som vi kaller "voksel-sporing". Denne metodologien gir grunnlag for å hente ut mest mulig korrekt anatomisk og fysiologisk informasjon fra MR-skanninger. Vi korrigerer feil i blodvolumsmålinger, utvikler prognostiske markører basert på forflytninger i vev, og utvikler en modell for hvordan kreften vokser og påvirker hjernen.

Resultater fra denne forskningen legger et grunnlag for å gjennomføre mer avanserte studier av hjernekreft. Et potensielt resultat av forskningen er å utvikle mer persontilpassede behandlingsforløp for kreftpasienter. Ved å bedre forstå hvordan sykdommen utvikler seg, kan legene sette opp mer effektive behandlingsforløp som potensielt gir bedre utfall for pasientene.

Other related articles

1. Gu, X., Eklund, A., 2019. Evaluation of Six Phase Encoding Based Susceptibility Distortion Correction Methods for Diffusion MRI. Frontiers in Neuroinformatics 13. https://doi.org/10.3389/fninf.2019.00076 (software acknowledgements).
2. Fløgstad Svensson, S., Fuster-Garcia, E., Latysheva, A., Fraser-Green, J., Nordhøy, W., Isam Darwish, O., Thokle Hovden, I., Holm, S., Vik-Mo, E.O., Sinkus, R., Eeg Emblem, K., 2022. Decreased tissue stiffness in glioblastoma by MR elastography is associated with increased cerebral blood flow. European Journal of Radiology 147, 110136. https://doi.org/10.1016/j.ejrad.2021.110136

Other communications

Table 1: Other written communications (i.e. essays, conference abstracts and posters that are part of the doctoral fellowship).

Year	Title	Type
2018	Internet of Heads	MNSES9100 essay
2019	Hovden, I.T., Digernes, I., Emblem, K.E.. Susceptibility Distortion Correction for Registration of Perfusion and Anatomical MRI	ISMRM 2019 abstract
2019	Optimizing Artificial Neural Network Hyperparameters and Architecture	IN9400 review
2019	Echo Planar Imaging (EPI) Distortion Correction for Accurate Coregistration of Perfusion and Anatomical MRI	NMFM 2019 abstract and poster
2019	Hovden, I.T., Digernes, I., Geier, O.M., Digernes, Løvland, G., Vik-Mo, E., Meling, T.R., Emblem, K.E. How does magnetic susceptibility distortion impact EPI-based perfusion MRI?	ESNR 2019 & GeiloWS 2020 abstract and poster
2019	Hovden, I.T., Geier, O.M., Digernes, I., Fuster-Garcia, E., Løvland, G., Vik-Mo, E., Meling, T.R., Emblem, K.E. Increased cerebral blood volume in cortical and subcortical brain regions in Glioblastoma patients after EPI distortion correction	ISMRM 2020 abstract
2020	Installation and documentation of remote access (VPN) connection for computational radiology and artificial intelligence (CRAI) during and after the Covid pandemic	Research support documentation
2021	Fuster-Garcia, E., Albarracín, J.J., Hovden, I.T., Ávarez-Torres, M., Rovira, A., Oleaga, L., Revert, A.J., Filice S., García-Gómez, J.M., Emblem, K.E. The use of a DSC-MRI perfusion atlas for cerebral blood volume normalization and its impact in improving prognostic estimation	ISMRM 2021 abstract and poster

Table 2: Oral communications (mostly presentation slides) highlighting the various research meetings and discussions of the doctoral fellowship.

Year	Title	Type
2018	Geometrisk korreksjon av EPI for perfusjonsbilder	Presentation
2019	Echo-planar Imaging distortion correction in Glioblastoma patients	Presentation KRN PhD Seminar
2019	The Impact of EPI-based Distortion Correction of Dynamic Susceptibility Contrast MRI in Patients with Glioblastoma	Presentation MAGNETOMforum
2019	3. Semesterrapportering	Presentation
2019	Programvaretips for dyp læring	Presentations

2019	Workshop i bruk av Git og GitHub, avdeling for diagnostisk fysikk (ADF), Oslo universitetssykehuss (OUS)	Presentation
2019	Visuell tolkning av (dype) konvolusjonelle nevralnett	Presentation
2020	Hovden, I.T., Geier, O.M., Digernes, I., Fuster-Garcia, E., Løvland, G., Vik-Mo, E., Meling, T.R., Emblem, K.E., 2020. Increased cerebral blood volume in cortical and subcortical brain regions in Glioblastoma patients after EPI distortion correction	Presentation ISMRM 2020
2020	Two models for pushing tumor growth	Presentation
2020	Synthetic tumor growth models for validating displacement estimation algorithms on Glioblastoma progression	Presentation
2020	Installation and documentation of remote access (VPN) connection for CRAI during and after the Covid pandemic	Research support
2021	Validating the use of nonrigid registration methods for tracking tumor growth by benchmarking methods on synthetic growth cases with known ground truth displacements	Presentation
2021	Displacement in brain cancer	Presentation
2021	Displacements in brain cancer imaging	Presentation
2021	Synthetic and estimated tissue displacement in high-grade glioma	Presentation
2021	Retrospektiv analyse av glioblastom	Presentation
2021	Statistisk modellering av behandlingsrespons	Presentation
2021	Principal components, autoencoder and glioblastoma	Presentation
2020-2021	cancer-sim	Presentations
2022	Quantification of ventricle and tumor volume change in treatment of glioblastoma (tumors vs. ventricles)	Presentations
2022	CBV vs. ventricles	Presentation
2022	Developing reproducible research imaging datasets	Presentation
2022	MRI processing for tracking	Presentation
2019-2022	Hardware and software installation and user management support for data analysis servers at Department of Physics and Computational Radiology (FBA) and CRAI: gpu-fys, Miniserver1, Miniserver2, Miniserver3. Disposal by researchers, physicists, engineers and students at UiO and OUS	Research support

Acronyms and important symbols

AAIR Age-adjusted incidence rate

ADC Apparent diffusion coefficient

AE Autoencoder

AI Artificial intelligence

AIF Arterial input function

AIR Affine image registration

ANOVA Analysis of variance

ANTs Advanced normalization tools

AUC-ROC Area under the receiving operating characteristic curve

$\boldsymbol{B}$ Magnetic field, flux density (vector field) [$Tesla$]

BBB Blood-brain barrier

BIDS Brain imaging data structure

BOLD Blood oxygenation level dependent

CA Contrast agent

CBF Cerebral blood flow

CBV Cerebral blood volume

CC Cross-correlation

CLI Command-line interface

CNS Central nervous system

CRT Chemoradiotherapy

CSF Cerebrospinal fluid

CT Computed tomography

ΔB Inhomogeneities in $\boldsymbol{B}$ (scalar field)

$\boldsymbol{d}$ Voxel coordinate displacement field (vector field)

DCE Dynamic contrast-enhanced

DCT Discrete cosine transform

DFT Discrete Fourier transform

DICOM Digital imaging and communications in medicine

DIR Deformable image registration

DL Deep learning

DSC Dynamic susceptibility contrast

DTI Diffusion tensor imaging

DVC Data version control

EEG Electroencephalography

EGFR Epidermal growth factor receptor

EPI Echo-planar imaging

EPIC EPI distortion correction method

FID Free induction decay

FLAIR Fluid-attenuated inversion recovery

fMRI Functional MRI

FSL FMRIB Software Library

GBCA Gd-based CA

Gd Gadolinium

GE Gradient echo

GPU Graphics processing unit

GUI Graphical user interface

HGG High-grade glioma

ICBM International consortium for brain mapping

IDH Isocitrate dehydrogenase

K_2 CA leakage parameter from Boxerman et al. CA leakage correction in DSC

K_a CA apparent transfer constant from Bjørnerud et al. CA leakage correction in DSC

K^{trans} CA volume transfer constant from kinetic analysis in DCE

KM Kaplan-Meier

LDDMM Large deformation diffeomorphic metric mapping

LIR Linear image registration (consisting or RIR and AIR)

MEG Magnetoencephalography

MGMT Methylated O-6-methylguanine-DNA methyltransferase

MI Mutual information

MNI Montreal neurological institute

MR Magnetic resonance

MRI Magnetic resonance imaging

MTT Mean transit time

NN Nearest neighbor

NAWM Normal-appearing white matter

NIFTI Neuroimaging informatics technology initiative

NIPALS Non-linear iterative partial least squares

NMR Nuclear magnetic resonance

OASIS Open access aeries of imaging studies

OF Optical flow

PCA Principal component analysis

PET Positron emission tomography

PFS Progression-free survival

PNS Peripheral nervous system

QC Quality control

R_2 T_2 relaxation rate

R_2^* FID relaxation rate

RANO Response assessment in neuro-oncology

RAVEL Removal of artificial voxel effect by linear regression

RBF Radial basis function

rCBV Relative CBV

RF Radiofrequency

RIR Rigid image registration

ROI Region of interest

SE Spin echo

SPM (12) Statistical parametric mapping (version 12)

SVD Singular value decomposition

SyN Symmetric normalization

T Dense voxel coordinate displacement transformation

T_1 Tissue dependent transversal (spin-lattice) relaxation time constant

T1w T_1 weighted

T1wc T_1 weighted post-contrast

T_2 Tissue dependent longitudinal (spin-spin) relaxation time constant

T_2^* FID time constant

T2w T_2 weighted

T2*w T_2^* weighted

TE Echo time

TERT Telomerase reverse transcriptase

TI Inversion time

TMZ Temozolomide

TOPUP EPI distortion correction method from FSL

TR Repetition time

URL Uniform resource locator

WHO World Health Organization

χ Magnetic susceptibility (dimensionless quantity)

Contents

1. Introduction

Brain cancer is a deadly form of central nervous system (CNS) cancer within the restricted space of the skull in the brain leading to poor treatment options and prognosis. Magnetic resonance imaging (MRI) is the preferred method for imaging and assessing response from all stages of treatment, involving pre-surgical planning, surgery, chemo, and radiotherapy.

MRI provides excellent tissue contrast for imaging cancer and treatment specific biological processes. Some examples are quantification of volume change in delineated regions of interest (ROIs), detecting structural deformations from the mass effect of a growing tumor, and detecting intensity increase from active tumor regions because of endogenous paramagnetic contrast agent (CA) accumulation on T1-weighted post-contrast (T1wc) MRI. Two other examples are intensity image increase on T2-weighted (T2w) fluid attenuated inversion recovery (T2w-FLAIR) MRI, as well as cerebral blood volume increase on perfusion MRI.

Because brain cancer diagnostics and prognostics depend on these MRI methods, it is essential that they provide stable and comparable images and values. The thesis tackles such issues by investigating diagnostic and prognostic aspects and utilities of various image geometry and intensity correction methods as well as deformable image registration (DIR).

Using these advanced computational tools to improve patient care requires adequate crosstalk between physicists, computer scientists and oncologists to fulfil the needs of the oncologists, and to overcome the technical burden of terminology used by physicists and computer scientists.

The main outcome of this work is an investigation into tracking clinically meaningful imaging properties of single series and longitudinal MRI of brain cancer. It provides methodology to achieve fine grained analysis of structural and functional changes as function of disease progression and treatment response. This may enable better and earlier stratification of brain cancer patients into different treatment regimen and thus more personalized treatment options.

2. Aims

The three publications which are the main scientific contributions in the doctoral work, constitute the following aims:

Paper 1

Investigate the impact of magnetic susceptibility distortion correction on geometry and intensity of cerebral blood volume estimated from perfusion MRI.

Paper 2

Develop tissue displacement biomarkers from deformable image registration associated with radiological assessment of brain tumor treatment response and overall survival prediction.

Paper 3

Develop a tumor tissue deformation model for performing parametric evaluations of geometric accuracy of deformable image registration methods in brain tumor MRI.

3. Background

3.1.The brain

The brain is a vital organ that together with the spinal cord forms the CNS. This is where we process and interpret thoughts, memory, emotion, touch, motor skills, vision, breathing, temperature, hunger, and every process that regulates our body.

It runs on chemical energy, mostly glucose transmitted through the blood supply, to process and make sense of sensory input using combined electrical and chemical signals within and across functional tissue of various brain regions. Sensory information such as touch, vision, hearing, and smell are transmitted through spinal nerves from either the spinal cord or cranial nerves which make up the peripheral nervous system (PNS).

Some characteristic properties of the brain are hollow-like cavities called ventricles, which are filled with a colorless watery fluid called cerebrospinal fluid (CSF). The brain is also immersed in this CSF which can flow from the ventricles through special drainage canals. The CSF cushions the brain from injury and is constantly being absorbed and replenished. As an effect it washes out waste and impurities as well as delivers additional nutrients [1], [2].

3.1.1. Brain matter and cellular composition

The average adult healthy brain is a mass of about $1.4\ kg$ consisting of approximately $60\ \%$ fat and $40\ \%$ water, protein, carbohydrates and salts [2]–[4]. On a cellular level, its composition is mainly formed by nerve (neurons) and glial cells which carries out computation and nourishment tasks, respectively. A study found that on average, the human brain contains about 86 billion neurons and about the same amount of non-neuronal cells [5]. A less than $1{:}\ 1$ ratio of glia to neurons in the entire human brain was also

supported in a recent review [6]. The location of these cells, however, depends on brain structure and function. Only about 16 billion neurons exist in the cortical gray and white matter, with most of the remaining neurons are located in the cerebellum (hindbrain) [5], [7]. Cortical gray and white matter may take up as much as 80 % of the total brain volume [3], [5].

In general, neurons have their cell body (the soma) located in outer layers of the various brain regions and structures. This describes the gray matter of the brain. Within the gray matter, neurons can pick up messages from other nerve cells from dendrites, over synaptic gaps. Neurons transmit signals through long nerve fibers called axons, which connect brain regions to each other. These nerve fiber tracts make up the white matter, which is the lighter inner section underneath gray matter.

Some types of glial cells are astrocytes which are involved in numerous functions such as blood-brain barrier (BBB), homeostasis and neuronal growth [8], and oligodendrocytes which are involved in insulating neuronal axons for faster signal transmission [9]. Oligodendrocytes do this by creating and adding a myelin (fat) layer to axons within the white matter. The color difference between gray and white matter in the brain mainly arises from the whiteness of myelin. Unlike most cell bodies of neurons existing in gray matter, their axons exist in both white and gray matter. However, only axons in white matter are myelinated. Some other cell types in the brain are endothelial cells [10] (in blood vessels) and ependymal cells [11] (in ventricular walls) (Figure 1 [12]).

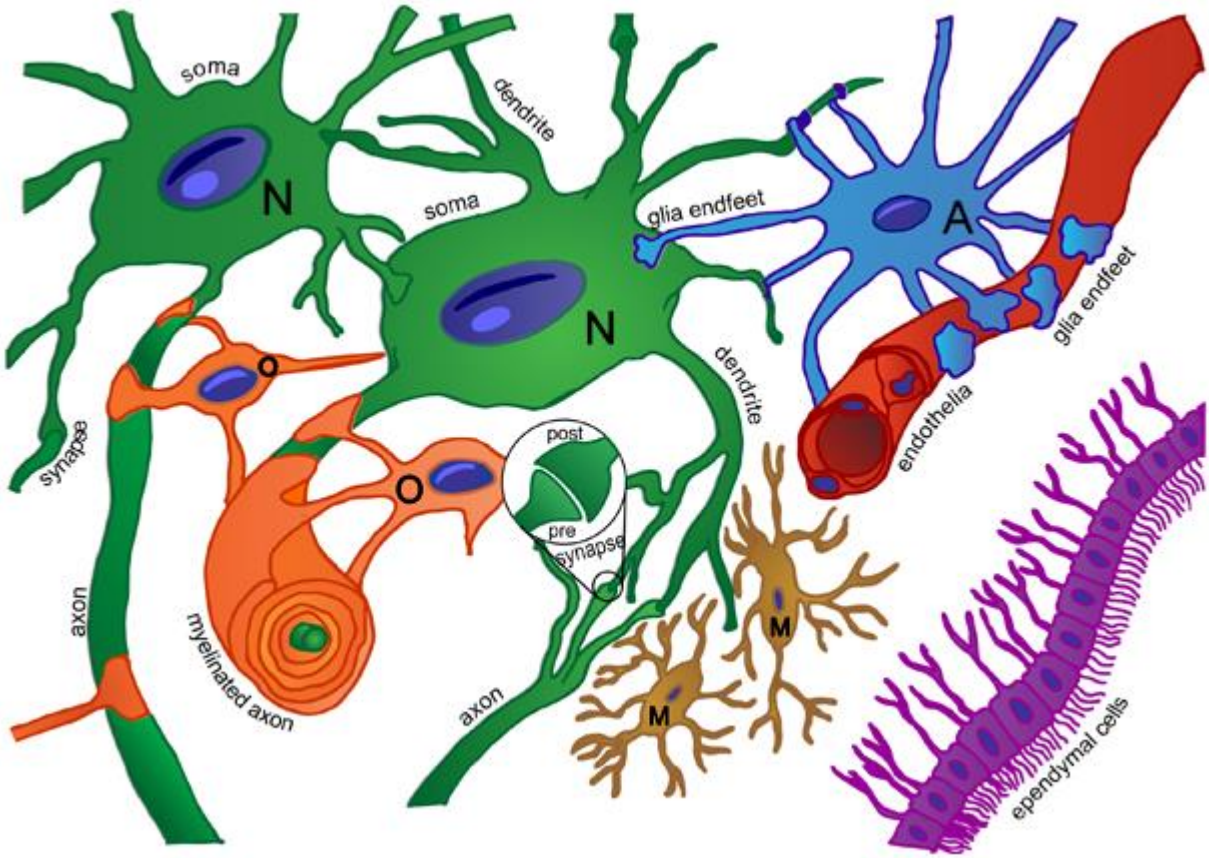

Figure 1: The different types of neurological cell classes (ependymal cells, purple and endothelial cells, red)), subpopulations (A=astrocytes, blue; M=microglia, brown; N=neuron, green; O=oligodendrocytes, orange), and subcellular locations (axon, dendrite, synapse, and glia endfeet). Used with permission from proteinatlas.org.

3.1.2. Brain structure

The brain is divided into the cerebrum (main part), cerebellum (hindbrain) and brain stem. The cerebrum and cerebellum have a symmetric structure consisting of left and right hemispheres. The hemispheres of the cerebrum are connected through a c-shaped nerve fiber structure called the corpus callosum. Each cerebrum hemisphere has four distinct parts; the frontal, parietal, temporal and occipital lobe as seen in Figure 2 [13].

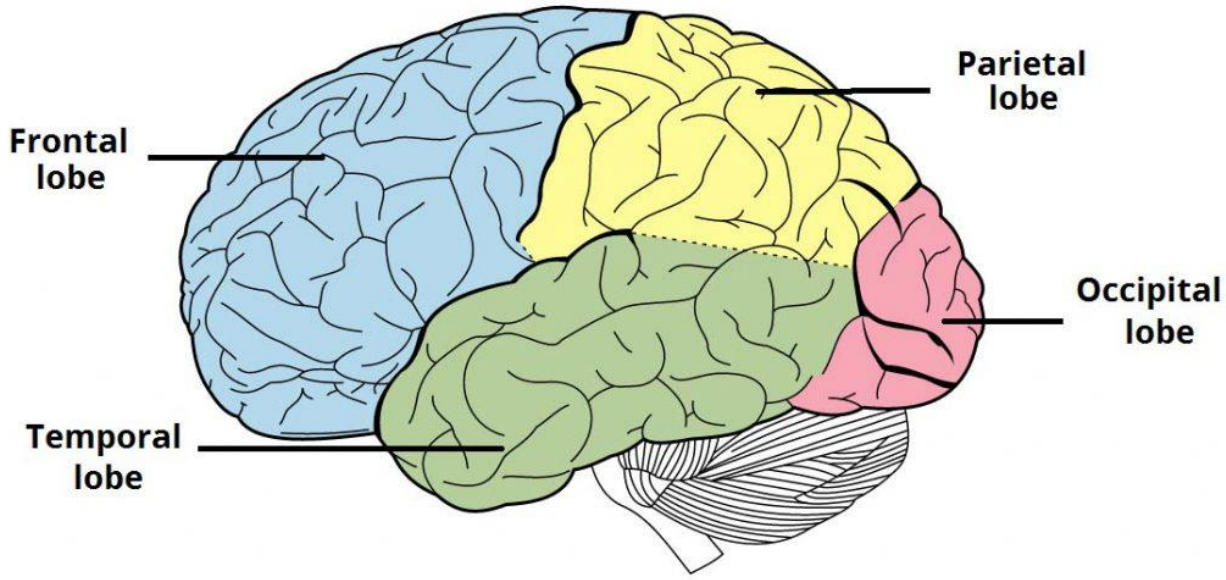

Figure 2: The major parts of the brain. The colored parts are the cerebrum. Used with permission from teachmesurgery.com.

The outer gray matter of the cerebrum is the cortex (latin for “cork or “bark”), for which Figure 3 [14] shows the various cortical regions. The cortex has many ridges (gyri) and folds (sulci), which leads to a large total cortical surface within the confined area of the skull. Cortical regions are also found along the mid/medial coronal cross section of the brain as shown in Figure 4 [14]. Figure 3 and Figure 4 was generated by a recent three-dimensional (3D) brain atlas application [15]. Moreover, deep brain structures are further classified into subcortical regions, most of which are located within the cerebrum. Gray matter exists also in some subcortical regions in deep gray nuclei (Figure 5) [16]. For further description of brain structure, see the reference for the Figure 5 [16].

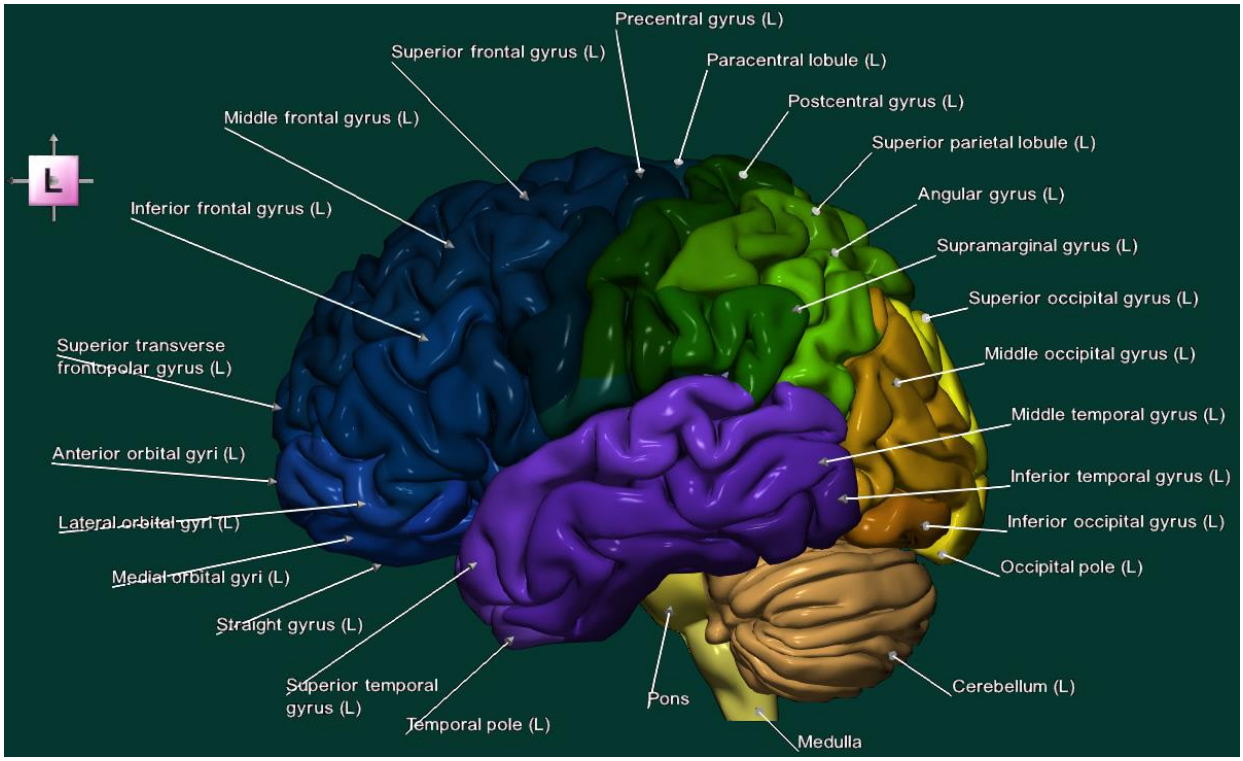

Figure 3: Cortical regions in the left-brain hemisphere. Most of these regions have right-brain counterparts. Used with permission from nowinbrain.org.

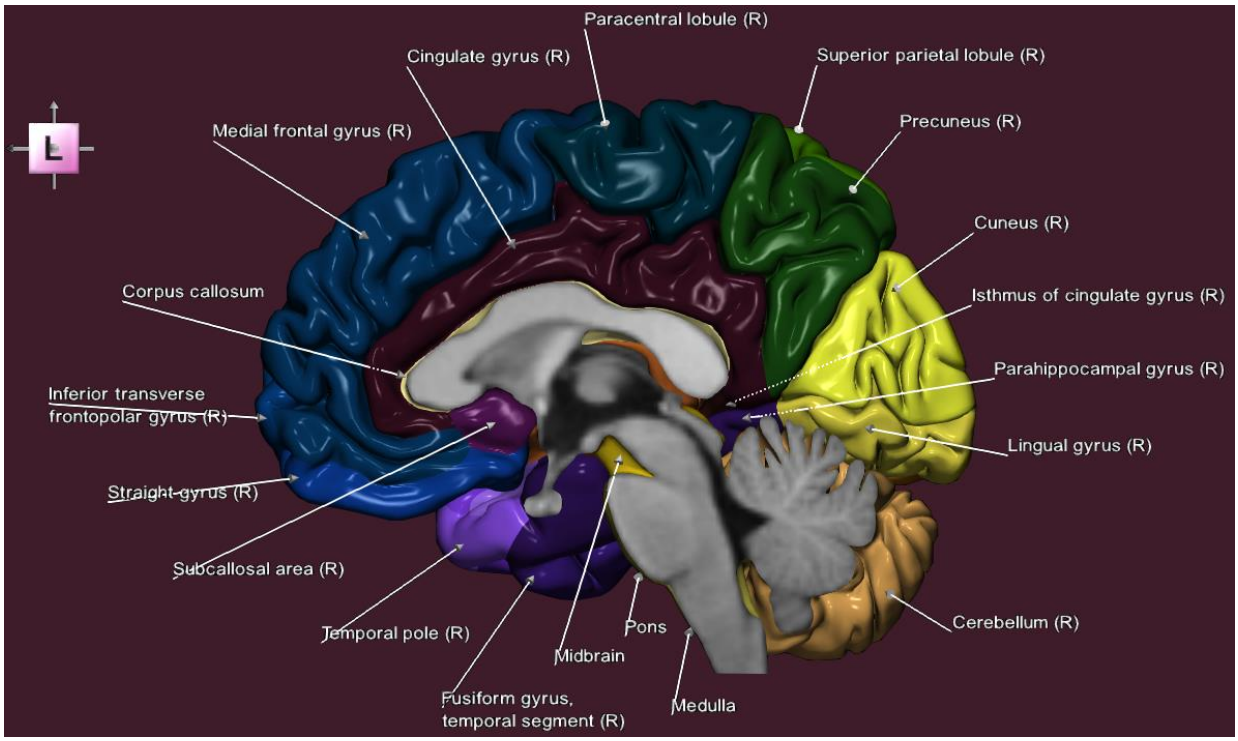

Figure 4: Mid-sagittal (medial) section, showing the beginning of the right-hemisphere brain. Multiple cortical and subcortical regions are shown. Opposed to the cerebellum and brainstem, the cerebrum right and left hemisphere consists of gyri and sulci folding inwards before they are joined.

Corpus callosum is the main structure connecting the left and right brain hemispheres of the cerebrum. Used with permission from nowinbrain.org.

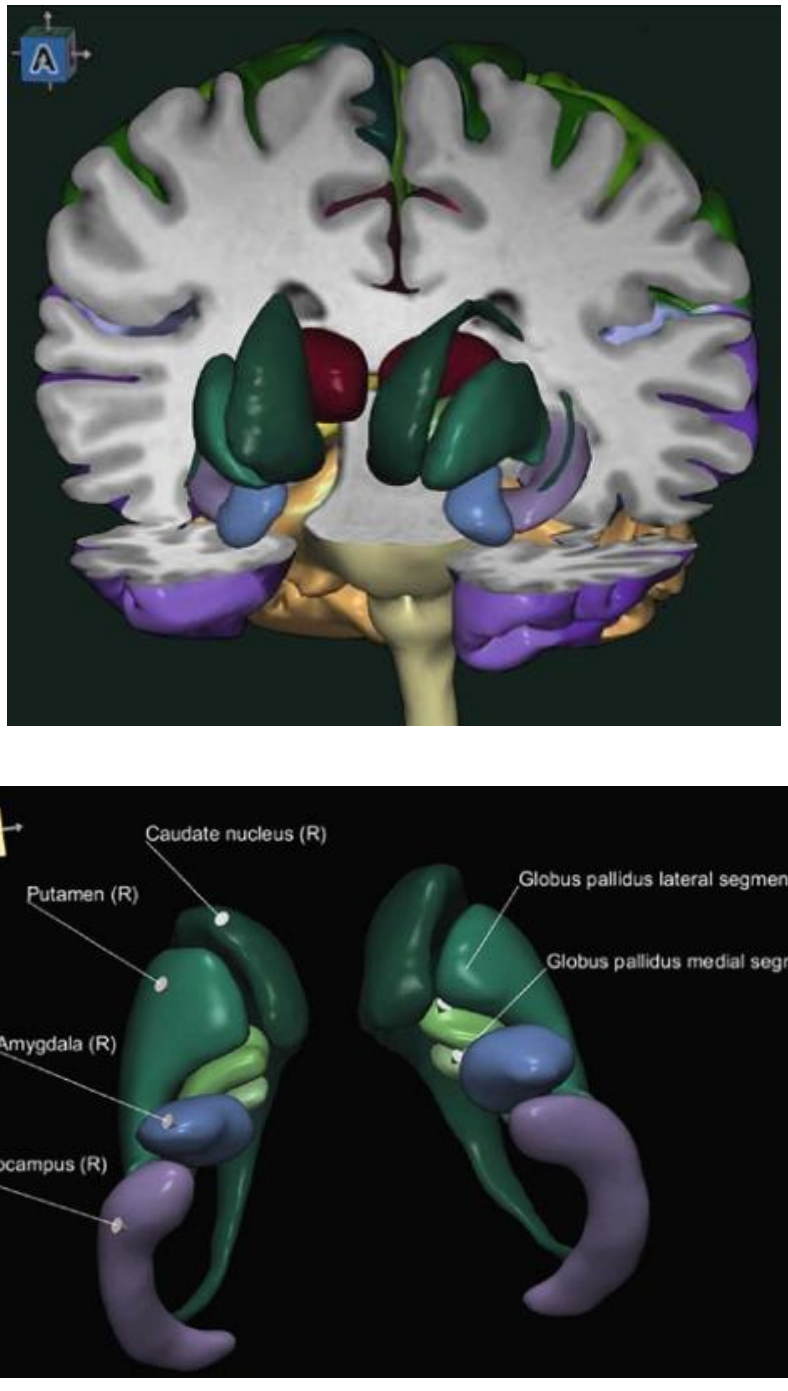

Figure 5: Deep gray nuclei embedded into the brain (top) and shown in isolation (bot). Used with permission from Springer Nature (License number: 5434900686146) and corresponding author (nowinbrain.org).

3.1.3. Brain function

Various brain regions are known to carry out specific tasks [2], [7], [17], [18]. The frontal lobes are associated with higher-level functions such as personality characteristics, decision making, complex body movement (motor strip), producing speech and short-term memory. Occipital lobe is primarily associated with vision, while the parietal lobe is associated with interpreting language and words, sense of touch and smell, and spatial and visual perception among others. The temporal lobe is associated with language understanding, hearing, navigation, and long-term memory among others. Some important subcortical regions are hypothalamus for controlling body temperature and hunger, hippocampus (in the temporal lobes) for long-term memory and midbrain for hearing and movement control, among others. Last, the cerebellum is associated with lower-level functions such as muscle movement and posture.

Language and speech are some of the functions that occur commonly in only one of the hemispheres, such as the left hemisphere typically for right-handed people [19]. Also, communication between the various regions is necessary in performing some tasks, such as speech and learning.

A neuron-centric description of brain function is that gray matter is responsible for processing and interpreting information (through neurons), while white matter transmits that information to other parts of the CNS (through axon fiber bundles). Neurons and their interconnections are the most essential parts in the computational description of the brain, attempting to explain all mental processes known as cognition.

The brains' functional characteristics are however not limited to sensory processing by neurons. For instance, blood vessels and non-neuronal cells play essential roles in

nourishment, protection, and structural support. Much is yet to be discovered about the brain. The glymphatic system [1] is another example of brain function which was recently classified as a system for waste clearance in the CNS [20].

3.1.4. Eloquent areas

In treatment such as neurosurgery, it is important to avoid damage to areas that are essential for the kinds of functional sensory processing described previously. An eloquent area or eloquent cortex is a region that, if removed, will result in loss of sensory processing, or linguistic ability, or paralysis [21], [22]. The most common eloquent areas are in the left temporal and frontal lobes. Some examples are Wernicke's area of speech comprehension in the temporal lobe, and Broca's area of speech production in the frontal lobe. Moreover, a surgeon must make sure to not damage important axon fiber bundles between regions.

3.1.5. Conventional imaging planes

Like other tomographic medical imaging techniques, brain MRI follows conventions in axial, sagittal and coronal sections as illustrated in Figure 6. The most common image view is the axial view of a brain (termed "horizontal section" in Figure 6), which typically shows the characteristic symmetric brain structures.

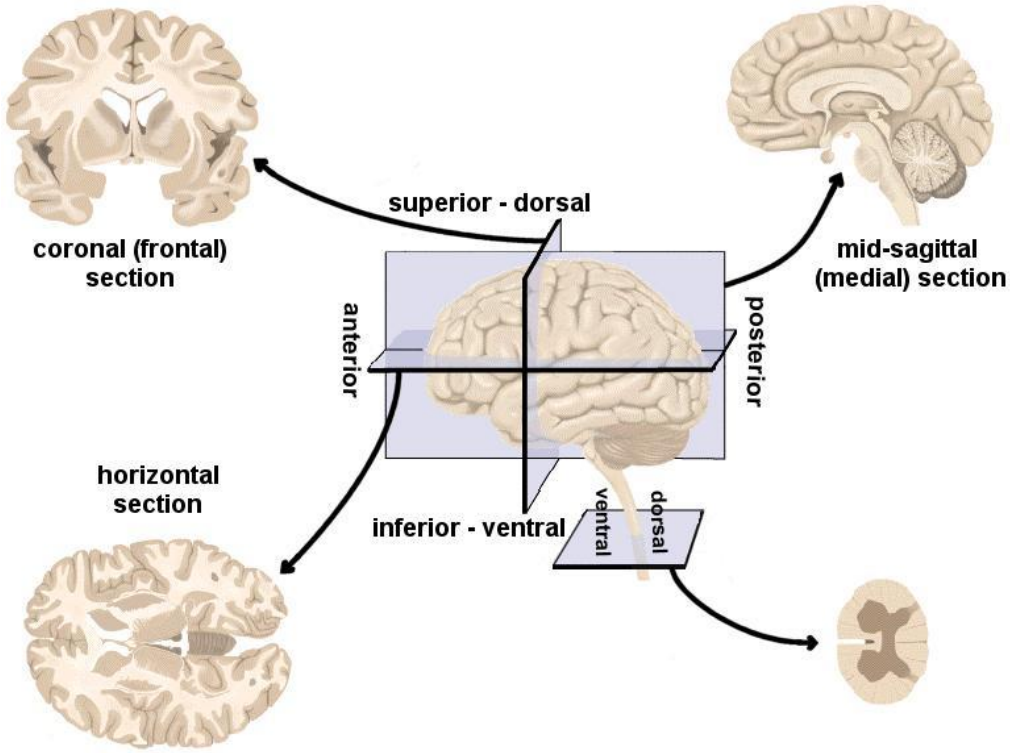

Figure 6: Conventions in brain imaging planes and naming. Used with permission from My-MS.org.

3.1.6. Imaging brain structure and function

There are various techniques for imaging brain structure and function, such as MRI, computed tomography (CT) and positron emission tomography (PET). The thesis focuses on MRI, which will be described later. Most of these techniques image tissue on a macroscopic level due to limitations in spatial resolution (0.5 to $5\ mm^3$). They are generally non-invasive methods, meaning that no physical procedure (such as surgery) is necessary for imaging. Intravenous injection of a CA is common to increase image contrast in regions where it accumulates, which then makes the imaging method an invasive method.

3.1.6.1. Imaging brain structure

T1w MRI directly presents gray matter as having lower intensity values (are grayer) than the white matter regions. This is a result of differences in T_1 relaxation times whereby grey matter exhibit longer T_1-times than white matter. The concept of relaxation times and

weighting in MRI is explained in section 3.3.3 and 3.3.4, respectively. Typically, various combinations of T1w and T2w in MRI result in imaging the brain structure of interest, which may involve imaging with an intravenous MR active (paramagnetic) compound (=CA) to highlight pathology such as tumors. This is due to the fact the CA tends to accumulate in regions with cancerous tissue, for reasons such as disrupted BBB and abnormal vessel formation (angiogenesis). Moreover, diffusion tensor imaging (DTI) based tractography is an advanced technique to map and track the white matter axon fiber bundles, which is useful in surgical planning. This kind of tracking is not investigated in the thesis. The structural tracking methods addressed in the thesis focuses on tracking and interpreting intensity values and displacement of signal as seen on high-resolution MRI that are of clinical interest (such as structural deformations) from longitudinal MRI of cancer progression and treatment follow-up.

3.1.6.2. Imaging brain function

Functional imaging typically acquires images with lower spatial resolution than structural imaging due to the requirement for high temporal resolution. Blood oxygenation level dependent (BOLD) imaging is the most common functional MRI technique where small variations in blood oxy/deoxygenation levels related to sensory or auditory processing is detected based on their differential magnetic susceptibility (deoxygenated hemoglobin is paramagnetic and oxygenated hemoglobin is diamagnetic) [23]. This is called the hemodynamic response resulting from delivering nutrients (like oxygen and glucose) to neuronal tissue through blood flow. BOLD fMRI may be applied to determine eloquent areas prior to surgical removal of brain tumors [24], [25]. Electroencephalography (EEG) [26] and Magnetoencephalography (MEG) [27] are two complementary non-invasive techniques for

directly recording electric and magnetic field potentials, respectively, resulting in higher temporal resolution signals than BOLD fMRI. EEG and MEG are not imaging methods but may accompany medical imaging to further elucidate brain function. The functional side of brain cancer MRI is not focused on direct imaging of cognitive processes, but rather on imaging vascular properties of the brain and disease that may aid diagnostics and treatment. One such method, blood perfusion MRI, is the functional imaging method investigated in the thesis. Here, the consistency of cerebral blood volume (CBV) values from perfusion MRI during geometric susceptibility distortion correction, is investigated through careful tracking their pixel-wise intensity value and displacement.

3.2. Brain cancer

Brain cancer is cancer in the CNS characterized by various abnormalities in cell growth and death occurring within the brain, either as primary tumors where the cancer originates from cells within the brain, or as secondary tumors originating from cancer in other parts of the body and then spreading to the brain and forming secondary tumors as metastases [28]. Glioblastoma, the main type of cancer investigated in the thesis, is the most common and most deadly type of primary brain tumor in adults [29].

3.2.1. Incidence

Although incidence is low compared to other types of cancers [30], brain and other CNS tumors are among the leading causes of cancer deaths for young adults with only one-third of individuals surviving at least 5 years after diagnosis [31], [32]. The overall age-adjusted incidence rate (AAIR [33]) of glioblastoma in the United States is $3.22/100000$ persons and increases with age. Moreover, the 5-year relative survival varies by age at diagnosis and by sex (Figure 7 [29]).

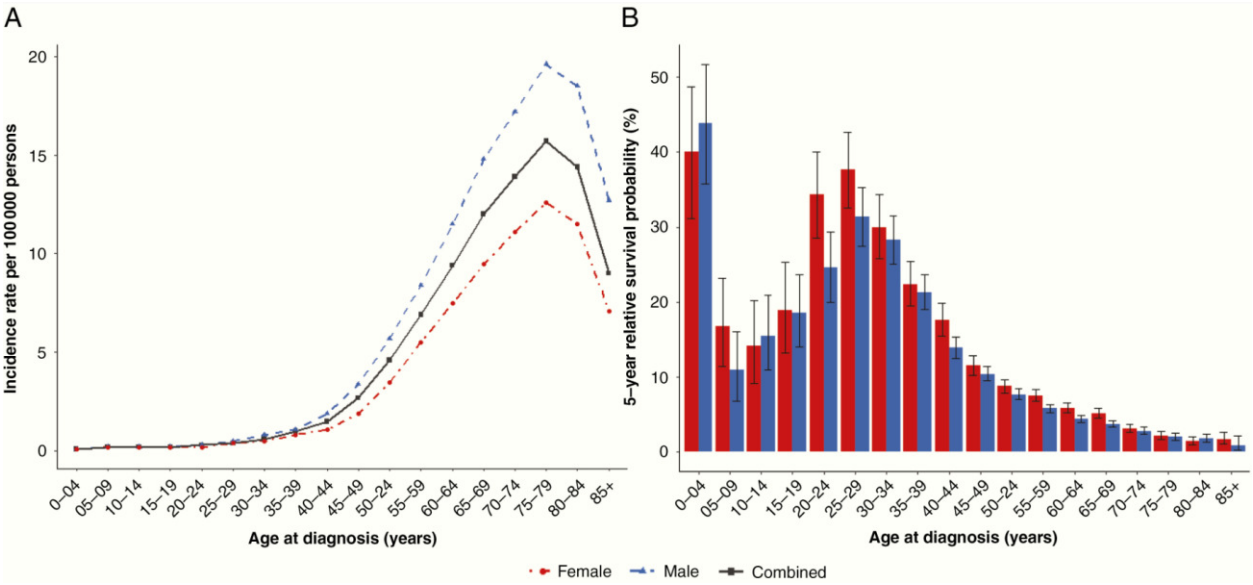

Figure 7: Age distribution of incidence (A) and 5-year relative survival probability (B) of Glioblastoma. Used with permission from Oxford University Press and corresponding authors (License number: 5431381256692).

In general, AAIR of malignant brain and other CNS tumors are higher in western and European countries than in other parts of the world (roughly $AAIR/100000 \sim 6$ vs. ~ 3), and dominated by astrocytic tumors in males [31], [34]–[36]. Moreover, cancers in other parts of the body such as lung cancer with ~ 7 times higher incidence than primary CNS tumors in 2020 [30], may also contribute to increased mortality of CNS tumors when causing secondary brain tumor metastases.

3.2.2. Characterization and grading

There are more than 100 different subtypes of CNS tumors, of either malignant or benign type [37]. Gliomas consist of multiple subtypes of astrocytic tumors originating from glial cells of the brain and make up approximately 80 % of all malignant brain tumors. They are the most common primary CNS brain tumors [38]. Of gliomas, glioblastoma is the most aggressive type, and it compromises of approximately 57 % of all gliomas and 48 % of all primary malignant CNS tumors [39].

The 2016 World Health Organization (WHO) guidelines [37], [40] uses a combination of MRI, histopathological and molecular features for CNS tumor characterization, which typically involves determining the presumed cell of origin and a grade of aggressiveness (I-IV) together with various genotype and phenotype markers. Grade III and IV gliomas are commonly referred to as high-grade gliomas (HGG), with grade IV being a glioblastoma. The grade of aggressiveness of a glioma is traditionally determined by comparing cells of origin with different levels of tumor cell differentiation on light microscope of histology tissue samples. An important molecular feature is mutation in the gene coding for the enzyme isocitrate dehydrogenase (IDH), to further distinguish subtypes of glioma. In general, the prognosis of an IDH-mutant glioma is better than the IDH wild-type counterpart.

The 2021 WHO guidelines [41] consist of revised tumor characterization and grading by incorporating additional genetic parameters, such as telomerase reverse transcriptase (TERT) gene promoter mutation or epidermal growth factor receptor (EGFR) gene amplification for identifying IDH-wild-type glioblastoma. Roman numerals describing tumor grade (I-IV) is also revised to using Arabic numerals (1-4) to eliminate possible misdiagnosis from typographical errors. Another important revision is eliminating the term IDH-mutant glioblastoma in favor of IDH-mutant astrocytoma. Further descriptions of the 2016 and 2021 WHO grading systems and their differences for glioma grading, can be found in this recent thesis [42]. Due to limited molecular data for our patients, our data is described in line with the 2016 WHO guidelines.

3.2.3. Treatment

The standard treatment for glioblastoma is known as the Stupp regimen [43] and consists of tumor resection (stereotactic surgery) followed by stereotactic radiation therapy and

concomitant and adjuvant chemotherapy (CRT with temozolomide (TMZ)). Stereotactic (word roots *stereo-* meaning "solid" and *-taxis* meaning "arrangement"), here refers to the use of a three-dimensional coordinate system to accurately locate small targets inside the brain. Still, this treatment leads to a dismal median overall survival of $12 - 15$ months with less than $5\ \%$ of all patients surviving 5 years after diagnosis [44]–[46]. High quality imaging methods are important to ensure the best suited treatment regimen and follow-up, and thereby highest possible quality of life for the patient. Maximal surgical resection of the tumor according to high intensity regions on T1wc MRI is the standard practice and associated with survival benefits [47]. However, resecting also larger regions with high intensity value on T2w-FLAIR surrounding the high intensity T1wc regions may also lead to increased survival [48]. Biopsies may be collected both before and during treatment for optional histopathological assessment [49].

3.2.4. Presentation on MRI

On T1wc MRI, a glioblastoma usually presents as an irregularly shaped mass with a dense hyperintense ring of enhancement, and with a hypointense center of necrosis (Figure 8 and Figure 9). The supplementary files **animation.mp4** and **animation-multi.mp4** provided with the thesis, visualize longitudinal T1w, T1wc, T2w and T2w-FLAIR for the patient in Figure 9. They are also available at the following URLs (as accessed December 3rd, 2022):

https://www.mn.uio.no/fysikk/english/people/aca/ivarth/works/viz/animation.mp4

https://www.mn.uio.no/fysikk/english/people/aca/ivarth/works/viz/animation-multi.mp4

To further visualize the disease, the supplementary file **rbf-interp-animation.mp4** approximates a smooth time evolution of the T1wc scans as will be explained later. It is also

available at the following URL (as accessed December 3rd, 2022):

https://www.mn.uio.no/fysikk/english/people/aca/ivarth/works/viz/rbf-interp-animation.mp4

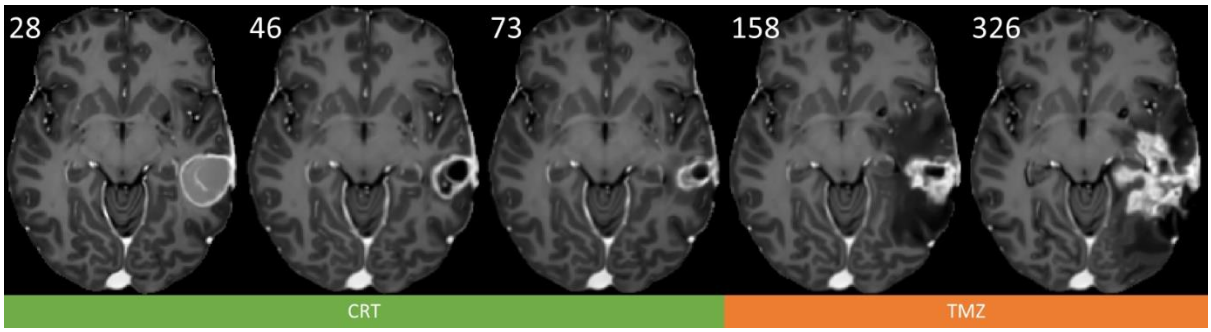

Figure 8: Time-lapse of contrast enhanced T1w MRI of standard treatment of glioblastoma with infiltrative recurrence. A 47-year-old male with confirmed glioblastoma received stereotactic surgery for removal of most of the tumor tissue at day 0 (not shown). About four weeks later (day ~28), the post-surgical cavity in the left temporal lobe was visible and surrounded by contrast enhancement of excess or new tumor tissue. Repeated chemoradiotherapy (CRT) and imaging presented shrinkage of the tumor cavity and surrounding regions (days 46 and 73 at completion of CRT). Then following chemotherapy with temozolomide (TMZ) only presented images with infiltrative recurrence with edema (day 158) and with contrast enhancement (day 326). Some tissue deformations were also seen in subcortical regions such as the basal ganglia and midbrain. Overall survival for this patient was around 16 months (480 days). This is subject nine from our second cohort (SAILOR, MRI 1,2,4,6,8).

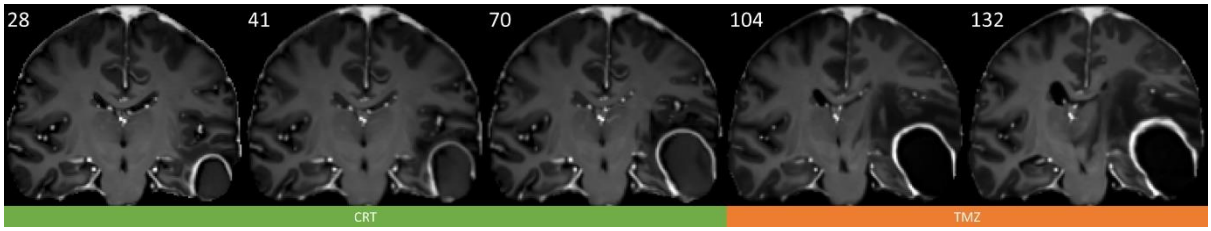

Figure 9: Time-lapse of contrast enhanced T1w MRI of standard treatment of glioblastoma with strictly nodal ("pushing") phenotype. A 64-year-old female with confirmed glioblastoma received stereotactic surgery for removal of most of the tumor tissue at day 0 (not shown). About four weeks later (day ~28), the post-surgical cavity in the left temporal lobe was visible and surrounded by contrast enhancement of excess or new tumor tissue. Repeated chemoradiotherapy (CRT) and imaging presented expansion of the tumor cavity resulting in compression of surrounding tissue regions (days 41 and 70 at completion of CRT). Then following chemotherapy with temozolomide (TMZ) images further showed cavity expansion, compression of surrounding tissue and edema (days 104 and 132). Overall survival for this patient was around 33 months (990 days), which may indicate that the treatment response and tumor recurrence represented pseudoprogression. This is subject one from our second cohort (SAILOR, MRI 1,2,4,5,6).

The tumor may also be surrounded by vasogenic edema, hemorrhage, and ventricular and midline shifts [44], [46]. Figure 9 presents midline shift as well as edema as dark peritumoral regions in T1wc MRI. In addition, T2w and T2w-FLAIR MRI are usually hyperintense at pathology such as edema (Figure 10). Tumoral and peritumoral CBV may provide additional clinical information in follow-up of glioblastoma such as prediction of survival and cancer progression [50], or differentiation of glioblastoma and brain metastasis [51]. One or more of T1w, T1wc, T2w, T2w-FLAIR and CBV MRI (Figure 9) are thus frequently used together as follow-up scans during standard treatment of glioblastoma.

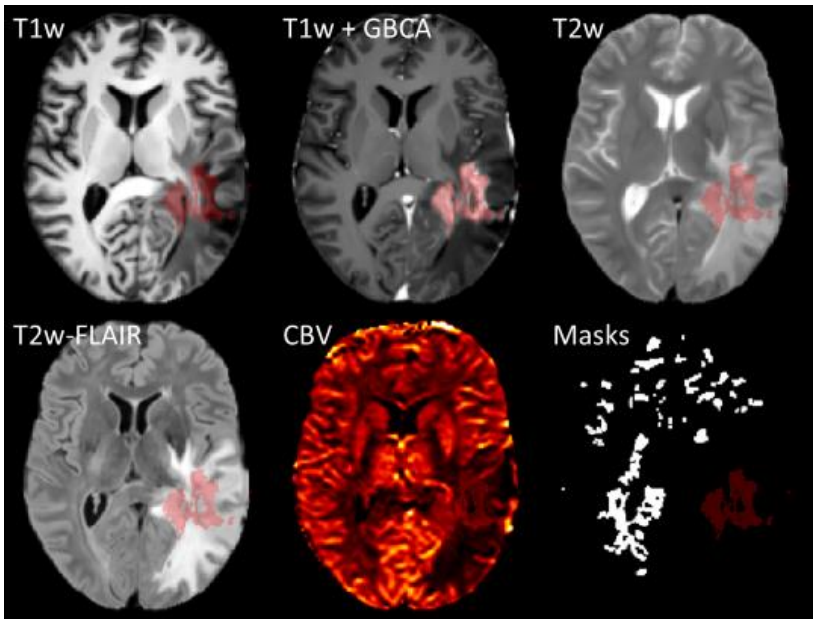

Figure 10: Various sequences in brain cancer MRI. GBCA: Gadolinium-based contrast agent, CBV: Cerebral blood volume. Overlaid in red is a segmentation mask of the hyperintense regions from accumulation of GBCA on T1w (upper row, middle). Normal appearing white matter regions (lower row, right) is used to normalize CBV maps.

3.2.5. Treatment response assessment

3.2.5.1. RANO

Response Assessment in Neuro-Oncology (RANO) is a consensus for how to categorize treatment response of HGG into the classes complete response, partial response, stable

disease and progression [52] as shown in Table 3. In general terms, response is working treatment leading to less cancer, while progression is the opposite leading to more cancer.

At its core, the assessment is performed at some time point during treatment by measuring the length of the two longest perpendicular diameters of the contrast enhanced tumor at a two-dimensional T1w scan, then computing the product of the diameters. This product is then compared to the corresponding product from a pretreatment baseline scan to determine response, and to the smallest product (at either baseline or a later time point) to determine progression. The required pretreatment baseline scan must be performed shortly after surgery, but before initiation of concomitant and adjuvant CRT.

Percentage thresholds of change of the products as well as complementary and clinical information are used in the assessment. Measuring perpendicular diameters of contrast enhanced tumor is not always feasible for reasons such as presence of cystic or necrotic tumor, surgical cavities, or lack of disruption of the BBB. RANO imposes guidelines for handling such cases by distinguishing between measurable and non-measurable lesions [52], [53]. A highly infiltrative tumor may for instance be non-measurable from lack of contrast enhancement on T1wc scans but still presenting as large regions on T2w or T2w-FLAIR scans. RANO classification is difficult for this scenario. Some other important clinical factors used in RANO are usage of corticosteroids and general clinical (Karnofsky performance) status [54] of the patient.

Table 3: Response Assessment in Neuro-Oncology (RANO) criteria.

Response	Criteria
Complete response	Requires all of the following: complete disappearance of all enhancing measurable and nonmeasurable disease sustained for at least 4 weeks; no new lesions; no corticosteroids; and stable or improved clinically
Partial response	Requires all of the following: $\geq 50\,\%$ decrease compared with baseline in the sum of products of perpendicular diameters of all measurable enhancing lesions sustained for at least 4 weeks; no new lesions; stable or reduced corticosteroid dose; and stable or improved clinically
Stable disease	Requires all of the following: does not qualify for complete response, partial response, or progression; and stable clinically
Progression	Defined by any of the following: $\geq 25\,\%$ increase in sum of the products of perpendicular diameters of enhancing lesions; any new lesion; or clinical deterioration

Presence of pseudoprogression and complex tumor behavior from novel and advanced treatment such as immunotherapy challenge the accuracy of RANO. It is likely that more robust methods such as automatic volumetric measurements and analysis from segmentation pipelines [55], [56] will replace RANO in the future. No patients in the longitudinal exams used in the second publication (our second cohort) experienced a complete response from the standard treatment. Here the following combined RANO+pseudoprogression classes were used instead; stable disease, pseudoprogression, partial response and progression. More information about our second cohort can be found in original data sources [50], [57].

3.2.5.2. Progression vs. pseudoprogression

Pseudoprogression is a type of classification of treatment response where it is not possible to distinguish between true (early) progression of the cancer and treatment effects (from e.g. radiation) on conventional follow-up MRI of glioblastoma [58], [59, p. 1]. One such scenario is when it is difficult to determine whether an intensity increase in the T2w-FLAIR image is caused by an increase in amount of cancer cells (thereby progression of non-enhancing tumor), or by inflammatory effects of the chemo- and radiotherapy (pseudoprogression) [60], [61]. Or, detecting intensity increase from CA accumulation in T1wc MRI that is not caused by cancer progression (enhancing tumor) but likely by increased permeability of the tumor vasculature from irradiation [52]. Mass effect, peritumoral edema, and CA enhancement due to BBB breakdown may appear in both progression and pseudoprograssion on conventional MRI [62]. Figure 9 illustrates a likely case pseudoprogression in our second cohort, partly due to the long survival of this patient.

Genetic data and fine-grained analysis of changes associated with the disease and treatment on conventional and advanced MRI as well as on histopathological images, may lead to insights for better distinguishing progression from pseudo-progression. Methylated O-6-methylguanine-DNA methyltransferase (MGMT) promoter methylation status has been valuable for this task [63], [64]. Some other valuable features are T1wc contrast-enhanced and T2w/T2w-FLAIR edema tumor shapes from radiomics analysis on conventional MRI [65], as well as histopathological radio-phenotypic signatures [58]. Advanced MRI techniques such as perfusion, diffusion and spectroscopic MRI have also proven useful in distinguishing progression from pseudoprogression [66]. For instance, relative CBV from dynamic susceptibility contrast (DSC) perfusion MRI studies have been reported to be significantly

lower in radiation-induced brain injury (pseudoprogression) than in glioma recurrence (progression) groups [67]–[69]. However, these are controversial results [69], [70]. Incorporating diffusion and perfusion MRI into a radiomics model also led to improved diagnostic performance for identifying pseudoprogression [71].

3.3.MRI physics

Medical MRI [72], [73] is a mainly non-invasive imaging method that exposes a near field magnetic interaction between tissue and external magnetic fields, to capture signals that are proportional to the proton density at various locations in the tissue. This interaction is called nuclear magnetic resonance (NMR), which is based on the fact that certain atomic nuclei with non-zero angular momentum (spin) absorb and re-emit electromagnetic radiation when exposed to a magnetic field [74], [75]. One such atomic nucleus is the single proton contained inside the hydrogen atom, which in the body is well represented in water (H_2O). This section provides a short introduction to the physics of MRI, such as weighting and pulse sequences. The book by Vlaardingerbroek et al. [73] is provided as reference to this section, unless a reference is explicitly given at the end of a sentence.

3.3.1. Spinning protons

Varying concentration of water (and to a lesser extent lipids) in tissue is responsible for making up the MRI signal. A spinning proton has a magnetic dipole moment which is a vector quantity that is defined by its spin. When experiencing magnetic induction through a magnetic vector field $\boldsymbol{B}$, a proton is capable of spinning in either a low or high energy quantum state with the magnetic dipole moment vector aligned either parallel or antiparallel to $\boldsymbol{B}$. This effect is best seen in a static uniform magnetic field ($\boldsymbol{B} = \boldsymbol{B}_0$). The angular frequency of the spin ω (the Larmor frequency), is proportional to the magnetic

field $\boldsymbol{B}$ according to $\omega = \gamma \boldsymbol{B}$ (Larmour equation), where γ is the gyromagnetic ratio. This is called Larmour precession.

3.3.2. Transversal magnetization

The basic principle of MRI is to control, spatially localize and record net proton spin densities by utilizing Larmour precession using spatially encoding spin dephasing magnetic field gradients and additional sender and receiver coils for emitting and receiving radiofrequency (RF) signals. When only exposed to a strong magnetic vector field $\boldsymbol{B}$ (e.g., $3\ Tesla$), protons are aligned in their low energy (equilibrium) state and not emitting electromagnetic radiation. However, when a well-defined sequence of RF excitation pulses with intrinsic frequency equal to the Larmor frequency for a given spatial location, is emitted through a transversal (orthogonal) weaker dynamic magnetic field, net proton spins are knocked out of their equilibrium state. A net transversal spin magnetization vector field $\boldsymbol{M}_T$ can then be recorded by induced currents in orthogonal receiver coils during the timespan that the spins return to equilibrium. This process is called relaxation.

3.3.3. Relaxation

Let $\boldsymbol{i}, \boldsymbol{j}, \boldsymbol{k}$ be the orthonormal basis vectors of three-dimensional x, y, z space, i.e. $\boldsymbol{i} = [1 \quad 0 \quad 0]^T$, $\boldsymbol{j} = [0 \quad 1 \quad 0]^T$ and $\boldsymbol{k} = [0 \quad 0 \quad 1]^T$. The Bloch equations [74], [76] describe the relation between the magnetic field (flux density) $\boldsymbol{B}$, total spin magnetization $\boldsymbol{M}$ and transversal (T_2) and longitudinal (T_1) relaxation time constants according to

$$\frac{dM_x}{dt} = \gamma(\boldsymbol{M} \times \boldsymbol{B})_{\boldsymbol{i}} - \frac{M_x}{T_2} = \gamma(M_y B_z - M_z B_y) - \frac{M_x}{T_2} \tag{3.1}$$

$$\frac{dM_y}{dt} = \gamma(\boldsymbol{M} \times \boldsymbol{B})_{\boldsymbol{j}} - \frac{M_y}{T_2} = \gamma(M_z B_x - M_x B_z) - \frac{M_y}{T_2}$$

(3.2)

$$\frac{dM_z}{dt} = \gamma(\boldsymbol{M} \times \boldsymbol{B})_{\boldsymbol{k}} + \frac{M_0 - M_z}{T_1} = \gamma\left(M_x B_y - M_y B_x\right) + \frac{M_0 - M_z}{T_1}$$

(3.3)

T_1 and T_2 are tissue-specific constants and MRI sequences (a given combination of RF pulses, magnetic gradients and received coil signal readouts) can be designed to maximize image contrast between different tissues of interest. Broadly speaking, T_1 results from thermal agitation while T_2 results from nuclear interactions. The relaxations occur exponentially and during Larmor precession and for which the solutions to the Bloch equations are

$$M_x(t) = e^{-\frac{t}{T_2}}[M_x(0)\cos(\omega_0 t) + M_y(0)\sin(\omega_0 t)]$$

(3.4)

$$M_y(t) = e^{-\frac{t}{T_2}}[M_y(0)\cos(\omega_0 t) - M_x(0)\sin(\omega_0 t)]$$

(3.5)

$$M_z(t) = M_z(0)e^{-\frac{t}{T_1}} + M_0(1 - e^{-\frac{t}{T_1}})$$

(3.6)

Equilibrium is found with $t \to \infty$ where $M_x(\infty) = M_y(\infty) = 0$ and $M_z(\infty) = M_0$. T_1 relaxation is called spin-lattice relaxation since T_1relaxation ends in thermodynamic equilibrium with its surroundings (the “lattice”). Comparingly, T_2 relaxation is called spin-spin relaxation since it is caused by the spins interacting with each other, leading to dephasing.

In practice, spins are also phase distorted due to inhomogeneities in the magnetic field (ΔB) caused by internal and external factors. In general, external factors are related to the scanner itself, while internal factors are related to the imaged object. Some external factors may be various scanner imperfections such as static field inhomogeneities [77], poor RF coil uniformity or eddy currents from switching gradients, which can be corrected for by shimming techniques and specialized imaging sequences, etc., as reviewed elsewhere [78]. Moreover, the N4 algorithm is a popular preprocessing method for correcting for intensity inhomogeneities in the image arising due to such a bias field [79]. Some examples of internal factors are presence of high water density, air and iron leading to rapid spatial transitions in magnetic susceptibility. Correction for distortions caused by factors of the imaged object may be more challenging than correcting distortions caused by external factors, since the extent of distortions increases linearly with field strength according to the Larmor equation. The field inhomogeneities leads to the more rapid T_2^* relaxation, which is called free induction decay (FID). It can be decomposed into

$$R_2^* = {}^1/_{T_2^*} = {}^1/_{T_2} + {}^1/_{T_2'} \tag{3.7}$$

where T_2' is affected by ΔB.

For a visual demonstration video of relaxation and the associated T_1, T_2 and T_2^* time constants, see the supplementary video file **Proton_spin_MRI.webm**. It is also available at the following URL (as accessed November 18th, 2022):

https://upload.wikimedia.org/wikipedia/commons/1/11/Proton_spin_MRI.webm

3.3.4. $\boldsymbol{T_1}$ and $\boldsymbol{T_2}$ weighting

In case of a two-dimensional image acquisition sequence with a slice-selective magnetic z-gradient applied to only collect transversal magnetization from a single slice of tissue, the total recorded data may be regarded as snapshots of this relaxation process (for a selected time t leading to a particular "weighting" of T_1 and T_2 in the image). Thus, the timing of acquisition during these relaxation processes, combined with tissue specific relaxation constants T_1 and T_2, determines the amount of T_1 and T_2 weighing in the MRI.

The two most basic parameters for timing acquisition of snapshots (or "echoes") during relaxation processes are repetition time (TR) and echo time (TE). These are integral parts of the RF pulse sequence. An effective image acquisition results in complex transversal magnetization values that were recorded from multiple repeated relaxation processes in a reference frame rotating around the z-axis (i.e. $\boldsymbol{M}_T = \boldsymbol{M}_{xy}$). The selection of TR and TE affects the weighting [80] of the tissue specific T_1 and T_2 relaxation constants after applying a 90 degree RF pulse according to

$$|\boldsymbol{M}_T| \propto M_0(1 - e^{-\frac{TR}{T_1}})e^{-\frac{TE}{T_2}} \tag{3.8}$$

T1w MRI is achieved when TR is short relative to the various T_1 tissue constants so that the degree of longitudinal magnetization recovery is highly tissue dependent. TE affects the degree of T2w MRI similarly. The most dominating weighting is used to describe the image. Compared to T1w, T2w is known to better express intensity differences outlining pathology, but T2w also presents homogenous and high intensity values in fluid regions. T1w and T2w MRI are typically high-resolution structural images, depending on the pulse sequence (Figure 10).

3.3.5. k-space frequency domain

For two-dimensional (2D) MRI, the total recorded transversal magnetization is the composite magnetization from all spatial positions in the 2D slice. The degree of frequency and phase modulation is position dependent (through use of magnetic gradients), and the resulting complex spatial frequency domain is named k-space [81] and can be written as

$$\boldsymbol{M}_T(k_x, k_y) = M_x(k_x, k_y) + jM_y(k_x, k_y) \tag{3.9}$$

where j is the imaginary unit.

$\boldsymbol{M}_T$ contains signals that are induced in receiver coils and are naturally in the complex spatial frequency domain if additional time-varying spin dephasing magnetic field gradients are used to restrict the signals to specific locations in the tissue and k-space. In particular, the signals induced in the receiver coils are called “echoes” and they are initiated by either RF pulses directly (spin echo (SE)) or by specific time-varying field gradients (gradient echo (GE)) in the pulse sequence. An MRI scan typically acquires signals from SE or GE.

3.3.6. Spin echo and gradient echo

These are the essential building blocks of a pulse sequence. RF pulses centered at the Larmor frequency knocks spins out of equilibrium to precess with a certain angle around the field direction. Slice, phase, and frequency (readout) encoding magnetic field gradients are then utilized to encode echo signals to various z-slices, as well as to various x and y-locations of k-space, respectively.

A SE is initiated by a 90-degree RF pulse under the influence of a slice-selective gradient. This leads to transversal magnetization (an echo) that gets phase encoded to a y-location in

k-space. An additional 180-dergree RF pulse is then applied on the same slice, which leads to re-focusing away most unwanted spin phase distortion from ΔB. After a designated TE, a new echo forms that is read into a single horizontal line of k-space with a frequency encoding gradient. A spin echo thus contains only the T_2 component of spin-spin relaxation (Figure 11).

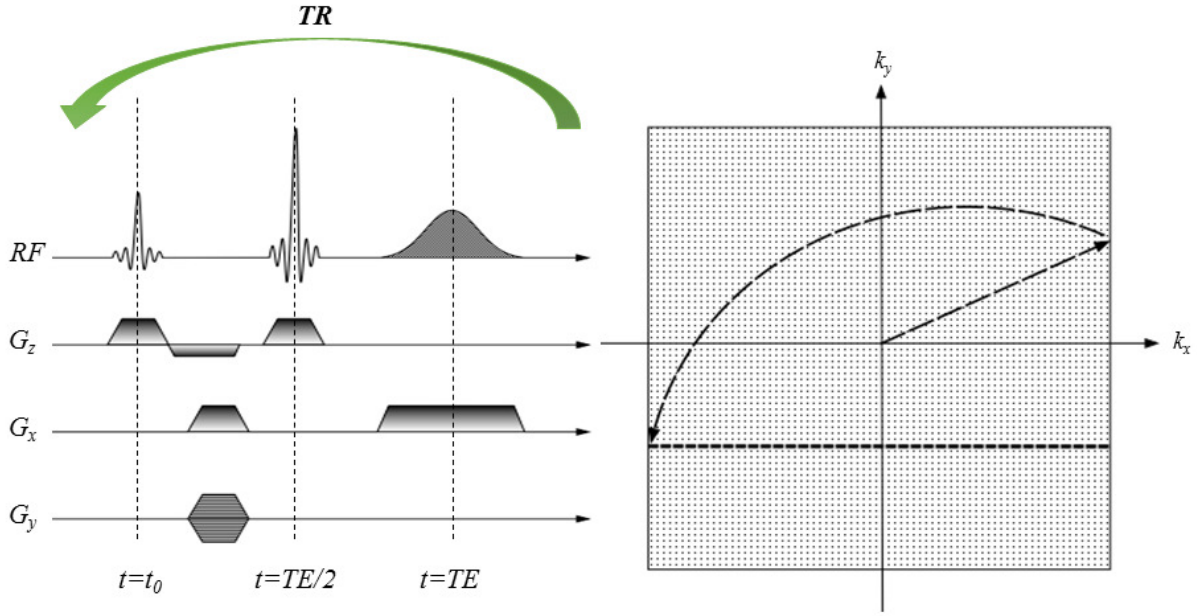

Figure 11: The spin-echo pulse sequence diagram (left) and corresponding k-space acquisition (right). RF: radiofrequency pulses and echo, G_z: slice-selective (phase-encode) gradient, G_x: frequency-encode gradient, G_y: phase-encode gradient, k_x: x-axis in k-space controlled by G_x, k_y: y-axis in k-space controlled by G_y. A spin-echo is induced by 1. a slice-selective RF pulse, 2. frequency and phase-encode gradients to control the spin orientation to certain locations in k-space, 3. a 180-degree slice-selective RF-pulse, then 4. a frequency-encode gradient during formation of the spin echo. The 180-degree RF pulse removes unwanted dephasing among the spins, which achieves a T2w transversal magnetization. This will record the echo as a single horizontal like in k-space. In addition to containing a specific T1w, the resulting echo will contain T2w transversal magnetization due to the 180-degree pulse. Used with modifications and permission from E. Grøvik.

The GE is induced more directly using a RF pulse with variable flip angle and similar slice and phase-encode gradients to the SE. Here, a small opposite sign frequency gradient is applied just before formation of the echo, to ensure that the echo is read into a complete horizontal

line in k-space. For SE, the same effect is achieved with the 180-degree RF-pulse. GE has no re-focusing RF-pulse, so it reads the raw T_2^* (FID) signal (Figure 12).

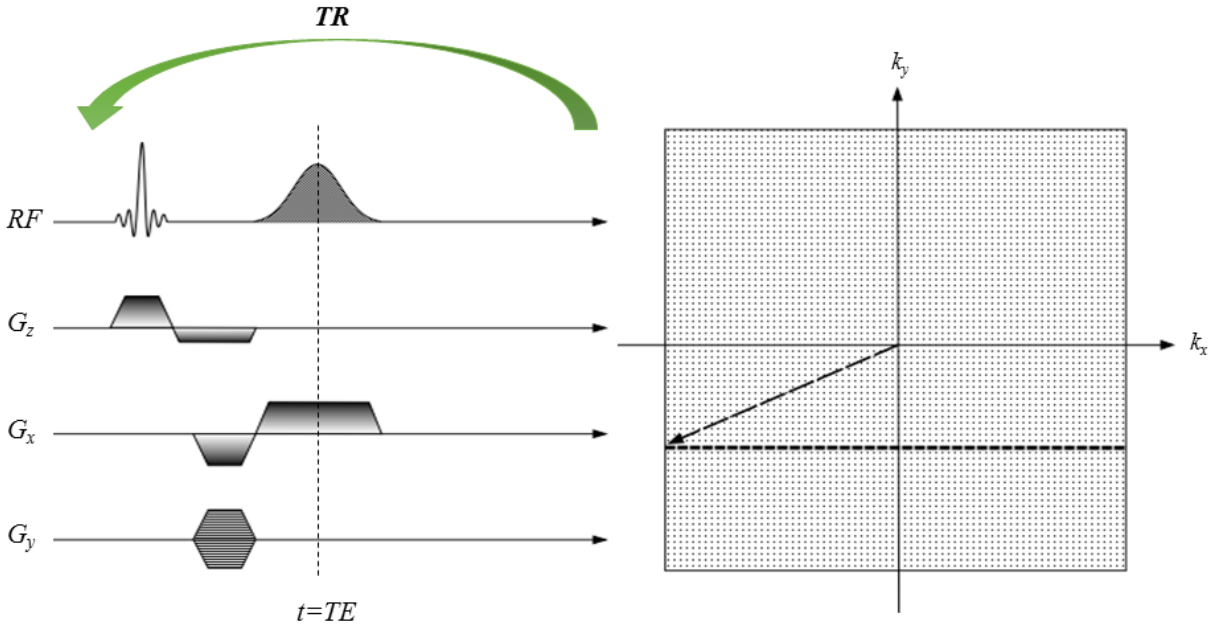

Figure 12: The gradient-echo pulse sequence diagram (left) and corresponding k-space acquisition (right). RF: radiofrequency pulse and echo, G_z: slice-selective (phase-encode) gradient, G_x: frequency-encode gradient, G_y: phase-encode gradient, k_x: x-axis in k-space controlled by G_x, k_y: y-axis in k-space controlled by G_y. A gradient-echo is induced by 1. a slice-selective RF pulse, then 2. frequency and phase-encode gradients to control the spin orientation to certain locations in k-space, then 3. a frequency-encode gradient during formation of the gradient echo. This will record the echo as a single horizontal like in k-space. In addition to containing a specific T1w, the resulting echo will contain (FID) T2*w transversal magnetization. Used with modifications and permission from E. Grøvik.

3.3.7. Pulse sequence

An inherent challenge in MRI is to record as much as possible of transversal magnetization in reasonable time, while also spatially encoding the signals so that an image can be reconstructed with enough spatial resolution. This is the task of the MRI pulse sequence and is characterized by the way k-space data is acquired. It consists of repetitive applications of RF pulses and magnetic field gradients to achieve and record either spin or gradient echoes.

As illustrated in Figure 11 and Figure 12, k-space encoding is achieved by applying additional spatial gradients on the magnetic field. Not only the strength but also the time-duration of the applied magnetic field gradient G dictates where to spatially localize spin densities and their corresponding entries in k-space. Hence the k-variables in equation (3.9) are expressed in forms of the time integrals

$$k = \gamma \int_0^t G(\tau)\, d\tau \tag{3.10}$$

In general, a pulse sequence has certain TR and TE values resulting in specific formation of T1w and T2w echoes.

3.3.8. Spatial image domain

For three-dimensional MRI, the final imaging volume I (in complex form) is the inverse Fourier transform [82] of k-space as follows

$$I(x, y, z) = \frac{1}{2\pi} \iiint_{k_x k_y k_z} \boldsymbol{M}_T(k_x, k_y, k_z) e^{j(k_x x + k_y y + k_z z)}\, dk_x\, dk_y dk_z \tag{3.11}$$

where $\boldsymbol{M}_T$ is the k-space encoded transversal magnetization for all z-slices of the imaged object. Note that for three-dimensional MRI, phase encoding is applied in two dimensions, where the second phase encoding direction replaces the slice selection gradient used for two-dimensional MRI. An intensity image is found by taking the complex modulus of I.

3.3.9. Contrast agent

The pulse sequence acquisition may be accompanied by intravenous injection of a Gadolinium (Gd) based CA (GBCA) targeted to alter the intensity values in or around tissue where is it present. This is due to GBCA having paramagnetic properties, which leads to both shorter T_1 and T_2 relaxation times [83], [84]. Consequently, T1w MRI with BGCA increases the image intensity values in regions where the CA is accumulated. T1w MRI with GBCA typically reveals active tumor regions since the CA tends to accumulate in regions with disrupted BBB associated with active tumor. The corresponding intensity decrease arising due to T_2 shortening is usually smaller than the intensity increase that arise due to T_1 shortening [83, p. 2], [84]. Post-contrast T2w and T2*w MRI is investigated in the thesis in terms of perfusion MRI. Here, the shorter T_2 and T_2^* relaxation times are ideally caused by the intravascular GBCA bolus passage [85], leading to a dynamic susceptibility contrast (DSC). If the T_2 and T_2^* relaxation times are additionally affected by CA accumulation, a specialized leakage correction method is needed. This will be described in the next section.

3.3.10. Advanced MRI

There exist specialized MRI pulse sequences developed for maximizing image contrast differences in tissue and regions that are of medical interest.

3.3.10.1. Fluid-attenuated inversion recovery

FLAIR is a specialized MRI sequence for suppressing the signal in T1w or T2w images originating from pure fluids such as CSF. In simplest form, the technique flips the longitudinal magnetization vector of spins and reads transversal magnetization with appropriate timing (inversion time (TI)) such that known magnetization for CSF is zero at

image readout. Water-like CSF is thus dark in T2w-FLAIR images whereas pathological tissue associated with edema remains bright, thereby improving the conspicuity of the pathology. In cancer MRI, such pathological tissue can be peritumoral regions with inflammation (edema) (Figure 10).

T2w-FLAIR is a popular method in cancer MRI because it is sensitive to detecting a range of localized brain pathologies and is thus suited for efficient screening. Moreover, combining multiple sequences (multiparametric MRI) in an analysis may lead to increased elucidation of disease, such as differentiating between IDH mutant and wild-type glioblastoma [86].

3.3.10.2. Dynamic susceptibility contrast MRI

One advanced MRI technique used to quantify cerebral hemodynamic parameters, like CBV, cerebral blood flow (CBF) and mean transit time (MTT) [87], is DSC-MRI [88]. DSC-MRI is a perfusion MRI method consisting of rapidly acquired T2w or T2*w volumes during intravenous injection of a GBCA. The imaging method trades some spatial resolution in favor of increased temporal resolution to capture vessel dynamics from a rapid GBCA bolus passage into the brain and is thus called (blood) perfusion MRI.

The presence of a CA induces magnetic susceptibility differences in or around the blood vessels, which are semi-quantifiable through the induced increase in T_2 relaxation rates in response to the presence of the CA in tissue according to

$$R_2 = {}^{1}/_{T_2} = {}^{1}/_{T_2(0)} + r_2[Gd] \tag{3.12}$$

where $r_2[Gd]$ is the in-vivo transversal relaxation rate for a specific concentration of Gadolinium (mmol/L). Visually, this is characterized as a "dip" in voxel intensities on the DSC-MRI as the CA passes through the brain vessels and is illustrated in Figure 13 [85].

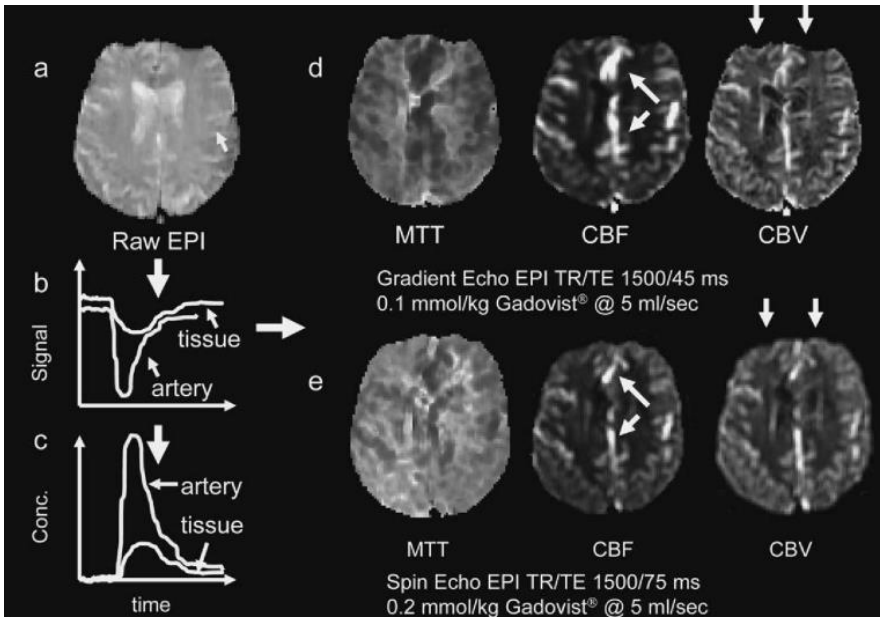

Figure 13: Cerebral blood volume (CBV), cerebral blood flow (CBF) and mean transit time (MTT) maps can be estimated by recording multiple spin-echo (SE) or gradient-echo (GE) echo-planar images (EPIs) from dynamic susceptibility contrast (DSC) MRI (a) along with injection of an intravenous contrast agent, and then performing mathematical operations on the raw EPIs. In simplest form, voxel signals from raw EPIs (b) can be converted to time-concentration curves (c), and CBV can be estimated thereof (e). CBV, CBF and MTT may also be estimated more precisely from mathematical deconvolution operations on arterial input functions (AIFs), and either from GE EPIs (d) or SE EPIs (e). Used with permission from Wolters Kluwer Health, Inc. and corresponding author (License number: 5433561360648).

Disruption of the BBB in brain cancer in or around tumor regions may lead to much of the CA leaking into extracellular space (CA extravasation) [89]. This gives rise to unwanted T_1 effects. CA extravasation may also reduce the magnetic susceptibility difference between intra- and extravascular space, which shortens the T_2^* relaxation [89]. Pharmacokinetic modeling in DSC-MRI analysis assumes no disruption of the BBB, and CA leakage correction is thus necessary in brain cancer for correctly computing hemodynamic parameters from DSC-MRI. CA leakage may lead an underestimation of CBV values in tumoral regions [90]–

[92]. This may lead to visibly lower CBV values in tumoral regions when compared to healthy regions as shown in Figure 10. Although the established leakage correction method by Boxerman et al. [90] improves the clinical utility of CBV from DSC-MRI, other techniques for estimating CBV without the unwanted T_1 and T_2^* effects from CA extravasation exist [93]–[99].

3.3.10.2.1. Pharmacokinetic modeling

Kinetic modelling assumes knowledge of CA in tissue over time. DSC-MRI measures signal change, which then needs to be converted to a metric which is proportional to CA concentration. It is commonly assumed the change in relaxation rate is directly proportional to CA concentration

$$\Delta R_2 \propto r_2[Gd] \tag{3.13}$$

By further assuming a mono-exponential relationship between signal and ΔR_2, the following concentration-time curve, where S_0 is the measured (average) signal prior to CA arrival and $S(t)$ is the temporal signal (magnitude) measured during CA passage, can be derived:

$$\Delta R_2(t) \propto -\frac{1}{TE}\ln\left(\frac{S(t)}{S_0}\right) \tag{3.14}$$

CBV can then be semi-quantified by computing the area under the concentration-time curve as follows [85], [87]

$$CBV \propto \int \Delta R_2 \, dt \tag{3.15}$$

Relative CBV (rCBV) can then be defined as CBV normalized relative to a normal-appearing white matter (NAWM) mask.

3.3.10.2.2. Spin-echo vs. gradient-echo DSC and vascularity

Equation (3.14) and (3.15) are for SE DSC-MRI. While SE DSC-MRI describe T_2 relaxation, GE DSC-MRI describe T_2^* relaxation. It is generally accepted that SE DSC image the microvascularity of blood perfusion by utilizing a GBCA to alter relaxation of blood inside the vessels. Since GE DSC is made of the FID signal, however, intra and inter-voxel dephasing as well as signal loss may result in imaging relaxation processes that are on a spatial scale that is larger than the vessels. This may result "dips" in image intensity in regions outside but close to vessels induced from GBCA inside vessels. GE DSC is thus known to image macrovascularity. The signals from GE DSC are typically stronger than from SE DSC. For this reason, CBV typically contains higher image intensity values for GE DSC than for SE DSC.

There are more precise ways of quantifying CBV from DSC-MRI using deconvolution with an arterial input function (AIF) [85], [87], [100], [101]. AIF here refers to the CA concentration in blood-plasma in an artery measured over time. These methods were intermitted in the thesis due to lack of manual AIF measurements and known limitations and additional sources of errors from computerized AIF estimation for DSC-MRI and similar methods [102], [103]. Instead, careful intra-patient normalization of CBV with normal-appearing white matter (NAWM) masks was performed.

3.3.10.3. Echo planar imaging

Single-shot echo planar imaging (EPI) [104] is the technique commonly used in DSC-MRI, DTI and BOLD fMRI. It is a two-dimensional fast acquisition method where multiple individually

phase encoded echoes are produced from a single spin or gradient echo readout. This enables all k-space lines to be recorded from a single SE or GE signal. The most common type is SE EPI. Here, the re-focused signal is split into multiple echoes with different phase and frequency encoding (Figure 14 [105]).

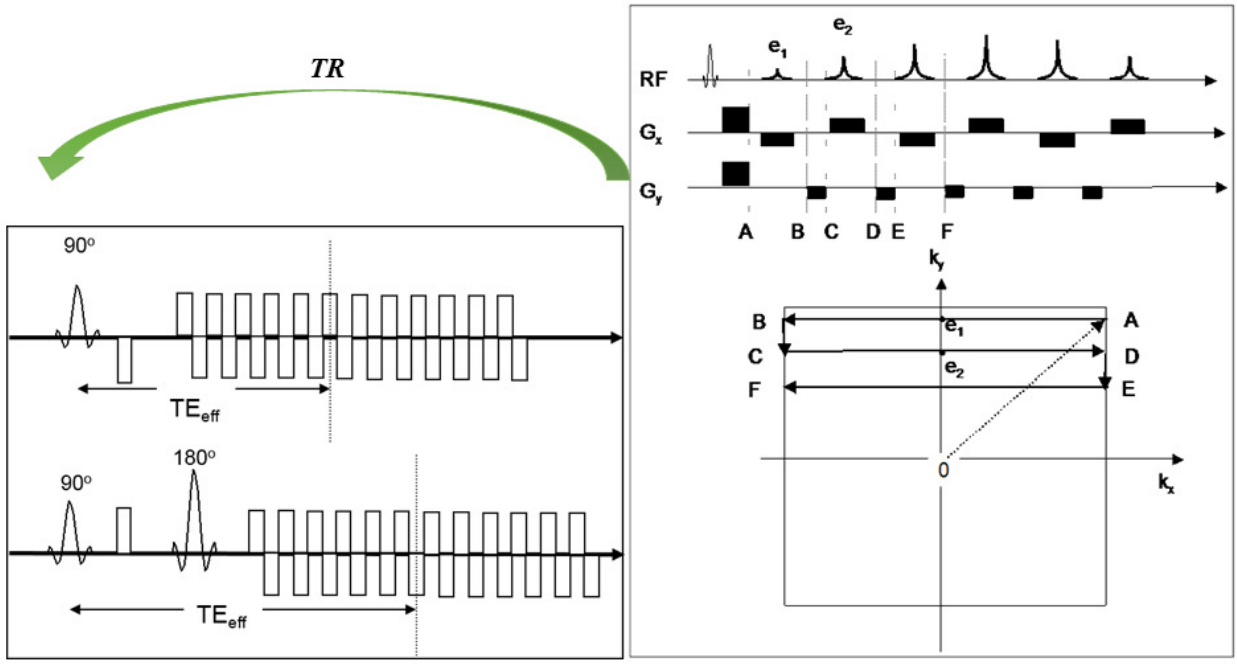

Figure 14: Spin-echo and gradient-echo pulse sequence diagrams for EPI and corresponding k-space capture for gradient-echo EPI. In the left image, RF pulses and frequency-encode gradients (G_x) for gradient-echo (top) and spin-echo (bottom) are shown, while the right image shows frequency- (G_x) and phase-encode (G_y) gradients and corresponding k-space capture for the gradient-echo version. For both versions, a slice-selective phase-encode (G_z) gradient is assumed applied prior to the gradients shown (like the pure spin- and gradient-echo sequences shown previously). Used with modifications and permission from A. Bjørnerud.

The EPI pulse sequence is constructed in such a way that each echo is read by following a rectilinear zig-zag path in k-space (Figure 14 (right) and Figure 16 E). More descriptions on EPI MRI theory can be found in these relevant Master's theses [106], [107].

3.4. Magnetic susceptibility

Magnetic susceptibility χ is a quantitative measure of a material's ability to become magnetized when exposed to a magnetic field, ranging -1 for superconductors to $\sim 10^5$ for strongly ferromagnetic materials [108].

3.4.1. Dia-, para- and ferromagnetism

Human tissues can either be diamagnetic ($\chi < 0$) or paramagnetic ($\chi > 0$), describing this tendency in form of either repelling or attracting the external magnetic field. Repelling or attracting may distort the external magnetic field. If a material can retain internal magnetization after being exposed to an external magnetic field (such as iron) or even without magnetic exposure, it is ferromagnetic ($\chi \gg 0$).

In MRI, magnetic susceptibility interacts with the magnetic field $\boldsymbol{B}$, leading to a longitudinal magnetization of proton spins $\boldsymbol{M}_z$ according to

$$\boldsymbol{M}_z = \frac{\chi}{\mu_0 \mu_r} \boldsymbol{B} \tag{3.16}$$

where $\mu_0 = 4\pi 10^{-7} [H/m]$ (Henry/meter) is the permeability of perfect vacuum and μ_r is relative permeability [109]. Relative permeability and magnetic susceptibility are related according to $\chi = \mu_r - 1$.

3.4.2. The susceptibility sensitive EPI sequence

As described in section 3.3.10.2, presence of an exogenous paramagnetic CA (e.g. Gd with $\chi \cong 0.32$) during DSC-MRI will affect T_2 relaxation by altering the susceptibility of the tissue and nearby tissue where it is present.

Although susceptibility for living tissue is comparingly weak ($|\chi| \ll 1$), local variations in χ can lead to minor field inhomogeneities (ΔB) resulting in undesired geometric and intensity distortions in MRI. EPI [104], which is the MRI sequence used for each axial slice ($\sim 100\ [ms]$) in each volume in DSC-MRI, possesses such distortions. For example, regions in and around the sinuses in the frontal lobe or ear canals contain sharp transitions from water-heavy regions (water $\chi = -9.05 * 10^{-6}$) to air ($\chi = 0.36 * 10^{-6}$) [108], which typically leads to geometric and intensity distortions in EPI. Geometrically, this can result in anteroposterior voxel displacement of a centimeter or more [110]. Figure 15 [111] presents simulated distortions for GE EPI along with the inhomogeneity field.

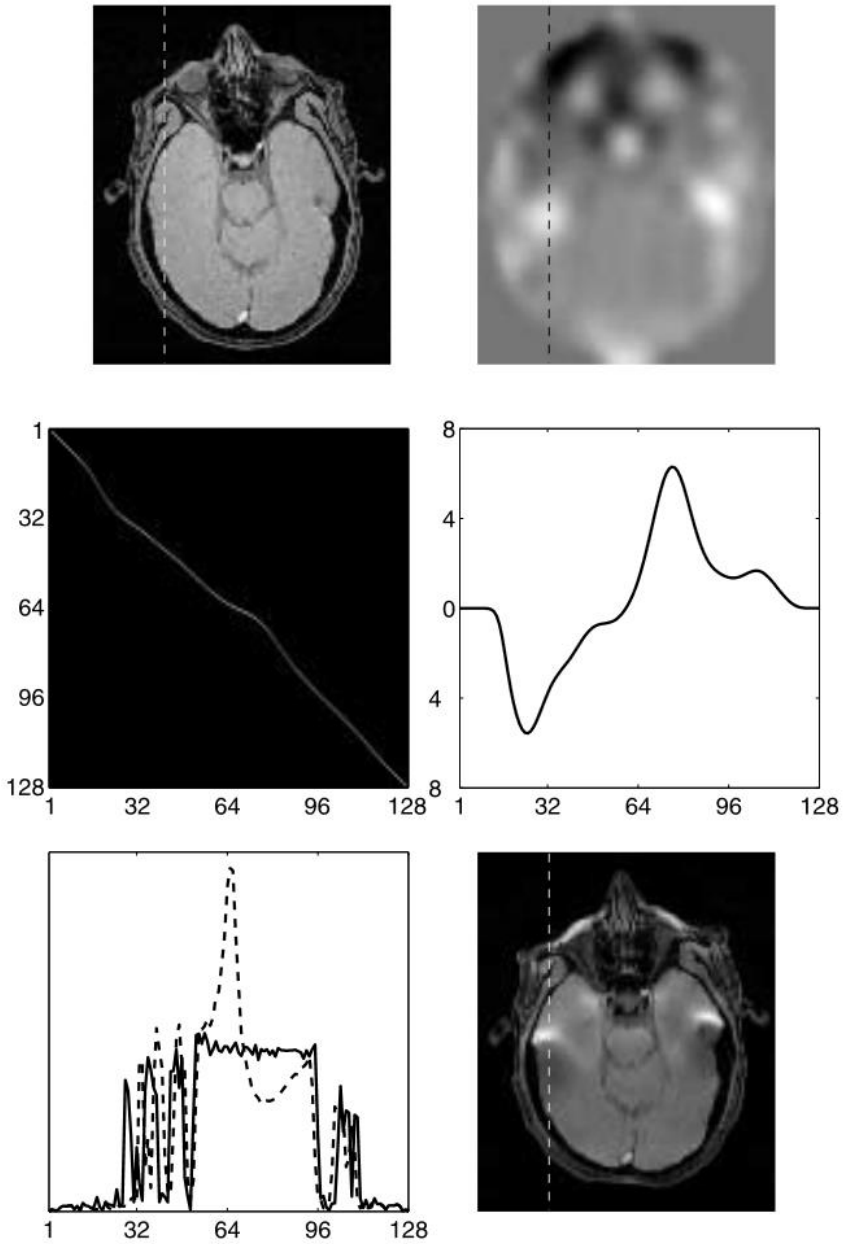

Figure 15: Simulated susceptibility geometrical and intensity distortions in GE EPI. Top row left shows a baseline GE (non-EPI) image, while top row right shows the inhomogeneity field ΔB as a result of varying tissue susceptibility. Middle row left shows the interpolation matrix ($\boldsymbol{K}_+$) between non-distorted and EPI distorted GE image, while middle row right shows the associated pixel displacements in the y-direction that is evident in EPI. In the top row right image, dark areas indicate a downwards displacement and the bright areas an upwards displacement for an EPI acquisition with positive (bottom-up) phase-encode k-space traversal. This results in deviations in pixel y-displacements in EPI that is proportional to the inhomogeneity field ($d \propto \Delta B$). Deviations in pixel y-displacement proportional to the intensity profile along the dashed line in the inhomogeneity field, is illustrated in middle row right. Resulting geometrical and intensity distortions is seen in the simulated EPI image in bottom row right. Bottom row left compares the intensity profile between the baseline and EPI GE image (whole and dashed line) in the corresponding locations. It is seen that the positive phase-encode EPI contains both deviations in pixel y-displacement (compression) and intensity, which is most prominent near water-tissue transitions and ear canals, respectively. Used with permission from Elsevier and corresponding author (License number: 5433660486292).

The thesis assumes two-dimensional (axial) EPI by applying a slice selective gradient in the z-direction, so the z-dimension in equation (3.11) can be omitted. An EPI consists of k-space magnetization acquired from a single RF excitation pulse (single-shot) in a zig-zag (blipped trapezoidal) manner, and with significant longer time spent on traversing from one side to the other along the phase-encode (y)-direction than along the frequency-encode (x)-direction. With one echo to fill in a single horizontal (x) line (readout) of k-space and N echoes to fill all of k-space, this time difference is approximately N. See Figure 16 for a depiction of the resulting EPI distortions and k-space traversal. The next section describes the functional cause for these distortions.

3.4.3. Effect of susceptibility variations on EPI

The field inhomogeneities from magnetic susceptibility variations are also dependent on time [112]

$$\delta B(x,y,t) = \gamma \int_0^t \Delta B(x,y,\tau)\, d\tau \tag{3.17}$$

and will affect the k-space encoding gradients (equation (3.10)). In two-dimensional EPI, this results in geometrical and intensity distortions according to

$$\tilde{I}(x,y,t) = \frac{1}{2\pi} \iint_{k_x k_y} \boldsymbol{M}_T(k_x,k_y) e^{j\left(k_x x + k_y y + \delta B(x,y,t)\right)} e^{-\frac{t}{T_2^*}} dk_x dk_y \tag{3.18}$$

The resulting real distortions are shown for GE and SE EPI in Figure 16.

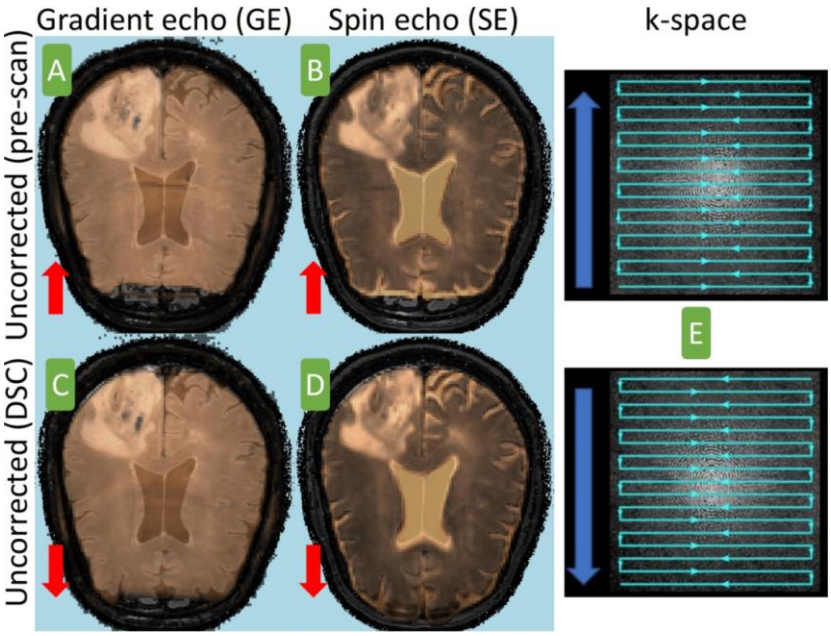

Figure 16: Distortions in uncorrected EPI. GE and SE EPI overlaid on a T2w-FLAIR MRI. A: Positive (bottom-up) phase-encode GE EPI, B: positive (bottom-up) phase-encode SE EPI, C: negative (top-down) phase-encode GE EPI, D: negative (top-down) phase-encode SE EPI, E: conceptual illustration of a positive phase-encoded image readout (top) and a negative phase-encoded image readout (bottom), respectively. Local spin compression is seen in the frontal brain (red arrows) in A and B, whereas local spin de-compression (stretching) is seen in the frontal brain in the DSC captures C and D. GE EPI contain additional signal loss in the frontal lobe. The underlaid T2w-FLAIR images do not possess such susceptibility driven distortions. Figure from our first paper.

Equation (3.18) also introduces another distortion in EPI which is caused by the $e^{-\frac{t}{T_2^*}}$ term. This leads to blurring and can be corrected for using specialized methods [113] not assessed in the thesis. Owing to the zig-zag sampling of k-space in EPI, both spatial and blurring distortion is much more prominent in the phase-encode (y)-direction than in the frequency-encode/readout (x)-direction. The sampling scheme also leads to a weaker effective gradient, and thus lower acquisition bandwidth, in the phase-encoding direction than in the frequency-encoding direction, which makes the EPI sequence sensitive to minor field imperfections, and resulting in distortions, primarily along the phase-encode direction [111].

3.5. MRI preprocessing

MRI preprocessing describes various image processing carried out to perform the main analysis processing in a study. As is seen in the papers, preprocessing methods and their order of execution depends on task. Table 4 gives an overview of all preprocessing methods encountered in the thesis.

Our goal with MRI preprocessing is to ensure, for each patient, that all structural (T1w, T2w, etc.) and perfusion (DSC) MRI sequences are properly spatially aligned both between different series and longitudinally for the same series. This is solved by intra-modal and inter-modal rigid image registration (RIR), respectively. Moreover, intensity normalization and standardization are important additional steps to ensure intra-subject intensity consistency of both structural and perfusion MRI when involving more than one exam per subject in the analysis. An important outcome of preprocessing is that a longitudinal series of MRI sequences for a patient have identical voxel resolutions and data matrices. This involves not only registration, but also resampling (re-slicing) images. As a result, voxel tracking methods such as DIR can be more easily applied and analyzed on longitudinal MRI. Resampling means in this context that the three-dimensional grid containing the image intensity values are modified as an effect of rotation of the image or resolution change of the grid. This involves using some interpolation method [114], [115], which is discussed later. At last, Montreal neurological institute (MNI) normalization ensures that images can be compared (on an approximate spatial scale) across multiple subjects. For an in-depth description of MRI preprocessing, see this book chapter [116]. Due to their importance in the thesis, separate sections about linear image registration (LIR)/spatial normalization and longitudinal intensity standardization are provided below.

Table 4: Overview of preprocessing methods in the thesis. Order of applying methods to image data may follow according to reading the table from top to bottom. However, exact preprocessing methods and order may vary depending on analysis task. Left-centered text: For structural MRI, right-centered text: For functional MRI, centered text: For both structural and functional MRI.

Structural MRI (T1w, T1wc, T2w, T2w-FLAIR)	**Functional MRI (T2*w/T2w GE/SE DSC EPI)**
Anonymization	
Brain extraction/de-facing	
DICOM->NIFTI conversion	
Intensity inhomogeneity/nonuniformity correction (N4ITK)	
De-noising	
	EPI correction (EPIC, TOPUP, paper 1)
	CA leakage correction
	NAWM normalization
Field-of-view reduction	
Linear image registration/spatial normalization	
Isotropic resampling/re-slicing	
Longitudinal intensity standardization (PLHM)	
Segmentation pipelines (cortical/subcortical atlas, tumor lesions)	
MNI (spatial) normalization	

Anonymization is the process of removing patient-sensitive information, such as personal identification number, name, birth date, and name of person carrying out the exam. This information may be contained within the header of the scanner DICOM files (as DICOM tags) and can be removed by software. Brain extraction, skull stripping, or de-facing may be regarded as types of anonymization since it removes the possibility of identifying the patient in terms of face or general appearance. DICOM to NIFTI conversion is necessary to perform a lot of processing steps, which also involves preprocessing. N4ITK [79] is a popular improvement of the famous nonparametric nonuniform intensity normalization (N3) algorithm [117]. Here, the image is corrected for intensity nonuniformity caused by a bias field that arises mainly due to variations in sensitivity of the receiver coil and nonuniform RF excitation [117]. De-noising removes noise in the image using for instance a spatially adaptive filter [118]. EPI correction corrects for intensity and geometric distortions due to

variations in magnetic tissue susceptibility, while CA leakage correction and NAWM normalization can be described as intensity correction and normalization methods in perfusion MRI, respectively. These methods are described elsewhere in the thesis. A reduction of field-of view ensures that parts of the image not targeted for analysis are removed, such as the neck. This leads to a smaller data matrix and resultingly faster processing. Isotropic resampling or re-slicing simplifies the physical interpretation of intensity values and may be the last part of LIR. An interpolation method is used in re-slicing, such as trilinear or nearest neighbor (NN) interpolation. Segmentation pipelines such as FastSurfer [119] and ONCOHabitats [120], may be best run on minimally preprocessed images. Moreover, segmentation pipelines may involve their own preprocessing. As an example, FastSurfer performs both N4 correction and voxel isotropic re-slicing before segmentation. It is thus reasonable that segmentation pipelines, when included as a preprocessing step, are performed early in the preprocessing to ensure optimal performance. Spatial normalization using linear and possibly DIR methods, may then follow to transform images and segmentation masks to the same reference space.

3.5.1. The optimization problem in image registration

Registration (or co-registration) describes the process of spatially aligning an image with another image, by matching anatomical structures within or across patients, or to a template. This is an essential preprocessing step in multiparametric image analysis.

For any type of image registration, a moving image M is registered to a fixed image F by optimizing an objective function f with respect to a transformation model T;

$$f(T) = A(F, M \circ T) + R(T) \tag{3.19}$$

where A is a function quantifying the spatial alignment (alignment function or loss metric) between the images (e.g., mutual information (MI) or cross-correlation (CC) which are described later as statistical methods) and R is a regularization term [121]. Registered images are achieved by finding a T by either maximization or minimization of f depending on the definition of A and R and applying it to M.

3.5.2. Linear image registration

For LIR, T describes a global transformation of the physical homogenous coordinates of the intensity values in the moving image (T_{linear}: $\mathbb{R}^4 \rightarrow \mathbb{R}^4$) involving scaling, rotation, shearing and translation as follows [122]

$$T_{linear}(\boldsymbol{x_h}) = M\boldsymbol{x_h} \tag{3.20}$$

where $\boldsymbol{x_h} = [x \quad y \quad z \quad 1]^T$ and

$$M = \begin{bmatrix} R_{00} & R_{01} & R_{02} & t_0 \\ R_{10} & R_{11} & R_{12} & t_1 \\ R_{20} & R_{21} & R_{22} & t_2 \\ 0 & 0 & 0 & 1 \end{bmatrix} \tag{3.21}$$

is a transformation matrix. In the matrix M, the R's control the scaling, rotating, and shearing, while the t's control the translation. RIR and affine image registration (AIR) are thus subgroups of LIR. Equation (3.20) is called a homogenous coordinate transformation because the translation parameters are included in the matrix M. LIR is performed in physical coordinates and not in voxel coordinates [123], unlike our definition of voxel tracking.

It is important to emphasize that LIR only involves coordinate transformation and does not modify intensity values. However, intensity values may disappear of appear because of interpolation when re-slicing of the image or with image viewing software. As an example, it is may be preferred to transform a high-resolution tumor segmentation mask created in the image space of a T1wc scan, to low-resolution perfusion space using NN interpolation. Very small lesions in the high-resolution mask may resultingly disappear because of the NN interpolation method when re-slicing the mask to low resolution perfusion space.

Intra-subject longitudinal RIR is an important preprocessing step to enable displacement-based voxel tracking analyses in the thesis. Head motion correction is another similar application of longitudinal RIR where each time-point volume scan in DSC-MRI is registered to a fixed time-point volume, to remove possible head movement during DSC capture.

MNI normalization, which involves registering images to a common reference template, may be realized by AIR or DIR. A possible benefit of only using AIR in MNI normalization is that the characteristic anatomy of each patient's brain is kept, while achieving a brain in approximate MNI space. In large-scale studies, this may be preferable rather than warping each brain to become more equal to a template brain (using DIR such as the statistical parametric mapping (SPM) MNI normalization [124], [125]). AIR may however, like DIR, alter the physical interpretation of the image. One such example may be a compression of tumor stiffness maps from elastography, thereby distorting their physical interpretation and usefulness.

3.5.3. Longitudinal intensity standardization

Longitudinal intensity standardization is an important aspect of MRI analysis for voxel tracking, since it is expected that intensity values of non-changing tissue stay the same

across scans. However, this cannot be assumed in longitudinal MRI, since varying sequence parameters and existing preprocessing may lead to varying intensity values even for the same tissue type. The most basic intensity standardization method may be subtracting from all voxel values the mean, followed by dividing by the standard deviation (Z-score standardization [126]). Intensity values used in calculating the mean and standard deviations may preferably only be the values within a brain extraction mask, thus excluding non-brain, zero, and not-a-number (NaN) intensity values in the computation of mean and standard deviation. However, this may lead to inconsistent longitudinal intensity values since temporal image changes such as changing pathology may still alter the mean and standard deviation calculations significantly. Instead, piecewise linear histogram matching (PLHM) [127], [128] was investigated as a group-based intensity standardization method. This technique normalizes each image in a longitudinal series of MRI scans according to an average histogram calculated from all images. The histogram of each scan is then matched to this average histogram, thereby achieving consistent image intensity values across the time points. Some alternative techniques achieving consistent intensity values [126], are Least squares tissue mean normalization and removal of artificial voxel effect by linear regression (RAVEL) [129].

3.6. Data organization

3.6.1. Brain imaging data structure

Keeping conventions on file and folder organization of the research data is an important requirement when running various scripting tasks for analysis, improving quality, or adding to existing datasets. This involves most of the preprocessing and analysis methods described in the thesis.

BIDS [130] is a collaborative effort establishing a bare-bones standard for organizing and sharing data in neuroimaging experiments. It is supported by a large number of neuroscientists and comes with useful tools such as the BIDS-Validator [131] for minimally processed rawdata. It suggests a way to link raw, minimally processed, and processed data without mixing them by having the tree folders sourcedata, rawdata and derivatives with near-identical structures (Figure 17). This means that it is easier to visualize and process raw and processed data with little modifications of scripts. Sourcedata is intended for original DICOM files from the scanner, rawdata contains minimally processed NIFTI files converted from sourcedata, while derivatives contains processed data as well as derived data from experiments and analysis. The BIDS standard is therefore a practical guideline for how work with MR images within a consistent file structure, from original source DICOM files to derived NIFTI files and results. BIDS guidelines on longitudinal MRI for fMRI was used as a baseline for organizing and processing the research data.

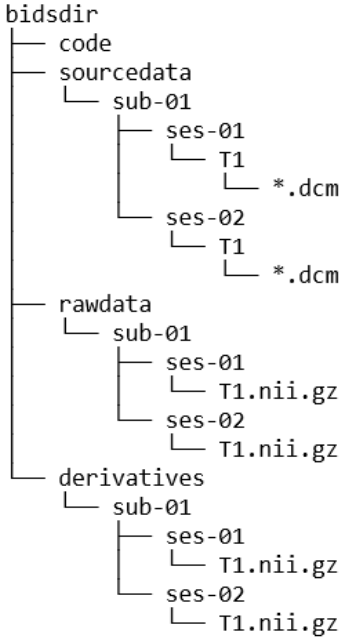

Figure 17: BIDS is a folder and file naming convention for neuroimaging experiments, enabling reproducible and shareable datasets. A typical neuroimaging experiment may involve DICOM to NIFTI conversion, thereby producing the rawdata from sourcedata. Then followed by analysis of the

NIFTI files in rawdata and producing results in derivatives. These results may involve registered images to a common reference space. A central point is to avoid having both raw and processed data in the same folders, which may increase the complexity and manageability of the datasets over time.

3.6.2. Data version control

Tracking of changes in the BIDS datasets is enabled by using Data version control (DVC) [132]. DVC is a Python-installable package that runs on top of Git to enable commit-based tracking of dataset changes. This means for instance, that the exact state of a dataset (the files, folders, and code) that was used in a publication, can be recovered (in BIDS form) in the same way as recovering an earlier version of scripts in a software Git project.

The information needed to get a specific version of the dataset, is having access to the Git repository for the DVC project, a self-hosted storage backend and knowing the commit string describing specific dataset version.

Modifications and improvements in datasets are logged/tracked by DVC in form of re-computing and summarizing MD5 hash sums from files, which is then tracked by Git in the usual manner. DVC is privacy oriented since the actual data is stored using a backend which can be hosted locally. Such a storage backend can be a local storage server providing SSH access or scalable self-hosted object storage such as S3/MinIO. A local SSH backend was used in the thesis.

3.7.MRI visualization

Different visualization tools are used for different steps in the preprocessing and analysis processing pipelines to quality control (QC) data and results. Volumetric longitudinal data is much heavier to handle than many other types of data such as text and tabular data. It is

suggested that a suited visualization tool is one that is efficient in visualizing a specific stage of the processing.

3.7.1. Raw DICOM and NIFTI

nordicICE/nICE (NordicNeuroLab, Bergen, Norway) provides fast simultaneous visualization of multiple raw images in both DICOM and NIFTI format. Since images are not overlaid by default, but displayed side-by-side, it is a good solution to get an overview of raw data without preprocessing such as LIR. If registered, however, synchronized scrolling through slices can be enabled for easy comparison of images. Since being available in our software environment and running on Windows, and most hospital computers with data access run Windows, it is suited for visualizing data close to its source. nICE is paid software but support was recently discounted, making it accessible for free.

3.7.2. Raw and processed DICOM and NIFTI

Aliza Medical Imaging & DICOM Viewer (Aliza Medical Imaging, Bonn, Germany) is used for efficient volumetric visualization (for instance maximum intensity projection) of longitudinal raw and registered images. Two strengths are its adaptive histogram-based adjustment of image brightness and saturation, and that it reads both DICOM and NIFTI formats. Its volume visualization capabilities are based on the established visualization toolkit (VTK) [133]. Aliza was free software at the beginning of the doctoral period, but later versions require payment. It runs on both Windows and Linux.

3.7.3. Processed NIFTI

ITK-SNAP [134], [135] is the preferred tool to QC LIR and DIR, since it by default overlays multiple images and synchronizes slice locations across all images. This makes it easy to for

instance compare structural change for specific anatomical locations across various time steps. It can visualize displacement vector fields both in form of individual components, vector magnitude and deformation grid. It provides no DICOM import but the NIFTI format common for processed images. Like much other NIFTI centric software, ITK-SNAP follows internal file handling conventions according to the insight segmentation and registration toolkit (ITK) [136]. For instance, it displays images by applying the provided affine transformation in the NIFTI header (qform and/or sform). This assures that RIR (and not necessarily re-sliced) images are correctly overlaid. Other software may contain incomplete handling of sform/qform leading to image flipping problems (like nICE) or requiring additional re-slicing to correctly display registered images (like Aliza). ITK-SNAP is free software and runs on both Windows and Linux.

As an alternative FSLeyes [137] from the FMRIB Software Library (FSL) [138] is occasionally used to visualize overlaid NIFTI images, for instance for checking the spatial correspondence between T2w-FLAIR and CBV. It reads in registered images with affine transformations like ITK-SNAP. This is a great visualizer of registered and longitudinal (functional MRI) NIFTI data since it is based on open-source software and has extensive documentation. Some strengths of FSLeyes are that it integrates well with Python environments (fslpy, pyopengl) and provides off-screen rendering. Rendering here means that a given visualization can be saved (rendered) to a file. Off-screen means that this process does not require a graphical user interface (GUI), but only access to a command-line interface (CLI). When compared to other viewers, it has good automatic adjustment of image contrast and saturation when opening images. Moreover, the exact visualization settings involving input images, layout, and visualization parameters, can be saved, and re-produced as a large CLI command. These

properties of FSLeyes make it suited for being automated in shell scripts. FSLeyes is most easily run in Linux environments.

At last, MATLAB® (Mathworks, Natick, Massachusetts, USA) with the well-known SPM software [124] provides good visualization tools for verification of MATLAB centric processing results in the first paper (e.g. SPM).

3.7.4. Processed numpy arrays

Through experimental image processing in the Python [139] programming language was a need for visualizing images directly from numpy arrays. Python is the most popular free programming language in data science and competes with other high-level languages such as MATLAB. Luckily, Python has good support for both DICOM and NIFTI file import using the pydicom and nibabel packages, which read images to numpy arrays.

Jupyter notebook and Jupyter lab are popular cross-platform client-server web-based interactive frameworks for rapid prototyping of Python code [140], which was done in the preliminary work of the first publication. For these cases, the easiest visualization of two-dimensional images was accomplished with the Matplotlib package.

Three-dimensional volumetric visualization within the Jupyter frameworks (such as ipyvolume) quickly shows suboptimal performance for full-resolution MRI data on a conventional computer, when compared with established NIFTI MR image viewers. An example of sub-optimal volumetric visualization performance is “lagging” when interactively using the mouse to rotate a visualized MRI volume. For this task, the Python software spimagine, using OpenGL graphics processing unit (GPU) accelerated volume rendering with pyopengl, provides efficient in visualizing full-resolution MRI. It also supports longitudinal

(four-dimensional) numpy arrays. Spimagine can be used from the Jupyter frameworks if the Jupyter server is run on a computer with GUI, from standard Python scripts, or as a standalone program.

3.8.Statistical methods

The following section contains a short description of the various statistical methods encountered in the thesis. Wilcoxon, Kruskal-Wallis, and one-way analysis of variance are statistical hypothesis tests for measuring differences among populations of measurements, while Bonferroni and Benjamin and Hochberg are correction methods for multiple hypotheses tests. Dice similarity coefficient is a metric measuring spatial alignment of two binary segmentation masks. Neighborhood CC and MI are two similarity loss metrics commonly used in image registration. Last, survival analysis describes a collection of statistical methods to model and predict the time to death typically from longitudinal patient data.

3.8.1. Wilcoxon signed rank test

This is a nonparametric statistical hypothesis test if two dependent paired samples come from the same distribution [141]. It accepts non-normally distributed data and tests whether the distribution of differences in median between the paired samples is symmetric about zero. A parametric analog to the Wilcoxon test that assumes normally distributed data is the paired Student's t-test.

3.8.2. Kruskal-Wallis test

Another nonparametric statistical hypothesis test for significance in median differences between two or more independent populations of observation data. It accepts non-

normally, but similarly shaped distributed data. It is an extension of the Mann-Whitney U test for more than two groups. The parametric equivalent of the Kruskal–Wallis test is the one-way analysis of variance (ANOVA).

3.8.3. One-way analysis of variance

A parametric statistical hypothesis test for whether the population means of two or more groups differ. With the null hypothesis that samples in all groups are from populations with the same mean values, it estimates variances and produces an F-statistic to test for significance. One-way ANOVA assumes independent and identically normally distributed values. Tukey's method for multiple comparisons is used in ANOVA to create confidence intervals for all pairwise differences between the group means. By setting a family-wise error rate (probability of making at least one type I error) of typically 0.05, significant difference in population means is indicated if a confidence interval does not include zero.

3.8.4. Bonferroni

This is a simple method to correct for multiple hypotheses tests that could otherwise result in type I errors (e.g., falsely rejecting a true null hypothesis, or false positive). When performing N tests and with a significance cutoff of $\alpha = 0.05$, the corrected cutoff for each test i is $p_i \leq \alpha/N$. It controls the family-wise error rate at $\leq \alpha$. The correction is conservative and gives a greater risk of failure to reject a false null hypothesis, or false negative, (type II errors) than more advanced methods.

3.8.5. Benjamin and Hochberg

A correction for multiple hypotheses tests that controls the false discovery rate, i.e., rate of type I errors. First an accepted false discovery rate is determined, e.g., $q = 0.2$.

Then, the p-values from all N tests are ranked from smallest to largest with rank $r = 1$ given to the smallest, rank $r = 2$ to the second smallest, etc. A Benjamin-Hochberg critical value for each test is then computed according to $\frac{r}{N} q$. The corrected cutoff for each test is then determined from the test with the largest p-value that is less than its Benjamin-Hochberg critical value. All tests with this or lower p-value are considered significant.

3.8.6. Dice similarity coefficient

Dice similarity coefficient [142], or F1-score, can be used to measure spatial alignment of two binary segmentation masks. It ranges between 0 and 1 and can be viewed as a similarity measure over sets. Assume that mask X and Y is defined as a collection of voxels. The Dice coefficient between the two masks can be computed as

$$Dice = \frac{2|X \cap Y|}{|X| + |Y|} \tag{3.22}$$

where the numerator is two times the count of intersecting voxels between the masks and the denominator is the total count of voxels for the masks.

3.8.7. Neighborhood cross-correlation

An image intensity-based statistical measure of local spatial alignment between two volumes where CC is computed for multiple sub volume (neighbor) pairs using a sliding cube method. It is thus suited for DIR tasks and works best for same sequence (monomodal) image pairs (e.g., T1w to T1w MRI). For registering the volume M to F, it may be written as [143]

$$CC(\boldsymbol{x}) = \frac{\sum_i \big((F(\boldsymbol{x}_i) - \mu_{F(\boldsymbol{x})})(M(\boldsymbol{x}_i) - \mu_{M(\boldsymbol{x})})\big)^2}{\sum_i \big(F(\boldsymbol{x}_i) - \mu_{F(\boldsymbol{x})}\big)^2 \sum_i \big(M(\boldsymbol{x}_i) - \mu_{M(\boldsymbol{x})}\big)^2}$$

(3.23)

where the voxel coordinate vector $\boldsymbol{x}$ is at the center of a N^3 cube, μ is the mean value within the cube and $\boldsymbol{x}_i$ iterates through the voxel coordinates of that cube. The cube dimension (or neighborhood size) when using the ANTs SyN algorithm in the thesis was the default of $N = 9\ mm^3$. Using neighborhood CC as a DIR loss metric involves computing its gradient, which is described in the ANTs SyN CC paper [144].

3.8.8. Mutual information

An image intensity-based statistical measure of global spatial alignment between two volumes based on information theory. Here, the intensity values of the two volumes are regarded as samples from two random processes. This leads to an interpretation of the area under curve normalized intensity histogram of a volume F as an empirical probability density function p_F of the most likely intensity values. MI is a measure of how well a spatially localized intensity value M_j in the second volume M can be predicted given the corresponding intensity value F_i in the first volume F. Specifically, it is the difference between the information contained in each volume and the joint information contained in the volumes according to [145]

$$MI(F; M) = \mathcal{H}(F) + \mathcal{H}(M) - \mathcal{H}(F, M)$$

(3.24)

where $\mathcal{H}(F)$ and $\mathcal{H}(M)$ is entropy of the fixed and moving volumes,

$$\mathcal{H}(F) = -\sum_i p_F(F_i)\log\left(p_F(F_i)\right)$$

(3.25)

and $\mathcal{H}(F, M)$ their joint entropy,

$$\mathcal{H}(F, M) = -\sum_i \sum_j p(F_i, M_j)\log\left(p\big(F_i, M_j\big)\right)$$

(3.26)

where p is the joint (2D) probability density function of the volumes. Mutual information can also be described in terms of relative entropy (Kullback-Leibler divergence). It is well suited for multimodal (e.g., T2w to T1w MRI) registration tasks. For DIR, MI can be extended to a voxel-vise variant as described in [143], which leads to faster but less accurate DIR when compared to using neighborhood CC. To optimize for registration transformation parameters, ANTs uses a variational method to compute the gradient of voxel-vise MI [143], [146].

3.8.9. Survival analysis

Survival analysis [147] is a collection of statistical methods for modeling and predicting the time to which an event occurs. The predicted event in the thesis is patient death due to progression of disease. These models investigate the survival prediction capability of pre-selected input data (explanatory or predictor variables). The survival time of a patient after being included in a survival study is modeled by the random variable T. Some examples are months until death (overall survival) or progression of disease (progression-free survival (PFS)) or patient age at death. If the survival time of a patient is not known exactly for reasons such as end or study or patient lost to follow-up or withdrawn from study for other

reasons, it is censored (Figure 18 [147]). The analyses incorporate specific ways to handle censored data by introducing the censorship variable δ (0=censored, 1=death).

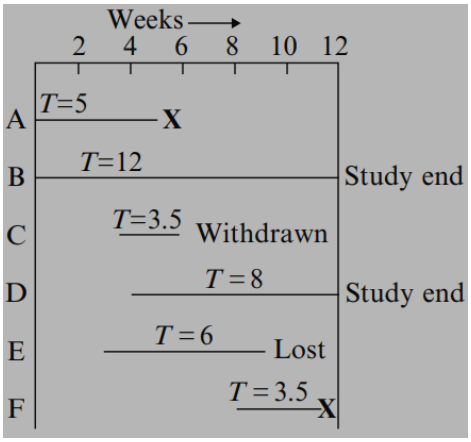

Figure 18: Examples of various types of data for survival analysis. Rows A-F describe patients included in the analysis. For each patient, T describes the time to an event. An X describes occurrence of the event of interest, which is typically death. Other events such as study end without death or patient lost or withdrawn from study for other reasons, leads to right-censored data. Survival analysis is focused on modeling and predicting the event of interest. Used with permission from Springer Nature (License number: 5434171145925).

3.8.9.1. Survivor and hazard functions

The probability density function of death at a specific time t is described by the transition time distribution $f(t)$. The actual probability of surviving until a time t (the survival curve or survivor function $S(t)$) is found by integrating over $f(t)$ for all times larger than t

$$S(t) = P(T > t) = \int_{t}^{\infty} f(t)dt \tag{3.27}$$

In theory, $S(0) = 1$ and $S(\infty) = 0$. However, in practice, S is a step function since it is based on obtaining survival probabilities for different values of t. Central in survival analysis is computing the failure rate or hazard function $h(t)$, which is the chance of death for the next time interval, given that the patient has not died already,

$$h(t) = \lim_{\Delta t \to 0} \frac{P(T \leq t + \Delta t | T > t)}{\Delta t} = \frac{f(t)}{S(t)} = -\frac{d}{dt} \ln (S(t))$$

(3.28)

$h(t)$ is a conditional failure rate, or the instantaneous potential of death per unit time, given that the patient has survived until time t. It is not a probability, and the obtained value will give a different number depending on the units of time used and may even be greater than 1. There is a relationship between $S(t)$ and $h(t)$; if one knows the form of $S(t)$, one can derive the corresponding $h(t)$ and vice versa as follows [147]

$$S(t) = e^{-\int_0^t h(u)du}$$

(3.29)

$$h(t) = -\frac{\frac{dS(t)}{dt}}{S(t)}$$

(3.30)

There are different ways to model the survival and hazard functions, dividing methods into nonparametric, semiparametric and parametric methods. Each impose different assumptions about the survival data.

3.8.9.2. Concordance index

$C - index$, or Harrell's concordance index [148], is a performance metric for survival models. It is a generalization of the area under the receiving operating characteristic curve (AUC-ROC) that considers censored survival data and is computed by summarizing the survival times and risk scores for all pairs of patients i and j ($i \neq j$) as follows:

$$C - index = \frac{\sum_{i,j} 1_{T_j<T_i} \cdot 1_{\eta_j>\eta_i} \cdot \delta_j}{\sum_{i,j} 1_{T_j<T_i} \cdot \delta_j}$$

(3.31)

where η_i is the risk score for patient i and

$$1_{T_j<T_i} = \begin{cases} 1, & T_j < T_i \\ 0, & else \end{cases}$$

(3.32)

$$1_{\eta_j>\eta_i} = \begin{cases} 1, & \eta_j > \eta_i \\ 0, & else \end{cases}$$

(3.33)

Like AUC-ROC, $C - index = 1$ corresponds to the best model prediction, while $C - index = 0.5$ corresponds to a random prediction. It represents the model's ability to correctly provide a reliable ranking of the survival times based on the individual risk scores. Continuous explanatory variables may be used as risk scores. In the second paper, the various displacement biomarkers were used as risk scores.

3.8.9.3. Kaplan-Meier

This is a nonparametric method where the survival curve $S(t)$ is estimated directly from the data by ordering the survival times (from smallest to largest) and estimating survival probabilities according to the product limit formula

$$\hat{S}(t) = \prod_{i|t_i \leq t} \hat{P}(T > t_i | T \geq t_i) = \prod_{i|t_i \leq t} (1 - \frac{d_i}{n_i})$$

(3.34)

where d_i is the number of deaths that happened at time t_i and n_i the number of patients known to have survived up to time t_i (i.e. not diseased or censored). Kaplan-Meier (KM)

allows only categorical explanatory variables. For testing significance in differences in KM survival time prediction capability between two subgroups (e.g. using a placebo vs. treatment explanatory variable, or stratification thresholds of our biomarkers for low and high survival subgroups), the log-rank test can be used.

Log-rank test for two subgroups

This is a nonparametric large-sample chi-square test for comparing the survival curves of two subgroups. With the null hypothesis that the two subgroups have a common survivor function, it tests for significance with the approximate formula

$$\chi^2 = \sum_{i}^{2} \frac{(O_i - E_i)^2}{E_i} \tag{3.35}$$

where O_i and E_i are formulas for observed and expected deaths for subgroup i as explained elsewhere [147].

3.8.9.4. Cox proportional hazards regression

This is a semiparametric method assuming a proportional hazards model. It separates time dependency (t) from explanatory variable dependency (x) in the hazards function such that

$$h(t|x) = h_0 e^{\beta x} \tag{3.36}$$

where h_0 is a parametric baseline hazard function (e.g. a Weibull hazard model). Unlike KM, it allows continuous explanatory variables, and the hazards function is estimated in terms of regression. Additive effects of categorical variables can be included in the model like KM analyses. Moreover, it is possible to estimate the β's (in terms of maximum likelihood) in

the exponential part of the model without deciding h_0. These are some reasons why Cox proportional hazards regression is a popular survival analysis.

4. Materials

4.1. Patient population

Two cohorts of adult glioblastoma patients were analyzed in the thesis. The first cohort included 45 patients (age range $40-84$ years, median 61 years) imaged before first-time surgery and with histopathological diagnosis confirmation (Intervention Centre (IVS)). The study was approved by the Institutional Review Board (ref: LOOPS) and the Regional Committee for Medical and Health Research Ethics (ref: 2013/1033). All patients signed a consent form before being included in the study.

The second cohort included 27 patients (age range $32-68$ years, median 56 years, female/male ratio of $7/20$) with histologically confirmed HGG (SAILOR). Among the 27 patients, 24 were originally diagnosed as glioblastoma (3 with IDH mutation, 2 with wild-type IDH mutation, 19 with unknown IDH mutation status) based on the 2016 WHO Classification of CNS Tumors. The remaining 3 were diagnosed as 1 anaplastic oligodendroglioma and 2 anaplastic astrocytoma. The study was approved by the Institutional Review Board and the Regional Committee for Medical and Health Research Ethics (ref: 2009/1867b). Patients were included only if informed consent was signed.

Both cohorts received the standard treatment described previously. Longitudinal data collected during treatment was included in the second cohort, as illustrated in Figure 19. This resulted in a total of 229 MRI exams from the 27 patients in the second cohort. Most of

these patients had cancer recurrence as described elsewhere [50], [57]. The median overall survival was 19 months.

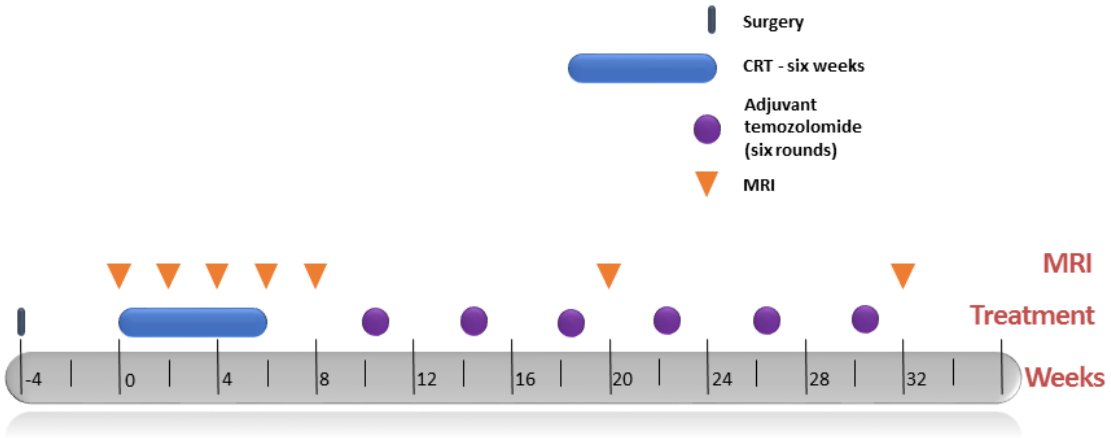

Figure 19: Illustration of longitudinal MRI protocol during standard treatment for our second patient cohort. CRT: chemoradiotherapy. The first scan (week 0 in the figure) was taken four weeks after surgery, before three successive follow-up scans during CRT and one during a pause in the treatment. Twelve-week interval scans were then performed within the six rounds of chemotherapy (adjuvant temozolomide). Some patients received more than six rounds of chemotherapy, depending on treatment response and clinical status. Used with permission from C. Larsson, M. Kleppestø and J. Vardal.

4.2. MRI and annotations

The data analyzed in this thesis consisted of multi-sequence/series (multiparametric) structural and functional MR images together with tumoral lesion segmentations, RANO classes and overall survival numbers. A structural MRI volume may be described as a three-dimensional grid consisting of equally (isotropic) or unequally (anisotropic) spaced integer or floating-point values, representing the imaged gray scale intensity value at various anatomical locations. A lesion segmentation can be described similarly, but with integer values describing different lesion tissue classes. Longitudinal, multi-sequence and functional MRI result in an additional fourth dimension (representing either time or image channel) of the volume after having performed necessary pre-processing steps.

4.2.1. MRI

MRIs were performed on two different $3\,Tesla$ Philips scanners (Philips Medical Systems, Best, The Netherlands); Ingenia for the first cohort and Achieva for the second cohort. The structural MRI included in the first cohort was 3D T2w-FLAIR (TE/TR/TI (ms) = $311/4800/1650$, voxel size $0.5x0.49x0.49\ mm$, flip angle of 90 degrees and pixel bandwith around $936\ Hz$) and T2w SE (TE/TR = $84/3800\ ms$, voxel size $0.3x0.3x5\ mm$). For the second cohort, structural images included 3D T2w-FLAIR (TE/TR/TI (ms) = $424/8000/2400$, voxel size $1.07x1.07x0.6\ mm$), 3D T1w GE before and after contrast CA injection (T1w, T1wc, TE/TR = $2.3/5.1\ ms$, voxel size $1\ mm^3$ and flip angle of 8 degrees) and T2w SE (TE/TR (ms) = $70/1349$, voxel size $1.88x1.88x4.0\ mm$ and flip angle of 90 degrees). T1wc was acquired following injection of $0.1\ mmol/kg$ body weight dose of gadobutrol (Gadovist, Bayer, Sweden) and saline flush. Acquisition times were 400, 400, 112 and $520\ s$ for T1w, T1wc, T2w and T2w-FLAIR respectively in the second cohort.

The functional MRI included in the first cohort was DSC with dual echo (GE-SE), single-shot EPI sequences (GyroToolsLLC, Zürich, Switzerland) (TR = $1300-1500\ ms$, GE: TE = $25-30\ ms$, SE: TE = $105-115\ ms$, echo train length = 78, partial Fourier acquisition of 0.61, SENSE factor 2, voxel size $1.8x1.8x6\ mm$ and flip angle of 90 degrees followed by a 190 degree RF pulse for inducing SE). Initially, 5 time points (image volumes) were acquired before CA injection (pre-scan), subsequently a DSC of 100 time points was acquired with opposite phase-encode direction during CA injection ($0.1\ mmol/kg$ body weight dose of contrast (Gadovist, Bayer Pharma AG, Germany), followed by a $20\ mL$ saline flush (BB. Melsungen AG, Melsungen, Germany)). Unlike the structural MRI, DSC included only $9-11$ axial slices to cover the tumor. Acquisition times were $\sim 15-22\ s$ for the pre-can GE-SE

EPIs and $135 - 161\ s$ for the GE-SE DSC. The functional MRI in the second cohort was SE DSC (TE/TR = $70/1349\ ms$, voxel size $1.88x1.88x4\ mm$) consisting of 13 axial slices and with acquisition time of $112\ s$, and within the same CA injection and saline flush as the first cohort.

4.2.2. Annotations

Lesion segmentation of tumoral regions with contrast accumulation in T1wc, necrosis, as well as hyperintense regions on T2w/T2w-FLAIR, were provided for both cohorts. In the first cohort, ONCOhabitats [120] delineated edema, necrotic, and contrast enhanced tumor regions based on intra-patient T1w, T1wc, T2w and T2w-FLAIR exams, while in the second cohort, edema, necrotic and contrast enhanced tumor were delineated based on T1wc and T2w-FLAIR exams using a ONCOhabitats (paper 3) or a semi-automatic method with QC from an experienced neuroradiologist (paper 2) [50], [57]. See Figure 20 for an overview of lesion volume at baseline scans. In the first cohort, NAWM tissue masks used in CBV normalization were automatically generated using a k-means ($k = 5$) clustering method [149], while in the second cohort they were generated as part of ONCOhabitats. Overall survival times and the combined RANO+pseudoprogression classes previously described were included in the second cohort, as well as number of days in-between the longitudinal exams (extracted from DICOM scan dates). Similarly, age was extracted for both cohorts from DICOM information or from Excel sheets provided to the author.

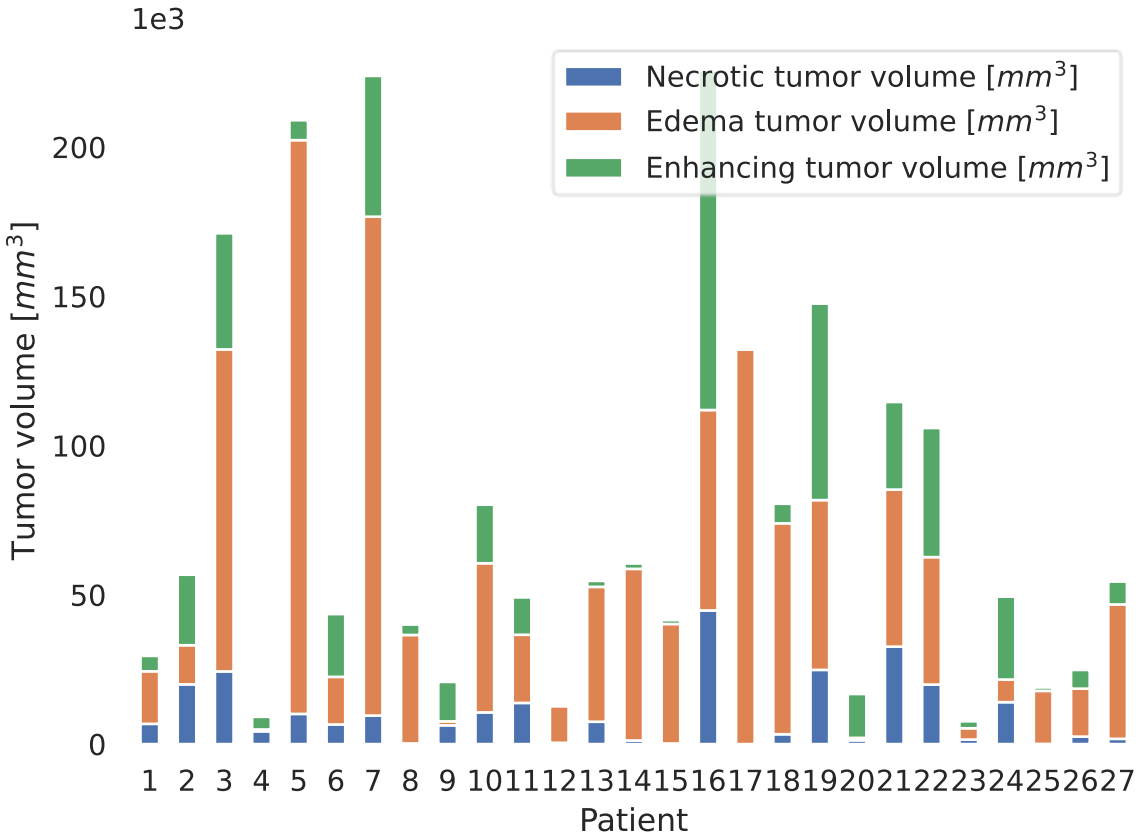

Figure 20: Variations in baseline lesion volume for the 27 patients diagnosed with HGG in our second cohort. The huge variation in lesion volume illustrates the heterogeneity of the disease. Figure from our third paper.

5. Methods

5.1. Preprocessing and organization

With the main objective of investigating how geometric distortion from a specific type of functional MRI sequence impacts CBV, paper one performed analysis in native low-resolution functional (perfusion) space. The preprocessing carried out for structural MRIs were 1. removal of facial structures (spm_deface), 2. DICOM to NIFTI conversion and 3. RIR and DIR to transform structural MRIs and a template of brain regions to patient-specific low-resolution DSC space. The de-facing and registrations were performed with SPM 12 (Statistical Parametric Mapping; spm_deface) [124] and ANTs [150], while DICOM to NIFTI

file format conversion was performed with dcm2niix [151]. NN interpolation was used at all relevant steps. The DSC-MRIs were corrected for head motion using nordicICE 4.0.0 (NordicNeuroLab, Bergen, Norway), before applying either TOPUP [111] or EPIC [110] geometric susceptibility distortion correction as the main analysis methods to investigate. CBV maps from DSC-MRI were corrected for CA extravasation using the Boxerman leakage correction method [90] and normalized relative to healthy NAWM values.

The objectives of paper two and three were to quantify and model tumor-induced structural changes. Thus, the focus here on structural effects, incentivized to work with the MRIs in high-resolution structural (anatomical) space. The MRI preprocessing steps follow much of the scientific recommendations for developing clinical imaging biomarkers [116], with some additional steps for approximate MNI (spatial) normalization and longitudinal intensity standardization. The full preprocessing pipeline for structural MRI can be summarized as 1. DICOM to NIFTI conversion, 2. denoising, 3. correction for nonuniform intensities, 4. $1\ mm^3$ voxel isotropic resampling, 5. brain extraction, then 6. longitudinal intensity standardization and 7. Spatial MNI normalization. DICOM to NIFTI file format conversion were, again, carried out with dcm2niix [151], then the NIFTI files were de-noised with a spatially adaptive filter [118] and corrected for nonuniform intensities with the N4ITK algorithm [79]. Voxel isotropic resampling for the cases of anisotropic MRI voxels, were performed with FLIRT [152] using linear interpolation, brain extraction with BET [153], and longitudinal intensity standardization by piece-wise linear histogram matching within brain masks [127], [128]. Lastly, all MRIs were intra-patient rigid registered (RIR) based on a structural MRI, then inter-patient spatially normalized by RIR and AIR to the MNI-International Consortium for Brain Mapping (ICBM)-152 2009c nonlinear symmetric T1w or T2w template [154], [155]. All registrations were performed using ANTs.

Version controlled datasets [132] following brain imaging data structure (BIDS) [130] recommendations were standards of practice in most of the thesis' work. Moreover, suited visualization tools were important and dependent on the preprocessing and analysis steps as described previously. The perfusion module of nordicICE was used in the thesis to generate CBV maps from uncorrected and TOPUP and EPIC corrected DSC-MRI.

5.2. RBF interpolation

Interpolation with radial basis functions (RBFs) in four dimensions is investigated as a method for visualizing and understanding high-resolution longitudinal MRI. It is used to create an approximate MRI volume for each day estimating the general cancer and treatment patterns. An example of RBF interpolated MRI was presented in section 3.2.4. RBF interpolation is a form of Gaussian process regression ("kringing"), or interpolation with Gaussian kernels. A Gaussian process may be described as an infinite dimensional generalization of a multivariate normal distribution. A parallelized version of this method was implemented. This is a meshfree in approximation method [156], [157] that takes scattered data points in arbitrary dimensions as input and describes them as a weighted linear combination of strictly positive definite [158] radial functions (Figure 21 [159]).

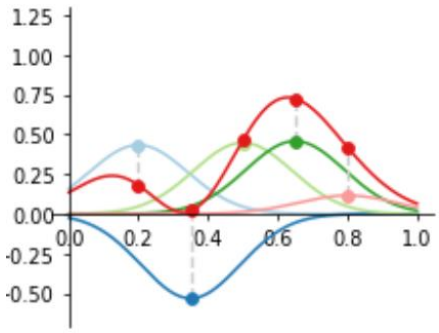

Figure 21: One-dimensional Gaussian RBF interpolation. A continuous function passing through all the red dots is a weighted linear combination of Gaussians with varying center offset and width. The source code for this figure is openly available at the figure reference.

Longitudinal MRI of a single patient (with isotropic voxel dimensions and irregular amount of days between the scans) may be regarded as scattered data in four dimensions. Assume that the spatial coordinate and time point for a given voxel in linearly registered longitudinal MRI for a patient is $\boldsymbol{x}_j = [x, y, z, t]$ and its intensity value is y_j. Then, all N $\boldsymbol{x}_j$-y_j pairs can be fitted to a linear combination of certain basis functions B_k creating the continuous function

$$\mathcal{P}_f(\boldsymbol{x}) = \sum_{k=1}^{N} c_k B_k(\boldsymbol{x}) \tag{5.1}$$

The number of basis functions B_k is the number of data points N and

$$B_k(\boldsymbol{x}_j) = \varphi(||\boldsymbol{x}_j - \boldsymbol{x}_k||) = \phi(\boldsymbol{r}) \tag{5.2}$$

is a RBF centered at $\boldsymbol{x}_k$ where $\boldsymbol{r} = ||\boldsymbol{x}_j - \boldsymbol{x}_k||$ is the radial distance from its center position $\boldsymbol{x}_k$ to the true data point $\boldsymbol{x}_j$. B_k is radial because its output value is only dependent on the magnitude of the input vector $\boldsymbol{r}$. B_k is thus symmetric. A common RBF is the Gaussian function $\phi(\boldsymbol{r}) = e^{-(\epsilon \boldsymbol{r})^2}$ where ϵ is a positive shape parameter (Figure 22 [157]).

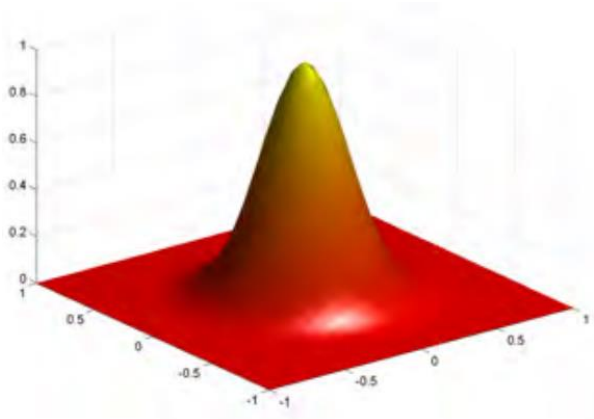

Figure 22: Gaussian radial basis function for two dimensions.

RBF interpolation amounts to finding the appropriate center $\boldsymbol{x}_k$, shape parameter ϵ_k and weighting c_k for all N RBFs by solving the linear equation system $A\boldsymbol{c} = \boldsymbol{y}$ where $A_{jk} = B_k(\boldsymbol{x}_j),\ j,k \in [1,N],\ \boldsymbol{c} = [c_1 \quad \cdots \quad c_N]^T,\ \boldsymbol{y} = [y_1 \quad \cdots \quad y_N]^T$. An interpolated value y can be obtained by sampling $\mathcal{P}_f$ on any desired input value $\boldsymbol{x}$.

5.3. Voxel tracking

Voxel tracking is the common denominator in the three publications in the thesis, where the objective is tracking displacement and possibly intensity shift of voxels between two MRI scans. The true track of a voxel restricted piece of tissue may be complex. This thesis focuses on tracking only the final displacement vector and intensity shift between MRIs (Figure 23).

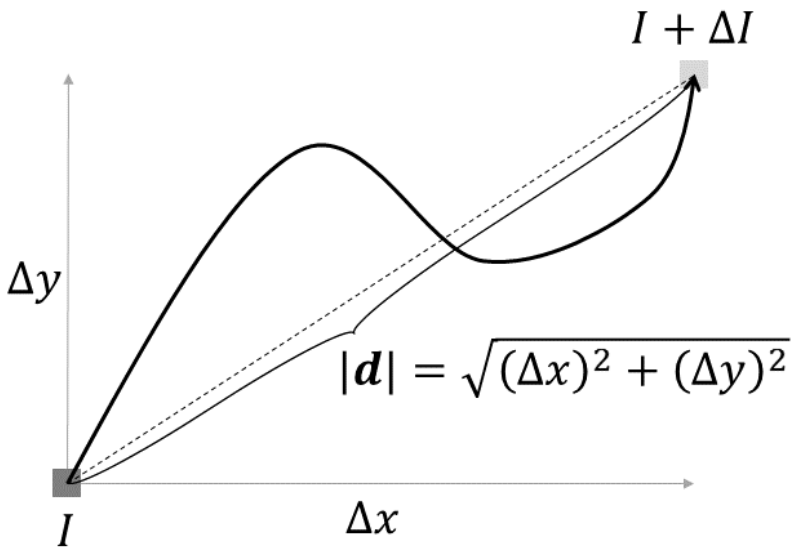

Figure 23: Illustration of tracking the final displacement and intensity change of a pixel. Final displacement is the dotted line. Voxel tracking is achieved by adding a third dimension z.

Assume that the displacement $\boldsymbol{d}(\boldsymbol{x})$, $\boldsymbol{x}, \boldsymbol{d} \in \mathbb{R}^3$ (i.e. $\boldsymbol{x} = [x \quad y \quad z]^T$ and $\boldsymbol{d}(\boldsymbol{x}) = [\Delta x(\boldsymbol{x}) \quad \Delta y(\boldsymbol{x}) \quad \Delta z(\boldsymbol{x})]^T$) and intensity change ΔI of a voxel restricted piece of tissue is known between two MRI scans I_t, I_{t+1} with sufficient high isotropic voxel resolution (e.g. $1\ mm^3$). If allowing any displacement and intensity change of voxels, the macroscopic spatiotemporal transformation of MRI I_t to MRI I_{t+1} can be written as

$$I_{t+1}(\boldsymbol{x}) = (I_t + \Delta I) \circ T \tag{5.3}$$

where $\circ$ is the function composition operator, i.e. $g \circ f = g(f(\boldsymbol{x}))$ and $T: \mathbb{R}^3 \to \mathbb{R}^3$ is a non-linear dense transformation of voxel coordinates,

$$T(\boldsymbol{x}) = \boldsymbol{x} - \boldsymbol{d}(\boldsymbol{x}) \tag{5.4}$$

In equation (5.4), $\boldsymbol{d}(\boldsymbol{x})$ is a displacement vector field describing the tissue displacement from MRI I_t to MRI I_{t+1} at starting voxel coordinate position $\boldsymbol{x}$. Equation (5.3) assumes that the voxel intensity change ΔI is known in the frame of the first MRI I_t, i.e., before applying the nonlinear displacement transformation T.

5.4. Voxel displacement path tracking

This is a longitudinal extension of voxel tracking when focusing on displacement only. The trajectory of a voxel or piece of tissue originating from the first (or last) image directly follows the pathline computed from the time-varying displacement vector field described by the consecutive dense voxel coordinate transformations $T_1, T_2, \dots, T_N$. If $\boldsymbol{d}(\boldsymbol{x}(t), t)$ describes the displacement fields evaluated at voxel coordinate $\boldsymbol{x}$ for the time duration $t \in [1, N]$, pathlines can be computed by solving

$$\frac{d\boldsymbol{x}}{dt}(t) = \boldsymbol{d}(\boldsymbol{x}(t), t) \tag{5.5}$$

Typically, a specific region (e.g., CA mask) is defines from where to start computing pathlines. If ignoring intensity changes ($\Delta I = 0$), equation (5.3) may be interpreted as the resampling (re-slicing) step in DIR (section 5.6). For this case, I_t and I_{t+1} in equation (5.3) is equivalent to the moving and fixed image equation (3.19). An example of DIR pathline visualization (cancer-sim.com) is presented below in Figure 24 using the X toolkit [160].

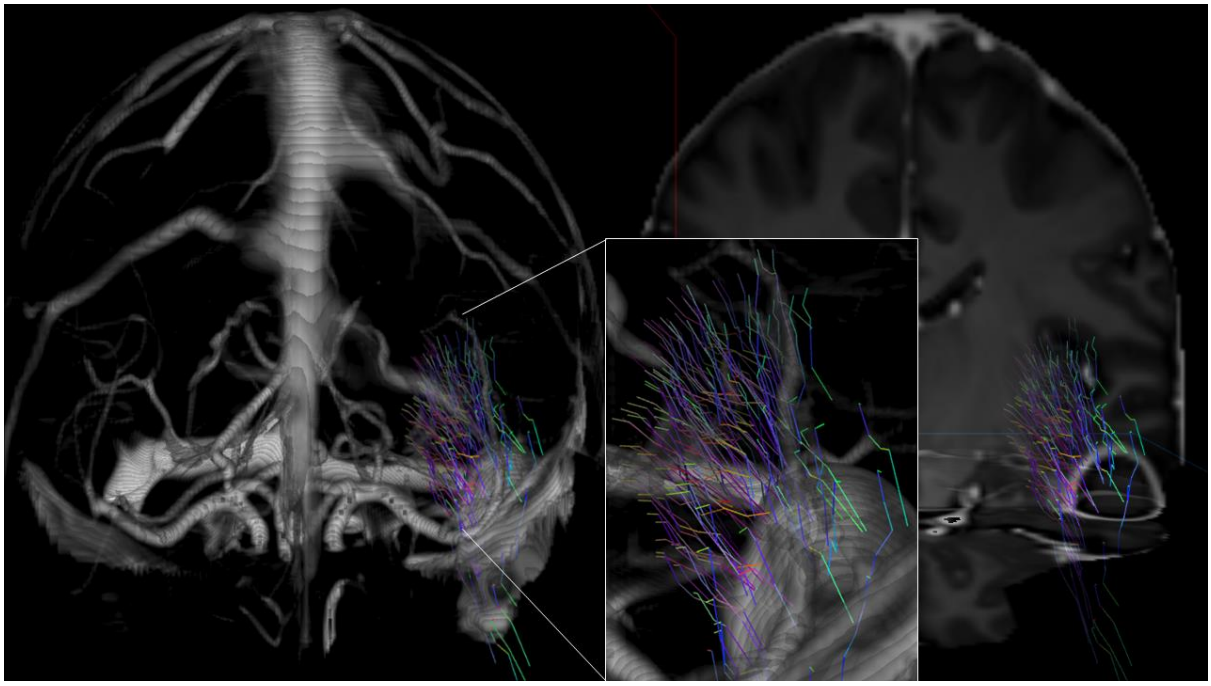

Figure 24: Voxel displacement path visualization with cancer-sim.com. Pathlines computed from estimated displacements from backwards-in-time ANTs SyN CC deformable image registration. A subset of 512 voxels in the contrast-enhanced ring of the last T1wc MRI was tracked backwards in time, many of which ended up in the contrast-enhanced ring shown in the first T1wc MRI in the figure. Pathlines are visualized like DTI fiber lines. This is subject one from our second patient cohort.

5.5. EPI correction

As described in section 3.4.3, EPI geometric susceptibility distortion occurs primarily due to the low bandwidth in the phase-encode direction. This means that ΔB causes additional shifts in phase of the nuclear spins, which translates into to pixel shifts along the y-axis in the axial EPI by a factor that is proportional to ΔB. In comparison, high bandwidth would mean that the phase shifts caused by ΔB would instead translate into intravoxel dephasing (leading to signal decay).

Specifically, both sign and magnitude of ΔB as well as direction of phase-encode traversal of k-space during EPI acquisition contributes to the final distortion in the EPI. A common EPI acquisition consists of positive (bottom-up) phase-encode traversal and for this type phase distortions results in a compression or squeezing effect along the y-axis in the EPI in addition

to intensity distortions (Figure 16 A, B). Moreover, opposite phase-encode transversal results comparingly in a stretching effect, which was the case for our DSC-MRI EPIs (Figure 16 C, D).

Generally correct assumptions are:

1. Pixel displacement d along the axial y-direction of the EPI is proportional to ΔB
2. The associated pixel intensity distortion ΔI is proportional to ΔB
3. d and ΔI is equal in magnitude but have opposite sign when describing an EPI pair with positive and negative phase-encode direction

The correction methods in the thesis (FSL TOPUP [111] and EPIC [110]) make these assumptions in order to formulate EPI distortion correction as a voxel tracking problem.

5.5.1. The voxel tracking problem for EPI correction

Let $\boldsymbol{x}_+$ and $\boldsymbol{x}_-$ be the voxel position coordinates for a positive and negative phase-encode EPI, and $\boldsymbol{x}$ the corresponding coordinates for a distortion corrected EPI. The opposite sign assumption of the displacement inherent in the EPIs (assumption 3.) can be described by the transformation pair $T_+, T_-: \mathbb{R}^3 \to \mathbb{R}^3$

$$T_+(\boldsymbol{x}): \boldsymbol{x} \to \boldsymbol{x}_+ = [x \quad y + d(\boldsymbol{x}) \quad z]^T \tag{5.6}$$

$$T_-(\boldsymbol{x}): \boldsymbol{x} \to \boldsymbol{x}_- = [x \quad y - d(\boldsymbol{x}) \quad z]^T \tag{5.7}$$

Furthermore, the relation between the EPIs in terms of geometrical and intensity distortions can be formulated similar to equation (5.3),

$$\left|\frac{\partial T_+}{\partial \boldsymbol{x}}\right| |_{x_+}(\tilde{I}_+ \circ T_+) = \left|\frac{\partial T_-}{\partial \boldsymbol{x}}\right| |_{x_-}(\tilde{I}_- \circ T_-)$$

(5.8)

where $\tilde{I}_+$ and $\tilde{I}_-$ is the positive and negative phase-encode (distorted) EPI. The derivative terms ($\left|\frac{\partial T}{\partial \boldsymbol{x}}\right|$) may be called Jacobian intensity modulations.

FSL TOPUP and EPIC use the formulation in equation (5.8) in slightly different ways to estimate a field that can be used to distortion correct the EPI. The difference between the methods is the type of field as well as the type of model used together with the field to perform correction. TOPUP estimates the off-resonance (scalar) field ΔB, while EPIC estimates the y-displacement (scalar) field d (Figure 25).

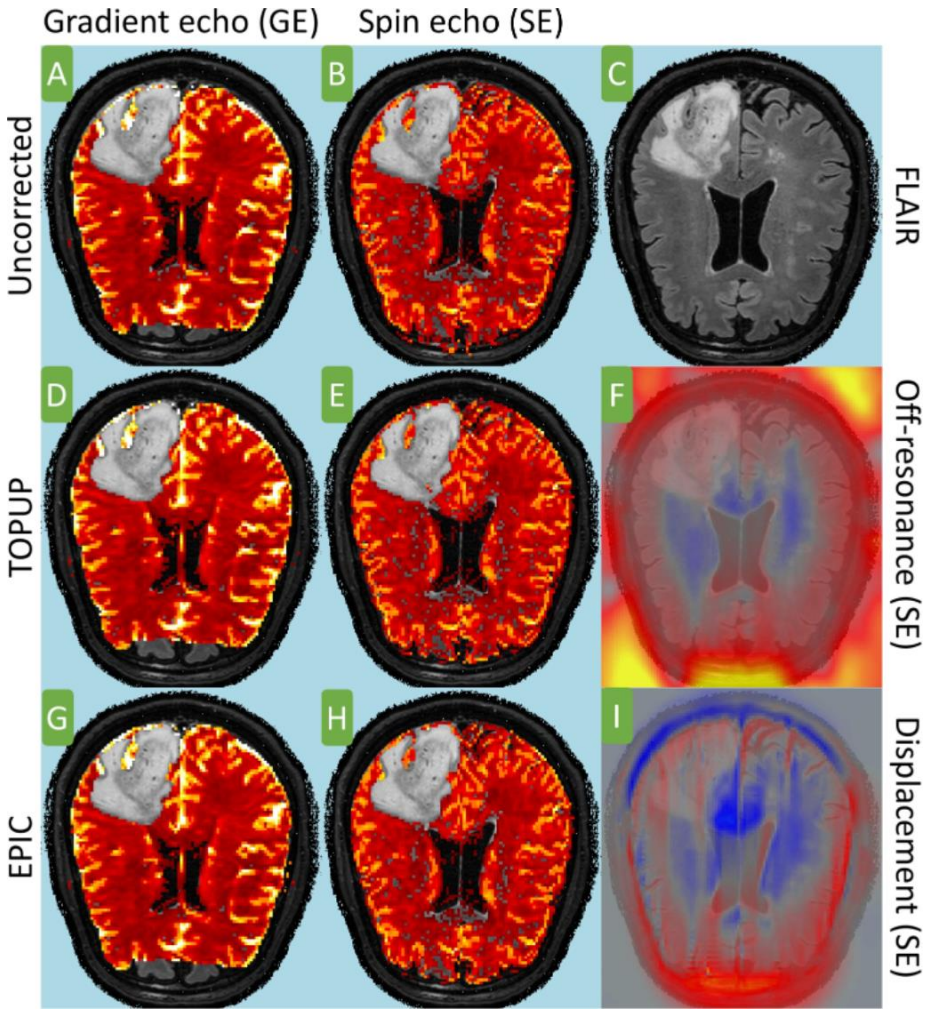

Figure 25: CBV estimated from A, B: uncorrected, D, E: TOPUP corrected, and G, H: EPIC corrected DSC-MRI for a patient. After CBV estimation, tumorous CBV voxels were excluded based on ground truth tumor lesions as described in the first paper. C: T2w-FLAIR as undistorted reference image. F: TOPUP-estimated spin-echo geometric distortion in terms of spin off-resonance ($[-10,10]\ Hz$ shown). I) EPIC-estimated spin-echo geometric distortion in terms of anteroposterior voxel displacement ($[-10,10]\ mm$ shown). Gradient-echo versions of F and I were also computed but are not shown in the figure. For F and I, blue and red illustrates negative and positive units, respectively. The window range used was $[0,7]$ for all CBV maps. Figure from our first paper.

TOPUP and EPIC are termed reverse gradient methods (reversed phase-encode correction methods) since the field is estimated by reversing the gradients (the transformations T) as will be explained in the next subsections. Moreover, this type of EPI correction is performed retrospectively after having captured two EPI scans with opposite phase-encode direction. Other EPI correction methods, such as direct field mapping using a double GE sequence [112], DIR [161], [162] or point spread function mapping [163], are not investigated in the

thesis. For a comparison of the different methods, see these theses [106], [164]. The reverse gradient correction methods can be performed on either SE or GE EPIs. Due to additional signal loss (drop-out) associated with GE, it is recommended to estimate the field from SE EPIs. As stated in section 2, the aim of the first paper is to investigate the impact of EPI distortion correction on CBV estimation (computed from DSC-MRI consisting of EPIs). Additional signal loss in GE (not accounted for in the thesis) is seen in the frontal areas in the axial CBV maps in Figure 25.

5.5.2. FSL TOPUP

TOPUP estimates ΔB (from equation (3.17)) as a linear combination of spatial basis functions consisting of a truncated tree-dimensional discrete cosine transform (DCT). DCT can be characterized as a real-valued version of the discrete Fourier transform (DFT), but which is asymmetric and has twice the frequency resolution when compared to DFT ([165], Chapter 7.4). These characteristics make DCT well suited for modeling ΔB. TOPUP specifically estimates $18 \cdot 18 \cdot 7 = 2268$ basis weights using a reverse gradient method based on equation (5.8). Details of the estimation method is thoroughly explained in the reference paper [111].

Equation (3.18) can be re-written as

$$\tilde{S} \propto \widetilde{\boldsymbol{M}}_T = \iint_{xy} I(x,y) e^{-j\left(k_x x + k_y y + \delta B(x,y,t)\right)} dxdy \tag{5.9}$$

and further discretized in form of a matrix-based transform ([165], Chapter 7.2) $\tilde{S} = AI$, where A implements the two-dimensional DFT. The main idea of correction in TOPUP is that

there exists a transform F that is like A but which contains zero magnetic susceptibility distortions ($\Delta B = 0$), such that the distorted EPI can be expressed as

$$\tilde{I} = FAI = KI$$

(5.10)

A Moore-Penrose pseudo-inverse K^+ of K can be computed to estimate the distortion corrected image $\hat{I} = K^+\tilde{I}$. However, this results in ringing artifacts in areas with large compression (due to resulting signal loss). Instead, since capturing both positive $\tilde{I}_+$ and negative $\tilde{I}_-$ phase-encode EPIs it is possible to express the distortion correction problem as

$$\begin{bmatrix}\tilde{I}_+\\ \tilde{I}_-\end{bmatrix} = \begin{bmatrix}K_+\\ K_-\end{bmatrix} I$$

(5.11)

With K_+ and K_- being the corresponding matrix transforms (termed interpolation matrices). A distortion corrected image $\hat{I}$ without artifacts produced by the Moore-Penrose pseudo-inverse can then be computed by the generalized inverse of the augmented matrix $\begin{bmatrix}K_+\\ K_-\end{bmatrix}$

$$\hat{I} = \left([K_+^T \quad K_-^T]\begin{bmatrix}K_+\\ K_-\end{bmatrix}\right)^{-1}[K_+^T \quad K_-^T]\begin{bmatrix}\tilde{I}_+\\ \tilde{I}_-\end{bmatrix}$$

(5.12)

To summarize, TOPUP models ΔB as a linear combination of DCT spatial basis functions as well as the image formation process of positive and negative phase-encode SE EPIs, to obtain a distortion corrected EPI from a generalized inverse. TOPUP is the magnetic susceptibility distortion correction method provided by the FMRIB Software Library (FSL) [138].

5.5.3. EPIC

EPIC modifies equation (5.8) by reversing the sign of the y-displacement d within the transformations T_+ and T_- and the Jacobian intensity modulations. It is then re-formulated into a cost function of the form

$$f(d) = \left| \left|\frac{\partial T_-}{\partial \boldsymbol{x}}\right| |_{\boldsymbol{x}}(\tilde{I}_+ \circ T_-) - \left|\frac{\partial T_+}{\partial \boldsymbol{x}}\right| |_{\boldsymbol{x}}(\tilde{I}_- \circ T_+)\right|^2 + \lambda_1 d^2 + \lambda_2 \nabla \mathrm{d}$$

$$= \left|\left(1 - \frac{\partial d}{\partial y}\right)(\tilde{I}_+ \circ T_-) - \left(1 + \frac{\partial d}{\partial y}\right)(\tilde{I}_- \circ T_+)\right|^2 + \lambda_1 d^2 + \lambda_2 \nabla \mathrm{d} \quad (5.13)$$

where λ_1 and λ_2 are added regularization parameters that control the quality of the displacement estimation. $\lambda_1 = 0$ and $\lambda_2 = 10^4$ were used as in the reference paper [110]. The displacement d for each voxel is then estimated using the following Hessian-based optimization:

0. Initialize the displacement field d to zero
1. Smooth the original positive and negative phase-encode EPIs using a Gaussian kernel with standard deviation to $3.5 - 4\ mm$
2. Compute the Hessian H_f and gradient ∇f of f for the current displacement field d
3. Solve the quadratic form approximation $H_f \cdot v = -\nabla f$ for v
4. Update the displacement field by $d = d + v$
5. Decrease the standard deviation (width) of the Gaussian smoothing kernel by $0.25 - 0.5\ mm$

Step 1.-5. is then repeated until there is no smoothing. Having the final estimated displacement d for each voxel, a distortion corrected EPI $\hat{I}$ is then computed from either of the positive or negative phase-encode EPI according to

$$\hat{I} = \left(1 - \frac{\partial d}{\partial y}\right)(\tilde{I}_+ \circ T_-) = \left(1 + \frac{\partial d}{\partial y}\right)(\tilde{I}_- \circ T_+)$$

(5.14)

In summary, EPIC estimates the voxel displacement associated with EPI geometric distortion by negating the sign of displacement in equation (5.8) in order to describe the mapping from distorted to non-distorted space for both positive and negative phase-encode EPIs. This allows re-formulating EPI distortion correction to a Hessian-based optimization problem as described above. The displacement is iteratively estimated together with Gaussian smoothing of decreasing width, to ensure increasingly fine-grained displacement estimation, and thus convergence over the iterations. The final estimated displacement field is then used to perform EPI distortion correction from either of the positive or negative phase-encode EPIs. Like TOPUP, both displacement and intensity shift of voxels is corrected.

For an example of incorporating EPIC into a clinical workflow, see this recent Master's thesis [106]. TOPUP and EPIC, among others, were also investigated in another recent Master's thesis [166].

5.5.4. Relation between displacement and intensity distortions and field inhomogeneities

One important insight in EPI geometric susceptibility distortion correction is that both ΔB, d and ΔI are related according to

$$\frac{\partial d}{\partial y} = T\gamma \frac{\partial \Delta B}{\partial y} = \Delta I$$

(5.15)

where $T = N\Delta t$ is the total time spent on a single-slice, single-shot EPI k-space recording, Δt is the time used to record an echo into a single frequency-encoded k-space line (readout),

and N the number of k-space acquisition lines. γ is the gyromagnetic ratio connecting the magnetic field strength to resonance frequency as explained in section 3.3.1. Different from equation (5.3), ΔI here belongs to the displaced (corrected) image space ($\hat{I}$). The partial derivative of the estimated y-displacement is the shift in voxel intensity and is proportional to the field inhomogeneities, EPI acquisition time and gyromagnetic ratio.

5.6. Deformable image registration

DIR is a non-linear (non-rigid) alignment of two MRIs that estimates a dense displacement field to describe the spatial transformation from one MRI to another. DIR results in displacement-only voxel tracking. Non-linear and non-rigid means, opposed to rigid or affine [123], that there are non-linear local spatial correspondences in the transformation, such as spatial warps. With the aim to estimate physical displacement of tissue voxels, DIR is only valid first after having applied LIR to rule out rigid and affine global correspondences between two images (Figure 26 [167, p. 14]). These preceding intra-patient rigid registrations (RIRs) were performed with ANTs [150] with the well-known MI loss metric [143] as the spatial alignment function A.

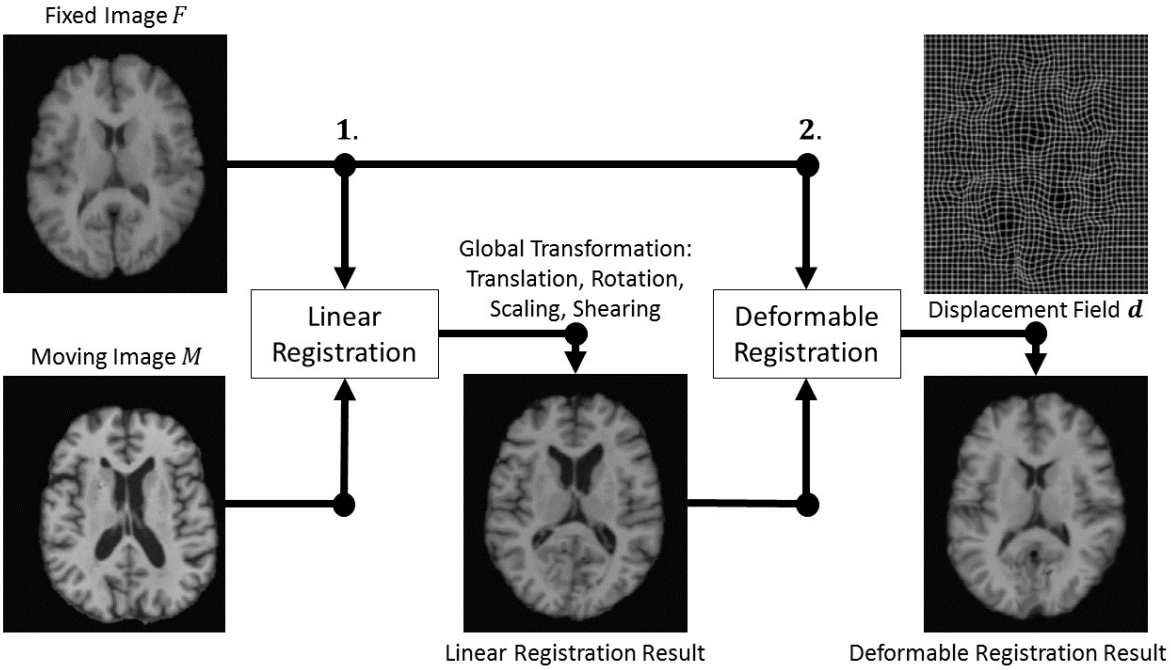

Figure 26: Deformable image registration for tracking structural deformations between two images of the same patient. 1. Linear image registration is performed to achieve global alignment between the images F and M in terms of linear transformations on M such as rotation and translation. 2. A displacement field $\boldsymbol{d}$ describing the remaining local non-linear tissue displacement between the F and the linearly transformed M is estimated. Finally, $\boldsymbol{d}$ can be used to deform the linearly transformed M into reconstructing F in terms of displacement only. Used with modifications and permission from Elsevier (License number: 5433670719364).

5.6.1. The voxel tracking problem for DIR

For DIR, T in equation (3.19) contains a vector field of the estimated displacement of each voxel coordinate from the first MRI to the second MRI, as described by the voxel tracking equation (5.4). Hence, T is a nonparametric deformation model described by a non-linear dense transformation. Only monomodal (e.g. T1w to T1w) DIR is investigated in the thesis. If DIR is used to estimate tissue displacement, it is thus reasonable to include intensity shift (ΔI) in the voxel tracking problem to model tissue transformation from biological processes such as cancer and treatment. The DIR conducted in the thesis is only intended to quantify voxel displacement and not intensity shift. DIR thus partly fulfills voxel tracking as it is defined in section 5.3.

5.6.2. Mathematical terminology

Medical DIR may be grouped according being based on physical models, interpolation and approximation theory, ap-priori knowledge or specific tasks [121], [168]. Some DIR methods estimate both the forward and backward displacement field allowing to transform each MRI into the other MRI in terms of displacement only (inverse consistency). A mapping preserves topology (is homeomorphic) if it is continuous, onto and locally one-to-one both forwards and backwards. Topology preserving mappings that are differentiable contain Jacobian determinants that are greater than zero. These mappings are termed diffeomorphic if they are also invertible. A symmetric mapping is achieved if the forward and backward displacement vectors describe the shortest displacement paths possible (are geodesics) and are equal in magnitudes [169]. A consequence of symmetric mapping is that the forward and backward displacement vectors meet in a midpoint that is half the distance from their origins (termed symmetric normalization, SyN) [143].

5.6.3. ANTs SyN

The main DIR method in the thesis is ANTs symmetric diffeomorphic image normalization (ANTs SyN) with neighborhood CC as the spatial alignment function A [144]. It is bundled with the advanced normalization tools (ANTs) software package [150]. ANTs SyN may also be used with other alignment functions such as voxel-vise MI [143]. ANTs SyN CC performs well compared to ANTs MI and other deformable medical registration algorithms [170], which is also shown in the third publication. ANTs SyN extends a physics-based deformation model in the Lagrangian specification of a velocity field [171] by using a symmetric formulation of forward and backward velocity fields for describing voxel displacement [144]. It belongs to a group of registration algorithms called large deformation diffeomorphic

metric mapping (LDDMM) [172], [173] in which diffeomorphic mapping is ensured by constraining the velocity field to be smooth in the regularization term R [121], [172].

5.6.4. Optical flow

Optical flow (OF) methods [174] may be described as small deformation monomodal DIR methods [121]. An essential assumption in OF is that voxel intensity values does not change during displacement ($\Delta I = 0$ in equation (5.3)). While DIR seeks to find spatial correspondences between images, OF seeks to recover the apparent motion of objects within images. OF is generally neither inversely consistent, nor homeomorphic, diffeomorphic, or symmetric. As a result, it is best suited for estimating motion within images that can be described by a displacement vector field having properties similar to incompressible flow [168]. In our third paper, however, OF by Farnebäck [175] showed similar voxel displacement estimation accuracy to ANTs SyN CC, and outperformed the iterative Lucas-Kanade [176] and TV-L1 [177, p.] dense OF methods. This highlights the potential utility of Farnebäck OF as a fast method for DIR.

5.7. Deformation biomarkers

Voxel-vise displacements estimated from DIR of longitudinal MRI lay the basis for longitudinal MRI analysis in the thesis. General quantifications of tumoral displacement and peritumoral compression may be obtained by computing displacement magnitudes and quantized divergences as follows: By writing out the voxel-vise displacement vector field $\boldsymbol{d}$ to component form (using the $\boldsymbol{i}, \boldsymbol{j}, \boldsymbol{k}$ orthonormal basis vectors) $\boldsymbol{d}(\boldsymbol{x}) = M(\boldsymbol{x})\boldsymbol{i} + N(\boldsymbol{x})\boldsymbol{j} + P(\boldsymbol{x})\boldsymbol{k}$, divergence is a scalar field computed by summarizing partial derivatives of $\boldsymbol{d}$ such that [178]

$$div\ \boldsymbol{d}(\boldsymbol{x}) = \nabla \cdot \boldsymbol{d} = \frac{\partial M}{\partial x}|_x + \frac{\partial N}{\partial y}|_x + \frac{\partial P}{\partial z}|_x$$

(5.16)

Displacement magnitudes describe a displacement scalar field computed as

$$|\boldsymbol{d}| = \sqrt{M^2 + N^2 + P^2}$$

(5.17)

In our second paper, divergence and magnitude maps computed from ANTs SyN CC displacement fields were used to develop four biomarkers as illustrated in Figure 27.

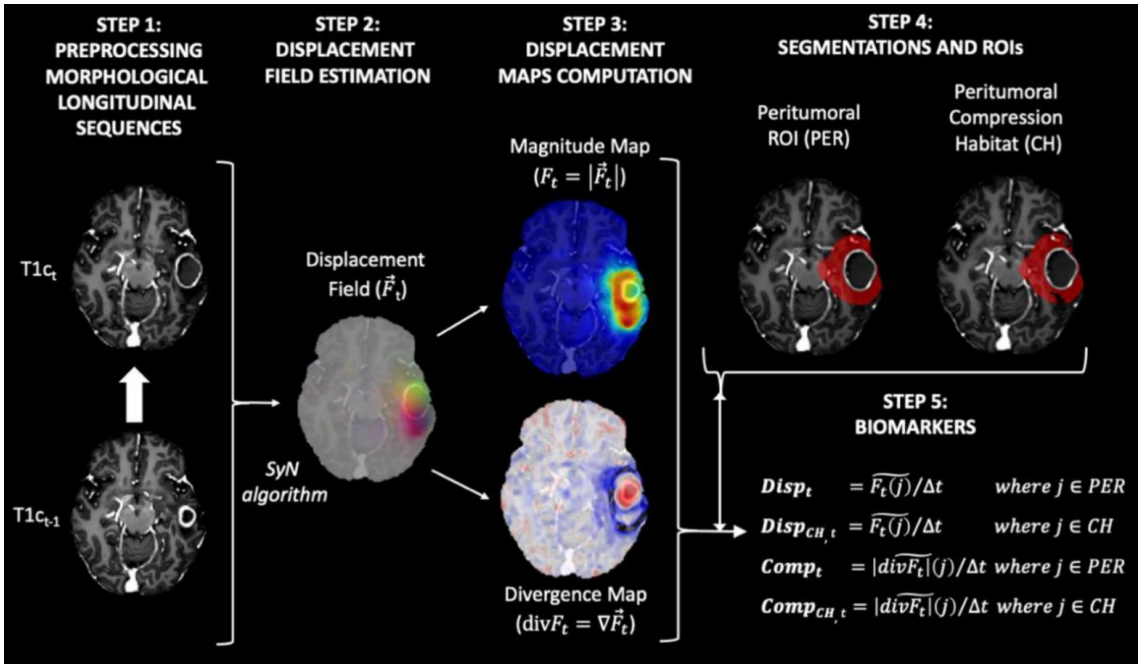

Figure 27: Developing four deformation biomarkers based on longitudinal consecutive deformable image registration using the ANTs SyN algorithm. Here $T1c_t$ and $T1c_{t-1}$ describe the fixed and moving scans (forward-in-time registration). Figure from our second paper.

The divergence and magnitude maps are analyzed within peritumoral ROIs in the second paper. Particularly interesting regions are the peritumoral regions presenting with negative divergence (i.e., $\nabla \cdot \boldsymbol{d} < 0$) from a longitudinal MRI pair, providing a basis for quantifying peritumoral tissue compression. Note that a nonzero divergence implies compressible flow, which is tricky for OF methods. However, the third paper presents evidence that Farnebäck

OF can perform similar to ANTs SyN CC and that it thus may still be a relevant candidate as a faster DIR method than ANTs SyN CC for capturing the tissue imaging biomarkers in our second paper.

5.8. Deformation model

A simple and robust deformation model of general macroscopic shrink and growth behavior in glioblastoma is developed (Figure 28). It models either shrinkage of regions from collapse and remodeling of tissue regions from surgery, radiation- and chemotherapy, or expansion/enlargement of regions as a result of cancer growth [179]–[181]. In the third paper, it is used to generate synthetic expansion deformations for benchmarking DIR methods. It is inspired from real-world longitudinal MRI such as Figure 9 presenting tumoral expansion from a pushing glioblastoma phenotype, and Figure 8 presenting both shrinkage and expansion from an infiltrative phenotype.

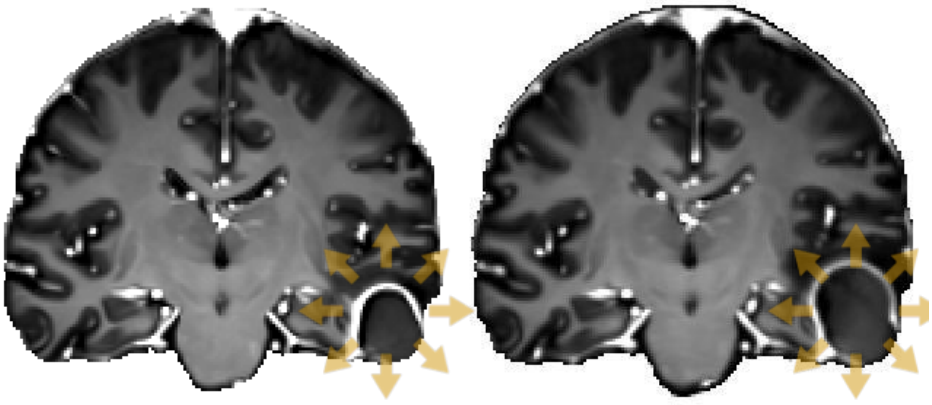

Figure 28: Illustration of expansion growth of lesion and cavity area followed by displacement and compression of peritumoral tissue. Figure from our third paper.

For a single execution, the algorithm creates a realistic displacement field $\boldsymbol{d}(M_l, M_b, \alpha, \beta, \gamma)$ using the information from the outlined lesion M_l and brain M_b masks, merged with three simulation parameters:

1. Maximum tissue displacement α $[mm]$
2. Infiltration β
3. Growth irregularity γ

By varying these three simulation parameters, it creates displacement fields and associated deformed scans as illustrated in Figure 29.

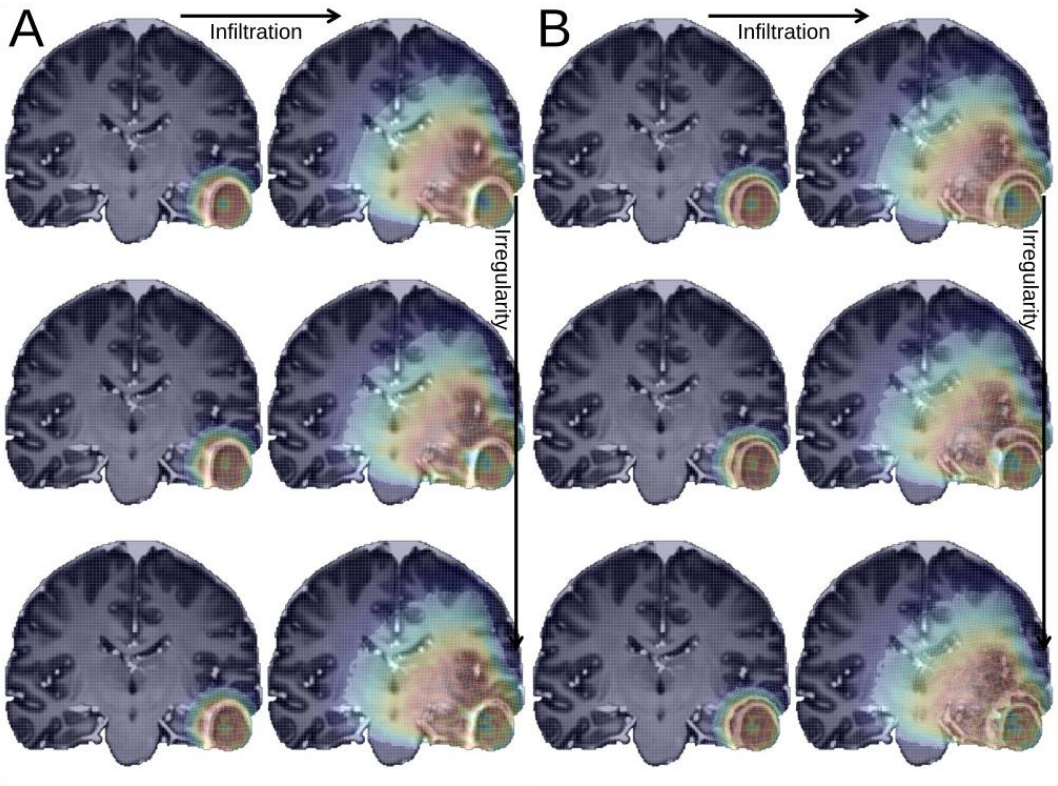

Figure 29: Growth simulations with the deformation model on T1wc MRI in the third paper. A: $\alpha = 3$ $[mm]$, B: $\alpha = 8$ $[mm]$. Two values of infiltration β (A, B horizonzal: low and high infiltration) and three values of irregularity γ (A, B vertical: no, intermediate and high irregularity). The resulting deformed T1wc MRI, magnitude of displacement field and deformation grid are overlaid. Figure from our third paper.

See Table 5 for a complete overview of the input data, simulation parameters and output as well as internal fixed parameters of the deformation model.

Table 5: Parameters of the synthetic deformation model. Shrinkage is modeled with a negative maximum displacement $\alpha < 0$, and growth with a positive $\alpha > 0$.

Input	Symbol	Range	Type	Description
Lesion mask	M_l	$[0,1]_2$	Binary scalar field	
Brain mask	M_b	$[0,1]_2$	Binary scalar field	
Displacement	α	$\mathbb{R}$	Scalar $[mm]$	Maximum tissue displacement
Infiltration	β	$[0,1]$	Scalar	Intensity decay fraction; 0: most infiltration, 1: least infiltration
Irregularity	γ	$< 0,1]$	Scalar	Perlin noise resolution; ~ 0: highest irregularity, 1: lowest irregularity
Noise	δ	$\mathbb{R}$	Scalar	Perlin noise maximum magnitude; fixed default $= 0.6$
Standard deviation	σ	$\mathbb{R}$	Scalar	Of g; fixed default $= 5$
Number of vectors	N_s	$[1, N]$	Integer	Number of directions for computing deformations; fixed default $= 32$
Angle deviation	θ	$< 0,90 >$	Scalar	2θ is the top angle of the directional cones; fixed default $= 7°$
Output				
Model	$\boldsymbol{d}(M_l, M_b, \alpha, \beta, \gamma)$	$\lvert\boldsymbol{d}\rvert \in [0, \alpha + \delta]$	Vector field	

Let w, h, d be the width, height, and depth of the bounding box for the outlined tumor segmentation mask M_l registered to $1\ mm^3$ voxel approximate MNI space as described in section 5.1.

The algorithm initially takes w, h, d as inputs to compute a three-dimensional Gaussian scalar field g consisting of σ standard normal deviations in each dimension, parameterized in equally spaced intervals and with resolution N according to equations (5.18) and (5.19).

$$g(x,y,z) = -e^{-\frac{x^2+y^2+z^2}{2}}$$

(5.18)

$$\begin{bmatrix} x \\ y \\ z \end{bmatrix} \in \begin{bmatrix} [-\sigma,\sigma]_{N(w)} \\ [-\sigma,\sigma]_{N(h)} \\ [-\sigma,\sigma]_{N(d)} \end{bmatrix}, \qquad N(l) = \begin{cases} l+1, & l\ odd \\ l, & l\ even \end{cases}$$

(5.19)

$N(l)$ in equation (5.19) results in an even number of sampling steps along each bounding box dimension of the lesion mask. This negligible simplification is required to be able to access the geometric center of the bounding box by simple matrix indexing. A selection of $\sigma = 5$ standard deviations ensures that the elliptic scalar field g is within the tumor bounding box entirely ($\sim 100\ \%$). See Figure 30 for an illustration of the one-dimensional (1D) variant of g.

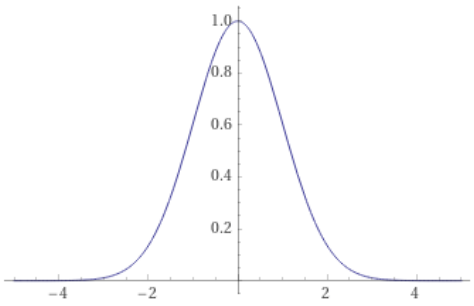

Figure 30: g in one dimension with $\sigma = 5$.

An initial model displacement vector field $\boldsymbol{d}(M_l)$ is then computed from the gradient (partial derivatives with respect to x, y and z) of g by $\boldsymbol{d} = \nabla \mathrm{g}$. Figure 31 illustrates how $\boldsymbol{d}$ is computed from the tumor mask M_l for various spatial dimensions.

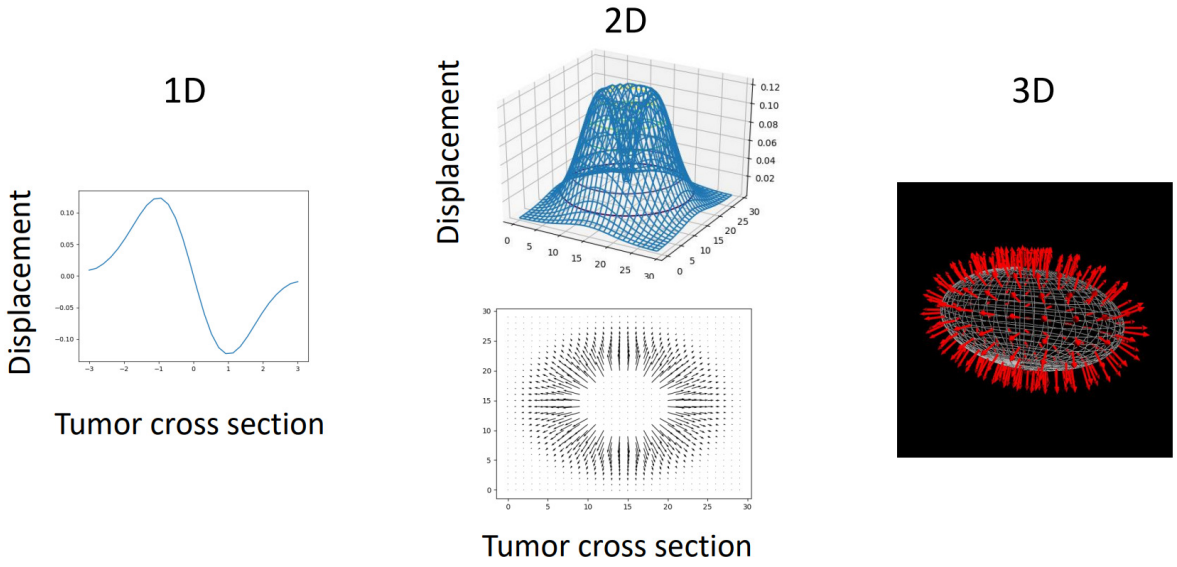

Figure 31: Illustration of computation of initial deformation model $\boldsymbol{d}$ based on 1D, 2D and 3D cross-section of the tumor mask M_l. $\boldsymbol{d}$ is the gradient of g.

Figure 32 C displays an ellipsoid and multiple directional cone shapes that are computed from $\boldsymbol{d}$. The purpose of the directional cones is guiding iterative deformation of $\boldsymbol{d}$ in terms of displacing the vector positions in $\boldsymbol{d}$ by $\boldsymbol{d}$ itself by an amount defined by the infiltration parameter β, and then linearly interpolating the displaced components of $\boldsymbol{d}$ to get a smooth displacement field.

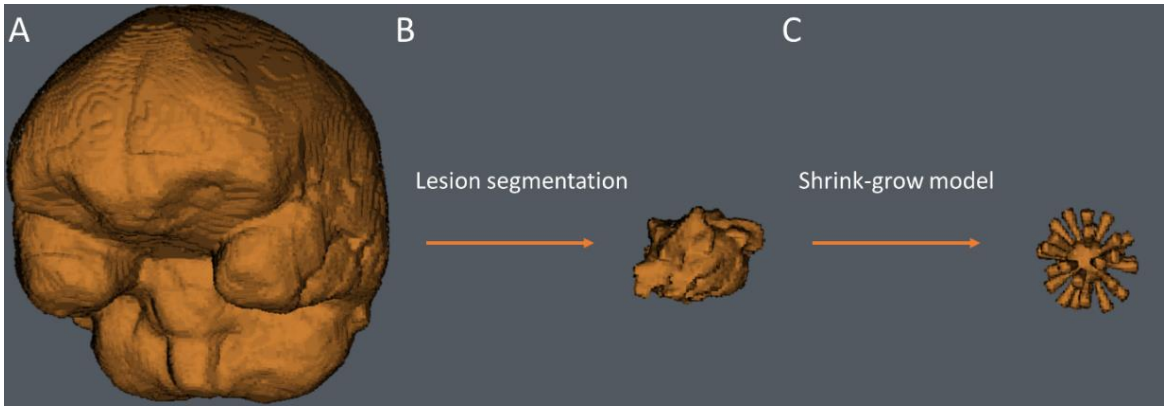

Figure 32: The initial deformation model $\boldsymbol{d}$ is computed from the tissue mask (B). At later steps, the brain mask (A) acts as a boundary for restricting physical displacement when deforming $\boldsymbol{d}$ by extending the "cones" computed from the initial $\boldsymbol{d}$ model (C).

The inner ellipsoid mask M_e presenting as the center of the initial deformation model in Figure 32 C is defined as

$$M_e := g < -e^{\frac{1}{2}}$$

(5.20)

The surface of M_e defines the locations with highest spatial intensity change in g, and resultingly the starting positions of the largest gradient magnitudes in $\boldsymbol{d}$. This is the inflection surface of G defined by $\nabla^2 g = 0$. The algorithm then scales $\boldsymbol{d}$ to have a maximum gradient magnitude of 1 by $\boldsymbol{d} = \frac{\boldsymbol{d}}{|\boldsymbol{d}|}$ and finds the approximate unit normal vectors V for the surface of M_e in MNI voxel isotropic resolution, by extracting vectors $V \in \mathbb{R}^{N\times 3}$ from $\boldsymbol{d}$ that have starting positions in the center of the voxels in a convex ellipsoid mask M according to equations (5.21) and (5.22)

$$V = \boldsymbol{d}[M]$$

(5.21)

$$M := M_e \; where \;\; \| \; V \; \|_F > 0.99$$

(5.22)

where [] describes tree-dimensional binary mask matrix indexing and $\| \; V \; \|_F \in \mathbb{R}^{N\times 1}$ is the Frobenius norm of V along its second axis dimension, which computes gradient magnitudes. To speed up the algorithm, a fixed subset of N_s maximum spread normal vectors $V_s \in \mathbb{R}^{N_s\times 3}$ is selected from V according to Pseudocode 1. A default $N_s = 32$ is selected empirically as a good trade-off between directional accuracy and computational efficiency for $1 \; [mm^3]$ isotropic voxel resolution and observed growth cases in the longitudinal MRI data.

A gradient magnitude threshold of 0.99 is suitable for realistic glioblastoma bounding box dimensions in $1 \; mm^3$ voxel isotropic space but may possibly need to be lowered with lower isotropic resolutions to ensure extraction of $\geq N_s$ normal vectors. A cone is then computed for each vector in V_s based on a fixed deviation θ in angles between each vector in V_s and $\boldsymbol{d}$

according to Pseudocode 2. 2θ is the resulting top angle in the generated cones as illustrated in Figure 32. A default of $\theta = 7°$ is selected empirically to result in a smooth deformation model.

The final mask M displayed in Figure 32 C is the conjunction of the ellipsoid mask M_c and all s computed cone masks M_c from Pseudocode 2 according to equation (5.23)

$$M = M_e \wedge \bigwedge_{i}^{s} M_{c,i} \tag{5.23}$$

Pseudocode 3 describes the next and main part of the algorithm. Here, $\boldsymbol{d}$ is iteratively deformed by an amount β that is proportional to the maximum distance to the end of the brain (Figure 33). This creates the infiltrative displacement field $\boldsymbol{d}_\beta$. An infiltrative gaussian g_β is created similarly.

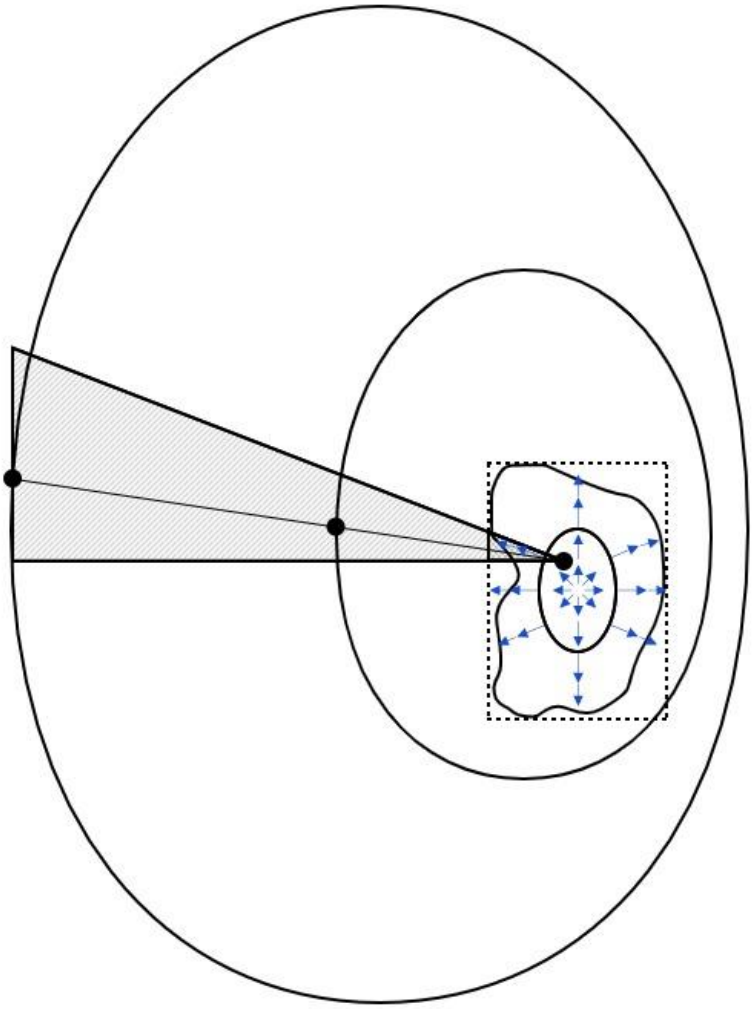

Figure 33: Simplified two-dimensional axial illustration of the infiltration algorithm described in Pseudocode 3. The components of the initial displacement field $\boldsymbol{d}$ (blue arrows) computed from the lesion tissue bounding box is displaced by itself by a fraction $1-\beta$ proportional to the maximum distance to the end of the brain. Here $\beta \sim 0.6$.

The final deformation model is then the displacement field computed according to equation (5.24)

$$\boldsymbol{d}(M_l, M_b, \alpha, \beta, \gamma) = \left|\alpha \cdot \boldsymbol{d}_\beta(M_l, M_b) + \boldsymbol{p}(\gamma)\right|_{M_b} \tag{5.24}$$

where $\boldsymbol{p}$ is a Perlin noise [182] vector field and $||_{M_b}$ restricts displacement to only occur inside the brain mask. For the latter task, displacements surpassing the brain mask are shortened to end at the brain mask barrier.

6. Summary of papers

The tree publications perform voxel tracking with the aims described previously. This involves, among others, EPI correction for obtaining more accurate estimates of blood volumes in the first paper, developing prognostic tissue deformation biomarkers from DIR in the second paper, and measuring DIR accuracy in tumoral regions in the last paper.

6.1. Paper 1

We performed geometric susceptibility distortion correction to improve the spatial alignment of perfusion MRI and structural MRI, as well as consistency of blood volume estimates from perfusion MRI. We investigated two methods for correcting EPIs for geometric susceptibility distortions, FSL TOPUP and EPIC, as described in previous sections. The impact of the correction methods on estimated CBV values in glioblastoma pre-treatment MRI from or first cohort ($N = 45$).

The raw EPIs in the DSC-MRI contained the stretching type of distortions described previously (Figure 16 C, D). Geometric distortion in the raw EPIs and the CBV map computed from raw DSC-MRI were various spatial misalignments particularly in frontal regions when compared to non-EPI structural MRI. This yielded for both investigated SE and GE DSC-MRI (Figure 25).

Our main result was that this type of EPI distortion resulted in underestimated CBV values. By performing either of the TOPUP or EPIC distortion correction methods on the GE and SE DSC EPIs and computing CBV from the distortion corrected EPIs, an increase in CBV values was observed when comparing to CBV values computed from distorted EPIs ($+\sim 0.06$ rCBV, $p < 0.0008$).

As described in previous sections, both TOPUP and EPIC modifies intensity values of voxels in the EPI in addition to displacing voxels when performing corrections. Correcting for the stretching type of distortion from a top-down phase encode k-space traversal will lead to an increase in EPI intensity values (related to the method of displacement correction) in the distortion corrected EPIs. Our work showed that this type of EPI distortion correction also leads to significant intensity increase in CBV as measured by paired Wilcoxon signed rank tests ($+\sim 0.05/\sim 0.05/\sim 0.04/\sim 0.08$ rCBV for TOPUP GE/EPIC GE/TOPUP SE/EPIC SE, respectively, all with $p < 0.0008$). This effect was most prominent in cortical regions close to air-tissue transitions, which experience high variations in local tissue magnetic susceptibility and subsequent ΔB (Figure 34). Of tumoral regions, only TOPUP correction of SE EPIs led to significant CBV change ($+\sim 0.03$ rCBV, $p = 0.0002$). This change was a CBV increase in contrast enhanced tumor regions. Second, we analyzed the volume change of multiple brain regions and tumor lesions associated with EPI correction. For this we used paired Wilcoxon signed rank tests on Dice similarity coefficients. Many regions experiencing significant CBV and Dice coefficient change were in cortical areas in the frontal, occipital and temporal lobes as illustrated in Figure 34.

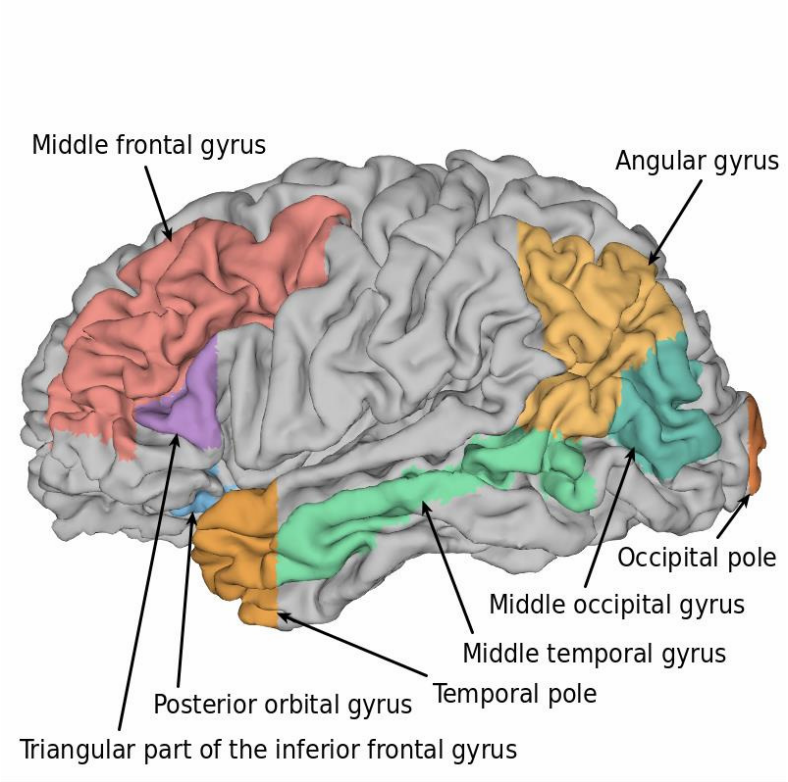

Figure 34: Cortical regions exhibiting change in CBV or Dice coefficient following EPI distortion correction. Temporal and occipital lobe are affected in terms of Dice improvement for GE images ($p < 0.0007$), while the remaining regions are affected in terms of rCBV increase for both GE and SE images ($p < 0.0008$). Distortion correction leads to rCBV increase in large cortical regions in mid frontal, occipital, and temporal lobe as well as in some subcortical regions as presented in the results section in our first paper. Only the left side hemisphere is shown. Surface rendering provided by Neuromorphometrics, Inc. (https://scalablebrainatlas.incf.org/human/NMM1103). Figure from our first paper.

In summary, this work highlighted the importance of performing EPI correction when assessing CBV values together with structural MRI in glioblastoma. An EPI that possesses lowered intensity values and stretched geometric distortions along the anteroposterior axis does not perfectly correspond to a high-resolution structural MRI. Since perfusion MRI utilizes EPIs, correction methods such as FSL TOPUP are warranted to ensure CBV values that correspond to tissue seen on structural MRI. Our results indicated that for this type of EPI distortion, CBV values from uncorrected EPIs tend to be underestimated and falsely displaced when compared to their true values and spatial locations in the cancerous brain.

6.2. Paper 2

Here we utilized DIR together with regions of interest, survival and RANO status, to derive and investigate DIR-based biomarkers. We analyzed their survival prediction capabilities, stratification capabilities into low and high survival subgroups, and association with RANO status.

We introduced four biomarkers based on magnitude and divergence maps of DIR displacement fields within peritumoral regions: two displacement biomarkers and two compression biomarkers (Figure 27). We defined subregions of peritumoral regions that had a negative divergence map as peritumoral tissue compression habitats. The displacement fields were computed from ANTs SyN CC DIR of consecutive intervals of longitudinal MRI pairs of post-operative glioblastoma. A total of 127 longitudinal studies from the 23 patients in our second cohort with glioblastoma, were incorporated into the study.

Most of these patients experienced significant tissue deformations at later stages of the standard treatment because of recurring cancer and tumor mass effect. We stratified patients into low and high survival subgroups according to an optimal threshold value for our biomarkers in terms of maximizing the $C - index$. In this way, we linked low and high survival subgroups with biomarker values describing high and low mass effect. Mean values of the biomarkers were extracted from peritumoral regions as well as peritumoral compression regions. The analysis was carried out as follows:

1. Analysis of intrapatient association of the median biomarkers with RANO progression status by pairwise Wilcoxon signed rank tests.

2. Analysis of the association of biomarkers with interpatient overall survival as well as with intrapatient time-to-exitus (defined as the time from each MRI study to death) for each interval image pair using Cox proportional hazards regression analyses.

3. Kaplan-Meier analysis and log-rank tests to investigate stratification capabilities of the biomarkers when divided into thresholds for low and high survival subgroups according to maximizing the $C - index$.

For 1. we found that all biomarkers had significant higher values for the paired exams labeled as progressing compared to the pairs that were labeled with non-progression RANO status ($p < 0.05$). This effect was most prominent for the compression biomarkers. The Cox analyses in 2. returned all biomarkers to be significantly associated with time-to-exitus. Only the compression biomarkers had a significant interpatient association with overall survival. Moreover, the highest hazard ratios were observed in the peritumoral compression habitats and were larger for compression biomarkers than for the displacement biomarkers. Last, 3. returned the compression biomarkers to have significant stratification capability for low and high survival subgroups. The stratification thresholds that maximized the $C - index$ were $3.53/3.19\ mm$ and $0.09/0.1$ for the displacement magnitude and divergence biomarkers within perotumoral/peritumiral compression habitats, respectively. Moreover, the stratification capability increased when restricting measurements to within peritumoral compression habitats. Figure 35 displays the biomarkers for one of the patients.

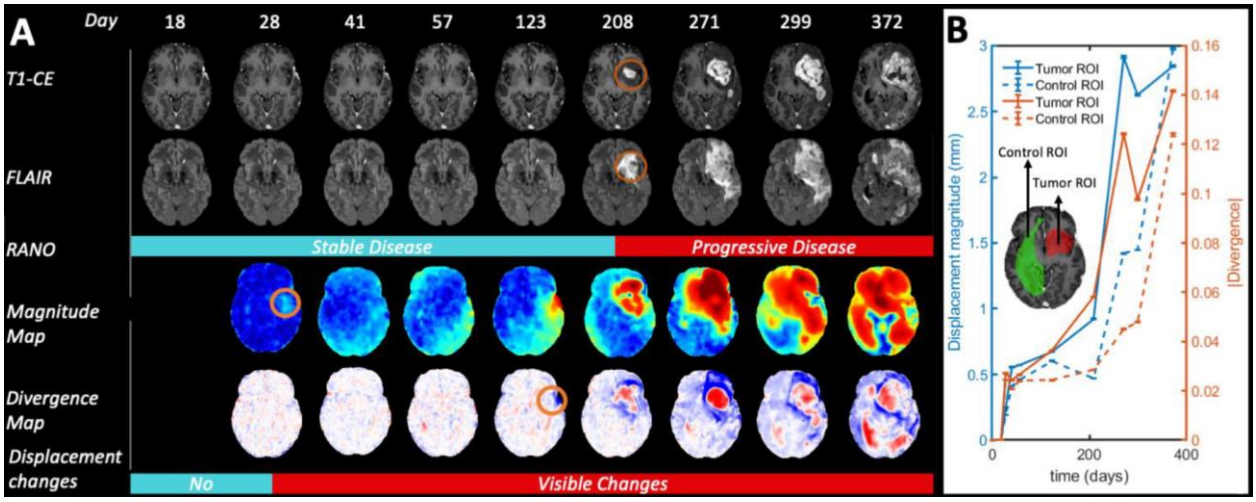

Figure 35: Deformation biomarkers and longitudinal evolution of a patient after start of CRT. A: According to RANO criteria, tumor progression started on day 208. However, the displacement maps show significant deformations already at day 28. Circles in orange highlight preliminary visual evidence of tumor growth. B: Quantification of the displacement magnitude and absolute divergence in control and tumor ROIs, respectively. This is subject four from our second patient cohort. Figure from our second paper.

In summary, this work indicated that deformation biomarkers computed from longitudinal DIR in glioblastoma, and particularly peritumoral compression biomarkers, may have prognostic significance in predicting survival outcomes in patients with glioblastoma receiving standard treatment. High peritumoral compression as measured by our divergence-based biomarker may indicate reduced survival prognosis. In general, clinically relevant effects of tumor growth on tissue may be predicted by these deformation biomarkers, such as early detection of recurrence. Moreover, peritumoral regions with tissue compression as measured by negative divergence may be particularly relevant regions to examine during patient follow-up, as they may provide a causal link between solid stress and neurological dysfunction [183].

6.3. Paper 3

In this work we investigated the geometric accuracy of DIR-based tissue displacement estimates in tumoral regions. We created a framework for measuring DIR performance in

glioblastoma by generating realistic synthetic ground truth tissue deformations as possible projections of cancer progression and recurrence on structural MRIs (Figure 29).

This involved developing a tissue deformation model of cancer growth with a controlled set of clinically meaningful simulation parameters: 1. maximum radial tissue displacement α, 2. infiltration β and 3. growth irregularity γ as described previously. The deformation model thus allowed us to perform a parametric evaluation of DIR methods for use in tumor growth assessment.

We generated 12 synthetic deformations of early post-operative baseline T1wc MRI from the 27 patients with HGG in our second cohort by varying our simulation parameters. We selected simulation parameters to describe low and high tumor mass effect, low and high infiltration and no, intermediate, and high irregularity. Figure 29 presents 12 displacement fields $\boldsymbol{d}(M_l, M_b, \alpha, \beta, \gamma)$ and resulting deformed T1wc images for a given patient lesion M_l and brain M_b mask. These synthetically deformed T1wc MRIs were then regarded as possible projections of growth as may be seen on future follow-up scans.

Five well-known DIR methods (ANTs SyN with CC and MI loss metrics, and the Farnebäck [175], iterative Lucas-Kanade [176] and TV-L1 [177, p.] OF methods) were then set to estimate the voxel-vise displacement between each pair of baseline and synthetic follow-up scan. We analyzed the voxel-vise displacement estimation error from comparing our synthetic ground truth displacements with the estimated displacements from the DIR methods within edematous, contrast-enhanced, and necrotic lesion regions. Pairwise Wilcoxon signed rank tests, Kruskal-Wallis tests and ANOVA with Tukey pair comparisons were conducted to investigate the significance in estimation errors when varying the simulation parameters, as well as performance differences between the registration

methods, within the lesion tissue classes. We also performed a grid search [184] (of α and β) to investigate how well our model could fit to describe real follow-up scans at two weeks. The evaluation function in the grid search was spatial CC [138] between model deformed and true second exam T1c MRI within outer ellipsoid masks defined by $g_\beta > 0.05$.

Our study returned highest performance of the DIR methods for tumor growth projections containing low maximum radial tissue displacement (low mass effect) combined with high infiltration phenotypes. Moreover, displacements were most accurate in contrast-enhanced and edematous lesions when compared to necrotic lesions. Of the investigated DIR methods, ANTs SyN with CC loss metric and Gunnar-Farneback OF performed with lowest displacement estimation errors.

The grid search for the optimal simulation parameters on baseline and real second scans pairs from all 27 second cohort patients, revealed some interesting aspects of the early treatment regimen. Our deformation model was best fit to describe two-week later scans when exhibiting a high infiltration parameter combined with a low maximum radial tissue displacement (low mass effect). An example of optimal parameters illustrating simulated low mass effect and high infiltration ($\hat{\alpha} = 3.4\ [mm]$ and $\hat{\beta} = 0.14$) is seen for a single patient in Figure 36 along with the corresponding estimated displacement field from ANTs SyN. Low infiltration was also associated with larger total tumor volume, as described in the paper.

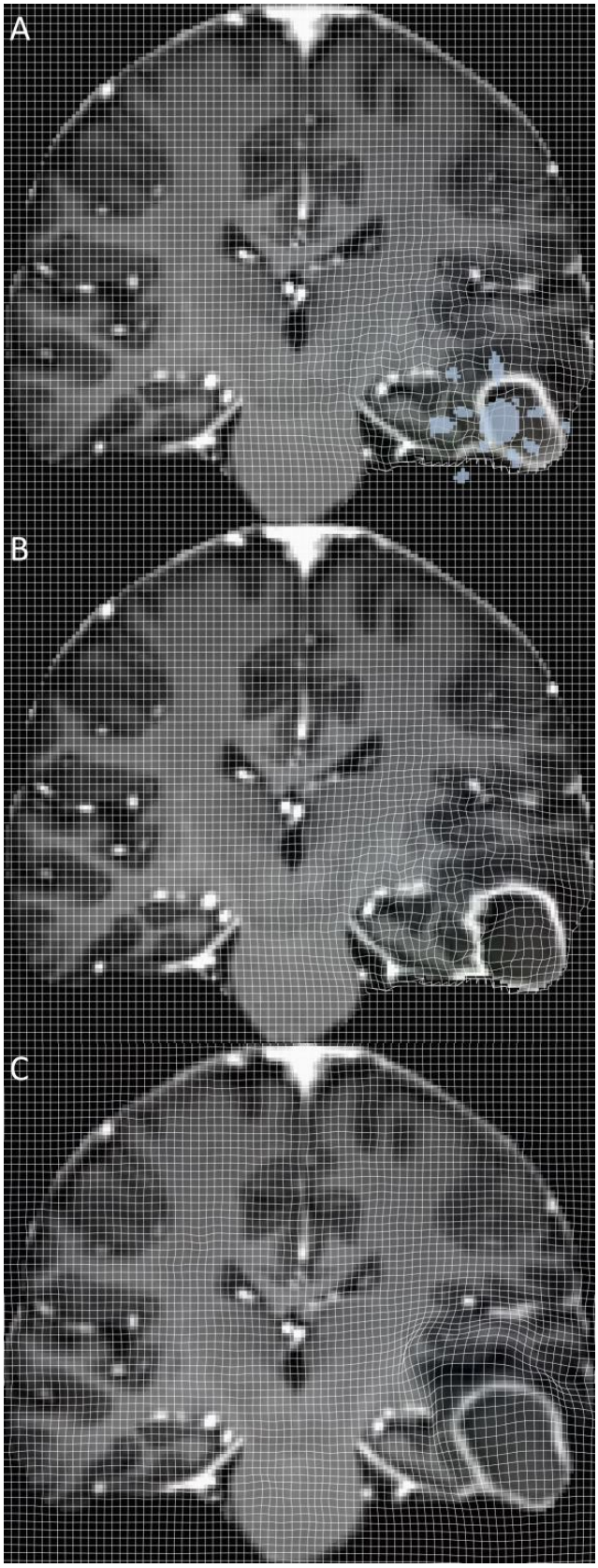

Figure 36: Example of synthetic and real deformation for a patient. A: First scan with the deformation prediction model overlaid as a deformation grid, ellipsoid, and cone masks. B: First scan deformed by our deformation model. The deformation grid is the same as in A. C: Real second scan

with SyN overlaid as a deformation grid. The main objective of the third paper was the following: We tested how well the deformable image registration methods could estimate the synthetic deformation grid in B, based on the images in A and B. For assessing how well the deformation model conformed to real data, we performed a grid search for optimal model parameters based on A and C scans. For comparison, the estimated displacement field from the SyN algorithm between A and C is illustrated as a deformation grid in C.

In summary, this work highlighted the favorable clinical conditions when using DIR to develop prognostic displacement-based analyses to patients with glioblastoma. Our results indicated that high infiltration and low mass effect phenotypes may lead to the highest accuracy of displacement estimates from DIR within tumoral regions. Moreover, early and short-interval post-operative longitudinal MRI of glioblastoma is warranted to achieve accurate DIR results. DIR methods may accurately quantify small tumoral and peritumoral tissue displacements for use in early treatment response assessment. This work provided empirical evidence for the well-suitedness of using the prognostic deformation biomarkers from DIR in the second paper. Furthermore, our deformation model provided robust predictions of near-future tissue displacements based on few simulation parameters. This led to insights about the typical low mass effect and high infiltration conditions seen on early post-operative longitudinal MRI of glioblastoma.

Although we did not include more than baseline and single follow-up scans in the paper, we performed a complementary grid search on all longitudinal scan interval pairs to check how well our model could fit to all examination intervals. This resulted in many best fit projections also describing macroscopic shrinkage of regions (accomplished with a negative α) early in the treatment regimen (Figure 37). Interpreting these results remains as a future study. However, an immediate result is that the patients tend to have a general macroscopic shrinkage of tumoral and peritumoral regions early in the treatment (possibly as a result if CRT), followed by macroscopic expansion upon completion of CRT and onset of TMZ.

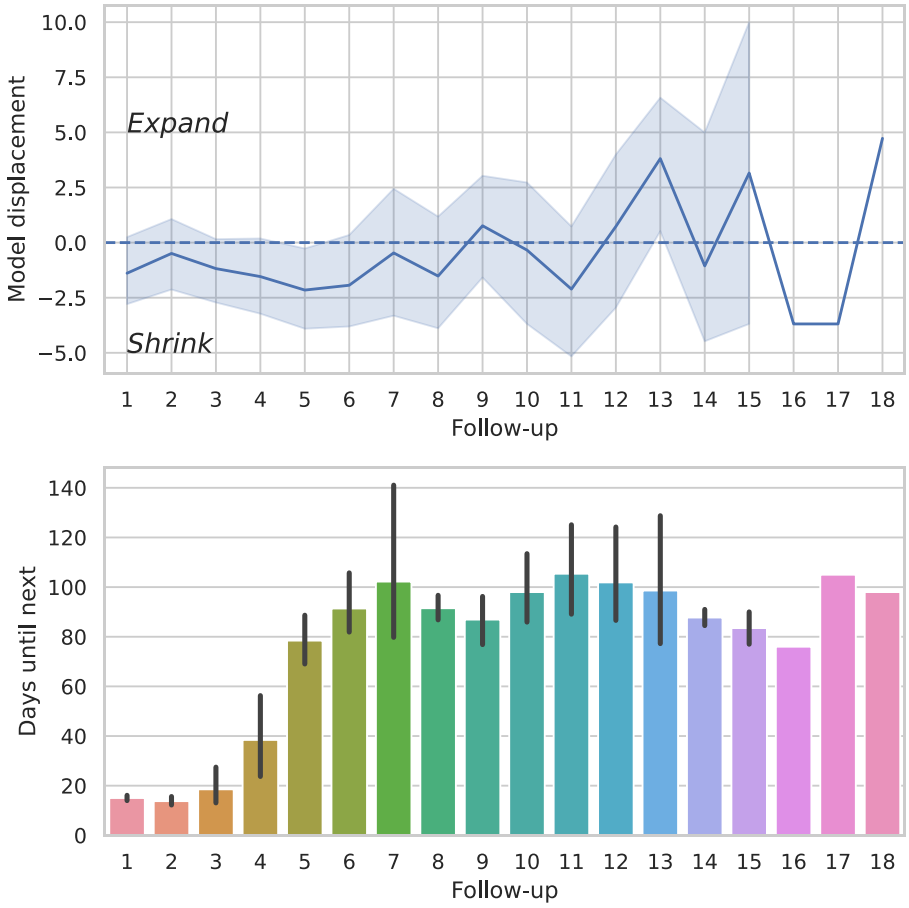

Figure 37: Additional unpublished results from grid search on all scan interval pairs for all 27 patients. Top row: Optimal maximum radial displacement simulation parameters revealed both an overall shrinkage early in the treatment, followed by expansion of regions as described by the deformation model. Bottom row: The days between the scan pairs were about two weeks in the early treatment follow-up, followed by about three-month intervals.

7. Discussion

7.1. Paper 1

EPI correction was performed by specialized spatial and intensity tracking methods which led to more accurate CBV maps. CBV maps captured from DSC-MRI are imaging features with clinical relevance and it is important that CBV is accurately matched with structural MRI for optimal treatment assessment. We investigated how spatial and intensity distortions caused by varying tissue susceptibility in DSC-MRI with stretching EPI distortions

affected CBV in multiple cortical and subcortical brain regions. This led to a recommendation for distortion correction to ensure improved spatial and intensity consistency of CBV compared with structural MRI in cancer.

Our main findings were that CBV estimated from the DSC-MRI have the risk of being underestimated when not performing EPI correction, and that this effect was most prominent in cortical areas in the frontal, occipital, and temporal lobes (Figure 34). As is discussed in the paper, the location of a tumor affects the survival prognosis. Moreover, several studies have associated the survival prediction capabilities of CBV in brain cancer [50], [185]–[187]. In our paper we presented evidence that CBV values of a tumor involving multiple brain regions with varying degree of EPI distortion may be underestimated, if not corrected for. This can impact the clinical accuracy of CBV. One such example is a recent study that associated patients with IDH wild-type glioblastoma with less than $10\ \%$ rCBV decrease between scans, to have longer PFS [188]. Moreover, this association was most prominent for those with MGMT methylation [188]. As mentioned previously, MGMT promoter methylation status has shown to be valuable in distinguishing pseudoprogression from progression in glioblastoma [63], [64].

There are some differences between the correction methods investigated, and in CBV values from SE and GE DSC-MRI. In general, TOPUP correction of SE EPIs led to the most precise correction and subsequent CBV estimation. A previous study using a $7\ Tesla$ scanner found that when compared to using GE EPIs, TOPUP with SE EPIs led to better correction only in the ventromedial prefrontal cortex [189]. This is a region consisting of medial orbitofrontal cortex, of medial orbital gyri in Figure 3. It is a region with large signal drop-out on GE EPIs. It is widely known that magnetic susceptibility distortions and drop-out

increase with magnetic field strength. Owing to the FID signal in GE EPIs being stronger than the pure T2w signal in SE EPIs, GE DSC-MRI also led to generally higher CBV values compared to those of SE DSC-MRI in our study, and independent of correction method.

Another important discussion that affects the impact of correction on CBV is the phase-encode direction in the EPI sequence. Note that in our paper the words “positive” and “negative” for describing phase-encode direction were swapped when compared to the images in the thesis. The reason for this was to keep terminology in the thesis more consistent with existing literature [111]. Specifically, bottom-up (=positive) and top-down (=negative) phase-encode direction results in compression and stretching distortions, respectively. To avoid confusion, it is suggested to use only the compression and stretching distortion terminology when referring to the two main types of EPI distortion that can occur and which depend only on the phase-encode direction in the EPI sequence. We hypothesize that the results in the first paper could be different if the EPIs in the DSC-MRI had the opposite phase-encode direction (leading to compression distortions). Intuitively, not correcting for these compression distortions, may result in overestimated CBV values and perhaps an inconsistency in Dice values for another set of brain regions. To investigate this, a separate study with EPIs containing the opposite phase-encode direction in the DSC-MRI sequence would be needed.

The impact of other EPI correction methods on CBV estimates could further identify potential shortcomings of FSL TOPUP and EPIC. Some relevant methods could the SPM ACID HySCO [190] and DR-BUDDI [191] reverse gradient methods, reverse gradient methods for specific locations in the brain such as the temporal lobe [192], or DL-based [193]–[195] methods. Geometric distortions may also be present on structural MRI [196], challenging

correct anatomical alignment of EPI and structural MRI. However, these distortions are mostly caused by external factors and corrected for as discussed previously.

7.2. Paper 2

DIR of longitudinal MRI of cancer provided robust spatiotemporal tracking. We developed four biomarkers based on estimated displacement from longitudinal DIR. The association of these deformation-based biomarkers with RANO tumor status, and survival prediction and low and high survival stratification capability was investigated. We showed that the biomarkers may have prognostic ability in predicting survival as well as being early markers for assessing cancer recurrence.

Compression of peritumoral healthy tissue is known to cause life-threatening neurologic symptoms [183]. Our deformation biomarkers may be especially useful for eloquent areas because compression in these areas may affect important cognitive functions. The stratification thresholds indicate that using our biomarkers within peritumoral regions, a displacement and divergence magnitude larger than $3.54\ mm$ and 0.09, respectively, are associated with worse survival prognosis. This association is also stronger when restricting the analysis to biomarkers within peritumoral compression regions (i.e., $\nabla \cdot \boldsymbol{d} < 0$), although with slightly different stratification thresholds. These results are consistent with literature suggesting that a higher mass effect (and subsequent larger peritumoral displacement magnitude and midline shift), is generally associated with worse survival outcome in glioblastoma [179], [197]. In current practice, a midline shift above $5\ mm$ usually requires immediate surgical intervention [197], [198]. However, the accuracy of these biomarkers highly depends on the accuracy of the DIR method. A discussion of DIR

accuracy is thus warranted. Investigating DIR accuracy is our main application of the deformation model in our third paper.

No voxel intensity changes and only spatial deformation between longitudinal MRIs (i.e., $\Delta I = 0$) may be a favorable scenario for using DIR for voxel displacement tracking of cancers with a strictly pushing phenotype or similar types with little voxel intensity changes. For this case, tracking peritumoral and non-cancerous regions would closer resemble homeomorphic (one-to-one) mapping if no appearance or disappearance of mass (resulting in intensity changes) occurs during the tracking. Since diffeomorphic DIR does not shift intensity values, only spatial deformation between MRIs may result in the highest possible registration accuracy.

An example of erroneous use of DIR for displacement tracking is when an intensity change ($\Delta I \neq 0$) leads to a false displacement estimate $\boldsymbol{d}$ when no displacement occurred. Selection of suited loss metric is an important aspect to achieve accurate DIR. As discussed previously, it is well known that CC is best suited for same modality (i.e., monomodal) registration (e.g., T1w to T1w), while MI can be used for multimodal registration. Various cases for intensity change of a voxel for monomodal longitudinal registration are discussed. First, MRI sequence parameters (such as TR and TE) may have been changed by the radiographer although the image is of the same weighting type (e.g., T1w), which could alter the intensity value for the same type of tissue. Therefore, longitudinal intensity standardization may be an important preprocessing step. Second, image intensity depends on water (~proton) density. An increase in water density would result in a (lower) darker or brighter (higher) intensity value on a T1w or T2w MRI, respectively. Third is the use of CA, which in the context of T1w structural imaging selectively increases the voxel intensity value in regions

where it is accumulated. Fourth, water density and CA accumulation may depend on cancer phenotype. As examples, the T1wc MRIs in Figure 9 clearly shows intensity increase in contrast accumulated tumor regions, while Figure 8 and Figure 9 show intensity decrease in peritumoral regions as a potential result of tissue inflammation at exams late in the treatment. These aspects may impact DIR accuracy and subsequent impact our deformation-based biomarkers.

Changes in tissue mass with cancer and treatment is another aspect that challenges DIR accuracy. We hypothesize that with aggressive tumor growth and subsequent intensity change from mass increase, DIR may provide the most accurate results if the moving image is registered backwards-in-time to a fixed first time-point image. The rationale is that a DIR algorithm may more likely track existing mass that disappears than track new mass that appears. Non-spatial transformation of tissue may thus be best described by an additive intensity term ΔI in the frame of the fixed image in a DIR problem (i.e., backwards-in-time registration). This, to exclude the intensity recording task from DIR.

Whether performing forward or backwards-in-time registration may however not be crucial for correct tracking of displacement, because tissue mass may both disappear and appear during brain tumor growth or as results of successful and unsuccessful treatment. New or restructured tissue mass resulting in image changes are expected in cancer, which challenges the physical accuracy of DIR for use in cancer diagnostics. In addition, how well a registration method describes the actual tissue displacement highly depends on the mathematical and physical guarantees of the registration method. Some other factors may be the selection of regularization method and alignment function for the optimization process of the registration algorithm. If the symmetric property of SyN is not required,

Greedy [199] may be a better option since it provides diffeomorphic registration at reduced computational cost. Farnebäck OF may be a second alternative, as discussed previously.

Previous studies have investigated the use of DIR for measuring mass effect in form of lateral ventricle displacement [179] and peritumoral tissue deformation heterogeneity [200], [201]. However, these studies measured mass effect induced deformations relative to an MNI brain template and did not incorporate longitudinal exams to perform voxel tracking.

Last, future work could involve developing a method for voxel tracking involving both displacement and intensity shift. Optimally, tracking both displacement and intensity change should be biologically possible, i.e., the same piece of brain tissue in a patient should be identifiable across same modality MRI scans even when exposed to biological transformation from treatment or cancer resulting in voxel intensity change on MRI. The voxel tracking problem may then be seen as a multimodal image matching problem [202]. Correctly quantifying voxel intensity change and displacement, would fully realize voxel tracking as it is defined in the thesis. This could lay the basis for developing more imaging biomarkers for use in early prediction of treatment response and recurrence.

7.3. Paper 3

The third paper investigated the geometric accuracy of DIR methods for MR images. To assess this, synthetic voxel displacements were produced by our deformation model. We drew inspiration from longitudinal MRI of GBM to model realistic tissue deformations from a growing tumor exerting a mass effect on its surrounding tissue. A radial voxel displacement field outward from brain and lesion tissue masks was simulated, with model parameters for maximum tissue displacement, tumor infiltration and growth irregularity.

We showed that all DIR methods returned the highest accuracy in estimating the displacement field when simulating low tissue displacement (low mass effect) and high infiltration. The most profound effects were observed within contrast-enhanced and edematous lesion tissue types. Moreover, we identified ANTs SyN with CC loss metric as the image registration method with overall highest registration accuracy. To this end, our findings suggest an increase in true tissue displacement may also lead to a subsequent increase in the error (in mm) of the DIR methods. Hence, we may conclude that DIR methods can accurately measure displacements in a scenario of HGG progression with small displacements (i.e., low mass effect as defined by a maximum radial tissue displacement around the selected $3\ mm$, opposed to the selected $8\ mm$ for high mass effect in our model). This may be accomplished by short longitudinal time intervals between the MRI exams which may be a challenge for routine examinations, but relevant for clinical trials. It is generally known that an increase in mass effect is associated with worse survival prognosis in glioblastoma [179], [203], [204]. Short longitudinal time intervals between MRI exams may thus be especially important for ensuring accurate DIR results, for patients with worse survival prognosis and with tumor expressing highly nodal ("pushing") phenotype. The optimal exam frequency of a patient could depend on tumor phenotype. This, to guarantee a stable performance of DIR across patients and time points. Otherwise, maintaining a fixed exam frequency for all types of cancers could result in unstable and inaccurate displacement estimates. This could lower the clinical utility of the deformation biomarkers in the second paper. Another important discussion of these results is how realistic the simulated ground truth displacement fields were when varying the parameter configurations for mass effect, infiltration, and irregularity. Thus, a general discussion about the anatomical correctness of the deformation model and its application in evaluating DIR methods follows.

The main strength of Paper 3 was, to introduce a robust and interpretable model with the ability to efficiently generate and control synthetic deformations from binary segmentation masks. Our goal was not to generate the most realistic or physically and biologically accurate model of brain cancer deformations. To do so, we modeled the most typical deformations as seen on MRI of patients with GBM MRI receiving standard treatment. This also included segmentation annotations from expert readers (neuroradiologists). Compared to reaction-diffusion [180], [205] and DL [206], [207] based models, our model was methodically simpler and computationally more efficient. The most typical deformations include structural compression of surrounding peritumoral tissue as a mass effect [179] from cancer growth, usually also associated with midline shift and shorter survival [204], or alternatively, shrinkage of the tumor bed from response to treatment.

To date, existing literature has been more focused on modeling cancer growth (with a resulting tissue expansion) compared to assessing shrinkage of tissue areas [180], [205]–[210]. Many of these tumor growth models do not incorporate treatment-related changes. Most of our patients experienced a radiographic shrinkage of lesion areas in the early stages of treatment (possibly by cell kill as a response to the radiation treatment), followed by aggressive expansion of existing and new lesions areas because of cancer recurrence. Our model fitting indicated that radiographic shrinkage may be just as common as expansion in the early treatment assessment (Figure 37). Thus, another perspective of modeling mass effect may be whether the patient's brain experienced a mass increase effect or a mass decrease. Glioblastoma is a highly complex cancer with large inter- and intra-tumor heterogeneity and analyzing images of patients undergoing treatment makes the data even more complex. A strength of our deformation model is that it can use few simulation

parameters and little input data to generate plausible tissue displacements for assessing the accuracy of DIR methods.

There are limitations in our deformation model. First, image intensity changes were not modeled. An investigation into registration accuracy under the influence of synthetic intensity shifts remains as further work and possible extension of our model. In true infiltrative tumor growth, intensity shift of voxels caused by transforming tissue, may be just as apparent as displacement of voxels. It is possible that advanced MRI techniques could provide information to model such intensity changes. Some of them may be the strength and spatial distribution of the radiation field from radiation therapy, apparent diffusion coefficient (ADC) from diffusion MRI [211], K^{trans} CA volume transfer constant from dynamic contrast-enhanced (DCE) MRI [212], and the K_2 and K_a parameters from Boxerman et al. [90] and Bjørnerud et al. [93] CA leakage correction of DSC-MRI, respectively.

Incorporating intensity shift would however not result in a model of tissue deformation, but in a model of the spatiotemporal transformation of tissue from tumor growth. DIR is only aimed at estimating displacement. A model of spatiotemporal transformation would thus not be suited to assess the accuracy of DIR methods (the objective in the third paper). Our infiltration parameter thus controlled only the displacement aspect of infiltrative growth. It was built on the assumption that high infiltration results in cancer spread to larger regions of the brain compared to those with low infiltration. A more correct infiltration model could incorporate intensity changes as well.

Another extension of the model may be to allow for more specialized directions of the cone masks either by random deviations in the directions or possibly by aligning the cone directions with principal diffusion directions from DTI. Or, incorporating perfusion maps

such as CBV to guide model parameters such as infiltration β and irregularity γ. With increased complexity of input data, the need for more parameters and model assumptions may however outweigh the possible benefit of using a more realistic model. Also, including additional preprocessed data would make the model less robust against preprocessing errors and noise.

7.4. General discussion

The general objective of most of the work in this thesis was improving computer aided description of clinically relevant MR imaging regions and features and thereby accurately describing and improving patient prognosis in brain cancer. In addition to maintaining good practices in file organization and QC, this involved accurate characterization of brain and cancer regions through manual and automatic segmentation, preprocessing such as LIR and longitudinal intensity standardization, followed by monitoring of the spatial and intensity transformations in and around regions of interest during cancer treatment. The main scientific contribution of the thesis was thus an investigation into various methods for obtaining spatiotemporal tracking of clinical image features.

Better standards for dealing with data (e.g., file types and data structures) could improve reproducibility and cross-collaboration among research groups and significantly alleviate technical dept for research containing heavy processing and preprocessing tasks. Most of the work in the thesis drifted towards complying to the brain imaging data structure (BIDS) consensus among researchers. Since working with research data often means continuously discovering and solving processing errors, while simultaneously consenting to share data that was used in previous publications, updates to a data set should optimally be tracked

like code in a software project. For this task, the data version control (DVC) software was used on the BIDS datasets.

Having standards simplifies visualization and QC, since necessary assumptions about file types, locations and file organization structure can be made in software and scripts. Aliza, ITK-SNAP and FSLeyes supports being started from the CLI. By utilizing BIDS, CLI visualization tools and conventional Unix shell scripting and tools, it is possible to automate the process of visualizing longitudinal data. A Unix shell is a scripting language for natively running commands in CLIs. Bash is among the most common shells and proved as a useful tool throughout the thesis.

For instance, the following commands will open all T1wc images into the same visualizing window of Aliza, for a first patient organized into the BIDS derivatives structure (Figure 38):

aliza $(find sub-01 -type f -name T1c-icor.nii.gz | sort -V)

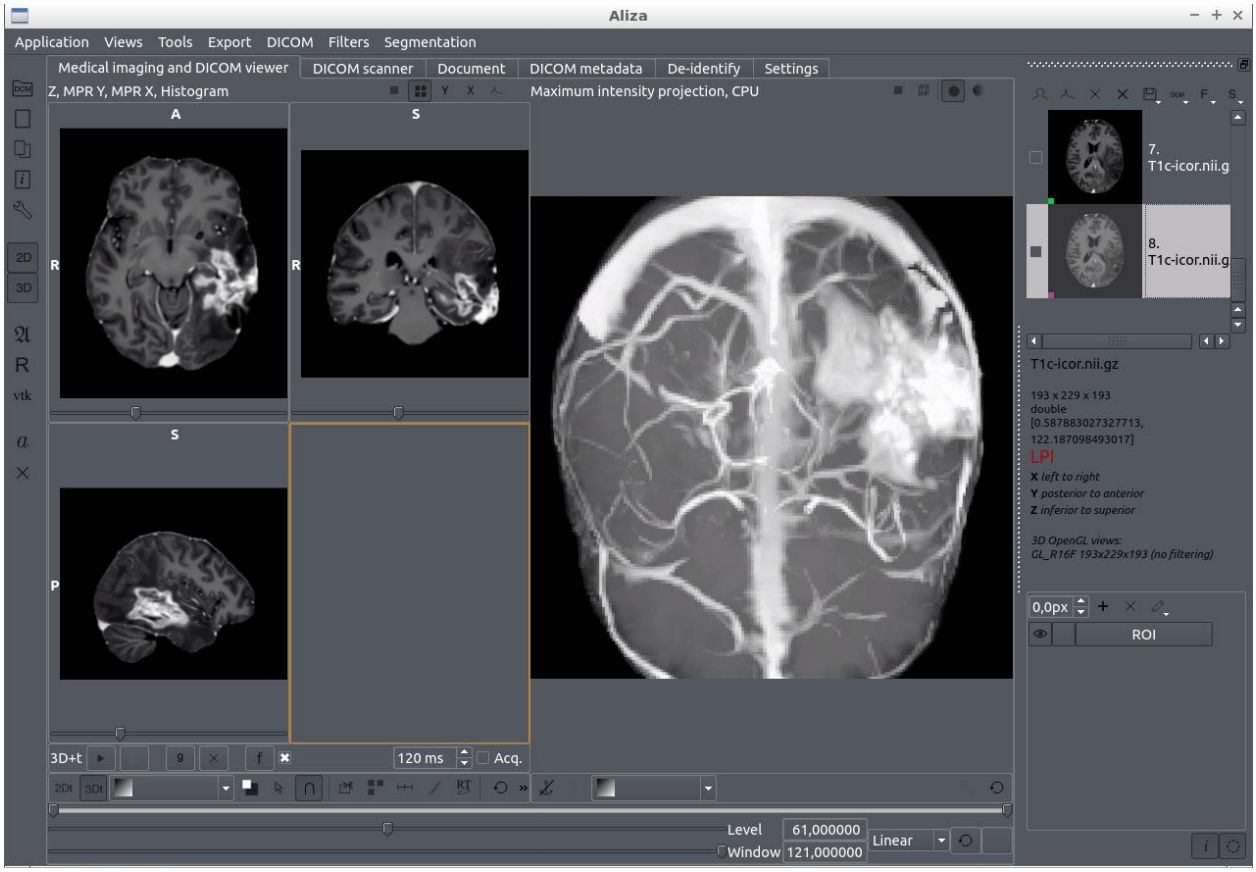

Figure 38: Scriptable visualization of preprocessed T1wc MRI in Aliza. This is subject nine from our second cohort.

The corresponding commands for ITK-SNAP could be (Figure 39):

readarray -t files < <(find sub-01 -type f -name T1c-icor.nii.gz | sort -V)

itksnap -g ${files[0]} -o ${files[*]:1:${#files[*]}}

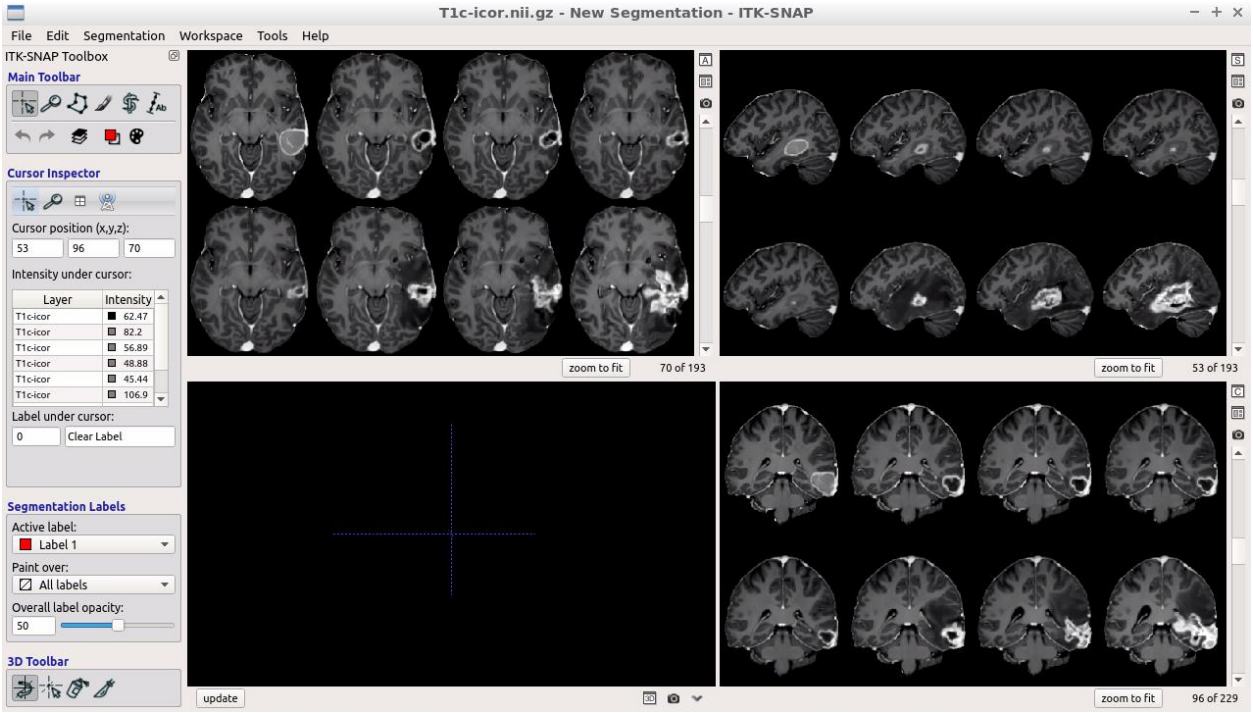

Figure 39: Scriptable visualization of preprocessed T1wc MRI in ITK-SNAP. This is subject nine from our second cohort.

FSLeyes can be utilized similarly from the command line with multiple MRIs to create .png snapshots with desired viewing settings. It supports CLI-based off-screen rendering. This means that an exact visualization can be re-produced and automated for multiple images and saved to .png files. PowerPoint friendly .mp4 and .gif animations of the time evolution of treatment images can be made from the .png files using the ImageMagick CLI tool to draw text and a progress bar line on each .png file, before inputting to the ffmpeg processing tool.

The orthographic and lightbox views of FSLeyes give quick overviews of volumes with minimal configurations. If the longitudinal data is linearly registered to approximate MNI space, assumptions on image orientation and voxel size can enable automatic longitudinal visualization with minimal intervention. The whole process may be automated in bash scripts resulting in the animation videos presented previously in the thesis.

An example of easy QC was that the automatic longitudinal visualization quickly uncovered preprocessing (e.g., LIR) errors. This is seen for many of the T2w images in the visualization animation of the multiparametric MRI presented in section 3.2.4. Incorrect spatial alignment is a real-world example of a consequence of having erroneous data and should be uncovered early in the analysis from QC tools. If not, inclusion of these images in processing could possibly result in erroneous results.

Segmentation of various structures such as tumor tissue constitutes an important subfield in medical image analysis. The segmentation of brain structures in the first paper was performed using SPM normalization to a MNI brain atlas (OASIS, Neuromorphometrics, Inc.) [124], [125], while the tumor segmentations were either performed manually (by a neuroradiologist) (paper 2) or based on a deep learning (DL) method (paper 1 and 3) [120]. A reason for not using a more recent or more accurate brain segmentation method, such as FastSurfer [119], was the presence of tumor and pathology. The underlaying unified segmentation method [213] for MNI normalization in SPM 12 using tissue probability maps, proved robust to tumor pathology in our first paper. This method has been previously recommended as a robust MNI normalization technique for lesioned brains [214], and resulting in segmentation of brain structures based on a template. For automatic tumor segmentation pipelines, DL-based methods are currently considered the state-of-the art [215], [216] and have been outcompeting methods based on region growing and shallow machine learning [216]. The possibility for combining multiple modalities as input (for instance by having multiple input channels as with RGB-images) is an advantage of DL based tumor segmentation algorithms, which is likely a reason for its success.

An important aspect of our results is interpolation, as many of the pre-processing steps involved interpolating data. This is common when working with multi-resolution data (like combined analysis of functional and structural MRI). For instance, when re-slicing an image after registration it is important to decide whether to downscale or upscale the image resolution as well as decide which interpolation method to use for this task. Downscaling may lead to loosing important data, while on the other hand, upscaling may create false data. Interpolation method (such as NN, trilinear, polynomial/spline etc.) may also affect the severity of data loss or creation of false data points. For segmentation masks, it is suggested that NN interpolation is the method that provides the least amount of data modification, since it does not modify original intensity values. When downscaling resolutions, it NN interpolation (also called point sampling) selects the original intensity values that are closest each point in a resampling grid and simply discards the rest. The main advantage of NN interpolation is that it preserves discrete values which is important for segmentation masks. On the other hand, NN interpolation can lead to a common aliasing artifact when performed after LIR and re-slicing seen as diagonal line artifacts in axial images. This comes as a result of the combination of having a non-smooth interpolation method and rotating a volume [114]. Trilinear interpolation was thus preferred when registering structural images, since it is better to handles this rotation artifact. Since CBV from functional MRI is created natively in a low resolution, it was natural to perform the analysis in the first paper in this low-resolution space (since it was deemed important to preserve the integrity and original values of CBV). Thus, we used NN interpolation to downscale corresponding structural images to native CBV resolution.

In the second and third paper, we used trilinear interpolation to re-slice images to a common isotropic high resolution. Trilinear interpolation was preferred over polynomial

interpolation of higher degree for simplicity and interpretability. Trilinear interpolation is simply making straight lines between points, and possible data loss and false data from re-slicing are likely minimized when compared to methods of higher degrees. Although trilinear interpolation (like bilinear interpolation) is known to produce both blurring and aliasing artifacts from resampling [115], it was still preferred to avoid additional interpolation artifacts associated with higher degree methods. Moreover, these artifacts may be most pronounced when significantly changing voxel resolutions, which was not the case when performing registration and re-slicing. High degree polynomial interpolation may possess intensity oscillations towards the edges of the interpolation grid (Runge's phenomenon [217]), unlike cubic spline interpolation. Cubic spline interpolation methods may under- or overshoot in sharp transitions of intensity value or in boundary points in the interpolation grid leading to decreased or increased intensity values, an artifact which is known as haloing [218], [219]. This is closely related to ringing, which may be described as an oscillation of successive over- and undershooting of intensity values, with decreasing amplitude, near sharp intensity transitions. Moreover, oscillation artifacts from interpolation may occur in the objective function of a registration problem, leading to local optima in the objective function and subsequent worse spatial alignment from registration [114], [220]. This is an artifact associated with high degree basis splines [220], [221], which is the default interpolation method for registration in SPM [124]. This emphasizes the importance of selecting a proper objective function for DIR. Four-dimensional RBF interpolation was investigated as a method to create artificial MR images for each day during treatment. Although this was a minor method in the thesis, it provided a way of visualizing and understanding the most general image patterns in high-resolution longitudinal MRI of glioblastoma. Neither of the software for the other interpolation methods were

implemented for more than three dimensions, and thus this method was investigated. However, this method is also affected by Runge's phenomenon [217].

8. Conclusion and future aspects

8.1. Conclusion

The general objective of the research in this thesis was to improve the accuracy of patient prognosis in glioblastoma using magnetic resonance imaging postprocessing techniques. Various methods for obtaining spatiotemporal tracking of clinical image features were investigated. In the first paper, the effects of spatial and intensity distortions on cerebral blood volume maps derived from dynamic susceptibility contrast magnetic resonance imaging were investigated. These distortions are caused by variations in tissue susceptibility, and can lead to cerebral blood volume being underestimated, particularly in the frontal, occipital, and temporal lobes. We recommend correcting for these distortions to improve the accuracy of cerebral blood volume estimates and enhance their clinical usefulness. In the second paper, four deformation-based biomarkers based on displacement estimates derived from deformable image registration of longitudinal magnetic resonance imaging of brain cancer were developed. These biomarkers were found to have the potential to predict survival and assess cancer recurrence, which is particularly useful in eloquent areas where compression can cause significant neurologic symptoms. The accuracy of these biomarkers depends on the accuracy of the deformable image registration method, which can be affected by factors such as extent of voxel displacement and changes in voxel intensity and tissue mass. In the third paper, the geometric accuracy of deformable image registration methods for magnetic resonance imaging were investigated, by simulating synthetic voxel

displacements with a deformation model based on brain cancer growth. It was found that deformable image registration methods had the highest accuracy for low tissue displacement (loss mass effect) and high tumor infiltration, and that ANTs SyN with CC loss metric had the overall highest accuracy. We suggest that short longitudinal time intervals between MRI scans may be important for ensuring accurate deformable image registration results, particularly for patients with worse survival prognosis and highly nodal tumors. Last, several contributions were made to improve the reproducibility and collaboration of research involving heavy processing and preprocessing of magnetic resonance imaging data. This involved developing and validating methods for segmentation, preprocessing, and monitoring of spatial and intensity transformations in brain cancer. In summary, the methods investigated in the thesis were shown to have clinical relevance and lead to improved diagnostic accuracy compared to existing methods in the clinical routine of brain cancer imaging.

8.2. Future aspects

8.2.1. EPI correction software

A natural outcome of the first paper can be enabling researchers and clinicians to easily perform EPI correction and optimally having it as a part of the clinical workflow. Incorporating EPIC into such a workflow was the main objective in a previous Master's thesis [106]. In our work, FSL TOPUP was packaged into bash scripts for easier use and shared with other researchers at our hospital. These scripts can be run on Linux virtual machines (e.g. Docker, VirtualBox or VMware) with FSL installed. See the attached presentation **mri-processing.pdf** for TOPUP examples.

8.2.2. Interactive voxel displacement path visualization (cancer-sim.com)

Nervous system fiber tractography software can be utilized for visualizing pathlines. Both streamlines (in DTI) and pathlines can be stored identically and visualized with the same software. A web-based pathline viewer named cancer-sim.com was developed using the X toolkit [160]. A possible use case of cancer-sim.com is to present a brain cancer treatment tissue response atlas in approximate MNI space. If containing pathlines from many longitudinal patient cases, it can be an interesting way to present and the most typical tissue deformations. X toolkit may be regarded a lightweight version of VTK that is written in JavaScript. cancer-sim.com involves HTML, JavaScript and cascading style sheets (CSS). The visualizer can be hosted locally (intranet with Python's SimpleHTTPserver) for easy visualization of results from processing pipelines, or globally (cancer-sim.com with netlify) (Figure 40).

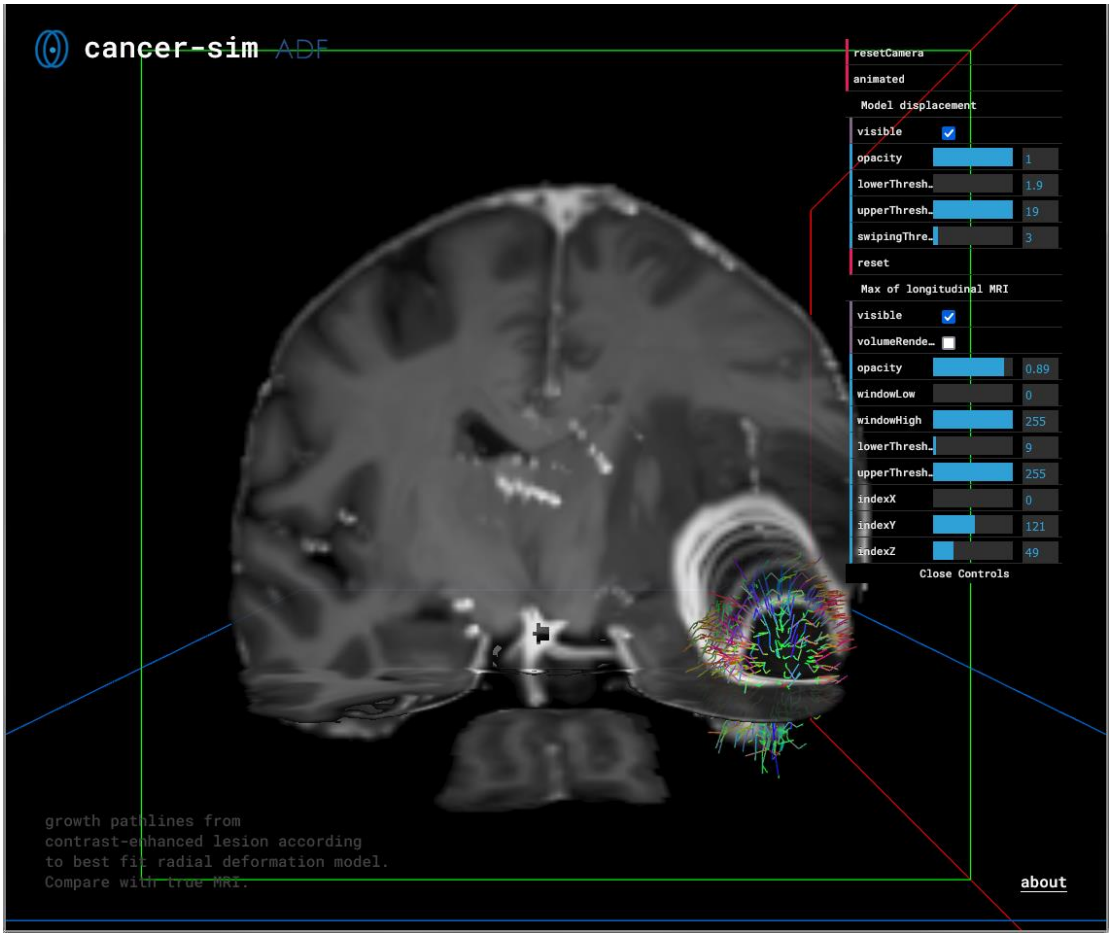

Figure 40: cancer-sim.com (web site) voxel displacement path visualization with maximum intensity values of longitudinal T1wc MRI underlaid.

8.2.3. Improving segmentation using the deformation model

Voxel-vise displacement estimation may not be required for the general task of tracking data with clinical relevance. Traditionally, volumetric or delineated surface changes have been used for treatment response assessment. As a sparser tracking approach, ROI-based tracking using segmentations may be used. This tracking approach does not enforce a direct description of voxel transformation and thereby overcomes a possible limitation of requiring voxel-vise tracking in physically difficult scenarios. Such a scenario may be major spatial and intensity transformations from cancer leading to uniform image gradients such as necrotic regions. The leading medical image segmentation methods are based on DL, which are commonly deep convolutional neural networks trained on large amounts of structural MRI

with multi-label segmentation masks as annotations [216], [222]. However, lack of large-scale medical training datasets is the leading factor in many DL brain tumor segmentation algorithms poor performance [222]. Data augmentation is a widely accepted solution to the problem of limited data for DL and machine learning model training [223].

Our deformation model may be used to generate synthetic MRIs and segmentation masks as illustrated with T2w-FLAIR in the supplementary file **cancer-sim.mp4**, which is available at the following URL (as accessed December 5th):

https://www.mn.uio.no/fysikk/english/people/aca/ivarth/works/viz/cancer-sim.mp4

By generating realistic longitudinal training data of brain cancer, it may improve longitudinal DL-based tumor segmentation performance. As such, the deformation model belongs to a class of domain-specific local data augmentation methods. Moreover, anatomically incorrect augmented examples may still manifest valid tumor features in segmentation, since unrealistic augmentations may still produce a more generalizable model [224], [225]. It may be further developed for offline and online (test-time) augmentation for use in DL training. One such improvement in the clinical accuracy of DL tumor segmentation may ultimately lead to successful adaptation of AI in the clinic [226].

8.2.4. Alternative use cases of DIR

There are other potential clinical use cases of DIR at our hospital. Hydrocephalus is a general life-threatening state in which CSF spaces are under pressure and enlarged. SyN may be used to provide a quantitative measure of this by measuring overall deformation change when comparing to a normal brain template. Another used case is midline shift quantification which may be solved similarly using a template. Last, displacement fields

from DIR may be used to deform segmentation masks (using NN interpolation) for ROI-based tracking.

8.2.5. Non-localized tracking

It is possible to track clinically meaningful imaging properties without defining a ROI. These are exploratory methods capable of categorizing more abstract and high-level patters in the data and which do not necessarily relate to voxel-vise or ROI-based properties. They are typically patterns learnt by DL models (and not hand-crafted such as our deformation model parameters), and interpretability techniques are often required to find and make use of the most useful patterns.

A future aspect of longitudinal MRI analysis in brain cancer may be to utilize clustering and unsupervised methods to find patterns that correlate well with clinical data such as treatment response, survival and various known medical conditions. An unsupervised DL model such as autoencoder (AE) could for instance be targeted at categorizing disease based on multiple patients analogous to the previously mentioned idea of having a treatment tissue response atlas of displacements. A new patient may then be associated with existing patients with treatment outcome already known by using similarity and interpretability techniques on the DL model.

A simple example of non-localized tracking of structural ventricle change was demonstrated in the thesis. Principal component analysis (PCA) [227] is a widely known and understood statistical dimensionality reduction method. Moreover, the simplest form of a linear AE spans the same subspace as the PCA loading vectors [228]. We reproduced this work using our longitudinal volumetric MRI of a patient and identified the second component in PCA to correlated with ventricular expansion as seen in Figure 41.

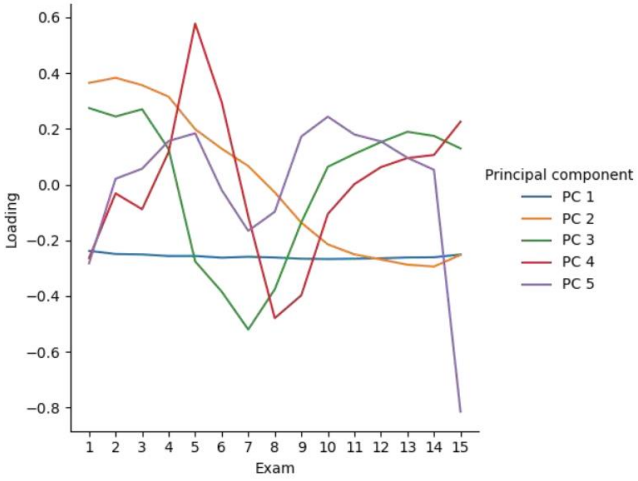

Loadings: Variable importance (Variable=Exam). First exam is the most important (has highest intensities in red regions) for PC 2

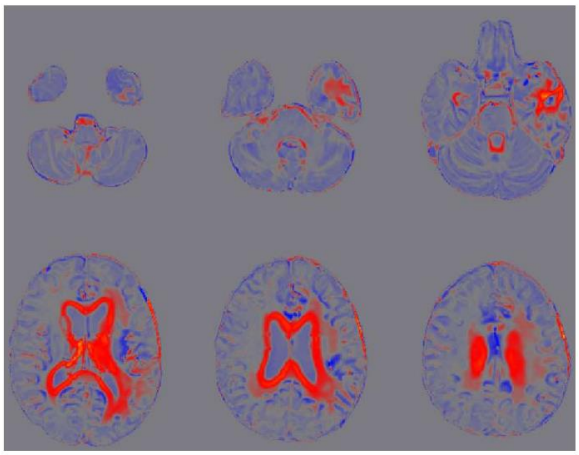

Scores for PC 2. Red regions represent intensity change caused by expanding ventricles. Red and blue represents positive and negative values, respectively

Figure 41: Example of tracking ventricle expansion without defining a ROI. PCA was performed on flattened versions of all time-point scans for a patient (one volume per column in the data matrix). Left: Loading plot showing that the second component (PC 2) had a smoothly decaying importance along with time progression (x-axis). Right: Scores for PC 2 visualized as an MRI volume revealed that PC 2 described (and tracked) the variation in the PCA model correlating with ventricular expansion during the longitudinal scans (atrophy). This is subject six from our second patient cohort.

Furthermore, we were able to reproduce the loadings plot in Figure 41 from a linear AE model trained on the dame data, by conducting singular value decomposition (SVD) on its decoder weights. Our point was to give an example of identifying a simple high-level pattern in the data correlating with atrophy and that this pattern was indeed captured by the simplest possible linear fully connected three-layer AE. In comparison, the widely successful U-Net [229] for medical segmentation tasks has 23 convolutional layers.

Most of our patients experienced ventricle volume increase during the time they were scanned, which is believed to be a consequence of brain atrophy due to CRT [230], [231]. This experiment illustrated that despite the huge dimensionality complexity of DL models, it is possible to build up intuition about their subspace complexity and resulting interpretability analogous to PCA loadings. These methods may enable us to capture and

interpret general patterns in data that may be clinically relevant without resorting to ROI-based analyses.

8.2.6. Multivariate analysis of clinical data

Multivariate analysis of structural ventricle changes in glioblastoma led to some additional results that may be worth looking more into. A PCA model was computed on data containing ventricle and tumor volume change, normalized relative CBV change in tumor and sub-ventricular zones, age, overall survival, and time from first scan. Two data sets with a total of 41 patients with glioblastoma consisting of 387 scan intervals was used. The non-linear iterative partial least squares (NIPALS) version of PCA [232] was used for this case due to some missing data. Outlier removal according to 95 % confidence intervals according to Hoteling's T^2 statistic (a multivariate generalization of Student's t-statistic) was performed. Figure 42 presents the loadings for the first two components where the overall correlations between the input data variables are seen.

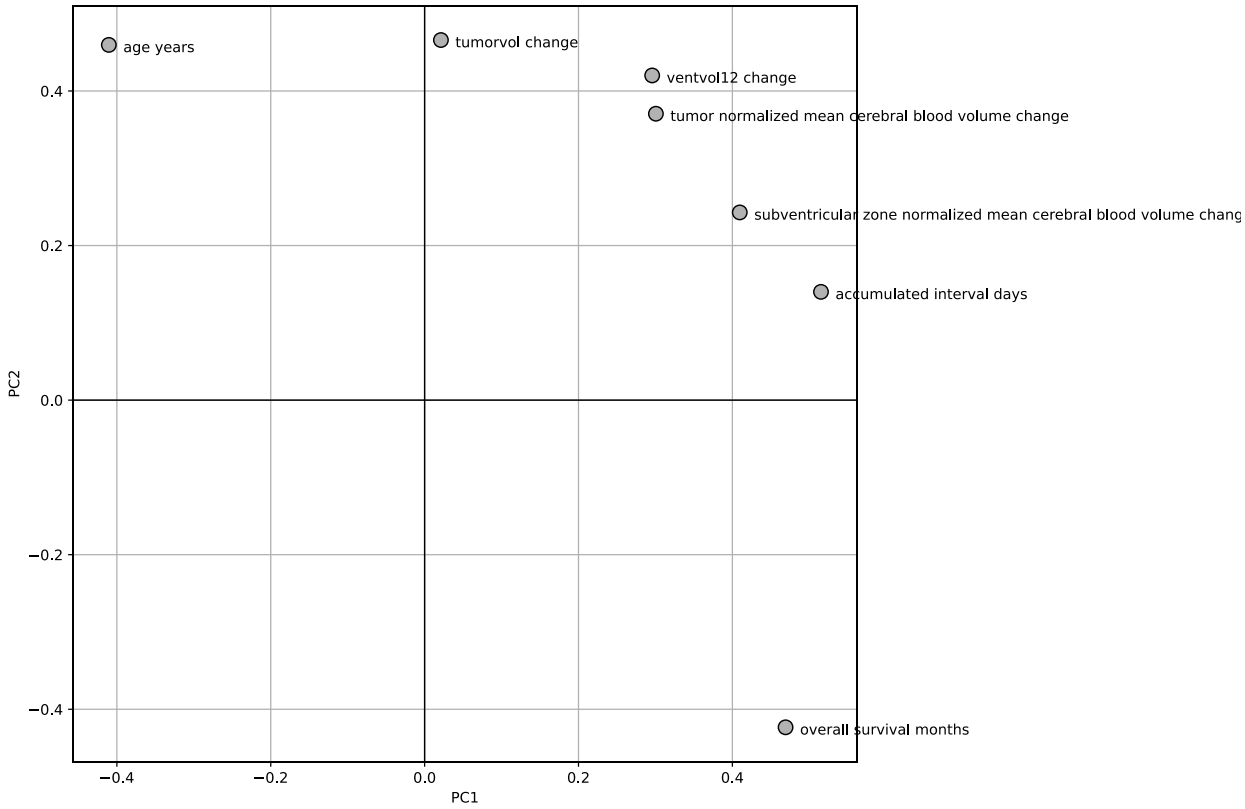

Figure 42: PC 1 and PC 2 loadings from PCA displays the correlations between age, overall survival, time from first examination, tumor, ventricle and subventricular zone volume change, as well as CBV change in tumor and subventricular zone from 387 scan intervals of 41 patients with glioblastoma undergoing standard treatment. This consisted of our second cohort plus another similar longitudinal dataset of glioblastoma under standard treatment (N=14 patients).

Some notable results were the negative correlation of overall survival and CBV increase and ventricle volume increase, as well as of age and CBV increase and ventricle volume increase. An increase in CBV was associated with worse survival prognosis, while younger patients were associated with less ventricle volume increase. A larger tumor volume increase correlated with worse survival prognosis, as expected. However, an older patient was not much associated with tumor volume increase.

9. Appendices

9.1.Source Code

A collection of processing scripts accompanying the thesis and papers is provided within the archive file **scripts.zip**. Preprocessing and processing methods using many of these scripts are documented with CLI examples (for Miniserver 3) in the presentation **mri-processing.pdf**. A repository containing these files is available at

https://github.com/CRAI-OUS/crai-lproc

In addition, links to the original code repositories for the papers and additional methods used in the thesis are provided below.

Paper 1

https://github.com/ivartz/epi_corrections

Paper 2

Contact corresponding author.

Paper 3

https://github.com/ivartz/cancer-sim

https://github.com/ivartz/cancer-sim-search

https://github.com/ivartz/ants-bcond

https://github.com/ivartz/opticalflow-bcond

Radial basis function interpolation

https://github.com/ivartz/mri-rbf-time

Voxel displacement path tracking

https://github.com/ivartz/cancer-sim-search/blob/main/make-pathlines.py

Displacement path tracking visualization (web site/server code)

https://cancer-sim.com/

https://github.com/ivartz/cancer-sim-viz

Data augmentation using the deformation model

https://github.com/ivartz/cancer-sim-search

DVC BIDS dataset repository

https://github.com/CRAI-OUS/bidsdir

9.2. Pseudocode

Deformation model (paper 3)

Pseudocode 1: Maximum spread normal vectors by maximizing mean starting distances.

```
algorithm max-spread-vectors is

       input: Normal vectors V

              Starting positions P of the normal vectors

              Number of vectors to return N_s

       output: Selection lists containing the subset V_s and P_s of the normal vectors and
       positions

       1      initialize empty lists for selected vectors and positions

       2      append to the selection lists the first input vector and position

       3      remove the selected vector and position from input lists

       4      for each selected vector 2 to N_s do

       5             for each selected vector position(s), compute the Euclidean distance to
non-selected vector position(s)

       6             append to the selection lists the input vector and position with the
       position that makes up the largest mean
       7                    Euclidean distance from the selected vector position(s)

       8             remove the selected vector and position from the input lists

       9      return V_s and P_s
```

Pseudocode 2: Directional cone masks.

```
algorithm max-spread-cones is

       input: Normal vectors V_s

              Displacement field d

              Deviation in degrees θ

       output: Cone masks M_c

       1      initialize empty list M_c for storing cone masks

       2      for each vector v in V_s do

       3             let ω be the angle difference in degrees between v and all other
displacement vectors in d

       4             let c be the cone mask defined by ω ≤ θ

       5             append to M_c the cone mask for vector v: c

       6      return M_c
```

Pseudocode 3: Infiltrative deformation of displacement field $\boldsymbol{d}$. For reading in detail, it is recommended to zoom in using the .pdf version of the thesis.

```
algorithm infiltration is

        input: Normal vectors V_s

               Normal vector starting positions P_s

               Displacement field d

               Cone masks M_c

               Brain mask M_b

               Infiltration β

        output: Infiltrative displacement field d_β

        let dnorm be |d|

        let displacements be a list containing one interpolated part of d for each spatial direction in s

        for each spatial direction i in in s do

                       let nvd, nvc, bmi be V_s[i], P_s[i], M_c[i] respectively

                       let p_max_bmi be the point furthest away nvc along nvd and within bmi

                       let disp_max_bmi be the length between nvc and p_max_bmi

                       let p_max_brain be the point furthest away nvc along nvd and within M_b

                       let disp_max_brain be the length between nvc and p_max_brain

                       let dnormcone be dnorm within bmi

                       let dxcone, dycone, dzcone be the components of d within bmi

                       (the following scales all displacement components to unit norm such that their starting coordinates can be displaced equally far)

                       let dxcone, dycone, dzcone be dxcone/dnormcone , dycone/dnormcone , dzcone/dnormcone respectively with element wise fraction

                       if β > 0 then

                                   let mask_pts be the points within bmi

                                   let extension be β*(disp_max_brain - disp_max_bmi)

                                   (the following displaces mask_pts according to the extension length)

                                   displace the mask_pts x, y, z coordinates extension*dxcone, extension*dxcone, extension*dzcone length respectively

                                   let bmi_copy be a copy of bmi

                                   add displaced mask_pts to bmi_copy

                                   let bm_geom_center and bm_widths be the geometric center coordinates and dimensions of bmi_copy containing displaced
                                    points

                       else

                                   let bm_geom_center and bm_widths be the geometric center coordinates and dimensions of bmi

                       let bmi_copy be a copy of bmi

                       let mask_pts be the points within bmi

                       let extension be disp_max_brain - disp_max_bmi

                       displace the mask_pts x, y, z coordinates extension*dxcone, extension*dxcone, extension*dzcone length respectively

                       add displaced mask_pts to bmi_copy

                       let bm_geom_center_interp and bm_widths_interp be the geometric center coordinates and dimensions of bmi_copy containing displaced
                        points

                       deform d by re-mapping components within bm_geom_center and bm_widths to be within bm_geom_center_interp and bm_widths_interp
                        using trilinear interpolation

                       append to displacements the deformed components of d for the spatial direction i

        let d_β be the mean of displacements over s for interpolated component data

        return d_β
```

9.3.Servers

Time and effort were spent in installing and maintaining research computing servers at our hospital (Miniserver 1, 2 & 3, gpu-fys), both for use in the thesis and by others. This especially aided students in the computational radiology and artificial intelligence (CRAI) research group in fulfilling their Master's and PhD degrees (e.g. providing working GPU accelerated training environments and software for DL), but also physicians and others employed at department of physics and computational radiology (FBA) for to developing and using research software in combined Windows and Linux environments.

10. Bibliography

[1] M. K. Rasmussen, H. Mestre, and M. Nedergaard, “Fluid transport in the brain,” *Physiol. Rev.*, vol. 102, no. 2, pp. 1025–1151, Apr. 2022, doi: 10.1152/physrev.00031.2020.

[2] “Brain Anatomy and How the Brain Works,” Jul. 14, 2021. https://www.hopkinsmedicine.org/health/conditions-and-diseases/anatomy-of-the-brain (accessed Aug. 25, 2022).

[3] S. Herculano-Houzel, “The Human Brain in Numbers: A Linearly Scaled-up Primate Brain,” *Front. Hum. Neurosci.*, vol. 3, p. 31, Nov. 2009, doi: 10.3389/neuro.09.031.2009.

[4] P. Hartmann, A. Ramseier, F. Gudat, M. J. Mihatsch, and W. Polasek, “[Normal weight of the brain in adults in relation to age, sex, body height and weight],” *Pathol.*, vol. 15, no. 3, pp. 165–170, Jun. 1994, doi: 10.1007/s002920050040.

[5] F. A. C. Azevedo *et al.*, “Equal numbers of neuronal and nonneuronal cells make the human brain an isometrically scaled-up primate brain,” *J. Comp. Neurol.*, vol. 513, no. 5, pp. 532–541, 2009, doi: 10.1002/cne.21974.

[6] C. S. von Bartheld, J. Bahney, and S. Herculano-Houzel, “The search for true numbers of neurons and glial cells in the human brain: A review of 150 years of cell counting,” *J. Comp. Neurol.*, vol. 524, no. 18, pp. 3865–3895, 2016, doi: 10.1002/cne.24040.

[7] “Brain anatomy, Anatomy of the human brain | Mayfield Brain & Spine Cincinnati, Ohio.” https://mayfieldclinic.com/pe-anatbrain.htm (accessed Aug. 25, 2022).

[8] B. S. Khakh and B. Deneen, “The Emerging Nature of Astrocyte Diversity,” *Annu. Rev. Neurosci.*, vol. 42, no. 1, pp. 187–207, Jul. 2019, doi: 10.1146/annurev-neuro-070918-050443.

[9] C. Stadelmann, S. Timmler, A. Barrantes-Freer, and M. Simons, “Myelin in the Central Nervous System: Structure, Function, and Pathology,” *Physiol. Rev.*, vol. 99, no. 3, pp. 1381–1431, Jul. 2019, doi: 10.1152/physrev.00031.2018.

[10] C. Hajal, B. Le Roi, R. D. Kamm, and B. M. Maoz, “Biology and Models of the Blood–Brain Barrier,” *Annu. Rev. Biomed. Eng.*, vol. 23, no. 1, pp. 359–384, Jul. 2021, doi: 10.1146/annurev-bioeng-082120-042814.

[11] N. Spassky and A. Meunier, “The development and functions of multiciliated epithelia,” *Nat. Rev. Mol. Cell Biol.*, vol. 18, no. 7, pp. 423–436, Jul. 2017, doi: 10.1038/nrm.2017.21.

[12] “The human brain - cell types - The Human Protein Atlas.” https://www.proteinatlas.org/humanproteome/brain/cell+types (accessed Aug. 25, 2022).

[13] “Glioma - Clinical Features - Management,” *TeachMeSurgery*. https://teachmesurgery.com/neurosurgery/neurological-malignancy/glioma/ (accessed Nov. 24, 2022).

[14] W. L. Nowinski, “NOWinBRAIN: a Large, Systematic, and Extendable Repository of 3D Reconstructed Images of a Living Human Brain Cum Head and Neck,” *J. Digit. Imaging*, vol. 35, no. 2, pp. 98–114, Apr. 2022, doi: 10.1007/s10278-021-00528-0.

[15] W. L. Nowinski, “3D Atlas of the Brain, Head and Neck in 2953 pieces,” *Neuroinformatics*, vol. 15, no. 4, pp. 395–400, Oct. 2017, doi: 10.1007/s12021-017-9339-8.

[16] W. L. Nowinski, “Introduction to Brain Anatomy,” in *Biomechanics of the Brain*, K. Miller, Ed. New York, NY: Springer, 2011, pp. 5–40. Accessed: Nov. 23, 2022. [Online]. Available: https://doi.org/10.1007/978-1-4419-9997-9_2
[17] “Brain Anatomy,” *Physiopedia*. https://www.physio-pedia.com/Brain_Anatomy (accessed Aug. 25, 2022).
[18] K. H. Jawabri and S. Sharma, “Physiology, Cerebral Cortex Functions,” in *StatPearls*, Treasure Island (FL): StatPearls Publishing, 2022. Accessed: Nov. 16, 2022. [Online]. Available: http://www.ncbi.nlm.nih.gov/books/NBK538496/
[19] S. Knecht *et al.*, “Handedness and hemispheric language dominance in healthy humans,” *Brain*, vol. 123, no. 12, pp. 2512–2518, Dec. 2000, doi: 10.1093/brain/123.12.2512.
[20] J. J. Iliff *et al.*, “Brain-wide pathway for waste clearance captured by contrast-enhanced MRI,” *J. Clin. Invest.*, vol. 123, no. 3, pp. 1299–1309, Mar. 2013, doi: 10.1172/JCI67677.
[21] “Eloquent cortex,” *Wikipedia*. Apr. 18, 2020. Accessed: Aug. 25, 2022. [Online]. Available: https://en.wikipedia.org/w/index.php?title=Eloquent_cortex&oldid=951728491
[22] “Eloquent area,” Jul. 14, 2021. https://operativeneurosurgery.com/doku.php?id=eloquent_area (accessed Aug. 25, 2022).
[23] S. Ogawa, T. M. Lee, A. R. Kay, and D. W. Tank, “Brain magnetic resonance imaging with contrast dependent on blood oxygenation.,” *Proc. Natl. Acad. Sci.*, vol. 87, no. 24, pp. 9868–9872, Dec. 1990, doi: 10.1073/pnas.87.24.9868.
[24] P. Due-Tonnessen, I. Rasmussen, E. M. Berntsen, A. Bjornerud, and K. E. Emblem, “Identifying the Central Sulcus in Patients With Intra-axial Lesions: A Multicenter Study Comparing Conventional Presurgical MRI to Topographical Analysis and BOLD-fMRI,” *J. Comput. Assist. Tomogr.*, vol. 38, no. 1, pp. 1–8, Feb. 2014, doi: 10.1097/RCT.0b013e3182a589e0.
[25] S. Fang *et al.*, “Anatomic Location of Tumor Predicts the Accuracy of Motor Function Localization in Diffuse Lower-Grade Gliomas Involving the Hand Knob Area,” *AJNR Am. J. Neuroradiol.*, vol. 38, no. 10, pp. 1990–1997, Oct. 2017, doi: 10.3174/ajnr.A5342.
[26] P. L. Nunez and R. Srinivasan, *Electric Fields of the Brain: The Neurophysics of EEG*. Oxford University Press, 2006.
[27] M. Hämäläinen, R. Hari, R. J. Ilmoniemi, J. Knuutila, and O. V. Lounasmaa, “Magnetoencephalography---theory, instrumentation, and applications to noninvasive studies of the working human brain,” *Rev. Mod. Phys.*, vol. 65, no. 2, pp. 413–497, Apr. 1993, doi: 10.1103/RevModPhys.65.413.
[28] “Primary and secondary brain tumours | Cancer Research UK.” https://www.cancerresearchuk.org/about-cancer/brain-tumours/types/primary-secondary-tumours (accessed Jan. 27, 2022).
[29] P. Y. Wen *et al.*, “Glioblastoma in adults: a Society for Neuro-Oncology (SNO) and European Society of Neuro-Oncology (EANO) consensus review on current management and future directions,” *Neuro-Oncol.*, vol. 22, no. 8, pp. 1073–1113, Aug. 2020, doi: 10.1093/neuonc/noaa106.

[30] “Brain, central nervous system fact sheet,” *Global Cancer Observatory*. https://gco.iarc.fr/today/data/factsheets/cancers/31-Brain-central-nervous-system-fact-sheet.pdf (accessed Jan. 27, 2022).
[31] K. D. Miller *et al.*, “Brain and other central nervous system tumor statistics, 2021,” *CA. Cancer J. Clin.*, vol. 71, no. 5, pp. 381–406, 2021, doi: 10.3322/caac.21693.
[32] R. L. Siegel, K. D. Miller, H. E. Fuchs, and A. Jemal, “Cancer Statistics, 2021,” *CA. Cancer J. Clin.*, vol. 71, no. 1, pp. 7–33, 2021, doi: 10.3322/caac.21654.
[33] “SEER*Stat Tutorials: Calculating Age-adjusted Rates,” *SEER*. https://seer.cancer.gov/seerstat/tutorials/aarates/definition.html (accessed Jan. 27, 2022).
[34] R. Leece, J. Xu, Q. T. Ostrom, Y. Chen, C. Kruchko, and J. S. Barnholtz-Sloan, “Global incidence of malignant brain and other central nervous system tumors by histology, 2003–2007,” *Neuro-Oncol.*, vol. 19, no. 11, pp. 1553–1564, Oct. 2017, doi: 10.1093/neuonc/nox091.
[35] E. Crocetti *et al.*, “Epidemiology of glial and non-glial brain tumours in Europe,” *Eur. J. Cancer Oxf. Engl. 1990*, vol. 48, no. 10, pp. 1532–1542, Jul. 2012, doi: 10.1016/j.ejca.2011.12.013.
[36] “Krebs - Cancer in the central nervous system.” https://www.krebsdaten.de/Krebs/EN/Content/Cancer_sites/Central_nervous_system_cancer/central_nervous_system_cancer_node.html (accessed Jan. 27, 2022).
[37] D. N. Louis *et al.*, “The 2016 World Health Organization Classification of Tumors of the Central Nervous System: a summary,” *Acta Neuropathol. (Berl.)*, vol. 131, no. 6, pp. 803–820, Jun. 2016, doi: 10.1007/s00401-016-1545-1.
[38] M. L. Goodenberger and R. B. Jenkins, “Genetics of adult glioma,” *Cancer Genet.*, vol. 205, no. 12, pp. 613–621, Desember 2012, doi: 10.1016/j.cancergen.2012.10.009.
[39] A. C. Tan, D. M. Ashley, G. Y. López, M. Malinzak, H. S. Friedman, and M. Khasraw, “Management of glioblastoma: State of the art and future directions,” *CA. Cancer J. Clin.*, vol. 70, no. 4, pp. 299–312, 2020, doi: 10.3322/caac.21613.
[40] L. B. Nabors *et al.*, “Central Nervous System Cancers, Version 3.2020, NCCN Clinical Practice Guidelines in Oncology,” *J. Natl. Compr. Canc. Netw.*, vol. 18, no. 11, pp. 1537–1570, Nov. 2020, doi: 10.6004/jnccn.2020.0052.
[41] D. N. Louis *et al.*, “The 2021 WHO Classification of Tumors of the Central Nervous System: a summary,” *Neuro-Oncol.*, vol. 23, no. 8, pp. 1231–1251, Jun. 2021, doi: 10.1093/neuonc/noab106.
[42] P. B. Due-Tønnessen, “Evaluation of functional magnetic resonance imaging in the diagnosis of brain tumors and other brain lesions for assessment of clinical efficacy,” 2022, Accessed: Sep. 06, 2022. [Online]. Available: https://www.duo.uio.no/handle/10852/92991
[43] R. Stupp *et al.*, “Radiotherapy plus Concomitant and Adjuvant Temozolomide for Glioblastoma,” *N. Engl. J. Med.*, vol. 352, no. 10, pp. 987–996, Mar. 2005, doi: 10.1056/NEJMoa043330.
[44] M. E. Davis, “Glioblastoma: Overview of Disease and Treatment,” *Clin. J. Oncol. Nurs.*, vol. 20, no. 5, pp. S2–S8, Oct. 2016, doi: 10.1188/16.CJON.S1.2-8.
[45] F. Hanif, K. Muzaffar, K. Perveen, S. M. Malhi, and S. U. Simjee, “Glioblastoma Multiforme: A Review of its Epidemiology and Pathogenesis through Clinical Presentation and Treatment,” *Asian Pac. J. Cancer Prev. APJCP*, vol. 18, no. 1, pp. 3–9, 2017, doi: 10.22034/APJCP.2017.18.1.3.

[46] P. Y. Wen and S. Kesari, “Malignant Gliomas in Adults,” *N. Engl. J. Med.*, vol. 359, no. 5, pp. 492–507, Jul. 2008, doi: 10.1056/NEJMra0708126.
[47] M. Lacroix *et al.*, “A multivariate analysis of 416 patients with glioblastoma multiforme: prognosis, extent of resection, and survival,” *J. Neurosurg.*, vol. 95, no. 2, pp. 190–198, Aug. 2001, doi: 10.3171/jns.2001.95.2.0190.
[48] A. F. Haddad, J. S. Young, R. A. Morshed, and M. S. Berger, “FLAIRectomy: Resecting beyond the Contrast Margin for Glioblastoma,” *Brain Sci.*, vol. 12, no. 5, Art. no. 5, May 2022, doi: 10.3390/brainsci12050544.
[49] E. K. Nduom *et al.*, “Re-evaluating Biopsy for Recurrent Glioblastoma: A Position Statement by the Christopher Davidson Forum Investigators,” *Neurosurgery*, vol. 89, no. 1, pp. 129–132, Jul. 2021, doi: 10.1093/neuros/nyab063.
[50] C. Larsson *et al.*, “Prediction of survival and progression in glioblastoma patients using temporal perfusion changes during radiochemotherapy,” *Magn. Reson. Imaging*, vol. 68, pp. 106–112, May 2020, doi: 10.1016/j.mri.2020.01.012.
[51] A. Server, T. E. D. Orheim, B. A. Graff, R. Josefsen, T. Kumar, and P. H. Nakstad, “Diagnostic examination performance by using microvascular leakage, cerebral blood volume, and blood flow derived from 3-T dynamic susceptibility-weighted contrast-enhanced perfusion MR imaging in the differentiation of glioblastoma multiforme and brain metastasis,” *Neuroradiology*, vol. 53, no. 5, pp. 319–330, May 2011, doi: 10.1007/s00234-010-0740-3.
[52] P. Y. Wen *et al.*, “Updated Response Assessment Criteria for High-Grade Gliomas: Response Assessment in Neuro-Oncology Working Group,” *J. Clin. Oncol.*, vol. 28, no. 11, pp. 1963–1972, Apr. 2010, doi: 10.1200/JCO.2009.26.3541.
[53] F. Gaillard, “RANO criteria for glioma | Radiology Reference Article | Radiopaedia.org,” *Radiopaedia*. https://radiopaedia.org/articles/rano-criteria-for-glioma (accessed Aug. 24, 2022).
[54] D. A. Karnofsky, W. H. Abelmann, L. F. Craver, and J. H. Burchenal, “The use of the nitrogen mustards in the palliative treatment of carcinoma. With particular reference to bronchogenic carcinoma,” *Cancer*, vol. 1, no. 4, pp. 634–656, 1948, doi: 10.1002/1097-0142(194811)1:4<634::AID-CNCR2820010410>3.0.CO;2-L.
[55] P. Vollmuth *et al.*, “Artificial intelligence (AI)-based decision support improves reproducibility of tumor response assessment in neuro-oncology: An international multi-reader study,” *Neuro-Oncol.*, p. noac189, Aug. 2022, doi: 10.1093/neuonc/noac189.
[56] P. Kickingereder *et al.*, “Automated quantitative tumour response assessment of MRI in neuro-oncology with artificial neural networks: a multicentre, retrospective study,” *Lancet Oncol.*, vol. 20, no. 5, pp. 728–740, May 2019, doi: 10.1016/S1470-2045(19)30098-1.
[57] C. Larsson, “Prognostic Value of Optimized Dynamic Contrast-Enhanced Magnetic Resonance Imaging of High-Grade Gliomas,” 2018, Accessed: Feb. 24, 2021. [Online]. Available: https://www.duo.uio.no/handle/10852/62008
[58] H. Akbari *et al.*, “Histopathology-validated machine learning radiographic biomarker for non-invasive discrimination between true progression and pseudo-progression in glioblastoma,” *Cancer*, vol. 126, no. 11, pp. 2625–2636, Jun. 2020, doi: 10.1002/cncr.32790.
[59] C. Le Fèvre *et al.*, “Pseudoprogression versus true progression in glioblastoma patients: A multiapproach literature review: Part 1 – Molecular, morphological and

clinical features," *Crit. Rev. Oncol. Hematol.*, vol. 157, p. 103188, Jan. 2021, doi: 10.1016/j.critrevonc.2020.103188.
[60] R. Roesler, S. Dini, and G. Isolan, "Brain tumours, brain metastases, and neuroinflammation: Insights from neuroimaging studies.," Preprints, preprint, Sep. 2021. Accessed: Oct. 03, 2021. [Online]. Available: https://www.authorea.com/users/435776/articles/538564-brain-tumours-brain-metastases-and-neuroinflammation-insights-from-neuroimaging-studies?commit=2809653a0bec1e4747a775ce302e533ce66ccae6
[61] C. Le Fèvre *et al.*, "Pseudoprogression versus true progression in glioblastoma patients: A multiapproach literature review. Part 2 – Radiological features and metric markers," *Crit. Rev. Oncol. Hematol.*, vol. 159, p. 103230, Mar. 2021, doi: 10.1016/j.critrevonc.2021.103230.
[62] R. J. Young *et al.*, "Potential utility of conventional MRI signs in diagnosing pseudoprogression in glioblastoma," *Neurology*, vol. 76, no. 22, pp. 1918–1924, May 2011, doi: 10.1212/WNL.0b013e31821d74e7.
[63] M. Li *et al.*, "Distinguishing Pseudoprogression From True Early Progression in Isocitrate Dehydrogenase Wild-Type Glioblastoma by Interrogating Clinical, Radiological, and Molecular Features," *Front. Oncol.*, vol. 11, 2021, Accessed: Aug. 24, 2022. [Online]. Available: https://www.frontiersin.org/articles/10.3389/fonc.2021.627325
[64] A. M. Rao, A. Quddusi, and M. S. Shamim, "The significance of MGMT methylation in Glioblastoma Multiforme prognosis," *JPMA J. Pak. Med. Assoc.*, vol. 68, no. 7, pp. 1137–1139, Jul. 2018.
[65] M. Ismail *et al.*, "Shape Features of the Lesion Habitat to Differentiate Brain Tumor Progression from Pseudoprogression on Routine Multiparametric MRI: A Multisite Study," *Am. J. Neuroradiol.*, vol. 39, no. 12, pp. 2187–2193, Dec. 2018, doi: 10.3174/ajnr.A5858.
[66] I. Sidibe, F. Tensaouti, M. Roques, E. Cohen-Jonathan-Moyal, and A. Laprie, "Pseudoprogression in Glioblastoma: Role of Metabolic and Functional MRI-Systematic Review," *Biomedicines*, vol. 10, no. 2, p. 285, Jan. 2022, doi: 10.3390/biomedicines10020285.
[67] A. J. Prager, N. Martinez, K. Beal, A. Omuro, Z. Zhang, and R. J. Young, "Diffusion and perfusion MRI to differentiate treatment-related changes including pseudoprogression from recurrent tumors in high-grade gliomas with histopathologic evidence," *AJNR Am. J. Neuroradiol.*, vol. 36, no. 5, pp. 877–885, May 2015, doi: 10.3174/ajnr.A4218.
[68] R. J. Young *et al.*, "MRI perfusion in determining pseudoprogression in patients with glioblastoma," *Clin. Imaging*, vol. 37, no. 1, pp. 41–49, Feb. 2013, doi: 10.1016/j.clinimag.2012.02.016.
[69] J. L. Boxerman *et al.*, "Longitudinal DSC-MRI for Distinguishing Tumor Recurrence From Pseudoprogression in Patients With a High-grade Glioma," *Am. J. Clin. Oncol.*, vol. 40, no. 3, pp. 228–234, Jun. 2017, doi: 10.1097/COC.0000000000000156.
[70] L. S. Rowe *et al.*, "Differentiating pseudoprogression from true progression: analysis of radiographic, biologic, and clinical clues in GBM," *J. Neurooncol.*, vol. 139, no. 1, pp. 145–152, Aug. 2018, doi: 10.1007/s11060-018-2855-z.
[71] J. Y. Kim *et al.*, "Incorporating diffusion- and perfusion-weighted MRI into a radiomics model improves diagnostic performance for pseudoprogression in glioblastoma

patients," *Neuro-Oncol.*, vol. 21, no. 3, pp. 404–414, Feb. 2019, doi: 10.1093/neuonc/noy133.
[72] R. W. Brown, Y.-C. N. Cheng, E. M. Haacke, M. R. Thompson, and R. Venkatesan, *Magnetic Resonance Imaging: Physical Principles and Sequence Design*. John Wiley & Sons, 2014.
[73] M. T. Vlaardingerbroek and J. A. Boer, *Magnetic Resonance Imaging: Theory and Practice*. Springer Science & Business Media, 2013.
[74] F. Bloch, "Nuclear Induction," *Phys. Rev.*, vol. 70, no. 7–8, pp. 460–474, Oktober 1946, doi: 10.1103/PhysRev.70.460.
[75] E. M. Purcell, H. C. Torrey, and R. V. Pound, "Resonance Absorption by Nuclear Magnetic Moments in a Solid," *Phys. Rev.*, vol. 69, no. 1–2, pp. 37–38, Jan. 1946, doi: 10.1103/PhysRev.69.37.
[76] F. Block, W. W. Hansen, and M. Packard, "The nuclear induction experiment," *Phys. Rev.*, vol. 70, no. 7–8, pp. 474–485, 1946.
[77] J. Assländer, "Static Field Inhomogeneities in Magnetic Resonance Encephalography: Effects and Mitigation," 2015.
[78] U. Vovk, F. Pernus, and B. Likar, "A Review of Methods for Correction of Intensity Inhomogeneity in MRI," *IEEE Trans. Med. Imaging*, vol. 26, no. 3, pp. 405–421, Mar. 2007, doi: 10.1109/TMI.2006.891486.
[79] N. J. Tustison *et al.*, "N4ITK: Improved N3 Bias Correction," *IEEE Trans. Med. Imaging*, vol. 29, no. 6, pp. 1310–1320, Jun. 2010, doi: 10.1109/TMI.2010.2046908.
[80] H. An and W. Lin, "Spin Density, T1, T2, T2* Relaxation and Bloch Equations," *Curr. Protoc. Magn. Reson. Imaging*, vol. 00, no. 1, Mar. 2001, doi: 10.1002/0471142719.mib0301s00.
[81] R. C. Gonzalez and R. E. Woods, "Filtering in the Frequency Domain," in *Digital image processing*, 4th ed., 2018.
[82] R. N. Bracewell and R. N. Bracewell, *The Fourier transform and its applications*, vol. 31999. McGraw-Hill New York, 1986.
[83] S. Yamada *et al.*, "T1 and T2 relaxation times on gadolinium-diethylenetriaminepentaacetic acid enhanced magnetic resonance images of brain tumors," *Tohoku J. Exp. Med.*, vol. 160, no. 2, pp. 145–148, Feb. 1990, doi: 10.1620/tjem.160.145.
[84] M. Rohrer, H. Bauer, J. Mintorovitch, M. Requardt, and H.-J. Weinmann, "Comparison of Magnetic Properties of MRI Contrast Media Solutions at Different Magnetic Field Strengths," *Invest. Radiol.*, vol. 40, no. 11, pp. 715–724, Nov. 2005, doi: 10.1097/01.rli.0000184756.66360.d3.
[85] L. Østergaard, "Cerebral Perfusion Imaging by Bolus Tracking," *Top. Magn. Reson. Imaging*, vol. 15, no. 1, pp. 3–9, Feb. 2004.
[86] L. Pasquini *et al.*, "Deep Learning Can Differentiate IDH-Mutant from IDH-Wild GBM," *J. Pers. Med.*, vol. 11, no. 4, p. 290, Apr. 2021, doi: 10.3390/jpm11040290.
[87] K. A. Rempp, G. Brix, F. Wenz, C. R. Becker, F. Gückel, and W. J. Lorenz, "Quantification of regional cerebral blood flow and volume with dynamic susceptibility contrast-enhanced MR imaging.," *Radiology*, vol. 193, no. 3, pp. 637–641, Dec. 1994, doi: 10.1148/radiology.193.3.7972800.
[88] G.-H. Jahng, K.-L. Li, L. Ostergaard, and F. Calamante, "Perfusion Magnetic Resonance Imaging: A Comprehensive Update on Principles and Techniques," *Korean J. Radiol.*, vol. 15, no. 5, pp. 554–577, Sep. 2014, doi: 10.3348/kjr.2014.15.5.554.

[89] C. C. Quarles, L. C. Bell, and A. M. Stokes, “Imaging vascular and hemodynamic features of the brain using dynamic susceptibility contrast and dynamic contrast enhanced MRI,” *NeuroImage*, vol. 187, pp. 32–55, Feb. 2019, doi: 10.1016/j.neuroimage.2018.04.069.

[90] J. L. Boxerman, K. M. Schmainda, and R. M. Weisskoff, “Relative Cerebral Blood Volume Maps Corrected for Contrast Agent Extravasation Significantly Correlate with Glioma Tumor Grade, Whereas Uncorrected Maps Do Not,” *Am. J. Neuroradiol.*, vol. 27, no. 4, pp. 859–867, Apr. 2006.

[91] E. S. Paulson and K. M. Schmainda, “Comparison of dynamic susceptibility-weighted contrast-enhanced MR methods: recommendations for measuring relative cerebral blood volume in brain tumors,” *Radiology*, vol. 249, no. 2, pp. 601–613, Nov. 2008, doi: 10.1148/radiol.2492071659.

[92] C. C. Quarles, D. F. Gochberg, J. C. Gore, and T. E. Yankeelov, “A theoretical framework to model DSC-MRI data acquired in the presence of contrast agent extravasation,” *Phys. Med. Biol.*, vol. 54, no. 19, p. 5749, Sep. 2009, doi: 10.1088/0031-9155/54/19/006.

[93] A. Bjornerud, A. G. Sorensen, K. Mouridsen, and K. E. Emblem, “T1- and T*2-Dominant Extravasation Correction in DSC-MRI: Part I—Theoretical Considerations and Implications for Assessment of Tumor Hemodynamic Properties,” *J. Cereb. Blood Flow Metab.*, vol. 31, no. 10, pp. 2041–2053, Oct. 2011, doi: 10.1038/jcbfm.2011.52.

[94] J. L. Boxerman, D. E. Prah, E. S. Paulson, J. T. Machan, D. Bedekar, and K. M. Schmainda, “The Role of preload and leakage correction in gadolinium-based cerebral blood volume estimation determined by comparison with MION as a criterion standard,” *AJNR Am. J. Neuroradiol.*, vol. 33, no. 6, pp. 1081–1087, Jun. 2012, doi: 10.3174/ajnr.A2934.

[95] K. M. Donahue *et al.*, “Utility of simultaneously acquired gradient-echo and spin-echo cerebral blood volume and morphology maps in brain tumor patients,” *Magn. Reson. Med.*, vol. 43, no. 6, pp. 845–853, 2000, doi: 10.1002/1522-2594(200006)43:6<845::AID-MRM10>3.0.CO;2-J.

[96] L. S. Hu *et al.*, “Impact of Software Modeling on the Accuracy of Perfusion MRI in Glioma,” *AJNR Am. J. Neuroradiol.*, vol. 36, no. 12, pp. 2242–2249, Dec. 2015, doi: 10.3174/ajnr.A4451.

[97] K. Leu *et al.*, “Improved Leakage Correction for Single-Echo Dynamic Susceptibility Contrast Perfusion MRI Estimates of Relative Cerebral Blood Volume in High-Grade Gliomas by Accounting for Bidirectional Contrast Agent Exchange,” *AJNR Am. J. Neuroradiol.*, vol. 37, no. 8, pp. 1440–1446, Aug. 2016, doi: 10.3174/ajnr.A4759.

[98] C. C. Quarles, B. D. Ward, and K. M. Schmainda, “Improving the reliability of obtaining tumor hemodynamic parameters in the presence of contrast agent extravasation,” *Magn. Reson. Med.*, vol. 53, no. 6, pp. 1307–1316, 2005, doi: 10.1002/mrm.20497.

[99] A. M. Stokes, N. Semmineh, and C. C. Quarles, “Validation of a T1 and T2* leakage correction method based on multiecho dynamic susceptibility contrast MRI using MION as a reference standard,” *Magn. Reson. Med.*, vol. 76, no. 2, pp. 613–625, 2016, doi: 10.1002/mrm.25906.

[100] L. Østergaard, R. M. Weisskoff, D. A. Chesler, C. Gyldensted, and B. R. Rosen, “High resolution measurement of cerebral blood flow using intravascular tracer bolus passages. Part I: Mathematical approach and statistical analysis,” *Magn. Reson. Med.*, vol. 36, no. 5, pp. 715–725, 1996, doi: 10.1002/mrm.1910360510.

[101] F. Calamante, D. L. Thomas, G. S. Pell, J. Wiersma, and R. Turner, “Measuring Cerebral Blood Flow Using Magnetic Resonance Imaging Techniques,” *J. Cereb. Blood Flow Metab.*, vol. 19, no. 7, pp. 701–735, Jul. 1999, doi: 10.1097/00004647-199907000-00001.
[102] F. Calamante, “Arterial input function in perfusion MRI: A comprehensive review,” *Prog. Nucl. Magn. Reson. Spectrosc.*, vol. 74, pp. 1–32, Oktober 2013, doi: 10.1016/j.pnmrs.2013.04.002.
[103] M. Kleppestø, A. Bjørnerud, I. R. Groote, M. Kim, J. Vardal, and C. Larsson, “Operator dependency of arterial input function in dynamic contrast-enhanced MRI,” *Magn. Reson. Mater. Phys. Biol. Med.*, Jul. 2021, doi: 10.1007/s10334-021-00926-z.
[104] M. K. Stehling, R. Turner, and P. Mansfield, “Echo-Planar Imaging: Magnetic Resonance Imaging in a Fraction of a Second,” *Science*, vol. 254, no. 5028, pp. 43–50, Oct. 1991, doi: 10.1126/science.1925560.
[105] A. Bjørnerud, “The physics of magnetic resonance imaging,” *Kompend. FYS-KJM*, vol. 4740, 2008.
[106] I. F. Syversen, “Implementation of geometric distortion correction of EPI images in clinical workflow,” 2018, Accessed: Jun. 28, 2022. [Online]. Available: https://ntnuopen.ntnu.no/ntnu-xmlui/handle/11250/2506884
[107] J. A. Ottesen, “Accelerated Magnetic Resonance Imaging Using Deep Learning Reconstruction,” 2021.
[108] J. F. Schenck, “The role of magnetic susceptibility in magnetic resonance imaging: MRI magnetic compatibility of the first and second kinds,” *Med. Phys.*, vol. 23, no. 6, pp. 815–850, 1996, doi: 10.1118/1.597854.
[109] D. Jiles, *Introduction to Magnetism and Magnetic Materials*. CRC Press, 2015.
[110] D. Holland, J. M. Kuperman, and A. M. Dale, “Efficient Correction of Inhomogeneous Static Magnetic Field-Induced Distortion in Echo Planar Imaging,” *NeuroImage*, vol. 50, no. 1, p. 175, Mar. 2010, doi: 10.1016/j.neuroimage.2009.11.044.
[111] J. L. R. Andersson, S. Skare, and J. Ashburner, “How to correct susceptibility distortions in spin-echo echo-planar images: application to diffusion tensor imaging,” *NeuroImage*, vol. 20, no. 2, pp. 870–888, Oct. 2003, doi: 10.1016/S1053-8119(03)00336-7.
[112] P. Jezzard and R. S. Balaban, “Correction for geometric distortion in echo planar images from B0 field variations,” *Magn. Reson. Med.*, vol. 34, no. 1, pp. 65–73, Jul. 1995, doi: 10.1002/mrm.1910340111.
[113] I. A. Clark, M. F. Callaghan, N. Weiskopf, E. A. Maguire, and S. Mohammadi, “Reducing Susceptibility Distortion Related Image Blurring in Diffusion MRI EPI Data,” *Front. Neurosci.*, vol. 15, p. 706473, Aug. 2021, doi: 10.3389/fnins.2021.706473.
[114] I. Aganj, B. T. T. Yeo, M. R. Sabuncu, and B. Fischl, “On Removing Interpolation and Resampling Artifacts in Rigid Image Registration,” *IEEE Trans. Image Process.*, vol. 22, no. 2, pp. 816–827, Feb. 2013, doi: 10.1109/TIP.2012.2224356.
[115] A. S. Krylov, A. V. Nasonov, and A. A. Chernomorets, “Combined linear resampling method with ringing control,” p. 3, 2009.
[116] J. V. Manjón, “MRI Preprocessing,” in *Imaging Biomarkers: Development and Clinical Integration*, L. Martí-Bonmatí and A. Alberich-Bayarri, Eds. Cham: Springer International Publishing, 2017, pp. 53–63. Accessed: Feb. 07, 2022. [Online]. Available: https://doi.org/10.1007/978-3-319-43504-6_5

[117] J. G. Sled, A. P. Zijdenbos, and A. C. Evans, “A nonparametric method for automatic correction of intensity nonuniformity in MRI data,” *IEEE Trans. Med. Imaging*, vol. 17, no. 1, pp. 87–97, Feb. 1998, doi: 10.1109/42.668698.
[118] J. V. Manjón, P. Coupé, L. Martí-Bonmatí, D. L. Collins, and M. Robles, “Adaptive non-local means denoising of MR images with spatially varying noise levels,” *J. Magn. Reson. Imaging*, vol. 31, no. 1, pp. 192–203, 2010, doi: 10.1002/jmri.22003.
[119] L. Henschel, S. Conjeti, S. Estrada, K. Diers, B. Fischl, and M. Reuter, “FastSurfer - A fast and accurate deep learning based neuroimaging pipeline,” *NeuroImage*, vol. 219, p. 117012, Oct. 2020, doi: 10.1016/j.neuroimage.2020.117012.
[120] J. Juan-Albarracín, E. Fuster-Garcia, G. A. García-Ferrando, and J. M. García-Gómez, “ONCOhabitats: A system for glioblastoma heterogeneity assessment through MRI,” *Int. J. Med. Inf.*, vol. 128, pp. 53–61, Aug. 2019, doi: 10.1016/j.ijmedinf.2019.05.002.
[121] A. Sotiras, C. Davatzikos, and N. Paragios, “Deformable Medical Image Registration: A Survey,” *IEEE Trans. Med. Imaging*, vol. 32, no. 7, pp. 1153–1190, Jul. 2013, doi: 10.1109/TMI.2013.2265603.
[122] S. Rit, “(Rigid/Affine) Image registration,” 2018. [Online]. Available: https://www.creatis.insa-lyon.fr/~srit/2018_miss.pdf
[123] D. Tosun-Turgut, “Rigid image registration,” *Cent. Imaging Neurodegener. Dis. Dep. Radiol. Biomed. Imaging*, 2020, Accessed: Feb. 16, 2020. [Online]. Available: https://cind.ucsf.edu/sites/cind.ucsf.edu/files/wysiwyg/education/RigidRegistration.pdf
[124] W. D. Penny, K. J. Friston, J. T. Ashburner, S. J. Kiebel, and T. E. Nichols, *Statistical parametric mapping: the analysis of functional brain images*. Elsevier, 2011.
[125] B. Landman and S. Warfield, “MICCAI 2012 workshop on multi-atlas labeling,” in *Medical image computing and computer assisted intervention conference*, 2012.
[126] J. C. Reinhold, B. E. Dewey, A. Carass, and J. L. Prince, “Evaluating the impact of intensity normalization on MR image synthesis,” in *Medical Imaging 2019: Image Processing*, Mar. 2019, vol. 10949, pp. 890–898. doi: 10.1117/12.2513089.
[127] L. G. Nyúl and J. K. Udupa, “On standardizing the MR image intensity scale,” *Magn. Reson. Med.*, vol. 42, no. 6, pp. 1072–1081, 1999, doi: 10.1002/(SICI)1522-2594(199912)42:6<1072::AID-MRM11>3.0.CO;2-M.
[128] M. Shah *et al.*, “Evaluating intensity normalization on MRIs of human brain with multiple sclerosis,” *Med. Image Anal.*, vol. 15, no. 2, pp. 267–282, Apr. 2011, doi: 10.1016/j.media.2010.12.003.
[129] J.-P. Fortin, E. M. Sweeney, J. Muschelli, C. M. Crainiceanu, and R. T. Shinohara, “Removing inter-subject technical variability in magnetic resonance imaging studies,” *NeuroImage*, vol. 132, pp. 198–212, May 2016, doi: 10.1016/j.neuroimage.2016.02.036.
[130] K. J. Gorgolewski *et al.*, “The brain imaging data structure, a format for organizing and describing outputs of neuroimaging experiments,” *Sci. Data*, vol. 3, p. 160044, Jun. 2016, doi: 10.1038/sdata.2016.44.
[131] “BIDS-Validator.” Brain Imaging Data Structure, Jun. 04, 2022. Accessed: Jun. 10, 2022. [Online]. Available: https://github.com/bids-standard/bids-validator
[132] “Data Version Control · DVC,” *Data Version Control · DVC*. https://dvc.org/ (accessed Jun. 10, 2022).
[133] W. Schroeder, K. M. Martin, and W. E. Lorensen, *The visualization toolkit (2nd ed.): an object-oriented approach to 3D graphics*. USA: Prentice-Hall, Inc., 1998.

[134] P. A. Yushkevich *et al.*, “User-guided 3D active contour segmentation of anatomical structures: Significantly improved efficiency and reliability,” *NeuroImage*, vol. 31, no. 3, pp. 1116–1128, Jul. 2006, doi: 10.1016/j.neuroimage.2006.01.015.
[135] “ITK-SNAP Home.” http://www.itksnap.org/pmwiki/pmwiki.php (accessed Dec. 01, 2022).
[136] M. McCormick, X. Liu, L. Ibanez, J. Jomier, and C. Marion, “ITK: enabling reproducible research and open science,” *Front. Neuroinformatics*, vol. 8, 2014, Accessed: Dec. 01, 2022. [Online]. Available: https://www.frontiersin.org/articles/10.3389/fninf.2014.00013
[137] P. McCarthy, “FSLeyes.” Zenodo, Aug. 31, 2022. doi: 10.5281/zenodo.7038115.
[138] M. Jenkinson, C. F. Beckmann, T. E. J. Behrens, M. W. Woolrich, and S. M. Smith, “FSL,” *NeuroImage*, vol. 62, no. 2, pp. 782–790, Aug. 2012, doi: 10.1016/j.neuroimage.2011.09.015.
[139] R. G. Van and F. Drake, “Python 3 reference manual,” *Scotts Val. CA Creat.*, vol. 10, p. 1593511, 2009.
[140] T. Kluyver *et al.*, *Jupyter Notebooks-a publishing format for reproducible computational workflows.*, vol. 2016. 2016.
[141] F. Wilcoxon, “Individual Comparisons by Ranking Methods,” *Biom. Bull.*, vol. 1, no. 6, pp. 80–83, 1945, doi: 10.2307/3001968.
[142] L. R. Dice, “Measures of the amount of ecologic association between species,” *Ecology*, vol. 26, no. 3, pp. 297–302, 1945.
[143] B. B. Avants, N. J. Tustison, G. Song, P. A. Cook, A. Klein, and J. C. Gee, “A reproducible evaluation of ANTs similarity metric performance in brain image registration,” *NeuroImage*, vol. 54, no. 3, pp. 2033–2044, Feb. 2011, doi: 10.1016/j.neuroimage.2010.09.025.
[144] B. B. Avants, C. L. Epstein, M. Grossman, and J. C. Gee, “Symmetric diffeomorphic image registration with cross-correlation: Evaluating automated labeling of elderly and neurodegenerative brain,” *Med. Image Anal.*, vol. 12, no. 1, pp. 26–41, Feb. 2008, doi: 10.1016/j.media.2007.06.004.
[145] K. P. Wilkie, “Mutual Information Based Methods to Localize Image Registration,” 2005.
[146] G. Hermosillo, C. Chefd’Hotel, and O. Faugeras, “Variational Methods for Multimodal Image Matching,” p. 15.
[147] D. G. Kleinbaum and M. Klein, *Survival analysis: a self-learning text*, vol. 3. Springer, 2012.
[148] H. Uno, T. Cai, M. J. Pencina, R. B. D’Agostino, and L. J. Wei, “On the C-statistics for Evaluating Overall Adequacy of Risk Prediction Procedures with Censored Survival Data,” *Stat. Med.*, vol. 30, no. 10, pp. 1105–1117, May 2011, doi: 10.1002/sim.4154.
[149] K. E. Emblem and A. Bjornerud, “An Automatic Procedure for Normalization of Cerebral Blood Volume Maps in Dynamic Susceptibility Contrast−Based Glioma Imaging,” *Am. J. Neuroradiol.*, vol. 30, no. 10, pp. 1929–1932, Nov. 2009, doi: 10.3174/ajnr.A1680.
[150] B. B. Avants, N. Tustison, and G. Song, “Advanced normalization tools (ANTS),” *Insight J*, vol. 2, no. 365, pp. 1–35, 2009.
[151] X. Li, P. S. Morgan, J. Ashburner, J. Smith, and C. Rorden, “The first step for neuroimaging data analysis: DICOM to NIfTI conversion,” *J. Neurosci. Methods*, vol. 264, pp. 47–56, May 2016, doi: 10.1016/j.jneumeth.2016.03.001.

[152] M. Jenkinson, P. Bannister, M. Brady, and S. Smith, “Improved Optimization for the Robust and Accurate Linear Registration and Motion Correction of Brain Images,” *NeuroImage*, vol. 17, no. 2, pp. 825–841, Oktober 2002, doi: 10.1006/nimg.2002.1132.
[153] S. M. Smith, “Fast robust automated brain extraction,” *Hum. Brain Mapp.*, vol. 17, no. 3, pp. 143–155, 2002, doi: 10.1002/hbm.10062.
[154] V. Fonov, A. Evans, R. McKinstry, C. Almli, and D. Collins, “Unbiased nonlinear average age-appropriate brain templates from birth to adulthood,” *NeuroImage*, vol. 47, p. S102, Jul. 2009, doi: 10.1016/S1053-8119(09)70884-5.
[155] V. Fonov, A. C. Evans, K. Botteron, C. R. Almli, R. C. McKinstry, and D. L. Collins, “Unbiased average age-appropriate atlases for pediatric studies,” *NeuroImage*, vol. 54, no. 1, pp. 313–327, Jan. 2011, doi: 10.1016/j.neuroimage.2010.07.033.
[156] G. E. Fasshauer, *Meshfree approximation methods with MATLAB*, vol. 6. World Scientific, 2007.
[157] G. Fasshauer, “Meshfree Approximation with Matlab - Lecture I: Introduction.” [Online]. Available: https://drna.padovauniversitypress.it/system/files/papers/Fasshauer-2008-Lecture1.pdf
[158] F. Derrien, “Strictly positive definite functions on the real line,” 2010.
[159] “Data Interpolation with Radial Basis Functions (RBFs).” http://shihchinw.github.io/2018/10/data-interpolation-with-radial-basis-functions-rbfs.html (accessed Dec. 03, 2022).
[160] H. Daniel, R. Nicolas, A. Banu, G. Ellen, and P. Rudolph, “Neuroimaging in the Browser using the X Toolkit,” *Front. Neuroinformatics*, vol. 8, 2014, doi: 10.3389/conf.fninf.2014.08.00101.
[161] J. Kybic, P. Thevenaz, A. Nirkko, and M. Unser, “Unwarping of unidirectionally distorted EPI images,” *IEEE Trans. Med. Imaging*, vol. 19, no. 2, pp. 80–93, Feb. 2000, doi: 10.1109/42.836368.
[162] M. O. Irfanoglu, L. Walker, S. Sammet, C. Pierpaoli, and R. Machiraju, “Susceptibility Distortion Correction for Echo Planar Images with Non-uniform B-Spline Grid Sampling: A Diffusion Tensor Image Study,” in *Medical Image Computing and Computer-Assisted Intervention – MICCAI 2011*, Berlin, Heidelberg, 2011, pp. 174–181. doi: 10.1007/978-3-642-23629-7_22.
[163] H. Zeng and R. T. Constable, “Image distortion correction in EPI: Comparison of field mapping with point spread function mapping,” *Magn. Reson. Med.*, vol. 48, no. 1, pp. 137–146, Jul. 2002, doi: 10.1002/mrm.10200.
[164] A. Nordio, “Correction of distortions in MR Echo Planar images using a super-resolution T2-Weighted volume,” 2019.
[165] R. C. Gonzalez and R. E. Woods, *Digital image processing*. New York, NY: Pearson, 2018.
[166] G. G. McGinley, “Magnetic Susceptibility Artefact Correction of Spin-Echo and GradientEcho EPI Images,” 2015, Accessed: Sep. 03, 2018. [Online]. Available: https://www.duo.uio.no/handle/10852/46019
[167] X. Cao, J. Fan, P. Dong, S. Ahmad, P.-T. Yap, and D. Shen, “Chapter 14 - Image registration using machine and deep learning,” in *Handbook of Medical Image Computing and Computer Assisted Intervention*, S. K. Zhou, D. Rueckert, and G. Fichtinger, Eds. Academic Press, 2020, pp. 319–342. Accessed: May 23, 2022.

[Online]. Available: https://www.sciencedirect.com/science/article/pii/B9780128161760000193
[168] M. Wang and P. Li, “A Review of Deformation Models in Medical Image Registration,” *J. Med. Biol. Eng.*, vol. 39, no. 1, pp. 1–17, Feb. 2019, doi: 10.1007/s40846-018-0390-1.
[169] B. Avants, C. L. Epstein, and J. C. Gee, “Geodesic Image Normalization in the Space of Diffeomorphisms,” presented at the 1st MICCAI Workshop on Mathematical Foundations of Computational Anatomy: Geometrical, Statistical and Registration Methods for Modeling Biological Shape Variability, Oct. 2006, pp. 125–135. Accessed: Dec. 04, 2020. [Online]. Available: https://hal.inria.fr/inria-00636082
[170] A. Klein *et al.*, “Evaluation of 14 nonlinear deformation algorithms applied to human brain MRI registration,” *NeuroImage*, vol. 46, no. 3, pp. 786–802, Jul. 2009, doi: 10.1016/j.neuroimage.2008.12.037.
[171] B. B. Avants, P. T. Schoenemann, and J. C. Gee, “Lagrangian frame diffeomorphic image registration: Morphometric comparison of human and chimpanzee cortex,” *Med. Image Anal.*, vol. 10, no. 3, pp. 397–412, Jun. 2006, doi: 10.1016/j.media.2005.03.005.
[172] P. DUPUIS, U. GRENANDER, and M. I. MILLER, “VARIATIONAL PROBLEMS ON FLOWS OF DIFFEOMORPHISMS FOR IMAGE MATCHING,” *Q. Appl. Math.*, vol. 56, no. 3, pp. 587–600, 1998.
[173] M. F. Beg, M. I. Miller, A. Trouvé, and L. Younes, “Computing Large Deformation Metric Mappings via Geodesic Flows of Diffeomorphisms,” *Int. J. Comput. Vis.*, vol. 61, no. 2, pp. 139–157, Feb. 2005, doi: 10.1023/B:VISI.0000043755.93987.aa.
[174] D. Fortun, P. Bouthemy, and C. Kervrann, “Optical flow modeling and computation: A survey,” *Comput. Vis. Image Underst.*, vol. 134, pp. 1–21, May 2015, doi: 10.1016/j.cviu.2015.02.008.
[175] G. Farnebäck, “Two-Frame Motion Estimation Based on Polynomial Expansion,” in *Image Analysis*, Berlin, Heidelberg, 2003, pp. 363–370. doi: 10.1007/3-540-45103-X_50.
[176] G. L. Besnerais and F. Champagnat, “Dense optical flow by iterative local window registration,” in *IEEE International Conference on Image Processing 2005*, Sep. 2005, vol. 1, p. I–137. doi: 10.1109/ICIP.2005.1529706.
[177] A. Wedel, T. Pock, C. Zach, H. Bischof, and D. Cremers, “An Improved Algorithm for TV-L1 Optical Flow,” in *Statistical and Geometrical Approaches to Visual Motion Analysis*, Berlin, Heidelberg, 2009, pp. 23–45. doi: 10.1007/978-3-642-03061-1_2.
[178] J. R. Hass, M. D. Weir, and G. B. Thomas Jr, *University Calculus: Early Transcendentals*. Pearson Higher Ed, 2011.
[179] T. C. Steed *et al.*, “Quantification of glioblastoma mass effect by lateral ventricle displacement,” *Sci. Rep.*, vol. 8, no. 1, p. 2827, 12 2018, doi: 10.1038/s41598-018-21147-w.
[180] S. Subramanian, A. Gholami, and G. Biros, “Simulation of glioblastoma growth using a 3D multispecies tumor model with mass effect,” *J. Math. Biol.*, vol. 79, no. 3, pp. 941–967, Aug. 2019, doi: 10.1007/s00285-019-01383-y.
[181] J. Lipková, B. Menze, B. Wiestler, P. Koumoutsakos, and J. S. Lowengrub, “Modelling glioma progression, mass effect and intracranial pressure in patient anatomy,” *J. R. Soc. Interface*, vol. 19, no. 188, p. 20210922, 2022, doi: 10.1098/rsif.2021.0922.

[182] K. Perlin, “An image synthesizer,” *ACM SIGGRAPH Comput. Graph.*, vol. 19, no. 3, pp. 287–296, Jul. 1985, doi: 10.1145/325165.325247.
[183] G. Seano *et al.*, “Solid stress in brain tumours causes neuronal loss and neurological dysfunction and can be reversed by lithium,” *Nat. Biomed. Eng.*, vol. 3, no. 3, pp. 230–245, Mar. 2019, doi: 10.1038/s41551-018-0334-7.
[184] P. Liashchynskyi and P. Liashchynskyi, “Grid Search, Random Search, Genetic Algorithm: A Big Comparison for NAS.” arXiv, Dec. 12, 2019. doi: 10.48550/arXiv.1912.06059.
[185] J. Y. Kim, M. J. Yoon, J. E. Park, E. J. Choi, J. Lee, and H. S. Kim, “Radiomics in peritumoral non-enhancing regions: fractional anisotropy and cerebral blood volume improve prediction of local progression and overall survival in patients with glioblastoma,” *Neuroradiology*, vol. 61, no. 11, pp. 1261–1272, Nov. 2019, doi: 10.1007/s00234-019-02255-4.
[186] J. Lee *et al.*, “Texture Feature Ratios from Relative CBV Maps of Perfusion MRI Are Associated with Patient Survival in Glioblastoma,” *AJNR Am. J. Neuroradiol.*, vol. 37, no. 1, pp. 37–43, Jan. 2016, doi: 10.3174/ajnr.A4534.
[187] M. Law *et al.*, “Gliomas: Predicting Time to Progression or Survival with Cerebral Blood Volume Measurements at Dynamic Susceptibility-weighted Contrast-enhanced Perfusion MR Imaging,” *Radiology*, vol. 247, no. 2, pp. 490–498, May 2008, doi: 10.1148/radiol.2472070898.
[188] J. Goldman *et al.*, “Paradoxical Association Between Relative Cerebral Blood Volume Dynamics Following Chemoradiation and Increased Progression-Free Survival in Newly Diagnosed IDH Wild-Type MGMT Promoter Methylated Glioblastoma With Measurable Disease,” *Front. Oncol.*, vol. 12, 2022, Accessed: Dec. 03, 2022. [Online]. Available: https://www.frontiersin.org/articles/10.3389/fonc.2022.849993
[189] M. Schallmo, K. B. Weldon, P. C. Burton, S. R. Sponheim, and C. A. Olman, “Assessing methods for geometric distortion compensation in 7 T gradient echo functional MRI data,” *Hum. Brain Mapp.*, vol. 42, no. 13, pp. 4205–4223, Jun. 2021, doi: 10.1002/hbm.25540.
[190] L. Ruthotto, S. Mohammadi, C. Heck, J. Modersitzki, and N. Weiskopf, “Hyperelastic Susceptibility Artifact Correction of DTI in SPM,” in *Bildverarbeitung für die Medizin 2013*, Berlin, Heidelberg, 2013, pp. 344–349. doi: 10.1007/978-3-642-36480-8_60.
[191] M. O. Irfanoglu, P. Modi, A. Nayak, E. B. Hutchinson, J. Sarlls, and C. Pierpaoli, “DR-BUDDI (Diffeomorphic Registration for Blip-Up blip-Down Diffusion Imaging) method for correcting echo planar imaging distortions,” *NeuroImage*, vol. 106, pp. 284–299, Feb. 2015, doi: 10.1016/j.neuroimage.2014.11.042.
[192] K. V. Embleton, H. A. Haroon, D. M. Morris, M. A. L. Ralph, and G. J. M. Parker, “Distortion correction for diffusion-weighted MRI tractography and fMRI in the temporal lobes,” *Hum. Brain Mapp.*, vol. 31, no. 10, pp. 1570–1587, Feb. 2010, doi: 10.1002/hbm.20959.
[193] Z. Hu *et al.*, “Distortion correction of single-shot EPI enabled by deep-learning,” *NeuroImage*, vol. 221, p. 117170, Nov. 2020, doi: 10.1016/j.neuroimage.2020.117170.
[194] S. T. M. Duong, S. L. Phung, A. Bouzerdoum, and M. M. Schira, “An unsupervised deep learning technique for susceptibility artifact correction in reversed phase-encoding EPI images,” *Magn. Reson. Imaging*, vol. 71, pp. 1–10, Sep. 2020, doi: 10.1016/j.mri.2020.04.004.

[195] A. Legouhy *et al.*, “Correction of susceptibility distortion in EPI: a semi-supervised approach with deep learning.” bioRxiv, p. 2022.07.12.499591, Jul. 13, 2022. doi: 10.1101/2022.07.12.499591.
[196] D. Wang and D. Doddrell, “Geometric Distortion in Structural Magnetic Resonance Imaging,” *Curr. Med. Imaging Rev.*, vol. 1, no. 1, pp. 49–60, Jan. 2005, doi: 10.2174/1573405052953029.
[197] P.-H. Tu, Z.-H. Liu, C.-C. Chuang, T.-C. Yang, C.-T. Wu, and S.-T. Lee, “Postoperative midline shift as secondary screening for the long-term outcomes of surgical decompression of malignant middle cerebral artery infarcts,” *J. Clin. Neurosci.*, vol. 19, no. 5, pp. 661–664, May 2012, doi: 10.1016/j.jocn.2011.07.045.
[198] R. G. Ellenbogen, L. N. Sekhar, and N. Kitchen, *Principles of Neurological Surgery E-Book*. Elsevier Health Sciences, 2017.
[199] P. A. Yushkevich, J. Pluta, H. Wang, L. E. M. Wisse, S. Das, and D. Wolk, “IC-P-174: Fast Automatic Segmentation of Hippocampal Subfields and Medial Temporal Lobe Subregions In 3 Tesla and 7 Tesla T2-Weighted MRI,” *Alzheimers Dement.*, vol. 12, no. 7S_Part_2, pp. P126–P127, 2016, doi: 10.1016/j.jalz.2016.06.205.
[200] P. Prasanna *et al.*, “Mass Effect Deformation Heterogeneity (MEDH) on Gadolinium-contrast T1-weighted MRI is associated with decreased survival in patients with right cerebral hemisphere Glioblastoma: A feasibility study,” *Sci. Rep.*, vol. 9, no. 1, p. 1145, 04 2019, doi: 10.1038/s41598-018-37615-2.
[201] M. Ismail *et al.*, “Radiomic Deformation and Textural Heterogeneity (R-DepTH) Descriptor to Characterize Tumor Field Effect: Application to Survival Prediction in Glioblastoma,” *IEEE Trans. Med. Imaging*, vol. 41, no. 7, pp. 1764–1777, Jul. 2022, doi: 10.1109/TMI.2022.3148780.
[202] X. Jiang, J. Ma, G. Xiao, Z. Shao, and X. Guo, “A review of multimodal image matching: Methods and applications,” *Inf. Fusion*, vol. 73, pp. 22–71, Sep. 2021, doi: 10.1016/j.inffus.2021.02.012.
[203] E. S. Gamburg, W. F. Regine, R. A. Patchell, J. M. Strottmann, M. Mohiuddin, and A. B. Young, “The prognostic significance of midline shift at presentation on survival in patients with glioblastoma multiforme,” *Int. J. Radiat. Oncol. Biol. Phys.*, vol. 48, no. 5, pp. 1359–1362, Dec. 2000, doi: 10.1016/s0360-3016(00)01410-3.
[204] J. Wach *et al.*, “Impact of initial midline shift in glioblastoma on survival,” *Neurosurg. Rev.*, vol. 44, no. 3, pp. 1401–1409, Jun. 2021, doi: 10.1007/s10143-020-01328-w.
[205] O. Clatz *et al.*, “Realistic Simulation of the 3D Growth of Brain Tumors in MR Images Coupling Diffusion with Biomechanical Deformation,” *Ieee Trans. Med. Imaging*, vol. 24, no. 10, pp. 1334–1346, Oct. 2005, doi: 10.1109/TMI.2005.857217.
[206] A. Elazab *et al.*, “GP-GAN: Brain tumor growth prediction using stacked 3D generative adversarial networks from longitudinal MR Images,” *Neural Netw.*, vol. 132, pp. 321–332, Dec. 2020, doi: 10.1016/j.neunet.2020.09.004.
[207] J. Petersen *et al.*, “Continuous-Time Deep Glioma Growth Models,” *ArXiv210612917 Cs Eess*, Jul. 2021, Accessed: Aug. 31, 2021. [Online]. Available: http://arxiv.org/abs/2106.12917
[208] S. Ruiz-Arrebola, D. Guirado, M. Villalobos, and A. M. Lallena, “Evaluation of Classical Mathematical Models of Tumor Growth Using an On-Lattice Agent-Based Monte Carlo Model,” *Appl. Sci.*, vol. 11, no. 11, Art. no. 11, Jan. 2021, doi: 10.3390/app11115241.

[209] S. Angeli, K. E. Emblem, P. Due-Tonnessen, and T. Stylianopoulos, “Towards patient-specific modeling of brain tumor growth and formation of secondary nodes guided by DTI-MRI,” *NeuroImage Clin.*, vol. 20, pp. 664–673, Jan. 2018, doi: 10.1016/j.nicl.2018.08.032.
[210] A. Mang, S. Bakas, S. Subramanian, C. Davatzikos, and G. Biros, “Integrated biophysical modeling and image analysis: application to neuro-oncology,” *Annu. Rev. Biomed. Eng.*, vol. 22, pp. 309–341, 2020.
[211] D. Le Bihan, E. Breton, D. Lallemand, P. Grenier, E. Cabanis, and M. Laval-Jeantet, “MR imaging of intravoxel incoherent motions: application to diffusion and perfusion in neurologic disorders.,” *Radiology*, vol. 161, no. 2, pp. 401–407, 1986.
[212] Y. Gordon *et al.*, “Dynamic contrast-enhanced magnetic resonance imaging: fundamentals and application to the evaluation of the peripheral perfusion,” *Cardiovasc. Diagn. Ther.*, vol. 4, no. 2, pp. 147–164, Apr. 2014, doi: 10.3978/j.issn.2223-3652.2014.03.01.
[213] J. Ashburner and K. J. Friston, “Unified segmentation,” *NeuroImage*, vol. 26, no. 3, pp. 839–851, Jul. 2005, doi: 10.1016/j.neuroimage.2005.02.018.
[214] J. Crinion, J. Ashburner, A. Leff, M. Brett, C. Price, and K. Friston, “Spatial normalization of lesioned brains: Performance evaluation and impact on fMRI analyses,” *Neuroimage*, vol. 37, no. 3, pp. 866–875, Sep. 2007, doi: 10.1016/j.neuroimage.2007.04.065.
[215] A. Wadhwa, A. Bhardwaj, and V. Singh Verma, “A review on brain tumor segmentation of MRI images,” *Magn. Reson. Imaging*, vol. 61, pp. 247–259, Sep. 2019, doi: 10.1016/j.mri.2019.05.043.
[216] E. S. Biratu, F. Schwenker, Y. M. Ayano, and T. G. Debelee, “A Survey of Brain Tumor Segmentation and Classification Algorithms,” *J. Imaging*, vol. 7, no. 9, Art. no. 9, Sep. 2021, doi: 10.3390/jimaging7090179.
[217] B. Fornberg and J. Zuev, “The Runge phenomenon and spatially variable shape parameters in RBF interpolation,” *Comput. Math. Appl.*, vol. 54, no. 3, pp. 379–398, Aug. 2007, doi: 10.1016/j.camwa.2007.01.028.
[218] F. Lebowsky, Y. Huang, and H. Wang, “Perceptual image quality improvement for large screen displays,” in *Human Vision and Electronic Imaging XI*, Feb. 2006, vol. 6057, pp. 203–212. doi: 10.1117/12.643207.
[219] M. Giassa, “Image Processing - Bicubic Spline Interpolation | GIASSA.NET,” Dec. 27, 2009. https://www.giassa.net/?page_id=274 (accessed Nov. 30, 2022).
[220] G. K. Rohde, A. Aldroubi, and D. M. Healy, “Interpolation Artifacts in Sub-Pixel Image Registration,” *IEEE Trans. Image Process.*, vol. 18, no. 2, pp. 333–345, Feb. 2009, doi: 10.1109/TIP.2008.2008081.
[221] M. Unser, A. Aldroubi, and M. Eden, “B-spline signal processing. I. Theory,” *IEEE Trans. Signal Process.*, vol. 41, no. 2, pp. 821–833, Feb. 1993, doi: 10.1109/78.193220.
[222] T. Magadza and S. Viriri, “Deep Learning for Brain Tumor Segmentation: A Survey of State-of-the-Art,” *J. Imaging*, vol. 7, no. 2, Art. no. 2, Feb. 2021, doi: 10.3390/jimaging7020019.
[223] C. Shorten and T. M. Khoshgoftaar, “A survey on Image Data Augmentation for Deep Learning,” *J. Big Data*, vol. 6, no. 1, p. 60, Jul. 2019, doi: 10.1186/s40537-019-0197-0.
[224] J. Nalepa, M. Marcinkiewicz, and M. Kawulok, “Data Augmentation for Brain-Tumor Segmentation: A Review,” *Front. Comput. Neurosci.*, vol. 13, 2019, Accessed: Mar. 10,

2022. [Online]. Available: https://www.frontiersin.org/article/10.3389/fncom.2019.00083
[225] P. Chlap, H. Min, N. Vandenberg, J. Dowling, L. Holloway, and A. Haworth, “A review of medical image data augmentation techniques for deep learning applications,” *J. Med. Imaging Radiat. Oncol.*, vol. 65, no. 5, pp. 545–563, 2021, doi: 10.1111/1754-9485.13261.
[226] I. S. Boon, T. P. T. Au Yong, and C. S. Boon, “Assessing the Role of Artificial Intelligence (AI) in Clinical Oncology: Utility of Machine Learning in Radiotherapy Target Volume Delineation,” *Medicines*, vol. 5, no. 4, Art. no. 4, Dec. 2018, doi: 10.3390/medicines5040131.
[227] I. Jolliffe, “Principal component analysis,” *Encycl. Stat. Behav. Sci.*, 2005.
[228] E. Plaut, “From Principal Subspaces to Principal Components with Linear Autoencoders,” *ArXiv180410253 Cs Stat*, Dec. 2018, Accessed: Sep. 21, 2021. [Online]. Available: http://arxiv.org/abs/1804.10253
[229] O. Ronneberger, P. Fischer, and T. Brox, “U-Net: Convolutional Networks for Biomedical Image Segmentation,” in *Medical Image Computing and Computer-Assisted Intervention – MICCAI 2015*, Cham, 2015, pp. 234–241. doi: 10.1007/978-3-319-24574-4_28.
[230] M. J. Prust *et al.*, “Standard chemoradiation for glioblastoma results in progressive brain volume loss,” *Neurology*, vol. 85, no. 8, pp. 683–691, Aug. 2015, doi: 10.1212/WNL.0000000000001861.
[231] K. Witzmann, F. Raschke, and E. G. C. Troost, “MR Image Changes of Normal-Appearing Brain Tissue after Radiotherapy,” *Cancers*, vol. 13, no. 7, p. 1573, Mar. 2021, doi: 10.3390/cancers13071573.
[232] W. Stacklies, H. Redestig, M. Scholz, D. Walther, and J. Selbig, “pcaMethods—a bioconductor package providing PCA methods for incomplete data,” *Bioinformatics*, vol. 23, no. 9, pp. 1164–1167, May 2007, doi: 10.1093/bioinformatics/btm069.

11. Papers

The final part of the thesis contains the three publications appended as well as their supplementary information.

I

European Journal of Radiology 132 (2020) 109278

Contents lists available at ScienceDirect

European Journal of Radiology

journal homepage: www.elsevier.com/locate/ejrad

The impact of EPI-based distortion correction of dynamic susceptibility contrast MRI on cerebral blood volume estimation in patients with glioblastoma

Ivar T. Hovden [a,*], Oliver M. Geier [a], Ingrid Digernes [a], Elies Fuster-Garcia [a], Grethe Løvland [b], Einar Vik-Mo [c], Torstein R. Meling [c,d], Kyrre E. Emblem [a]

[a] Department of Diagnostic Physics, Division of Radiology and Nuclear Medicine, Oslo University Hospital, Oslo, Norway
[b] The Intervention Centre, Oslo University Hospital, Oslo, Norway
[c] Department of Neurosurgery, Oslo University Hospital, Oslo, Norway
[d] Department of Neurosurgery, Geneva University Hospitals, Geneva, Switzerland

ARTICLE INFO

Keywords:
Echo-planar imaging
Distortion correction
Perfusion
Geometric distortions
Brain tumor
Brain regions

ABSTRACT

Purpose: Relative cerebral blood volume (rCBV) from dynamic susceptibility contrast (DSC)-MRI is a valuable biomarker in patients with glioblastoma for assessing treatment response and predicting overall survival. DSC-MRI based on echo planar images (EPI) may possess severe geometric distortions from magnetic field inhomogeneities up to the order of centimeters. The aim of this study is to assess how much two readily available EPI-based geometric distortion correction methods, FSL TOPUP and EPIC, affect rCBV values from DSC-MRI in patients with confirmed glioblastoma.

Method: We used a combined single-shot 2D gradient-echo (T2*), spin-echo (T2) EPI sequence to estimate both T2* and T2-weighted rCBV from the same contrast agent injection. Effects of distortion correction on the positive phase-encoded T2- and T2*-images were assessed in healthy anatomical brain regions in terms of Wilcoxon signed rank tests on median rCBV change and on Dice coefficients, as well as in tumor lesions in terms of Wilcoxon signed rank tests on median rCBV change.

Results: Our results show that following distortion correction, both gradient-echo and spin-echo rCBV increased in cortical areas of the frontal, temporal and occipital lobe, including the posterior orbital gyri in the frontal lobe and middle frontal gyri ($p < 0.0008$). Similar, improved Dice coefficients were observed for gradient-echo EPI in temporal, occipital and frontal lobe. Only spin-echo rCBV in enhancing lesion increased with correction ($p = 0.0002$).

Conclusion: Our study sheds light on the importance of performing geometric distortion correction on EPI-based MRI data before assessing functional information such as rCBV values. Our findings may indicate that uncorrected rCBV values can be underestimated from positive phase-encoding EPI and that geometric distortion correction is warranted when comparing EPI-based data to conventional MRI.

1. Introduction

Mapping tissue perfusion by dynamic susceptibility contrast magnetic resonance imaging (DSC-MRI) is a well-established and invasive (because of the use of an exogenous contrast agent) technique proven to give valuable information for both grading and prediction of glioma status [1,2]. DSC-MRI is typically based on low-resolution, heavily T2- or T2*-weighted images acquired during injection of a paramagnetic, gadolinium-based contrast agent. These images are used to estimate relative cerebral blood volume (rCBV) and relative cerebral blood flow (rCBF). Because fast data acquisition is required to capture the transient passage of the contrast agent (seconds), single-shot Echo-Planar Imaging (EPI) sequences are often used for DSC-MRI. However, with EPI, fast acquisition speed comes at the cost of geometric and intensity

Abbreviations: rCBV, relative Cerebral Blood Volume; rCBF, relative Cerebral Blood Flow; DSC, Dynamic Susceptibility Contrast; EPI, Echo-Planar Imaging; GE, Gradient Echo; SE, Spin Echo; FLAIR, Fluid-Attenuated Inversion Recovery; SENSE, SENSitivity Encoding; MNI, Montreal Neurological Institute; GT, Ground Truth.

* Corresponding author at: Department of Diagnostic Physics, Oslo University Hospital, Sognsvannsveien 20, 0372 Oslo, Norway.
E-mail address: ivarth@student.matnat.uio.no (I.T. Hovden).

https://doi.org/10.1016/j.ejrad.2020.109278
Received 29 June 2020; Received in revised form 2 September 2020; Accepted 7 September 2020
Available online 16 September 2020

distortions in the reconstructed image due to EPI being sensitive to magnetic field inhomogeneities caused by eddy-currents and local tissue susceptibility variations [3,4]. It is mainly along the low bandwidth phase-encoding direction that the EPI readout yields unwanted nonlinear spin dephasing effects. The results are images that may be both geometrically distorted and possess biased intensity values. These artifacts can easily lead to a centimeter or more of voxel displacement on a 3 T MRI exam [5]. Besides using alternative sequences such as multi-shot EPI or parallel acquisition methods that minimizes geometric distortionsthe most established methods for correction of geometric distortions in EPI estimates the B_0 field inhomogeneity from either multiple GE images with different echo times (field-mapping approach) or from pairs of opposite phase-encoded EPI (reverse gradient approach) [6].; DSC-MRI-based biomarkerssuch as rCBV, are typically used in combination with other higher resolution structural non-EPI images as overlays for treatment assessment, including planning of biopsies and surgery. In this context, the correction of EPI related distortions is relevant to ensure the spatial accuracy and correct EPI and rCBV values. To this end, the purpose of our study was to assess the impact of two readily available reverse gradient based EPI geometric distortion correction methods, FSL TOPUP [3] and EPIC [5], on the resulting GE and SE rCBV maps from simultaneously acquired GE-SE DSC-MRI. In a cohort of patients with newly diagnosed glioblastoma, our results identify brain regions most affected by the distortion corrections. Our study highlights the need for careful assessment when using uncorrected DSC-MRI data from these brain regions.

2. Materials and methods

2.1. Patients

The data included 45 adult glioblastoma patients (age range 40–84 years; median 61 years) imaged before first-time surgery and with histopathological diagnosis confirmation. The study was approved by the Institutional Review Board (ref: LOOPS) and the Regional Committee for Medical and Health Research Ethics (ref: 2013/1033). All patients signed a consent form before being included in the study.

2.2. MRI

All MRI exams were performed on a 3 T Philips Ingenia (Philips Healthcare, NL). DSC-MRI was acquired using GE-SE single-shot EPI sequences (GyroToolsLLC, Zürich, Switzerland). Initially, 5 time points (image volumes) were acquired with negative phase-encoding direction (pre-contrast injection), subsequently a dynamic scan of 100 time points were acquired with positive phase-encoding (during contrast injection). The image voxel resolution was 1.8 × 1.8 × 6 mm (x,y,z). The protocol included 9–11 axial slices to cover the tumor. The flip angle was 90° for the GE acquisition, followed by a 180 °SE pulse. For the positive phase-encoding scheme, a 0.1 mmol/kg body weight dose of contrast (Gadovist, Bayer Pharma AG, Germany) was injected followed by a 20 mL saline flush (BB. Melsungen AG, Melsungen, DE). All 45 GE-SE DSC-MRIs were accelerated with SENSE (factor 2), with a repetition time of TR = 1300ms or 1500 ms, echo times TE1 = 30 ms or 25 ms (GE) and TE2 = 115 ms or 105 ms (SE) and echo train length of 78. For the negative phase-encoded GE-SE EPI sequence, the total acquisition duration was ~15−22 s, for the positive phase-encoded GE-SE EPI DSC sequence it was 135−161 s. A partial Fourier acquisition of 0.61 was used. To warp a template of 66 brain regions from Montreal Neurological Institute (MNI) space to patient DSC space, we used 3D T2-weighted Fluid Attenuated Inversion Recovery (FLAIR) volumes with voxel size 0.5 × 0.49 × 0.49 mm (x,y,z), TR = 4800ms, TE = 311ms, TI = 1650ms, flip angle of 90 and pixel bandwidth around 936 Hz. T2-FLAIR volumes were used as undistorted ground truth volumes when investigating EPI distortion. Tumors were delineated based on pre- and post-gadolinium T1-weighted (voxel size 0.5 × 0.5 × 0.5 mm (x,y,z), TR = 5.2 ms, TE = 2.3 ms), as well as T2-weighted (in average; voxel size 0.3 × 0.3 × 5 mm (x,y,z), TR = 3800ms, TE = 84ms) and T2-FLAIR MRIs.

2.3. MRI pre-processing and EPI distortion correction

The T2-FLAIR data was defaced (facial structures removed) using SPM12 (Statistical Parametric Mapping; spm_deface) [7] as part of the anonymization process. The raw DICOM data were then converted to NIFTI1 format using a modified version of dcm2niix [8]. The modification was disabling dcm2niix from reorienting the images to the scanner's coordinate system during conversion. Edge-detection based head motion correction method implemented in nordicICE (v. 4.0.0, NordicNeuroLab, Bergen, Norway) was applied on the DSC data. FSL TOPUP [3] and EPIC [5] distortion correction was then performed individually on the GE and SE DSC data. TOPUP was set to scale all dynamic images to a common mean intensity, while EPIC was set to scale to a fixed intensity of 3400 (default) (Fig. 1).

2.4. DSC-MRI perfusion analysis

The rCBV maps were estimated from the area under the contrast curve from: 1) the uncorrected, 2) TOPUP-corrected, and 3) EPIC -corrected contrast enhanced DSC-MRIs in nordicICE [9] and normalized to a mean healthy white matter value. The method for healthy white matter segmentation from DSC-MRI uses k-means clustering with k = 5, including a separate pre-processing segmentation step to exclude tumor tissue from normal-appearing white matter regions [10]. To avoid additional variation in the quantification, no arterial input function was used. The data was corrected for potential positive (T2-weighted) and negative (T1-weighted) contrast agent extravasation effects [11]. See Fig. 2.

2.5. Definition of regions of interest

We used an atlas in MNI space provided by SPM12 to investigate the impact of non-corrected EPI sequences in different healthy brain regions. The original atlas was derived from the MICCAI 2012 Grand Challenge and Workshop on Multi-Atlas Labeling [12] and is based on MRI scans from the Open Access Series of Imaging Studies (OASIS) project. To increase the robustness of our results, mirrored regions from the left and right hemispheres were merged into single regions. Tumor lesions were automatically delineated using a convolutional neural network-based segmentation service called ONCOhabitats [13]. The ONCOhabitats glioblastoma service delineates the edema, necrotic, and enhancing tumor based on intra-patient pre- and post-gadolinium T1-weighted, T2-weighted and T2-FLAIR MRI exams. This service obtains a Dice of 0.92 in delineating the whole tumor region when tested over 260 cases manually segmented by experienced neuro-radiologists.

For the uncorrected, and TOPUP -and EPIC corrected DSC-MRI, we transformed the atlas and tumor lesions to DSC space in two different ways resulting in (A) undistorted ground truth (GT) brain regions and tumor lesions, and (B) EPI distorted versions.

The GT brain atlas was obtained as follows: 1) computing the nonlinear transformation of the T2-weighted 3D FLAIR image to MNI space using normalized mutual information as loss metric, 2) inverting the deformation matrix from 1), then 3) using the inverted deformation matrix to transform the atlas to T2-FLAIR space. Then, 4) rigid and affine co-registering the T2-FLAIR image to the first dynamic EPI image from the DSC-MRI and applying this transform on the atlas in T2-FLAIR space, resulted in undistorted GT atlas in DSC space. Because of the T2-weigthed DSC-MRIs, T2-FLAIR was considered as a reasonable choice for mapping between anatomical MRI and DSC-MRI.

GT tumor lesions were obtained by 1) transforming T1-weighted post contrast tumor lesions provided by ONCOHabitats to T2-FLAIR space, then following the same procedure as for the GT brain regions in step 4)

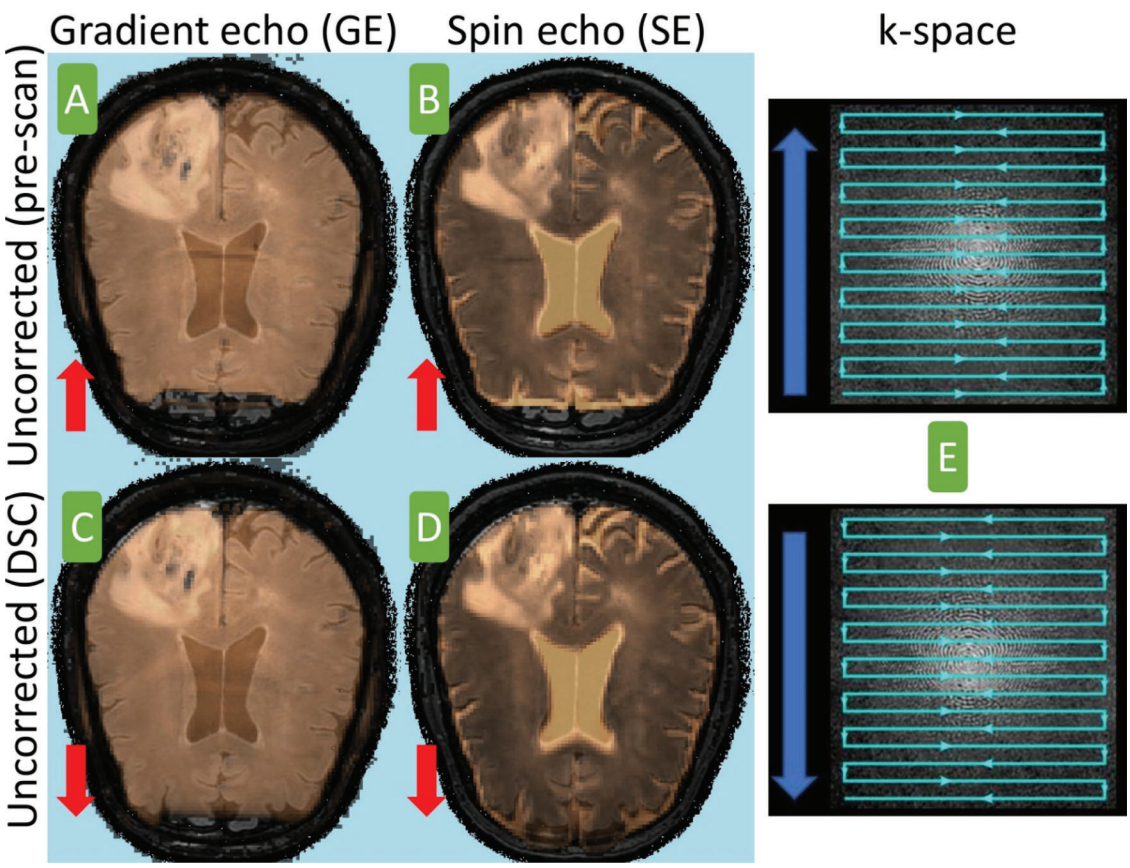

Fig. 1. Distortions in uncorrected EPI. GE and SE EPI overlaid on a T2-FLAIR MRI. A) Negative phase-encoded GE EPI, B) negative phase-encoded SE EPI, C) positive phase-encoded GE EPI, D) positive phase-encoded SE EPI, E) conceptual illustration of a negative phase-encoding image readout (top) and a positive phase-encoding image readout (bottom), respectively. Local spin compression is seen in the frontal brain (red arrows) in A) and B), whereas local spin de-compression is seen in the frontal brain in C) and D). The corresponding positive phase-encoded GE C) and SE EPI D) constitutes the original uncorrected DSC-MRI data. GE EPI contain additional signal loss in the frontal lobe.

to transform the undistorted tumor lesions in T2-FLAIR space to DSC space.

The distorted brain atlas lesions were obtained by 1) computing the nonlinear transformation of the first dynamic DSC image to MNI space using normalized mutual information as loss metric, 2) inverting the deformation matrix from 1), then 3) using the inverted deformation matrix to transform the atlas to distorted DSC space.

Distorted tumor lesions were computed like the distorted brain regions, starting with MNI tumor lesions from ONCOHabitats.

All steps were performed using SPM12 except when transforming T1-weighted post contrast tumor lesions to T2-FLAIR space where the ANTs registration suite [14] was used. K-nearest neighbor interpolation was used at all relevant steps.

The number of atlas regions in MNI space was 66. Because the axial DSC-MRI data only covered the tumor, the corresponding number of atlas regions in DSC space varied with patient. The impact of TOPUP and EPIC distortion correction on rCBV were analyzed in normal-appearing healthy regions as well as in GT necrotic, enhancing and edema tumor lesions. Healthy rCBV regions were defined as GT atlas regions in DSC space with GT necrotic, enhancing or edema tumor excluded. In short, we used the healthy GT brain regions as well as GT tumor lesions to extract median rCBV values before and after distortion correction. In order to have a representative median rCBV measure of a healthy GT brain region or tumor lesion, we required at least 70 % of the region to be covered with rCBV voxels. Moreover, GT and distorted healthy brain region pairs were used for computing Dice coefficients as described in Section 2.6.

2.6. Statistical analyses

Healthy regions with significant change in median rCBV following EPI distortion correction were detected using two-sided paired Wilcoxon signed rank tests [15]. Kernel density estimates [16] of median rCBV were used to visualize significant rCBV change. To ensure enough statistical power, only regions from which values could be extracted from at least 10 patients were included in the analysis. All tests were corrected for multiple comparisons using Bonferroni ($p < 0.05$ / number of tests). We performed the test with the same inclusion criterium and multiple comparison correction on lesion rCBV using GT necrotic, enhancing and edema tumor masks. Additionally, and regardless of rCBV, Dice coefficients [17] were computed between the GT and uncorrected, TOPUP and EPIC corrected brain template regions (covering both healthy tissue and tumor), and compared using Wilcoxon tests. For each patient and template region, we measured improvement in Dice coefficient as GT vs. corrected – GT vs. uncorrected Dice coefficient.

3. Results

The kernel density estimates of median rCBV for all regions with a significant ($p < 0.0008$) change following TOPUP and EPIC distortion correction are shown for GE rCBV in Fig. 3, and for SE rCBV in Fig. 4, respectively. Their median quartiles indicate a general *increase* in estimated rCBV after distortion correction. For lesions, only TOPUP correction of SE EPI returned significant rCBV change, which were rCBV increase in enhancing tumor lesions only (+0.03 median of medians, $p = 0.0002$). Additionally, the regions are sorted by median

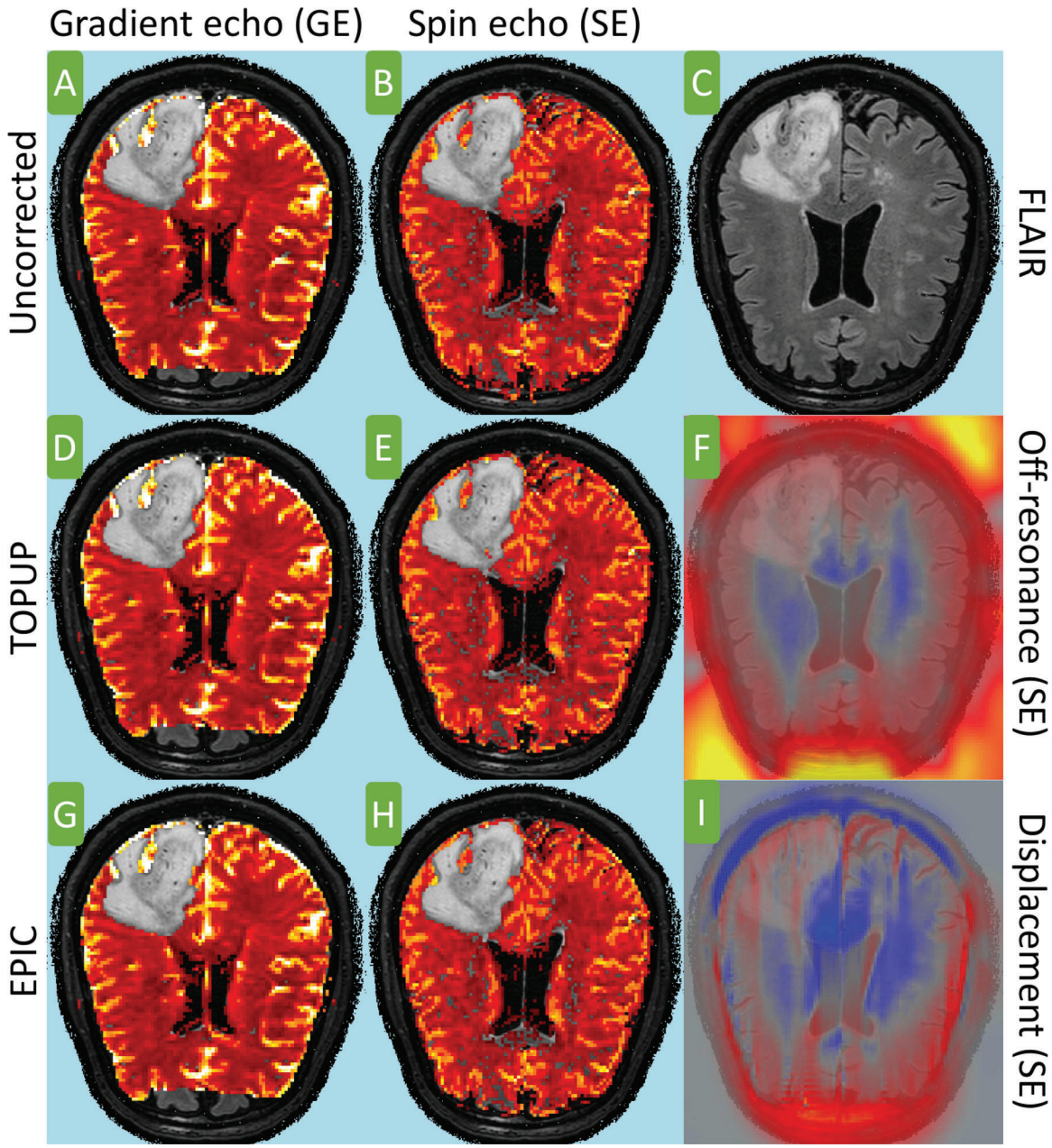

Fig. 2. rCBV estimated from A)-B) uncorrected, D)-E) TOPUP corrected, and G)-H) EPIC corrected DSC-MRI for a patient. After rCBV estimation, tumorous rCBV voxels were excluded based on ground truth tumor lesions as described in section 2.5. C) T2-FLAIR as undistorted reference image. F) TOPUP-estimated spin-echo geometric distortion in terms of spin off-resonance ([-10,10] Hz shown). I) EPIC-estimated spin-echo geometric distortion in terms of anteroposterior voxel displacement ([-10,10] mm shown). Gradient-echo versions of F) and I) were also computed but are not shown in the figure. For F) and I), blue and red illustrates negative and positive units, respectively. The window range used was [0,7] for all rCBV maps.

improvement in Dice coefficient (GT vs. corrected - GT vs. uncorrected). By comparing Figs. 3 and 4 we observe that when restricting the analysis to regions with significant rCBV increase, distortion correction of GE EPI lead to the biggest improvement in Dice coefficient. Moreover, most of the regions with improvement in Dice coefficient are in the frontal lobe. Conversely, correction of SE EPI lead to worse Dice coefficient in some cortical regions such as the occipital lobe.

Significant increase in Dice coefficients was observed for GE images in the occipital lobe (+0.2 median) and temporal lobe (+0.07 median) for TOPUP and EPIC correction, respectively ($p < 0.0007$). Neither of these regions returned significant rCBV changes and are therefore not apparent in Fig. 3. EPIC correction on SE images revealed significant decrease in the Dice coefficient in the parahippocampal gyrus (-0.06 median) and ventral diencephalon (DC) (-0.04 median) ($p < 0.0007$). The ventral DC also showed a significant decrease in rCBV for EPIC correction on SE EPI. Although TOPUP correction of SE EPI returned multiple regions with rCBV increase, no regions returned significant change in Dice coefficient.

Moreover, distortion correction of GE images returned fewer regions with increased rCBV levels (Fig. 3) compared to that of the SE images (Fig. 4), with 6 versus 10 regions for TOPUP, and 9 versus 18 regions for EPIC. The EPIC distortion correction returned a higher number of regions with rCBV change compared to the TOPUP distortion correction (27 regions versus 16 regions).

The cortical regions most affected by the distortion correction are shown in Fig. 5. While subcortical regions were also affected by the distortion correction, including the caudate nucleus and ventral diencephalon, a higher number of cortical regions was affected.

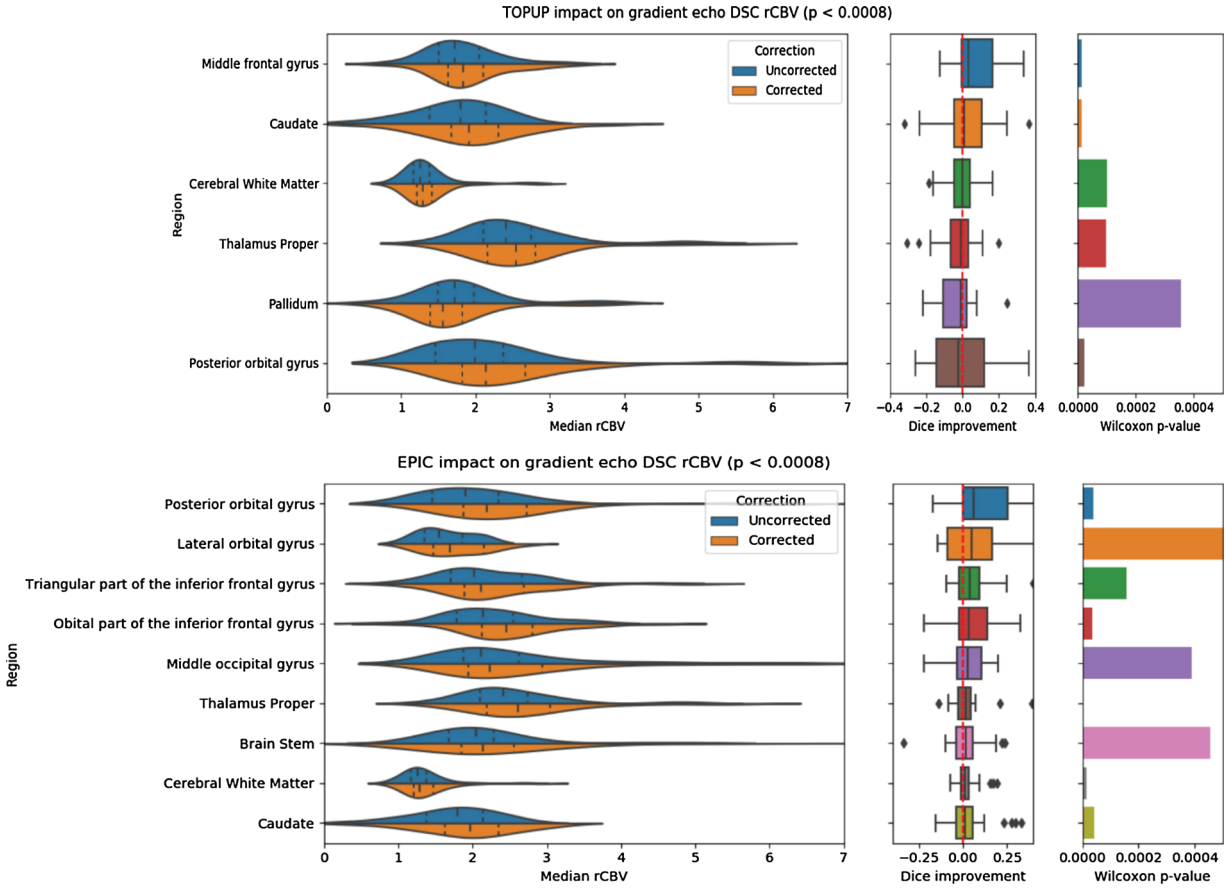

Fig. 3. Healthy brain regions with rCBV change ($p < 0.0008$) following TOPUP (top) and EPIC (bottom) distortion correction of GE EPI. In the leftmost column, distributions of median rCBV are shown for uncorrected and corrected rCBV in GT regions that experienced significant median rCBV change from correction. p-values from the Wilcoxon tests on median rCBV are shown for the individual regions in the outermost right column, while improvement in Dice coefficients are shown in the mid column. The median quartiles in the distribution plots indicate an increase in rCBV when performing EPI distortion correction. Improvement in Dice coefficient is computed as GT vs. corrected – GT vs. uncorrected Dice coefficient, as explained in Section 2.6. Lastly, the regions are sorted by decreasing Dice improvement (median). The dotted vertical red line in the mid column illustrates no Dice improvement (0).

4. Discussion

In this work, we investigated the impact of two EPI distortion correction methods, TOPUP and EPIC, on rCBV maps from pre-treatment DSC-MRIs of 45 patients with glioblastoma. Our main finding indicates that magnetic susceptibility distortions along the phase-encoding direction in positive phase-encoded EPI contribute to underestimation of rCBV values. Close to all regions with significant rCBV change after EPIC or TOPUP distortion correction constituted an apparent rCBV increase. In contrast, a negative phase-encoded EPI acquisition during the contrast injection however may return a different result which is not assessed in our study.

We investigated further how the apparent rCBV increase were related to geometric distortion in terms of Dice coefficients between rigid ground truth region masks and nonlinear distortion corrected region masks. Our findings revealed the most prominent rCBV and Dice change in cortical areas in the frontal, occipital and temporal lobes. Because most published work on clinical DSC-MRI depend on co-registration with structural MRI data, the accuracy of those findings may be challenged by the inherent geometric- and intensity distortions of the EPI acquisition. Therefore, if not corrected for, the outlining of pathologic signal on structural MRIs may simply not correspond to the aligned rCBV data.

Establishing the impact of EPI corrections in tumors may be as relevant as in healthy tissue when relying on rCBV aligned to structural images for treatment assessment. A glioblastoma located in the temporal lobe, or occipital lobe, have been previously associated with positive survival outcome compared to having a glioblastoma in the frontal or parietal lobe [18]. Another study reported that glioblastomas located in the middle (medial) temporal lobe tend to invade toward the temporal stem, insula, and basal ganglia [19]. Worse health-related quality of life (HRQoL) have been associated with motor-related regions such as the angular gyrus, than other regions [20]. Having rCBV values of a tumor involving multiple brain regions with varying degree of EPI distortion may return an artificial gradient of reduced rCBV values even within a tumor, if not corrected for. The observed increase in rCBV in only enhancing lesions, while not in necrotic or edema lesions, after TOPUP correction of SE EPI, may thus support the idea of varying degree of distortion and subsequent impact on rCBV across brain regions and tissue. Compared to that of homogenous healthy tissue however, heterogenous tumor tissue and its impact on image voxel values will probably introduce a different set of challenges from magnetic susceptibility distortions and its full assessment is warranted for future studies.

Most regions with a rCBV increase after EPI correction were cortical regions close to air-tissue transitions and thus areas with expected high B_0 field inhomogeneity caused by magnetic tissue susceptibility differences. Moreover, all cortical regions in the study with rCBV change returned a median increase in the rCBV. Hence, these findings could indicate that rCBV from DSC-MRI may be underestimated if not corrected for geometric distortions. In addition, cortical regions in the frontal lobe returned the overall biggest improvement in Dice coefficients for GE EPI. This may indicate that frontal cortical regions have

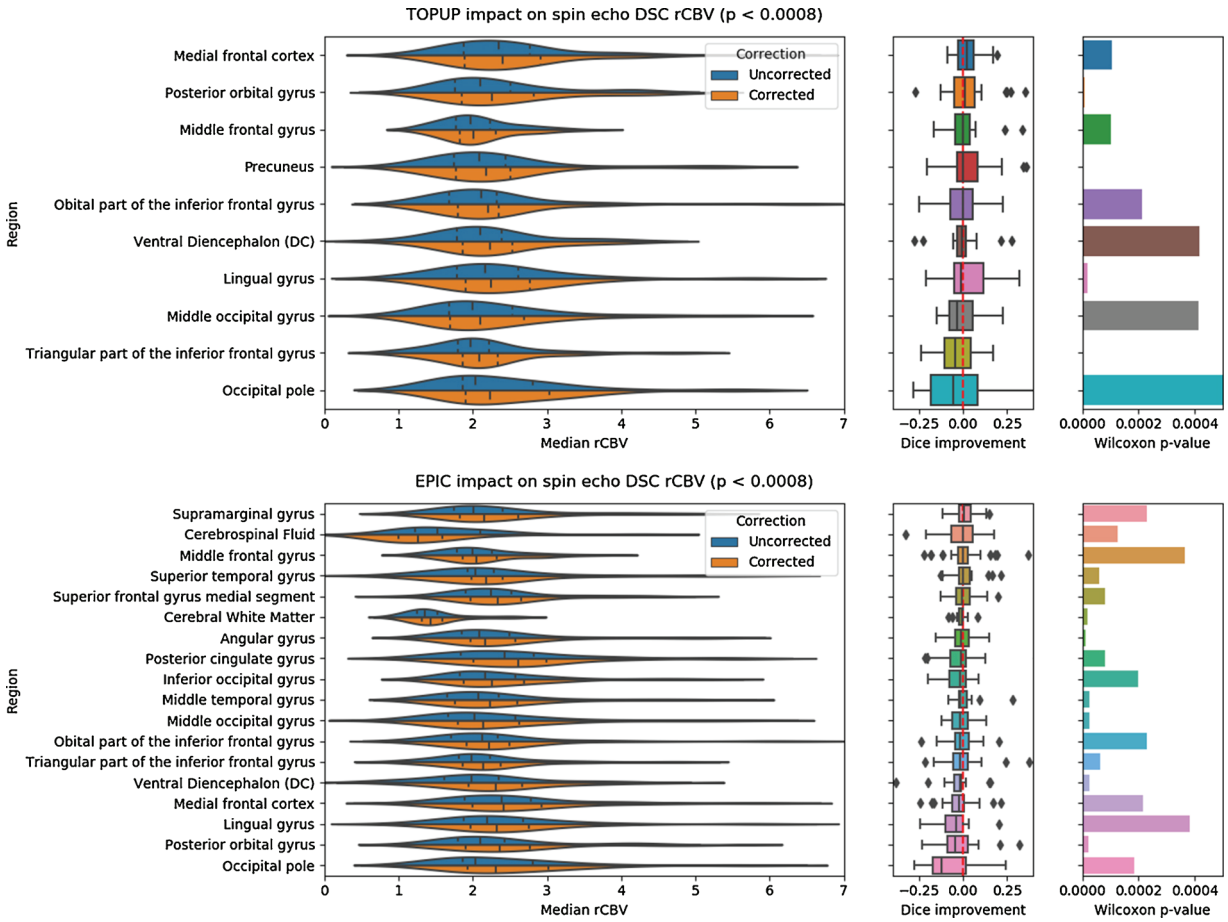

Fig. 4. Healthy brain regions with rCBV change ($p < 0.0008$) following TOPUP (top) and EPIC (bottom) distortion correction of SE EPI sorted by increasing Dice coefficient. In the leftmost column, distributions of median rCBV are shown for uncorrected and corrected rCBV in GT regions that experienced significant median rCBV change from correction. p-values from the Wilcoxon tests on median rCBV are shown for the individual regions in the outermost right column, while improvement in Dice coefficients are shown in the mid column. Also, for SE EPI, the median quartiles in the distribution plots indicate an increase in rCBV when performing EPI distortion correction. Improvement in Dice coefficient is computed as GT vs. corrected – GT vs. uncorrected Dice coefficient, as explained in Section 2.6. Lastly, the regions are sorted by decreasing Dice improvement (median). The dotted vertical red line in the mid column illustrates no Dice improvement (0).

the biggest impact of geometric distortion corrections.

This study investigated two different EPI correction methods, TOPUP and EPIC. Compared to EPIC, TOPUP relies on a strict modeling approach of the inhomogeneity field using discrete cosine basis functions [3]. In contradistinction, EPIC directly estimates image pixel displacements along the phase-encoding direction (Holland et al., 2010). For this reason and based on our observations, TOPUP may better preserve edges in the images, while EPIC tends to introduce image blurring. The result of the analysis of lesion rCBV change could indicate that TOPUP correction of SE EPI results in the most uniform correction across the brain, when compared to TOPUP correction of GE EPI and EPIC correction of GE and SE EPI. For some patients, EPIC corrected EPI depicted artefacts that may be caused by iterative blurring from increasingly smaller gaussian widths [5]. These artefacts were apparent during the processing of the opposite phase-encoded EPI pairs and visible around sharp spatial edges. The most prominent area for this artifact appeared in CSF regions superior to the cerebellum. The different ordering of significant regions between TOPUP and EPIC based on Dice improvement may reflect different degrees blurring between the methods.

The TOPUP and EPIC correction methods were originally based on SE EPI. The original method articles suggest a possible application on GE EPI given the fundamental cause of EPI-based geometric distortions are the same for SE and GE EPI [3,5]. In terms of rCBV change, we observed a higher number of regions affected by distortion correction for SE EPI. Moreover, only TOPUP SE EPI correction caused a significant lesion rCBV change. However, Dice improvement was most prevalent when correcting GE EPI. Signal loss in the frontal cortex could affect the results of the GE EPI corrections leading to fewer frontal areas available for analysis compared to that of SE-based EPI. We performed the EPI corrections separately in the GE and SE EPI to allow for T2*- and T2-weighted signal variations, respectively. If distinguishing between T2*- and T2-weighted signal variations is not important, an improved correction of GE EPI could potentially use the estimated off-resonance field (spline coefficients and movement parameters) or displacement field from the SE EPI counterparts for GE correction, for TOPUP and EPIC, respectively. This way, the correction would be unaffected by GE signal dropout. However, T2*-weighting contributes to higher perfusion sensitivity in the case of GE DSC [21].

Our study has limitations. The EPI correction led to a Dice decrease in some brain regions for SE EPI, particularly in the occipital lobe. This could have various reasons. We suspect that the non-linear T2-FLAIR to DSC co-registration could introduce unwanted morphological differences between the GT and corrected regions that are not manifested in geometric EPI distortions. Another reason could be unwanted translation and rotation from the rigid and affine co-registration from T2-FLAIR to DSC space when obtaining GT regions. We observed some misalignment along the lateral axis (pitch rotation) as well as some size shrinkage of GT regions when compared to uncorrected and corrected regions. A more direct approach to measure Dice improvement would be

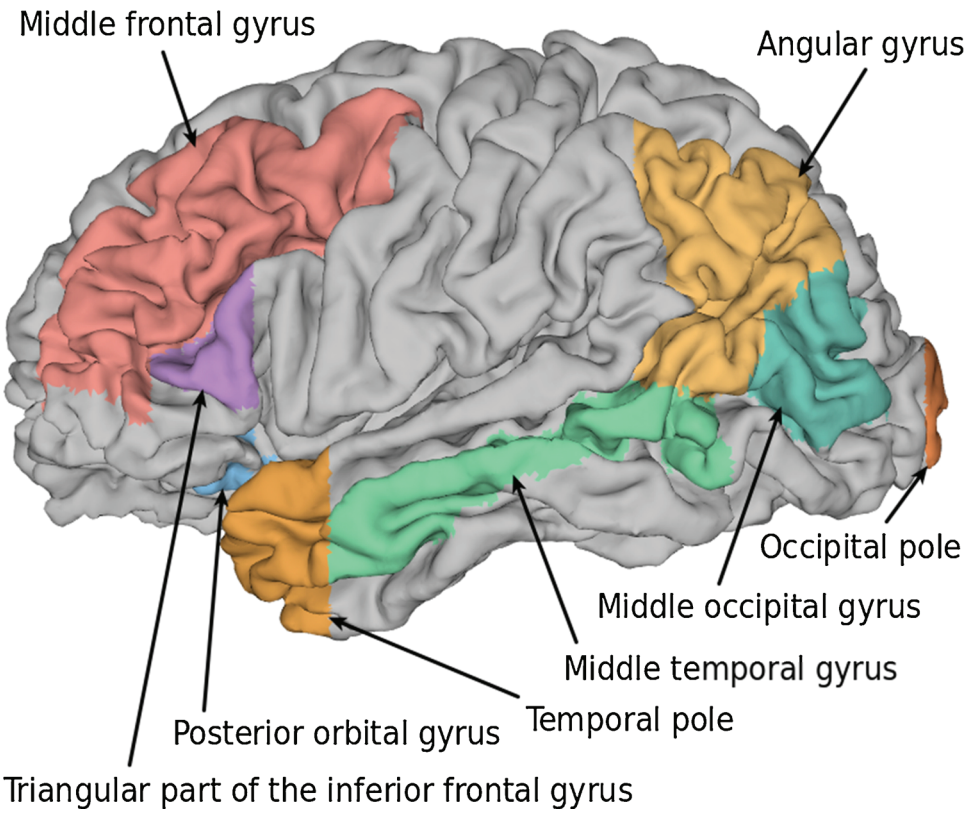

Fig. 5. Cortical regions most affected by distortion correction. Temporal and occipital lobe are affected in terms of Dice improvement for GE images ($p < 0.0007$), while the remaining regions are affected in terms of rCBV increase for both GE and SE images ($p < 0.0008$). Distortion correction leads to rCBV increase in large cortical regions in mid frontal, occipital and temporal lobe as well as in some subcortical regions as presented in the results section. Only the left side hemisphere is shown. Surface rendering provided by Neuromorphometrics, Inc. (https://scalablebrainatlas.incf.org/human/NMM1103).

to apply the computed TOPUP and EPIC correction fields directly on the brain region masks. However, this would require k-nearest neighbor interpolation, which is not available in neither of the methods. Moreover, the image intensity normalization inherent in the TOPUP and EPIC routines could be a confounding factor in the observed rCBV increase. However, in theory, any image intensity differences should be removed by the white matter normalization in the perfusion analysis. Finally, DSC-MRI differs from other EPI-based techniques by the inherent temporal variations in intra- and extravascular magnetization during the contrast agent passage [22]. We only performed EPI corrections based on the geometric distortions in the first volume of each dynamic EPI readout prior to the contrast bolus, thereby ignoring possible geometric distortions caused by the contrast passage. Potential contrast agent effects on the EPI signal are also influenced by the choice of flip angle. However, this temporal effect on the observed geometric distortions are believed to be minimal [22].

5. Conclusion

In our study we highlight the importance of EPI corrections for assessment of rCBV in patients with glioblastoma. Combining high-resolution structural images with DSC-MRI may require correction of EPI-based distortions for accurate assessment of disease. Our findings indicate that multiple cortical regions in the frontal, temporal and occipital lobe, as well as some subcortical regions such as the caudate nucleus and ventral diencephalon, return an apparent increase in rCBV following distortion correction of both GE and SE DSC-MRI. If not corrected for, rCBV may be underestimated in these brain regions with potential implications for the treatment decision making process.

Author contributions statement

ITH and KEE conceived the project, ITH and KEE wrote the main manuscript text; ITH, ID, GL, EVM and TRM collected the data; ITH and EFG performed the data analysis; OMG, GL, EVM, TRM and KEE provided expertise on the neuroscience aspects of the experiments and manuscript text; GL, EVM and TRM provided information on patients characteristics; EVM, TRM and KEE supervised the project and provided guidance on experimental design, data interpretation and writing of the manuscript; all authors contributed to discussions on crucial aspects of the project and reviewed the manuscript drafts; all authors read and approved the final version of the manuscript submitted for review.

CRediT authorship contribution statement

Ivar T. Hovden: Conceptualization, Methodology, Software, Formal analysis, Data curation, Writing - original draft, Writing - review & editing, Visualization. **Oliver M. Geier:** Software, Resources, Supervision. **Ingrid Digernes:** Investigation, Data curation. **Elies Fuster-Garcia:** Methodology, Software, Data curation, Writing - review & editing, Supervision. **Grethe Løvland:** Investigation, Data curation. **Einar Vik-Mo:** Investigation. **Torstein R. Meling:** Investigation. **Kyrre E. Emblem:** Conceptualization, Methodology, Writing - original draft, Writing - review & editing, Supervision, Project administration, Funding acquisition.

Declaration of Competing Interest

Oslo University Hospital, Oslo, Norway, has received payment from NordicNeuroLab AS, Bergen, Norway for patents and/or intellectual property rights for author (KEE). The other authors have no disclosures to report. The corresponding author declares that the work described has not been previously published in a peer-reviewed journal or proceedings.

Acknowledgements

We thank the patients and their relatives for involvement in the

study. We thank Dominic Holland at *Center for Multimodal Imaging and Genetics,* University of California at San Diego, La Jolla, CA, 92037*, USA* for sharing the EPIC source code on GitHub and Trygve Hock Storås at Department of Diagnostic Physics, Oslo University Hospital, Oslo, Norway, for assessing relevant Philips Ingenia (Philips Healthcare, NL) scanner parameters. This work received funding from the <GS1>Research Council of Norway FRIPRO<GS1/><GN1>(261984)<GN1/>; <GS2>SouthEastern Norway Regional Health Authority<GS2/> ,<GN2>(2017073, 2013069)<GN2/>.<GS3>European Research Council (ERC)<GS3/>, <GS4>European Union's Horizon 2020 Programme<GS4/><GN3/> (758657-ImPRESS)<GN3//><GS5>.European Union's Horizon 2020 research and innovation Programme <GS5/><GN4>(844646)<GN4/>.

Appendix A. Supplementary data

Supplementary material related to this article can be found, in the online version, at doi:https://doi.org/10.1016/j.ejrad.2020.109278.

References

[1] M.S. Shiroishi, G. Castellazzi, J.L. Boxerman, F. D'Amore, M. Essig, T.B. Nguyen, J. M. Provenzale, D.S. Enterline, N. Anzalone, A. Dörfler, À. Rovira, M. Wintermark, M. Law, Principles of T2*-weighted dynamic susceptibility contrast MRI technique in brain tumor imaging, J. Magn. Reson. Imaging 41 (2015) 296–313, https://doi.org/10.1002/jmri.24648.

[2] J. Zhang, H. Liu, H. Tong, S. Wang, Y. Yang, G. Liu, W. Zhang, Clinical applications of contrast-enhanced perfusion MRI techniques in gliomas: recent advances and current challenges, Contrast Media Mol. Imaging (2017) (accessed August 12, 2019), https://www.hindawi.com/journals/cmmi/2017/7064120/abs/.

[3] J.L.R. Andersson, S. Skare, J. Ashburner, How to correct susceptibility distortions in spin-echo echo-planar images: application to diffusion tensor imaging, NeuroImage 20 (2003) 870–888, https://doi.org/10.1016/S1053-8119(03)00336-7.

[4] J.L.R. Andersson, S.N. Sotiropoulos, An integrated approach to correction for off-resonance effects and subject movement in diffusion MR imaging, NeuroImage 125 (2016) 1063–1078, https://doi.org/10.1016/j.neuroimage.2015.10.019.

[5] D. Holland, J.M. Kuperman, A.M. Dale, Efficient correction of inhomogeneous static magnetic field-induced distortion in echo planar imaging, Neuroimage 50 (2010) 175, https://doi.org/10.1016/j.neuroimage.2009.11.044.

[6] Y. Xiong, G. Li, E. Dai, Y. Wang, Z. Zhang, H. Guo, Distortion correction for high-resolution single-shot EPI DTI using a modified field-mapping method, NMR Biomed. 32 (2019) e4124, https://doi.org/10.1002/nbm.4124.

[7] W.D. Penny, K.J. Friston, J.T. Ashburner, S.J. Kiebel, T.E. Nichols, Statistical Parametric Mapping: the Analysis of Functional Brain Images, Elsevier, 2011.

[8] X. Li, P.S. Morgan, J. Ashburner, J. Smith, C. Rorden, The first step for neuroimaging data analysis: DICOM to NIfTI conversion, J. Neurosci. Methods 264 (2016) 47–56, https://doi.org/10.1016/j.jneumeth.2016.03.001.

[9] A. Bjørnerud, K.E. Emblem, A fully automated method for quantitative cerebral hemodynamic analysis using DSC–MRI, J. Cereb. Blood Flow Metab. 30 (2010) 1066–1078, https://doi.org/10.1038/jcbfm.2010.4.

[10] K.E. Emblem, A. Bjornerud, An automatic procedure for normalization of cerebral blood volume maps in dynamic susceptibility contrast−based glioma imaging, Am. J. Neuroradiol. 30 (2009) 1929–1932, https://doi.org/10.3174/ajnr.A1680.

[11] J.L. Boxerman, K.M. Schmainda, R.M. Weisskoff, Relative cerebral blood volume maps corrected for contrast agent extravasation significantly correlate with glioma tumor grade, whereas uncorrected maps do not, Am. J. Neuroradiol. 27 (2006) 859–867.

[12] B. Landman, S. Warfield, MICCAI 2012 workshop on multi-atlas labeling, Medical Image Computing and Computer Assisted Intervention Conference (2012).

[13] J. Juan-Albarracín, E. Fuster-Garcia, G.A. García-Ferrando, J.M. García-Gómez, ONCOhabitats: A system for glioblastoma heterogeneity assessment through MRI, Int. J. Med. Inform. 128 (2019) 53–61, https://doi.org/10.1016/j.ijmedinf.2019.05.002.

[14] B.B. Avants, C.L. Epstein, M. Grossman, J.C. Gee, Symmetric diffeomorphic image registration with cross-correlation: evaluating automated labeling of elderly and neurodegenerative brain, Med. Image Anal. 12 (2008) 26–41, https://doi.org/10.1016/j.media.2007.06.004.

[15] F. Wilcoxon, Individual comparisons by ranking methods, Biom. Bull. 1 (1945) 80–83, https://doi.org/10.2307/3001968.

[16] E. Parzen, On estimation of a probability density function and mode, Ann. Math. Stat. 33 (1962) 1065–1076, https://doi.org/10.1214/aoms/1177704472.

[17] L.R. Dice, Measures of the amount of ecologic association between species, Ecology 26 (1945) 297–302.

[18] D. Nizamutdinov, E.M. Stock, J.A. Dandashi, E.A. Vasquez, Y. Mao, S. Dayawansa, J. Zhang, E. Wu, E. Fonkem, J.H. Huang, Prognostication of survival outcomes in patients diagnosed with glioblastoma, World Neurosurg. 109 (2018) e67–e74, https://doi.org/10.1016/j.wneu.2017.09.104.

[19] I. Shibahara, M. Hanihara, K. Miyasaka, S. Sato, T. Hide, T. Kumabe, Temporal glioblastoma mimicking basal ganglia invasion: distinguishing removable and unremovable tumors, World Neurosurg. 130 (2019) e213–e221, https://doi.org/10.1016/j.wneu.2019.06.035.

[20] L.M. Sagberg, D.H. Iversen, E.H. Fyllingen, A.S. Jakola, I. Reinertsen, O. Solheim, Brain atlas for assessing the impact of tumor location on perioperative quality of life in patients with high-grade glioma: a prospective population-based cohort study, Neuroimage Clin. 21 (2019) 101658, https://doi.org/10.1016/j.nicl.2019.101658.

[21] H. Schmiedeskamp, M. Straka, R.D. Newbould, G. Zaharchuk, J.B. Andre, J.-M. Olivot, M.E. Moseley, G.W. Albers, R. Bammer, Combined spin-and gradient-echo perfusion-weighted imaging, Magn. Reson. Med. 68 (2012) 30–40, https://doi.org/10.1002/mrm.23195.

[22] J. Vardal, R.A. Salo, C. Larsson, A.M. Dale, D. Holland, I.R. Groote, A. Bjørnerud, Correction of B0-distortions in echo-planar-imaging-based perfusion-weighted MRI, J. Magn. Reson. Imaging 39 (2014) 722–728, https://doi.org/10.1002/jmri.24213.

Data accessibility statement

The authors declare that all data supporting the findings of this study are acquired for the purpose of this study as described in the paper. Because of restrictions imposed by the administering institution concerning privacy issues of clinical data, the data cannot be made openly available at the time of publication. Instead, the datasets generated during and/or analyzed during the current study are available from the authors on request. To get access to the study data, please contract senior author Kyrre E. Emblem (Kyrre.eeg.emblem@rr-research.no at the Department of Diagnostic Physics, Oslo University Hospital, N-0027 Oslo, Norway. In order to share data, a signed copy of a standard and formal data sharing agreement between Oslo University Hospital and the third party is required.

Program code

The code and software used in this study, excluding NordicICE (NordicNeuroLab AS, Bergen, Norway) for perfusion analysis, is available at https://github.com/ivartz/epi_corrections. The commit hash 7f654ed436e7d2fbebd07748bf29e07814bd4713 marks the version of the repository at the time of publication. A Docker environment is provided for easier reproducibility of running EPIC and FSL TOPUP corrections.

II

cancers

MDPI

Article

Quantification of Tissue Compression Identifies High-Grade Glioma Patients with Reduced Survival

Elies Fuster-Garcia [1,*], Ivar Thokle Hovden [2,3], Siri Fløgstad Svensson [2,3], Christopher Larsson [4,5], Jonas Vardal [5,6], Atle Bjørnerud [3,5,7] and Kyrre E. Emblem [2]

1 Biomedical Data Science Laboratory, Instituto Universitario de Tecnologías de la Información y Comunicaciones, Universitat Politècnica de València, 46022 Valencia, Spain
2 Department of Diagnostic Physics, Oslo University Hospital, 0372 Oslo, Norway; ivarth@student.matnat.uio.no (I.T.H.); s.f.svensson@fys.uio.no (S.F.S.); kyrre.eeg.emblem@rr-research.no (K.E.E.)
3 Department of Physics, University of Oslo, 0316 Oslo, Norway; atle.bjornerud@fys.uio.no
4 Department of Neurosurgery, Oslo University Hospital, 0372 Oslo, Norway; larsch@ous-hf.no
5 Unit for Computational Radiology and Artificial Intelligence, Oslo University Hospital, 0372 Oslo, Norway; jonvar@vestreviken.no
6 Department of Radiology, Drammen Hospital, Vestre Viken Hospital Trust, 3004 Drammen, Norway
7 Department of Psychology, Faculty for Social Sciences, University of Oslo, 0851 Oslo, Norway
* Correspondence: elfusgar@upv.es

Simple Summary: A growing high-grade glioma exerts a local pressure on its surroundings, resulting in a tissue displacement known as the gross mass effect that is considered a major cause of acute neurological symptoms in patients with brain cancer. Mass effects are usually manifested when significant deformations caused by the tumor growth are observed radiologically or clinically; however, minor deformations in peritumoral tissue could provide early evidence of processes related to tumor relapse and recurrence. In this study, we propose an automated method to quantify the subtle deformations that occur in the peritumoral region. We also propose four biomarkers for differentiating where peritumoral displacements translate into compression. Biomarkers quantifying peritumoral compression were found to be associated with patient progression and prognosis and demonstrated the ability to stratify patients between long-time and short-time survivors. We conclude that compression biomarkers can be key to early treatment assessment during follow-up.

Abstract: The compression of peritumoral healthy tissue in brain tumor patients is considered a major cause of the life-threatening neurologic symptoms. Although significant deformations caused by the tumor growth can be observed radiologically, the quantification of minor tissue deformations have not been widely investigated. In this study, we propose a method to quantify subtle peritumoral deformations. A total of 127 MRI longitudinal studies from 23 patients with high-grade glioma were included. We estimate longitudinal displacement fields based on a symmetric normalization algorithm and we propose four biomarkers. We assess the interpatient and intrapatient association between proposed biomarkers and the survival based on Cox analyses, and the potential of the biomarkers to stratify patients according to their survival based on Kaplan–Meier analysis. Biomarkers show a significant intrapatient association with survival ($p < 0.05$); however, only compression biomarkers show the ability to stratify patients between those with higher and lower overall survival (AUC = 0.83, HR = 6.30, $p < 0.05$ for CompCH). The compression biomarkers present three times higher Hazard Ratios than those representing only displacement. Our study provides a robust and automated method for quantifying and delineating compression in the peritumoral area. Based on the proposed methodology, we found an association between lower compression in the peritumoral area and good prognosis in high-grade glial tumors.

Keywords: magnetic resonance imaging; high-grade glioma; longitudinal studies; compression; mass effect

Citation: Fuster-Garcia, E.; Thokle Hovden, I.; Fløgstad Svensson, S.; Larsson, C.; Vardal, J.; Bjørnerud, A.; Emblem, K.E. Quantification of Tissue Compression Identifies High-Grade Glioma Patients with Reduced Survival. *Cancers* **2022**, *14*, 1725. https://doi.org/10.3390/cancers14071725

Academic Editor: David Wong

Received: 17 February 2022
Accepted: 25 March 2022
Published: 28 March 2022

1. Introduction

High-grade brain tumors in adults are characterized by a highly infiltrative nature, cellular heterogeneity, and angiogenesis [1]. Despite advances in treatment modalities, high-grade glioma remains an incurable clinical challenge in which patient overall survival has not substantially improved in the last 20 years [2].

Owing to cancer cell proliferation and remodeling of the microenvironment [3], a growing high-grade glioma exerts a local pressure on its surroundings and results in a tissue displacement known as the gross mass effect. Mass effect is considered a major cause of acute neurological symptoms seen in patients with brain cancer [4], causing severe disability or even death, and it is a known prognostic factor for high-grade glioma [5–7]. Because the space occupied by the brain is restricted by the cranium, this pathological growth not only implies displacement, but also compression of the surrounding tissue [8]. The compression of peritumoral healthy tissue directly impacts the neurological function of the brain, psychological health, and patient quality of life [4].

Mass effects are usually manifested when significant deformations caused by the tumor growth is observed radiologically or clinically [5,9,10]. However, minor deformations in tissues close to the solid tumor mass have not been widely assessed and could provide early evidence of the processes related to tumor relapse and recurrence [11]. In vivo observations of structural displacements from tumor recurrence or growth are technically challenging, and are contingent on proper post-processing and interpretation tools. In a busy clinical workup, it is time consuming, and not technically feasible, for medical specialists to manually process longitudinal MRI exams for every single patient.

In this study, we propose an automated method for longitudinal image analysis that allows us to quantify and characterize the subtle deformations that occur in the peritumoral region. This method delineates subregions within peritumoral area that are most affected by compression phenomena (compression habitats) and quantify displacement and compression phenomena by defining four biomarkers. To study and compare the clinical relevance of these biomarkers, we assess the relationship between these biomarkers and progression status based on the RANO criteria. Moreover, we study the inter- and intrapatient association between the proposed biomarkers and the survival of high-grade glioma patients. Finally, we assess how tissue deformation may help stratify patients according to their overall survival.

Biomarkers characterizing peritumoral compression were associated with patient progression (according to RANO criteria) and patient prognosis, and demonstrated the ability to stratify patients between long-time and short-time survivors. We consider that the proposed method based on the definition of compression habitats and the quantification of the associated phenomena could provide a relevant tool for early progression assessment as well as provide key enabling information to improve monitoring of high-grade glioma patients.

2. Materials and Methods

2.1. Patient Population

Two-hundred and twenty nine MRI exams from 27 patients with histologically confirmed high-grade glioma treated at our institution were eligible for inclusion in this study [12]. Among the 27 patients, 24 were originally diagnosed as glioblastoma (3 with IDH mutation, 2 with wild-type IDH mutation, 19 with unknown IDH mutation status) based on the 2016 WHO Classification of Tumors of the Central Nervous System. The remaining 3 were diagnosed as 1 anaplastic oligodendroglioma and 2 anaplastic astrocytoma. All patients provided written informed consent before imaging and following approval from the regional ethics committee. Treatment was based on the standard protocol for adult patients with high-grade glioma as proposed by Stupp et al. [13], including surgery, followed by stereotactic radiotherapy approximately four weeks after surgery with concomitant and adjuvant chemotherapy with temozolomide for a minimum of 6 weeks. Imaging was performed immediately before the start of radio-chemotherapy, every sec-

ond week during this treatment, as well as two weeks after treatment. Imaging was then performed 2, 3, 6, and 12 months after chemotherapy initiation, and biannually afterward, until there was evidence of clinical deterioration, neurological deterioration, or death. Radiographic progression-free survival was defined as time to progressive disease according to the updated RANO criteria [14]. Three neuroradiologists (4–22 years of experience) made a consensus agreement for each patient case.

Of the 27 patients in the original cohort, 80 MR exams performed less than 30 days after the previous exam were excluded to ensure the quality in estimating deformation fields. As a result, 127 MRI longitudinal studies from 23 patients were finally included.

2.2. MRI and Lesion Segmentations

The MRI exams were performed on a 3 Tesla Philips Achieva (Philips Medical Systems, Best, The Netherlands), using an eight-channel head coil. Structural imaging included a 3D FLAIR (echo time (TE)/repetition time (TR)/inversion time (TI) (ms) = 424/8000/2400, voxel size 1.07 × 1.07 × 0.6 mm^3, matrix 224 × 224, 300 slices) and a 3D T1-weighted gradient echo before and after contrast agent injection (T1-CE, TE/TR = 2.3/5.1 ms, voxel size 1 × 1 × 1 mm^3, matrix 256 × 232, 190 slices).

Contrast-enhanced tumor and edema regions were annotated using a semi-automatic method previously described [12]. These ROIs were edited and approved by a radiologist (4 years of experience).

2.3. Biomarkers

In this study, we propose a methodology for the estimation of biomarkers consisting of the following steps: (1) image preprocessing of each MRI exam, (2) longitudinal intra-patient registration and displacement field estimation, (3) computation of displacement and divergence maps, (4) delineation of peritumoral ROI and identification of compression habitats, and (5) computation of biomarkers (see Figure 1).

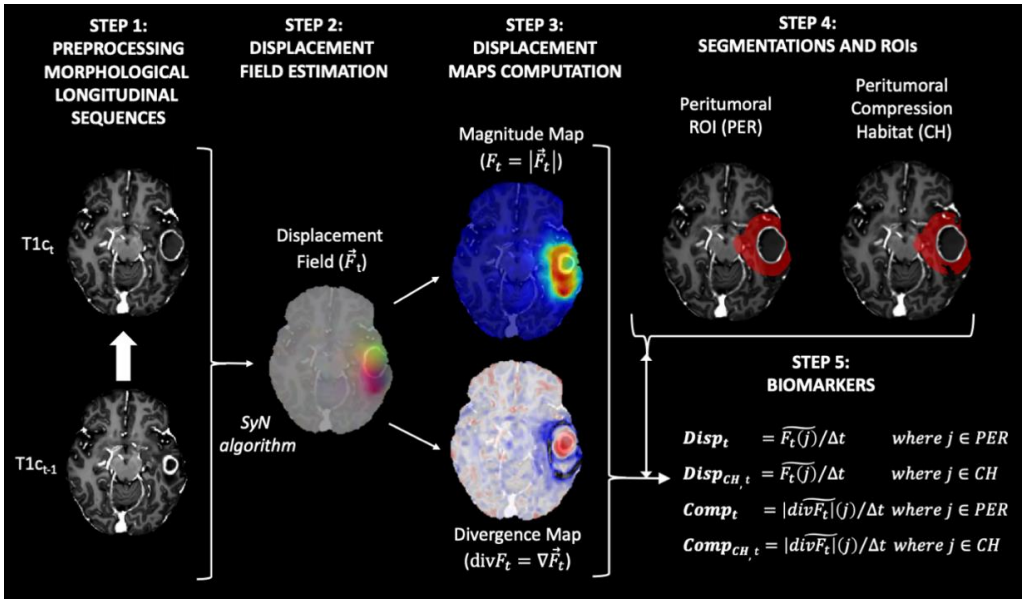

Figure 1. Diagram of the proposed method for obtaining the biomarkers proposed in our study. All maps and masks were superimposed on the T1-weighted contrast-enhanced image obtained at time t, with the exception of the maps in Step 3. In this step, the T1-weighted contrast-enhanced image obtained at time t−1 was used to improve interpretability.

Step 1 Image preprocessing of each MRI exam

Preprocessing of the structural MRI data was based on the ONCOhabitats pipeline defined in [15] and ANTs suite [16], and included the following steps: (a) voxel isotropic

resampling to $1 \times 1 \times 1$ mm^3 of all MR images using a linear interpolation, (b) denoising based on the adaptive non-local means filter, (c) rigid intrapatient registration between the different sequences, (d) affine registration to MNI space, (e) skull stripping based on convolutional neural networks, and (f) magnetic field inhomogeneity correction based on N4 algorithm.

Step 2 Longitudinal interpatient registration and displacement field estimation

All MRI exams for each patient were registered longitudinally to the patient's first longitudinal MR exam, which was used as reference. To do so, we used both rigid and affine transformations, with cross correlation as an optimization metric. After that we computed the displacement field between each contrast-enhanced T1-weighted (T1c) image and the corresponding T1c image of the previous exam. To compute the displacement field, a symmetric normalization (SyN) algorithm [16] implemented in the antsRegistration function of the ANTs suite [17] was used. The parameters used to compute the displacement field were: (1) metrics: ANTS neighborhood cross correlation; (2) transform type: SyN (gradient Step: 0.1, update Field Variance In Voxel Space = 3, total Field Variance in Voxel Space = 0); (3) convergence (iterations per level = $100 \times 70 \times 50 \times 20$, convergence Threshold = 1×10^{-6} convergence Window Size = 10; (4) shrink factors at each level: $8 \times 4 \times 2 \times 1$; (5) sigma of Gaussian smoothing at each level: $3 \times 2 \times 1 \times 0$ voxels.

The resulting displacement field represents the displacement in the three directions x, y, and z applied to each voxel to match each T1c image with their corresponding T1c image of the previous exam (see Figure 1, step 2).

Step 3 Computation of displacement and divergence maps

To transform the deformation fields into scalar maps, the magnitude (F_t) and the divergence maps (divF_t) were calculated from the deformation field ($\vec{F}_t$) (see Figure 1, step 2) as follows:

Magnitude Map $F_t = |\vec{F}_t|$.

Divergence Map $\text{div}F_t = \nabla \vec{F}_t$.

The magnitude map shows how much displacement is occurring around each voxel. In contrast, the divergence map shows the degree to which the tissue is expanding (positive divergence) or contracting (negative divergence) around each voxel.

Step 4 Delineation peritumoral ROI and identification of compression habitats

The region most affected by the mass effect produced by tumor growth is the one closest to the active tumor. This peritumoral region for each exam was defined as the segmented tumor core mask (i.e., enhancing tumor + necrosis + postsurgical cavities) obtained from the last image exam available for each patient and dilated by 2 cm, minus the tumor core mask at the current exam (see Figure 1, step 4).

In addition, we aim to assess regions where tissue displacement leads to tissue compression. For this purpose, we defined the compression habitats as the regions within the peritumoral ROI that showed a contractive behavior (i.e., present negative values in the divergence map).

Step 5 Computation of biomarkers

We propose four biomarkers to summarize the displacement and compression assessments in the peritumoral region for each MRI study:

- Displacement (Disp): median value of the magnitude map (F_t) in the peritumoral ROI.
- Displacement in the compression habitat (Disp$_{CH}$): median value of the magnitude map (F_t) in the peritumoral compression habitat.
- Compression (Comp): median absolute value of the divergence map ($divF_t$) in the peritumoral ROI.
- Compression in the compression habitat (Comp$_{CH}$): median absolute value of the divergence map ($divF_t$) in the peritumoral compression habitat.

To avoid biases due to different time intervals between MRI exams, all biomarkers were normalized by the time between the exams at timepoints t−1 and t (see Figure 1, step 1). This time between examinations is expressed in 90-day periods. In this way, the displacement values shown in mm represent the displacement caused by tumor growth during a typical follow-up period.

2.4. Statistical Analysis

We first analyzed whether the proposed biomarkers were related to the tumor progression status estimated by the RANO criteria. To do so, we compared the median values of biomarkers between progression and non-progression (including partial response, pseudo-response, and stable status) status examinations for each patient. In this way, we avoided the potential introduction of bias into the results due to the different numbers of MRI studies available for each patient. To assess the differences, we used the non-parametric Wilcoxon signed-rank test with a significance level of $p < 0.05$. Additionally, we repeated the analysis comparing all pairs of MRI studies (progressing vs. non-progressing) for each patient, instead of just the median, in order to visualize the patterns using all available data.

To analyze interpatient association between biomarkers and patient overall survival, we used uniparametric Cox Proportional-Hazards regression analyses. The biomarker value for each patient was defined as the median of all the longitudinal values available for the patient. To analyze intrapatient association between biomarkers and time-to-exitus (defined as the time from each MRI study to exitus), we used multiparametric Cox Proportional-Hazards regression analyses. To eliminate the dependency on each patient we included as binary co-variables whether each sample (i.e., biomarker value) belonged to each patient.

Additionally, we performed a Kaplan–Meier survival analysis with log-rank tests to assess differences in overall survival between patients divided by biomarker thresholds. Stratification thresholds for each biomarker were defined as those which best separated populations in terms of their C-index [18]. To avoid influence of non-representative subsets, we always ensured that the size of subpopulations was greater than 25% of the total number of cases. For censored cases, we set the date of censorship to the last date of contact with the patient or, in cases where this information was not available, the date of the last MRI exam.

All p-values were adjusted by false discovery rate (FDR) using the Benjamin and Hochberg procedure [19].

3. Results

In Figure 2A, a full longitudinal study of a patient with high-grade glioma is presented to illustrate how the magnitude maps and divergence maps characterize tumor evolution during follow-up. For this patient, changes in the divergence and magnitude maps are observed earlier than changes by traditional RANO criteria of recurrent hyperintensity in the T1-CE images as identified by the expert radiologist (see Figure 2B).

3.1. Association with Tumor Progression Based on RANO Criteria

The non-parametric Wilcoxon signed-rank paired test on the differences between median biomarkers in progressing versus non-progressing paired exams from each patient showed that all biomarkers (Disp, Disp_{CH}, Comp, Comp_{CH}) showed significantly higher values in MRI studies labeled as progressing compared those labeled as non-progressing for each patient ($p < 0.05$). These differences are more evident in the compression biomarkers (Comp, Comp_{CH}) than in the displacement biomarkers (Disp, Disp_{CH}).

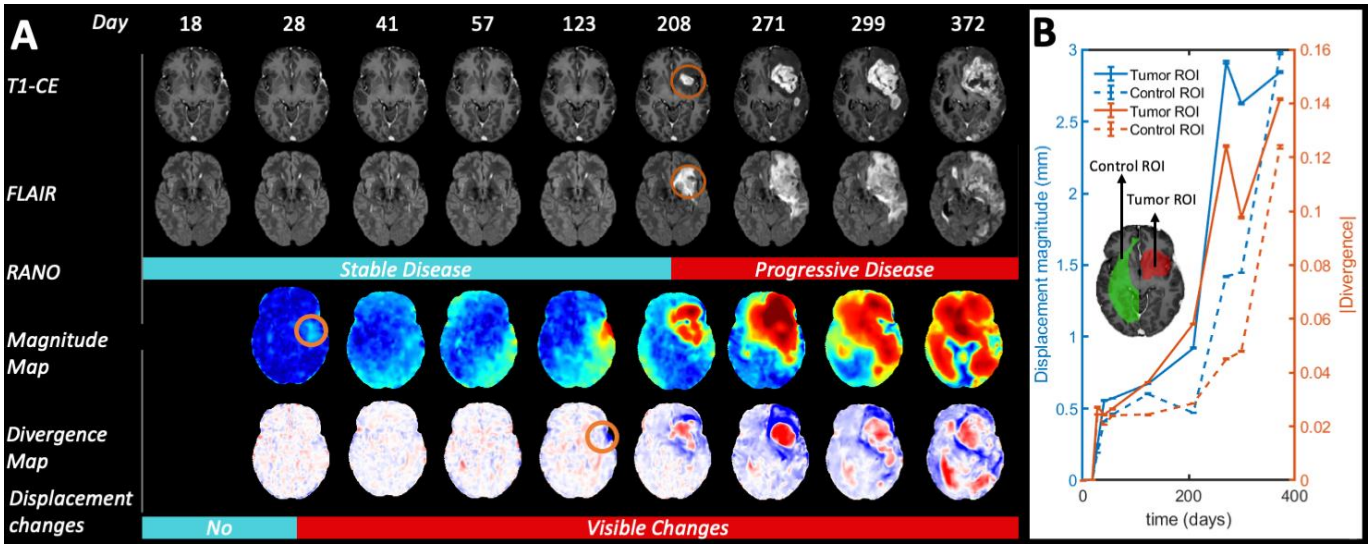

Figure 2. Longitudinal evolution of Patient 4 from day 18 after start of radio-chemotherapy treatment to day 372. For illustration purposes, we did not exclude the first MRI exams with periods shorter 30 days from the previous one in this figure, as described in the inclusion criteria for the rest of the statistical analysis. (**A**) According to RANO criteria, tumor progression started on day 208. However, the displacement maps show significant deformations already at day 28. Circles in orange highlight preliminary visual evidence of tumor growth. (**B**) Quantification of the displacement magnitude and absolute divergence in control and tumor ROIs, respectively.

3.2. Association with Patient Overall Survival

The interpatient association between the median biomarkers and patient overall survival is presented visually in the log-plot of Figure 3A. In this figure, an inverse relationship between the values of the four biomarkers and patient overall survival is observed. Figure 3B includes not only the mean values of the biomarkers for each patient, but also the values obtained in each of the longitudinal MRI studies carried out during the patient follow-up. In contrast to Figure 3A, in Figure 3B, the concept of overall survival is replaced with time-to-exitus. The different biomarkers' colors and shapes represent data from different patients (see legend).

Results of Cox regression for both interpatient and intrapatient associations between biomarkers and patient survival are presented in Table 1. The interpatient association between biomarkers and overall patient survival is visible, especially for the compression biomarkers (Figure 3A). However, due to the low number of cases, the Cox analysis only shows a significant association for Comp and $Comp_{CH}$ before correcting p-value for FDR. The intrapatient association between biomarkers and time-to-exitus assessed by Cox analysis is significant ($p < 0.05$) for all biomarkers, even after correction for FDR. Biomarker Hazard Ratios are higher when they are calculated in the peritumoral compression habitat. In addition, Hazard Ratios are higher for compression biomarkers than for displacement biomarkers.

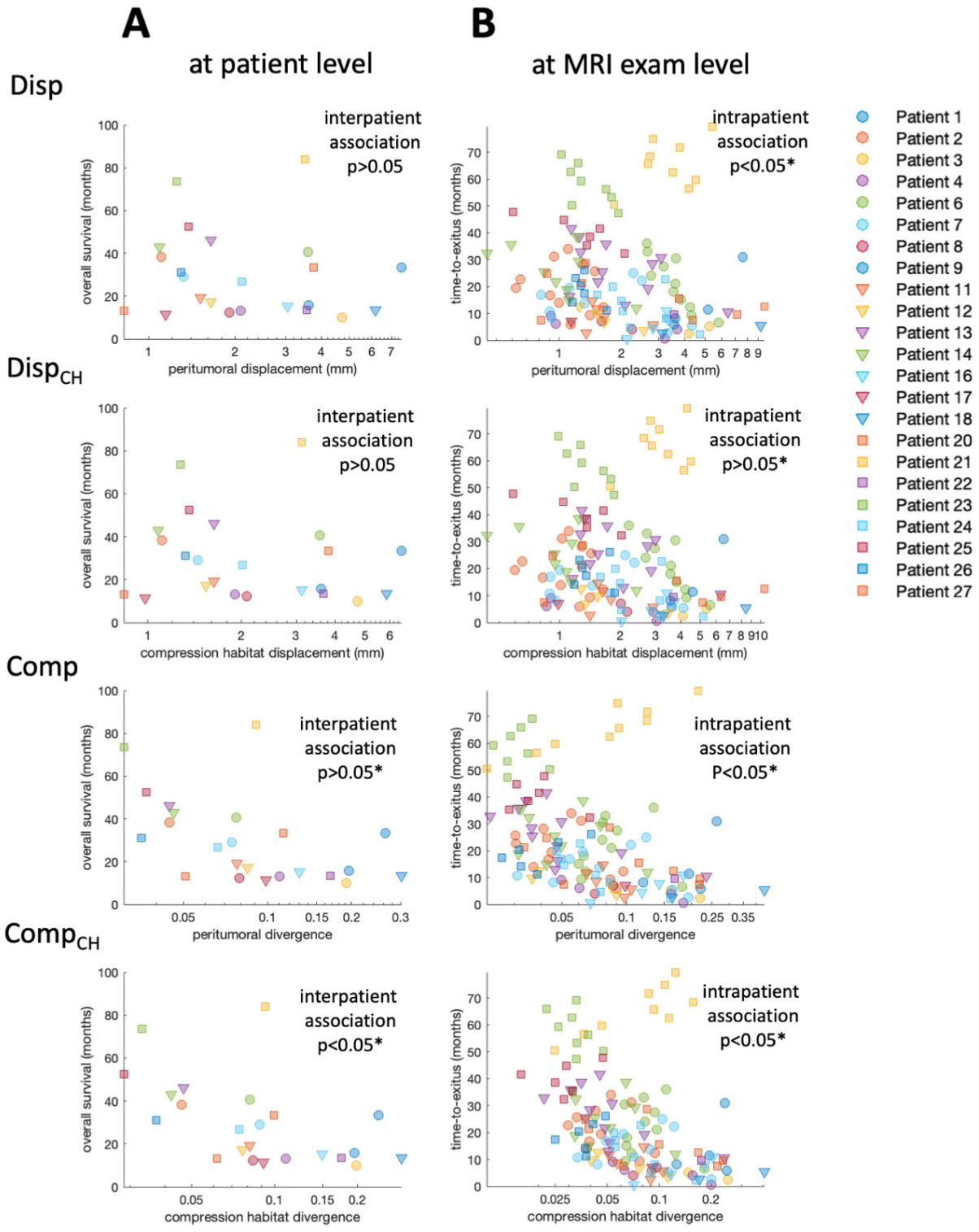

Figure 3. (**A**) Scatter plot showing the relation between median biomarker for each patient and overall survival. (**B**) Scatter plot showing the relation between biomarker for each MRI study and time-to-exitus. Each combination of marker color and shape corresponds to a different patient included in the study. * Indicates significant difference ($p < 0.05$).

Table 1. Results for the Cox regression analyses and their associations with patient prognostic. The interpatient association analysis shows the results of the uniparametric Cox regression for biomarkers to predict OS. The interpatient association analysis shows the results of the multiparametric Cox regression for biomarkers to predict OS. To eliminate the dependency on each patient, we included whether each biomarker value belonged to each patient as a binary co-variable. Asterisk * indicates significant difference ($p < 0.05$).

INTERPATIENT ASSOCIATION (n = 23 Patients)				
	Hazard Ratio [95% Conf. Interval]	**Hazard Ratio [95% Conf. Interval] Normalized Var.**	***p*-Value**	***p*-Value (FDR Adjusted)**
Disp	1.05 [0.83, 1.34]	1.43 [0.28, 7.37]	0.666	0.666
$Disp_{CH}$	1.09 [0.83, 1.44]	1.65 [0.35, 7.86]	0.527	0.666
Comp	250.27 [1.04, 6.02 $\times$ 10^4]	4.45 [1.01, 19.58]	0.048 *	0.097
$Comp_{CH}$	829.55 [2.15, 3.19 $\times$ 10^5]	5.75 [1.22, 27.10]	0.027 *	0.097
INTRAPATIENT ASSOCIATION (n = 127 MRI Exams)				
	Hazard Ratio [95% Conf. Interval]	**Hazard Ratio [95% Conf. Interval] Normalized Var.**	***p*-Value**	***p*-Value (FDR Adjusted)**
Disp	1.43 [1.20, 1.70]	26.07 [5.32, 127.83]	5.83 $\times$ 10^{-5} *	1.19 $\times$ 10^{-4} *
$Disp_{CH}$	1.39 [1.19, 1.64]	27.41 [5.44, 138.01]	5.93 $\times$ 10^{-5} *	1.19 $\times$ 10^{-4} *
Comp	3.72 $\times$ 10^4 [44.87, 3.08 $\times$ 10^7]	79.46 [4.86, 1.30 $\times$ 10^3]	0.0021 *	0.0021 *
$Comp_{CH}$	7.86 $\times$ 10^4 [1.10 $\times$ 10^2, 5.60 $\times$ 10^7]	81.40 [6.26, 1.06 $\times$ 10^3]	7.72 $\times$ 10^{-4} *	0.0010 *

3.3. Stratification Capability

The ability to stratify patients between those with higher and lower overall survival based on biomarkers is also observed to be significant ($p < 0.05$) for compression biomarkers (see Table 2 and Figure 4). Stratification based on those compression biomarkers (i.e., Comp and $Comp_{CH}$) obtains high AUC values (AUC = 0.82 and AUC = 0.83, respectively). Similarly to the results obtained in the Cox analysis, the stratification results improve when using compression biomarkers, and when the biomarkers are calculated from the values within the compression habitat.

Table 2. Results of the log-rank test of the Kaplan–Meier analysis. For each biomarker, the median OS and number of patients with high and low biomarker value are presented. Additionally, differences between OS (months), hazard ratios, area under the curve (AUC), and log-rank test resulting *p*-value are presented. * Indicates significant difference ($p < 0.05$).

	Cut-Off Threshold	**Patients per Group [Low, High]**	**AUC (C-Index)**	**Median OS per Group [Low, High]**	**Hazard Ratio [95% Conf. Interval]**	***p*-Value (Log-Rank Test)**	***p*-Value (FDR Adjusted)**
Disp	3.53	[16, 7]	0.73	[27, 16]	1.86 [0.65, 5.34]	0.250	0.250
$Disp_{CH}$	3.19	[16, 7]	0.74	[27, 16]	1.86 [0.65, 5.34]	0.250	0.250
Comp	0.09	[14, 9]	0.82	[31, 14]	5.33 [1.69, 16.80]	0.004 *	0.012 *
$Comp_{CH}$	0.10	[16, 7]	0.83	[31, 14]	6.30 [1.69, 23.42]	0.006 *	0.012 *

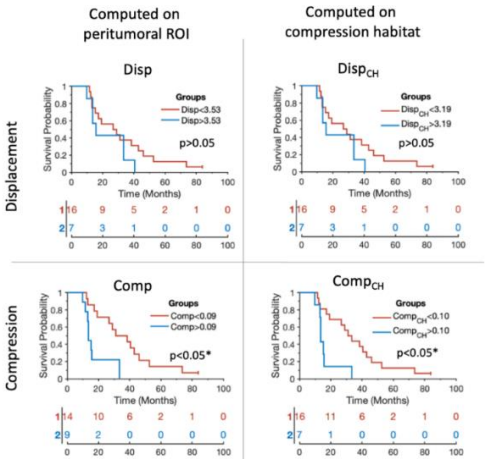

Figure 4. Kaplan–Meier plots showing the stratification capability of the median biomarkers proposed for each of the patients included in the study. Blue lines represent the patients showing higher tumor mass effect according to each of the biomarkers. Red lines represent the patients showing lower tumor mass effect according to each of the biomarkers. The x axes represent the overall survival in months. * Indicates significant difference ($p < 0.05$).

4. Discussion

The compression of peritumoral healthy tissue in brain tumor patients is considered a major cause of life-threatening neurologic symptoms [4]. Gross mass effect is usually assessed qualitatively by the treating physician, and only taken into consideration in the later stages of the disease when the deformation caused by the tumor growth is apparent and advanced. Numerous studies in the literature confirm the prognostic ability of the mass effect produced by tumor growth [5,6,20,21]. However, there are fewer studies dedicated to the quantification of these tissue displacements, and most of them are focused on the more macroscopic phenomena such as midline shift [9,10] or in the displacement of the lateral ventricles [5]. On the contrary, the quantification of minor tissue deformations and their associated compression has not been widely investigated.

In this work we proposed a methodology to automatically quantify small displacements from tumor growth. We use the information provided by nonlinear registration based on symmetric normalization algorithm to estimate the displacement field. Unlike previous work [11], we estimate the displacements with respect to a series of longitudinal MRI studies and not by a standard atlas. This allows us to monitor tumor evolution during patient follow-up. Moreover, we propose a method to characterize when and where these displacements translate into compression of tissues near the tumor (compression habitats) based on the estimation of the divergence of the displacement field. Although displacement and compression are associated phenomena, displacement observed in a region does not always imply compression in the same region. Compression in eloquent areas [22], and not just the displacement, may constitute a major impact on neurological function.

In this study, we first assessed whether the proposed biomarkers differed significantly with the progression versus non-progression status of each patient. The results show that all biomarkers had significantly higher values when the tumor was progressing than when the tumor was not progressing. In particular, the biomarkers characterizing tissue compression were differentiated between progressing and non-progressing tumor. This higher performance of the compression biomarkers may be because the divergence operation (in the basis of quantification of compression) could be more robust to suboptimal intrapatient registrations during preprocessing. That is, intrapatient rigid registration errors during preprocessing could generate a constant bias in the displacement field. This bias affects the quantification of the displacement biomarkers (as they are based on the magnitude of the displacement field), but not by the compression biomarkers (as they are based on divergence operator).

To assess the clinical relevance of the proposed biomarkers, we investigated the interpatient association between proposed biomarkers and the overall survival of each patient. To avoid introducing any bias by not having the same number of MRI scans during follow-up in each patient, the interpatient association analysis based on Cox regression was done using only one value for each patient (i.e., the median of the biomarkers over the entire follow-up). This conservative approach, together with the FDR correction, make this association non-significant in the Cox analysis. The visualization of the data shows a clear pattern between the median compression biomarkers and the overall survival. This pattern is consistent, and is even more evident if we do not use just the median value per patient, but use all available values obtained in each MRI exam acquired during the follow-up. We also analyzed the intrapatient association between biomarkers and time-to-exitus. This intrapatient association assessed by multiparametric Cox analysis is significant for all biomarkers. Analysis of the Hazard Ratios suggests that estimating biomarkers calculated in the compressed habitat rather than in the entire peritumoral area could improve the performance of these biomarkers. These results show that most of the proposed biomarkers could be relevant for monitoring the patient's evolution during follow-up and help in the estimation of prognosis. Finally, we analyzed whether the proposed biomarkers could be useful for stratifying patients according to their overall survival. The results obtained show that biomarkers based on compression characterization (i.e., Comp and $Comp_{CH}$) are able to divide the population of high and low survivors obtaining high AUC values, a substantial difference between the mean survival of both groups, and elevated Hazard Ratios. These results indicate that compression biomarkers show a stronger association with overall survival of high-grade glioma patients (interpatient variability) while displacement-based biomarkers are slightly more relevant for the study of intrapatient evolution.

Our results indicate that compression of peritumoral tissue due to tumor growth is associated with poor patient prognosis. A general trend indicates that both displacement and compression biomarkers improve their association with patient prognosis when estimated in the compression habitat. Based on these results, we consider the identification of compression habitats in the peritumoral area to improve the robustness of the biomarkers and provide valuable information to predict the effects of tumor growth. In addition, these results may indicate that compression habitats would be particularly relevant areas to examine during patient follow-up.

The methods presented in this study could be used to assess in humans the causal link between solid stress and neurological dysfunction found in recent preclinical studies [4]. Future work should use the proposed methodology and biomarkers to assess the influence of tissue compression near eloquent areas and its subsequent impact on neurological function. Additionally, future work should analyze the associations between the compression habitats and measures of mechanical stress in these regions, as obtained by magnetic resonance elastography [23–25]. This would allow us to validate the interpretation of the proposed habitats and to assess to what extent the information provided by both techniques are complementary for longitudinal monitoring of patients with high-grade gliomas. Finally, future work should evaluate the different levels of ability of the proposed markers for the assessment of early progression in compressive and infiltrative tumor phenotypes.

The relatively low number of patients included in the analysis represents a limitation of our study. However, a large number of time points (i.e., 127 MRI studies) were available for the 23 patients included. While logistically demanding, this setup allowed us to overcome the limitations of the few follow-up MRI exams that make out standard clinical diagnostic procedures. Therefore, our study provides a theoretical basis for the proposed biomarkers to be adapted in larger clinical cohorts where the number of available longitudinal examinations is restricted. Another limitation of the study is that it is hypothesized that the main contributor to tissue compression is tumor growth; nevertheless, other processes such as cystic changes, inflammation, the effects of radiotherapy, tissue relaxation after surgery, or ventricular expansion may also contribute to the observed effect. These phenomena could also contribute significantly to the value of biomarkers and should be

taken into consideration in their interpretation. In terms of the whole cohort, and despite all these confounding factors, we observed an association of the proposed biomarkers and clinical endpoints related to survival. Finally, the biomarkers proposed in this study show associations with patient survival; however, further work with larger cohorts and an independent test set are needed to confirm the possible prognostic capabilities of these markers and their ability to show the tendency for earlier recurrence.

5. Conclusions

In summary, our study provides a robust and automated quantification of compression in the peritumoral area and a methodology to assess the areas most affected by this phenomenon. Based on our proposed methodology, we found a significant association between lower compression in the peritumoral area and good prognosis for the patient. Future validation of our findings in multicenter cohorts may make this method a tool with the potential to improve the follow-up of patients with high-grade glioma.

Author Contributions: Conceptualization, E.F.-G., A.B. and K.E.E.; Data curation, C.L. and J.V.; Formal analysis, S.F.S., C.L. and J.V.; Methodology, E.F.-G.; Software, E.F.-G. and I.T.H.; Writing—original draft, E.F.-G., I.T.H., S.F.S., A.B. and K.E.E.; Writing—review & editing, E.F.-G., I.T.H., S.F.S., J.V., A.B. and K.E.E. All authors have read and agreed to the published version of the manuscript.

Funding: This work was partially supported by: The European Research Council (ERC) under the European Union's Horizon 2020 (Grant Agreement No 758657), the South-Eastern Norway Regional Health Authority Grants 2017073 and 2013069, the Research Council of Norway Grants 261984 and 325971 (K.E.E.), The European Union's Horizon 2020 research and innovation programme under the Marie Skłodowska-Curie (Grant Agreement No 844646), and South-Eastern Norway Regional Health Authority Grant 2021057 (E.F.G.).

Institutional Review Board Statement: The study was conducted in accordance with the Declaration of Helsinki and approved by the Institutional Review Board (or Ethics Committee) of Oslo University Hospital (SAILOR REC 2019/591).

Informed Consent Statement: Informed consent was obtained from all subjects involved in the study.

Data Availability Statement: The data presented in this study is available on request from the corresponding author.

Conflicts of Interest: The funders had no role in the design of the study; in the collection, analyses, or interpretation of data; in the writing of the manuscript, or in the decision to publish the results.

References

1. Wen, P.Y.; Kesari, S. Malignant Gliomas in Adults. *N. Engl. J. Med.* **2008**, *359*, 492–507. [CrossRef] [PubMed]
2. Drumm, M.R.; Dixit, K.S.; Grimm, S.; Kumthekar, P.; Lukas, R.V.; Raizer, J.J.; Stupp, R.; Chheda, M.G.; Kam, K.-L.; McCord, M.; et al. Extensive Brainstem Infiltration, Not Mass Effect, Is a Common Feature of End-Stage Cerebral Glioblastomas. *Neuro-Oncol.* **2020**, *22*, 470–479. [CrossRef] [PubMed]
3. Schiffer, D.; Annovazzi, L.; Casalone, C.; Corona, C.; Mellai, M. Glioblastoma: Microenvironment and Niche Concept. *Cancers* **2018**, *11*, 5. [CrossRef] [PubMed]
4. Seano, G.; Nia, H.T.; Emblem, K.E.; Datta, M.; Ren, J.; Krishnan, S.; Kloepper, J.; Pinho, M.C.; Ho, W.W.; Ghosh, M.; et al. Solid Stress in Brain Tumours Causes Neuronal Loss and Neurological Dysfunction and Can Be Reversed by Lithium. *Nat. Biomed. Eng.* **2019**, *3*, 230–245. [CrossRef]
5. Steed, T.C.; Treiber, J.M.; Brandel, M.G.; Patel, K.S.; Dale, A.M.; Carter, B.S.; Chen, C.C. Quantification of Glioblastoma Mass Effect by Lateral Ventricle Displacement. *Sci. Rep.* **2018**, *8*, 2827. [CrossRef] [PubMed]
6. Ropper, A.H. Lateral Displacement of the Brain and Level of Consciousness in Patients with an Acute Hemispheral Mass. *N. Engl. J. Med.* **1986**, *314*, 953–958. [CrossRef]
7. Gamburg, E.S.; Regine, W.F.; Patchell, R.A.; Strottmann, J.M.; Mohiuddin, M.; Young, A.B. The Prognostic Significance of Midline Shift at Presentation on Survival in Patients with Glioblastoma Multiforme. *Int. J. Radiat. Oncol. Biol. Phys.* **2000**, *48*, 1359–1362. [CrossRef]
8. Kalli, M.; Voutouri, C.; Minia, A.; Pliaka, V.; Fotis, C.; Alexopoulos, L.G.; Stylianopoulos, T. Mechanical Compression Regulates Brain Cancer Cell Migration through MEK1/Erk1 Pathway Activation and GDF15 Expression. *Front. Oncol.* **2019**, *9*, 992. [CrossRef]

9. Wach, J.; Hamed, M.; Schuss, P.; Güresir, E.; Herrlinger, U.; Vatter, H.; Schneider, M. Impact of Initial Midline Shift in Glioblastoma on Survival. *Neurosurg. Rev.* **2021**, *44*, 1401–1409. [CrossRef]
10. Liao, C.-C.; Chen, Y.-F.; Xiao, F. Brain Midline Shift Measurement and Its Automation: A Review of Techniques and Algorithms. Available online: https://www.hindawi.com/journals/ijbi/2018/4303161/ (accessed on 19 January 2021).
11. Prasanna, P.; Mitra, J.; Beig, N.; Nayate, A.; Patel, J.; Ghose, S.; Thawani, R.; Partovi, S.; Madabhushi, A.; Tiwari, P. Mass Effect Deformation Heterogeneity (MEDH) on Gadolinium-Contrast T1-Weighted MRI Is Associated with Decreased Survival in Patients with Right Cerebral Hemisphere Glioblastoma: A Feasibility Study. *Sci. Rep.* **2019**, *9*, 1145. [CrossRef]
12. Larsson, C.; Groote, I.; Vardal, J.; Kleppestø, M.; Odland, A.; Brandal, P.; Due-Tønnessen, P.; Holme, S.S.; Hope, T.R.; Meling, T.R.; et al. Prediction of Survival and Progression in Glioblastoma Patients Using Temporal Perfusion Changes during Radiochemotherapy. *Magn. Reson. Imaging* **2020**, *68*, 106–112. [CrossRef] [PubMed]
13. Stupp, R.; Mason, W.P.; van den Bent, M.J.; Weller, M.; Fisher, B.; Taphoorn, M.J.B.; Belanger, K.; Brandes, A.A.; Marosi, C.; Bogdahn, U.; et al. Radiotherapy plus Concomitant and Adjuvant Temozolomide for Glioblastoma. *N. Engl. J. Med.* **2005**, *352*, 987–996. [CrossRef] [PubMed]
14. Wen, P.Y.; Macdonald, D.R.; Reardon, D.A.; Cloughesy, T.F.; Sorensen, A.G.; Galanis, E.; Degroot, J.; Wick, W.; Gilbert, M.R.; Lassman, A.B.; et al. Updated Response Assessment Criteria for High-Grade Gliomas: Response Assessment in Neuro-Oncology Working Group. *J. Clin. Oncol. Off. J. Am. Soc. Clin. Oncol.* **2010**, *28*, 1963–1972. [CrossRef]
15. Juan-Albarracín, J.; Fuster-Garcia, E.; García-Ferrando, G.A.; García-Gómez, J.M. ONCOhabitats: A System for Glioblastoma Heterogeneity Assessment through MRI. *Int. J. Med. Inf.* **2019**, *128*, 53–61. [CrossRef] [PubMed]
16. Avants, B.B.; Epstein, C.L.; Grossman, M.; Gee, J.C. Symmetric Diffeomorphic Image Registration with Cross-Correlation: Evaluating Automated Labeling of Elderly and Neurodegenerative Brain. *Med. Image Anal.* **2008**, *12*, 26–41. [CrossRef]
17. ANTs by Stnava. Available online: http://stnava.github.io/ANTs/ (accessed on 22 March 2022).
18. Hanley, J.A.; McNeil, B.J. The Meaning and Use of the Area under a Receiver Operating Characteristic (ROC) Curve. *Radiology* **1982**, *143*, 29–36. [CrossRef]
19. Benjamini, Y.; Hochberg, Y. Controlling the False Discovery Rate: A Practical and Powerful Approach to Multiple Testing. *J. R. Stat. Soc. Ser. B Methodol.* **1995**, *57*, 289–300. [CrossRef]
20. McGirt, M.J.; Mukherjee, D.; Chaichana, K.L.; Than, K.D.; Weingart, J.D.; Quinones-Hinojosa, A. Association of Surgically Acquired Motor and Language Deficits on Overall Survival after Resection of Glioblastoma Multiforme. *Neurosurgery* **2009**, *65*, 463–469; discussion 469–470. [CrossRef]
21. Chaichana, K.L.; Chaichana, K.K.; Olivi, A.; Weingart, J.D.; Bennett, R.; Brem, H.; Quiñones-Hinojosa, A. Surgical Outcomes for Older Patients with Glioblastoma Multiforme: Preoperative Factors Associated with Decreased Survival. Clinical Article. *J. Neurosurg.* **2011**, *114*, 587–594. [CrossRef]
22. Hervey-Jumper, S.L.; Berger, M.S. Introduction: Surgical Management of Eloquent Area Tumors. *Neurosurgery* **2020**, *87*, 1076–1077. [CrossRef]
23. Bunevicius, A.; Schregel, K.; Sinkus, R.; Golby, A.; Patz, S. REVIEW: MR Elastography of Brain Tumors. *NeuroImage Clin.* **2020**, *25*, 102109. [CrossRef] [PubMed]
24. Svensson, S.F.; De Arcos, J.; Darwish, O.I.; Fraser-Green, J.; Storås, T.H.; Holm, S.; Vik-Mo, E.O.; Sinkus, R.; Emblem, K.E. Robustness of MR Elastography in the Healthy Brain: Repeatability, Reliability, and Effect of Different Reconstruction Methods. *J. Magn. Reson. Imaging JMRI* **2021**, *53*, 1510–1521. [CrossRef] [PubMed]
25. Streitberger, K.-J.; Reiss-Zimmermann, M.; Freimann, F.B.; Bayerl, S.; Guo, J.; Arlt, F.; Wuerfel, J.; Braun, J.; Hoffmann, K.-T.; Sack, I. High-Resolution Mechanical Imaging of Glioblastoma by Multifrequency Magnetic Resonance Elastography. *PLoS ONE* **2014**, *9*, e110588. [CrossRef] [PubMed]

III

Title

A Parametric Evaluation of Deformable Image Registration Methods for Assessing Glioblastoma Growth

Running title

Deformable Registration in Glioblastoma

Authors

Ivar T. Hovden MS[1,3*], Elies Fuster-Garcia PhD[2], Jingpeng Li MS[3,4], Atle Bjørnerud PhD[3,4], Christopher Larsson PhD[4,5], Siri F. Svensson MS[1,3] and Kyrre E. Emblem PhD[1]

[1)]*Department of Physics and Computational Radiology, Division of Radiology and Nuclear Medicine, Oslo University Hospital, Oslo, Norway*

[2)]*Biomedical Data Science Laboratory, Instituto Universitario de Tecnologías de la Información y Comunicaciones, Universitat Politècnica de València, Valencia, Spain*

[3)]*Department of Physics, Faculty of Mathematics and Natural Sciences, University of Oslo*

[4)]*Computational Radiology & Artificial Intelligence (CRAI) Research Group, Division of Radiology and Nuclear Medicine, Oslo University Hospital, Oslo, Norway*

[5)]*The Intervention Centre, Oslo University Hospital, Oslo, Norway*

*** Corresponding author**

Ivar T. Hovden, MS.

Address: Department of Physics and Computational Radiology, Oslo University Hospital, Sognsvannsveien 20, 0372 Oslo, Norway

Email: *ivarth@student.matnat.uio.no*

Phone: +4790857292

Abstract

Background

Glioblastomas are aggressive brain tumors with poor survival prognosis of 12-15 months after diagnosis. Following surgery, inescapable tumor progression is typically associated with visible displacements of tissue on MRI.

Purpose

Tumor-induced displacement of cancerous and healthy tissue, as estimated by deformable image registration methods, may constitute a valuable biomarker in characterizing cancer progression and detecting early tumor recurrence during treatment. We have developed a dedicated deformation model of glioblastoma-induced tissue displacement to assess the accuracy of estimated tissue displacements from deformable image registration methods under different realistic scenarios.

Methods

Post-contrast T1-weighted MR scans of 27 subjects with confirmed high-grade glioma; of which 4 with WHO grade III glioma and 23 with WHO grade IV glioblastoma, were deformed into synthetic second time-point scans by our model mimicking cancer progression. Model parameters included: (a) low (3 mm) and high (8 mm) maximum tissue displacement for simulating low and high tumor mass effect, (b) a parameter for low and high tumor infiltration, and (c) no, intermediate and high tumor growth irregularity. The geometric accuracy of five well-known deformable image registration methods were assessed by estimating the respective displacements within necrotic, contrast-enhanced, and edematous tumor tissue regions.

Results

Deformations with low mass effect and high tumor infiltration were associated with significant lower displacement estimation errors for all registration methods, when compared to the alternatives of high mass effect and low tumor infiltration (7 percentage points difference in mean relative error, P<0.001). SyN ANTs with the cross-correlation

metric and Farneback optical flow performed with significantly lower errors than the other methods investigated (P<0.002).

Conclusion

Deformable image registration may provide accurate displacement estimates for characterizing highly infiltrative glioblastoma growth and recurrence with small (~3 *mm*) mass effect affecting both tumor and healthy tissue.

Keywords

glioblastoma, displacement, deformable image registration, modeling, brain cancer, mass effect, infiltration

Introduction

Glioblastoma (GBM) is the most malignant type of central nervous system tumors in adults (1). With standard treatment (2) including surgery, and adjuvant and concomitant chemoradiotherapy, the overall survival is only 12-15 months, with less than 5 % of all patients surviving 5 years after diagnosis (3–5).

Symptoms of the disease may appear as increased intracranial pressure, including headache and focal and progressive neurologic deficits (4). On contrast-enhanced T1-weighted MRI, a GBM usually presents as an irregularly shaped mass with a dense hyperintense ring of enhancement, and with a hypointense center of necrosis. The tumor may also be surrounded by vasogenic edema, hemorrhage, and ventricular and midline shifts (4,5).

In GBM patients, contralateral ventricle displacement and midline shift have been associated with decreased survival (6,7). Tumor progression may lead to displacements of tissue as a “mass effect” from neoplastic growth (6). The mass effect has also been associated with subtle displacements that are not clearly visible to an expert observer and which may be valuable assessment of early treatment response (8,9). These tumor growth patterns, as observed between two consecutive MRI scans, may be quantified by a displacement vector field of displacement vectors for each image voxel. A common term for

the techniques used to estimate these displacement fields in radiation therapy is deformable image registration (DIR) (10). DIR techniques may be broadly grouped into physical, approximation, a-priori knowledge-based and task specific models (11). Optical flow and physics-based models with diffeomorphic guarantees (topology-preserving, differentiable and invertible) are among the best performing DIR methods in the medical domain, providing both accurate local and long-range deformation estimations (11,12). Deep learning aided techniques have also been investigated for DIR tasks (13–15), challenging state-of-the-art diffeomorphic registration.

In our work, we developed a macroscopic tissue displacement model for tumor mass effect, as observed between two consecutive high-resolution structural MRI scans. We then created synthetic ground truth tissue displacement fields with known conditions for testing the performance of the current state-of-the-art DIR methods on real MRI with GBM. We assessed the tumoral per-voxel displacement error within necrotic, contrast-enhanced and edematous lesion areas of the following registration methods; (a) ANTs Symmetric image Normalization (SyN) (16) with mutual information and cross-correlation loss metrics (17), and (b) the optical flow methods Farneback (18), Lucas-Kanade (19) and TV-L1 (20). Our main findings indicate that ANTs with cross-correlation and Farneback optical flow return the best voxel image tracking accuracy in lesions, and that all registration methods achieve higher accuracy for low mass effect (3 mm displacement) compared to larger mass effect (8 mm displacement).

Materials and Method

Patient population

We included longitudinal MRI data from 27 patients with initial and histologically confirmed High-Grade Glioma (HGG) (21). The study was approved by the Institutional Review Board and the Regional Committee for Medical and Health Research Ethics (ref: 2009/1867b). Patients were included only if informed consent was signed. Twenty-three patients had GBM (WHO grade IV), while four patients had WHO grade III glioma. Owing to the retrospective nature of our study, information on the isocitrate dehydrogenease (IDH) status for the GBM patients (IDH-mutant vs. IDH-wildtype GBM) were not available at the

time of diagnosis. The patients underwent surgery and chemoradiotherapy and experienced recurrence as described elsewhere (21,22). The 27 patients had a median age of 56 years (range 32 to 68 years) at the time of diagnosis, and a female/male ratio of 7/20. Median overall survival was 19 months. For modeling, we used only a single MRI exam per patient acquired approximately one month after tumor resection and during chemoradiotherapy. Follow-up MRI exams taken two weeks later were used for visual inspection to determine reasonable simulation parameters.

MR imaging

Post-operative 3-dimensional pre- and postcontrast T1-weighted (T1w, T1wc) as well as T2-weighted (T2w) with and without Fluid Attenuated Inversion Recovery (T2w-FLAIR) MRI scans were acquired from all patients during chemoradiotherapy (21). The T1w image parameters were 1 mm^3 voxels, 2.3/5.1 *ms* TE/TR, and 8 degree flip-angle, for T2w; 1.88x1.88x4.0 *mm* voxels, 70/1349 TE/TR, 90 degree flip-angle, and lastly, for T2w-FLAIR; 1.07x1.07x0.6 *mm* voxels, 424/8000 *ms* TE/TR and 90 degree flip-angle. Acquisition times were 400, 400, 112 and 520 *s* for T1w, T1wc, T2w and T2w-FLAIR respectively. T1wc was acquired following injection of 0.1 mmol/kg of gadobutrol (Gadovist, Bayer, Sweden) and saline flush. All scans were performed on a Philips Achieva 3-Tesla system (Philips Medical Systems, Best, the Netherlands).

Preprocessing

Necrotic, edematous and contrast-enhanced tissue masks and normal-appearing brain tissue masks were delineated based on T1w, T1wc, T2w and T2w-FLAIR images using the ONCOHabitats segmentation service (23). See Figure 1 for an overview of the total lesion volumes. The MRI data was resliced to 1 mm^3 Montreal Neurological Institute (MNI) space before applying our deformation model on T1wc in to create synthetically deformed T1wc scans. The morphological segmentation service in ONCOHabitats transforms all MRI sequences to voxel-isotropic 1 mm^3 MNI space by rigid and affine registration to a nonlinear symmetric International Consortium of Brain Mapping (ICBM) MNI152 T1w template (24) using ANTs (25).

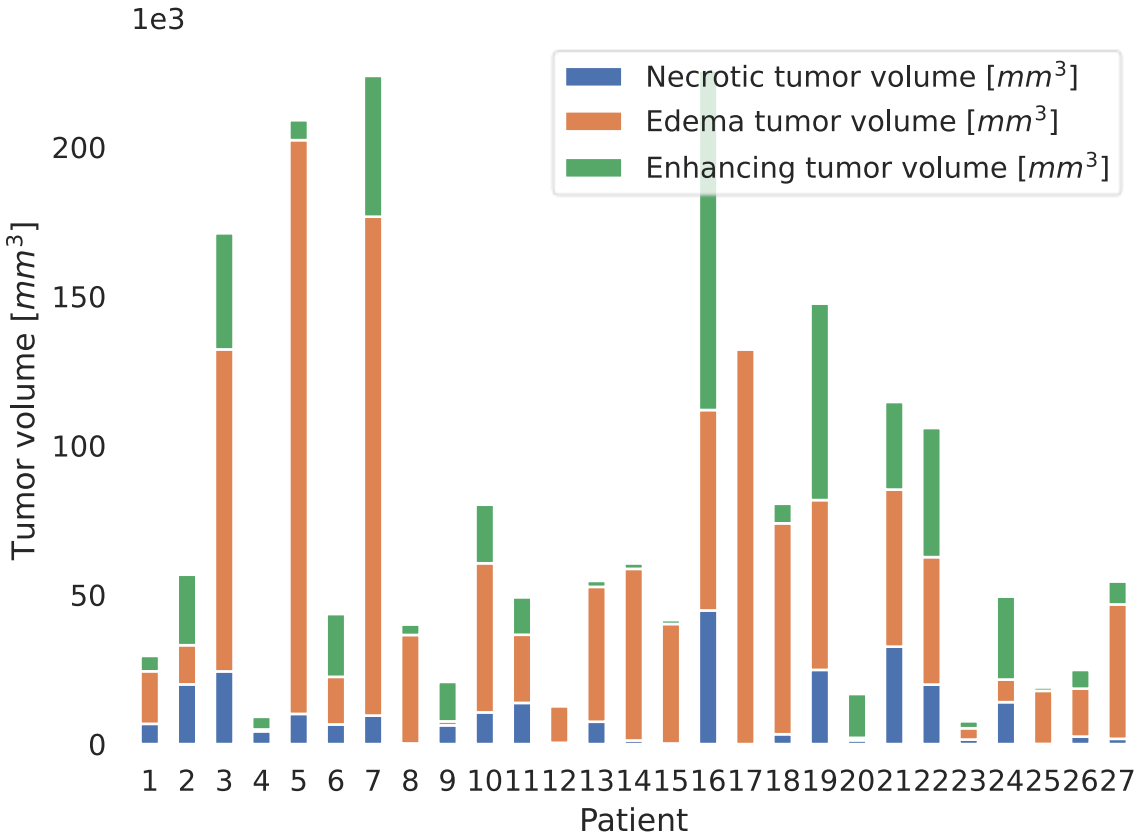

Figure 1: Variations in baseline lesion volume for the 27 patients diagnosed with HGG.

Deformation model

We developed an algorithm to synthetically deform brain tumor MRI that mimics radial pushing patterns (6) (Figure 2). The algorithm creates a 3D displacement field ($\boldsymbol{d}$) by using the information from the outlined regions-of-interest of the tumor lesion (M_l) and brain mask (M_b), merged with three simulation parameters: 1) maximum tissue displacement as a result of tumor mass effect (α $[mm]$), 2) infiltration (β), and 3) irregularity (γ), according to

$$\boldsymbol{d}(M_l, M_b, \alpha, \beta, \gamma) = \left|\alpha \cdot \boldsymbol{d}_\beta(M_l, M_b) + \boldsymbol{p}(\gamma)\right|_{M_b}$$

where $\boldsymbol{d}_\beta$ is a realistic-appearing displacement vector field constructed from lesion and brain masks and the growth infiltration parameter, $\boldsymbol{p}$ is a noise vector field and $||_{M_b}$ restricts displacement to only occur inside the brain mask. $\boldsymbol{d}_\beta$ is iteratively computed by displacing the partial derivatives of a 3D gaussian by itself. A detailed description of the algorithm is found in supplementary material.

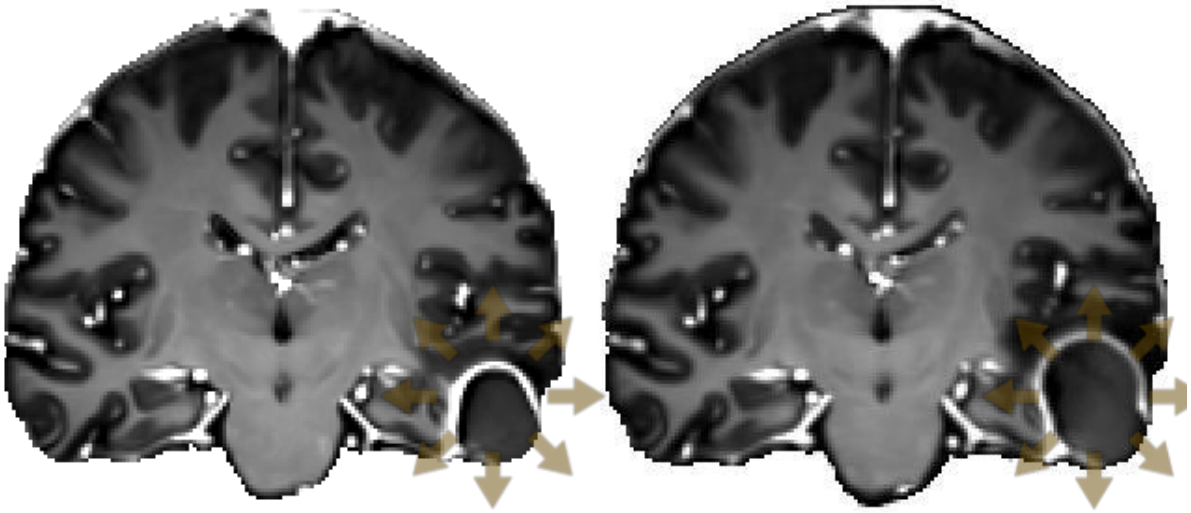

Figure 2: Example of radial pushing patterns between two consecutive real T1wc MRIs of GBM.

Simulation parameters

Infiltration was defined as a parameter ranging from 0 to 1 to control how rapid the magnitude of tissue displacement in a radial direction drops off away from the geometric center of the lesion mask. This drop follows a profile that is equal to the shape of a one-sided gaussian. At the value 0, any radial displacement profile pans across the maximum possible distance away from the lesion center ending at the brain mask edge. This models the maximum possible infiltration from growing cancer cells and is illustrated with a small drop in radial displacement. In contrast, an infiltration parameter of 1 leads to the shortest radial distance displacement profiles, which are derived directly from the 3D gaussian with dimensions equal to the edge of the lesion mask.

The maximum tissue displacement specifies the length of the largest displacement vectors in the displacement field, which are located on a surface that is dependent on the infiltration parameter. This surface could be located either inside or outside of the lesion mask. We simulated displacements using infiltration of 0.1 and 1, yielding maximum tissue displacement outside (high infiltration) and inside (low infiltration) lesion areas, respectively. The maximum tissue displacement parameter hence controls the intended tumor growth mass effect. A higher mass effect is generally associated with worse survival in GBM (6,26). Complex effects of the mass effect such as deformation heterogeneity (8)

and compression (9) may also negatively impact survival. In general practice, a midline shift above $5\ mm$ usually requires immediate surgical intervention (27,28). Based on these studies, we selected maximum tissue displacement of 3 mm and 8 mm to describe low mass effect (high survival) and high mass effect (low survival), respectively.

We modeled irregularity of tumor-induced displacements by adding continuous noise to each component of the displacement field. The noise parameter controls the spatial resolution of the noise. We modified an implementation of 3D Perlin noise (29) to only use a single irregularity parameter as input and in the range larger than 0 and less than 1, where 1 is a single spatial "wavelength" describing a single continuous "noise wave" across each spatial axis. We simulated three noise configurations: no noise (Perlin noise disabled, and nothing added to the displacement field), 0.05 (intermediate irregularity) and 0.03 (high irregularity). Figure 3 illustrates the selected parameters for mass effect, infiltration and irregularity. Table 1 gives an overview of the input data, simulation parameters and output as well as internal fixed parameters of the deformation model.

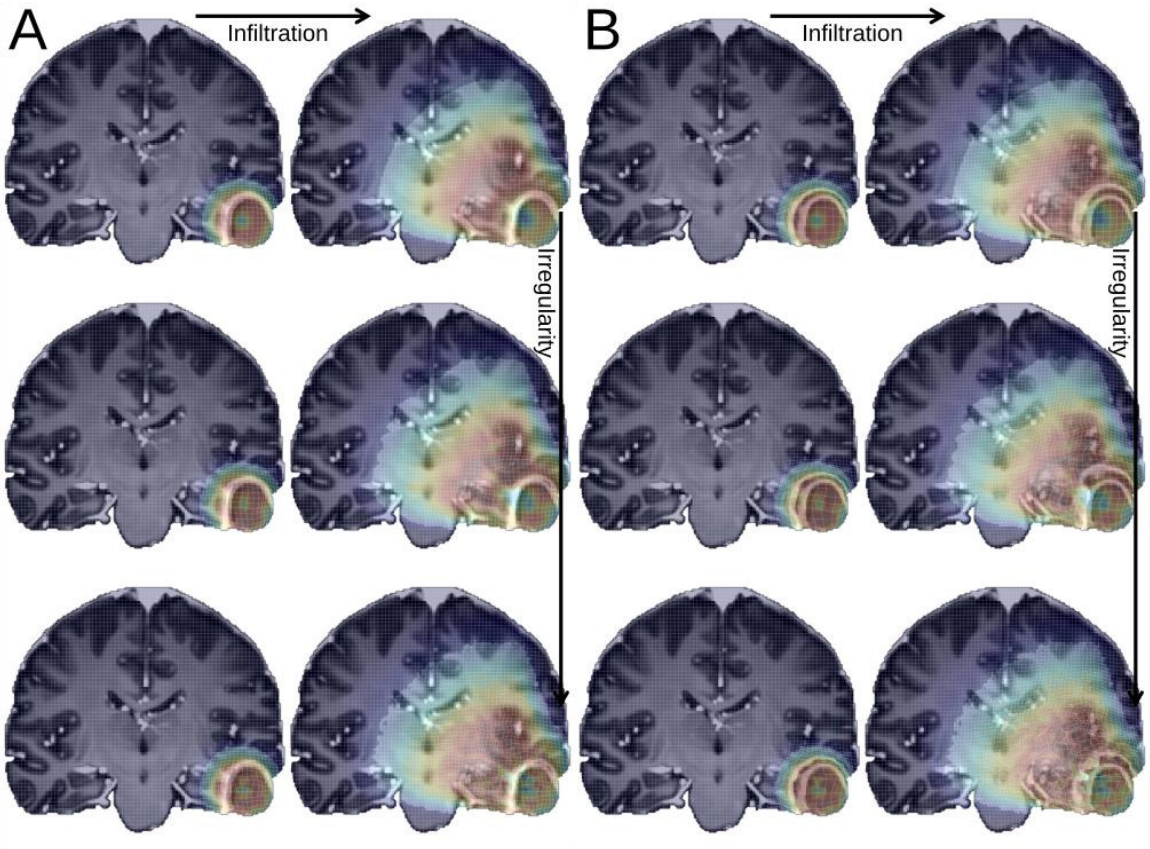

Figure 3: The deformation model applied on a real T1wc MRI with different input parameters. The resulting deformed T1wc MRI, magnitude of displacement field and

deformation grid are overlaid. A) low mass effect (3 mm maximum displacement), B) high mass effect (8 mm maximum displacement). A) and B) horizonzal: low and high infiltration, A) and B) vertical: no, intermediate and high irregularity.

Table 1: Parameters of the synthetic deformation model. Shrinkage is modeled with a negative maximum displacement $\alpha < 0$, and growth with a positive $\alpha > 0$. Only positive α was investigated in this work.

Input	Symbol	Range	Type	Description
Lesion mask	M_l	$[0,1]_2$	Binary scalar field	
Brain mask	M_b	$[0,1]_2$	Binary scalar field	
Displacement	α	$\mathbb{R}$	Scalar $[mm]$	Maximum tissue displacement (mass effect)
Infiltration	β	$[0,1]$	Scalar	Intensity decay fraction; 0: most infiltration, 1: least infiltration
Irregularity	γ	$< 0,1]$	Scalar	Perlin noise resolution; ~ 0: highest irregularity, 1: lowest irregularity
Noise	δ	$\mathbb{R}$	Scalar	Perlin noise maximum magnitude; fixed default $= 0.6$
Standard deviation	σ	$\mathbb{R}$	Scalar	Of the Gaussian; fixed default $= 5$
Number of vectors	N_s	$[1, N]$	Integer	Number of directions for computing deformations; fixed default $= 32$
Angle deviation	θ	$< 0,90 >$	Scalar	2θ is the top angle of the directional cones; fixed default $= 7°$
Output				
Model	$\boldsymbol{d}(M_l, M_b, \alpha, \beta, \gamma)$	$\lvert\boldsymbol{d}\rvert \in [0, \alpha + \delta]$	Vector field	

We applied the model displacement fields with ANTs to deform T1wc MRIs to create synthetic versions of the T1wc at a second time point. This allowed us to derive pairs of real first time point- and synthetic second time point MRIs, with an associated ground truth displacement field (Figure 3). We used the conjunction of necrotic, edematous, and contrast-enhanced tissue mask as the input tumor tissue mask to the model.

Parametric evaluation of deformable registration for tumor growth assessment

We evaluated the following methods for displacement estimation; Symmetric image Normalization (SyN) (16) with mutual information and cross-correlation metric (17), as well as optical flow by Gunnar-Farneback (18), iterative Lucas-Kanade (19) and TV-L1 (20). The five registration methods were used to estimate the displacements between each patient's first time-point MRI and the 12 different synthetic growth simulations generated (a total of 324 simulations).

Our assessments were designed to answer the following three questions:

1. Do the differences of the following parameters change the performance of the registration methods?
    a. Low and high mass effect.
    b. Low and high growth infiltration.
    c. No, intermediate and high growth irregularity.
2. Does the performance of the registration methods differ?
3. Is there a difference in the performance of the registration methods across the different lesion tissue types (necrotic, edematous, and contrast-enhanced)?

Statistical assessment

All registration methods were evaluated by absolute and relative errors from image voxels within the necrotic, edematous, and contrast-enhanced lesion masks. Median values were computed for each lesion, then summarized by mean values depending on the statistical test performed.

The absolute error e_{abs} was computed voxel-vise as the magnitude of the difference between the ground truth simulated reference displacement vector $\overrightarrow{d_{ref}}$ and the deformable registration estimated displacement vector $\overrightarrow{d_{est}}$:

$$e_{abs} = \left|\overrightarrow{d_{ref}} - \overrightarrow{d_{est}}\right|$$

The relative error e_{rel} was computed as e_{abs} divided by the magnitude of the ground truth displacement vector $\overrightarrow{d_{ref}}$:

$$e_{rel} = \frac{e_{abs}}{\left|\overrightarrow{d_{ref}}\right|}$$

We performed 27 (patients) * 12 (models) * 5 (methods) = 1620 registrations, each with 3 (lesion tissue types) * 2 (absolute and relative error) returning a total of 9720 error measurements.

Paired samples Wilcoxon signed-rank tests were performed to compare registration errors for low and high mass effect, and for low and high infiltration. To compare errors for no, intermediate and high growth irregularity, registration methods, as well as on tissue types, we used Kruskal-Wallis tests. One-way ANalysis-Of-VAriance (ANOVA) with Tukey pair comparisons was performed to assess significant differences between the performance of the registration methods. Before performing the ANOVA and Tukey comparisons, we log-transformed the errors for normality. To ensure N=27 individual samples for each test population, we calculated mean error values across all simulated parameter configurations except the one investigated. For all comparisons, except when comparing registration performance on lesion types, we used mean errors across the tissue types as overall representations of the error of the registration methods in the whole tumor volume. A significance level of P=0.05 was used for all analysis before any Bonferroni corrections for multiple comparisons.

Model agreement with follow-up MRI

Finally, for all patients except patient one, we conducted a grid search for the maximum tissue displacement, infiltration and irregularity to assess the best fit between the synthetic tumor growth projections and the real tumor growth from the MRI data at the second exam. One patient was excluded because of registration errors in the preprocessing between first and second time-point MRI. We used standard cross-correlation provided by FSL (30) within masks specific to each growth projection as the function to maximize. These are binary masks, produced by our simulations, of the respective brain regions with tissue displaced by the deformation model. We searched for optimal parameters using the same parameter range described earlier; 3- and 8-*mm* maximum tissue displacement, 1 (low) and 0.1 (high) infiltration, as well as no, 0.05 (intermediate) and 0.03 (high) growth irregularity. The optimal parameters were then compared with total tumor volume, to assess the relation between tumor size and ability of the model to describe real tumor growth. We also performed standard linear regression of total tumor volume and registration performance.

Results

Comparing low and high mass effect returned differences in performance of registration methods in terms of both absolute and relative errors, with lowest errors and thus higher registration performance for low mass effect growth projections (Wilcoxon; $P<0.001$, 7 percentage points difference in mean relative error). Furthermore, comparison of low- and high infiltration separated the registration methods only when assessing relative errors, where high infiltration was associated with the lowest error in registration performance (Wilcoxon; $P<0.001$, 7 percentage points difference in mean relative error). No difference in performance was associated between the different levels of growth irregularity.

ANTs SyN with cross-correlation metric and Farneback optical flow performed with lower relative errors than the rest of the methods (Kruskal-Wallis; $P=0.002$, ANOVA; $P=0.001$). The registration methods returned the lowest absolute errors in edematous tissue (Kruskal-Wallis; $p=0.019$), and lowest relative errors in edematous and contrast-enhanced tissue (ANOVA; $P=0.035$). See Figure 4 and Figure 5 for depictions of the results.

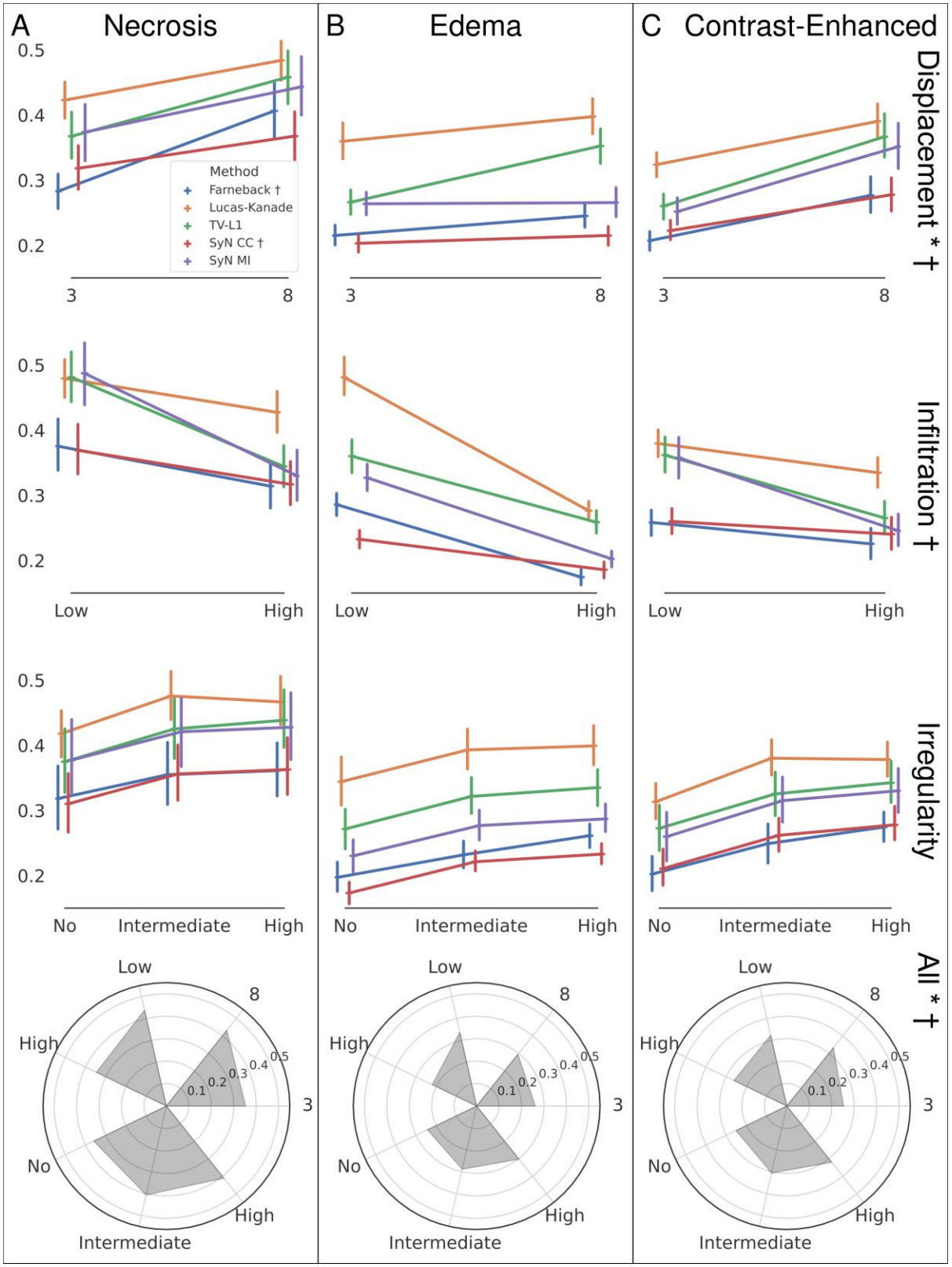

Figure 4: Results from measuring the performance of deformable registration methods in the tumoral regions A) necrosis, B) edema and C) contrast-enhanced lesion by varying the deformation model parameters mass effect (displacement), infiltration and irregularity. A lower relative error means higher registration performance. ANTs SyN with cross-correlation

loss metric returned highest performance. Deformable registration performed with overall lowest errors in edematous regions when compared to the necrotic/post-surgical cavity and contrast enhanced regions.

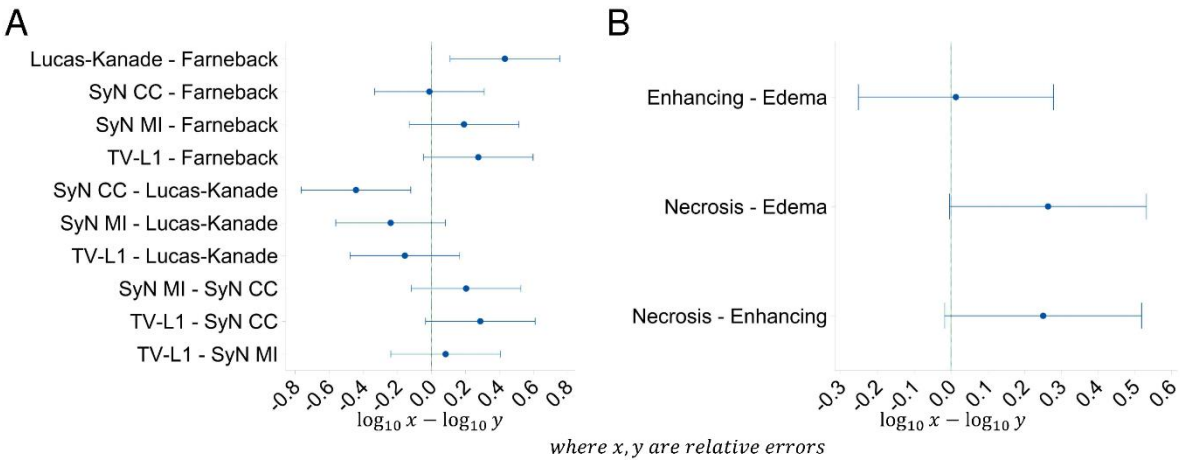

Figure 5: Results from ANOVA and Tukey pair comparisons of log-transformed relative errors to investigate differences in performance of the deformable registration methods (A) between themselves and B) between lesional regions).

Last, the grid search on the investigated parameters resulted in model projections with only low mass effect. Of these projections, 52 % had the low infiltration parameter setting, and close to all had no growth irregularity (all except one projection with intermediate, and three projections with high irregularity parameter setting). The projections with high infiltration had the highest cross-correlation with second time-point MRI (cross-correlation=0.73 and 0.67 for high infiltration and low infiltration respectively), shown in Figure 6.

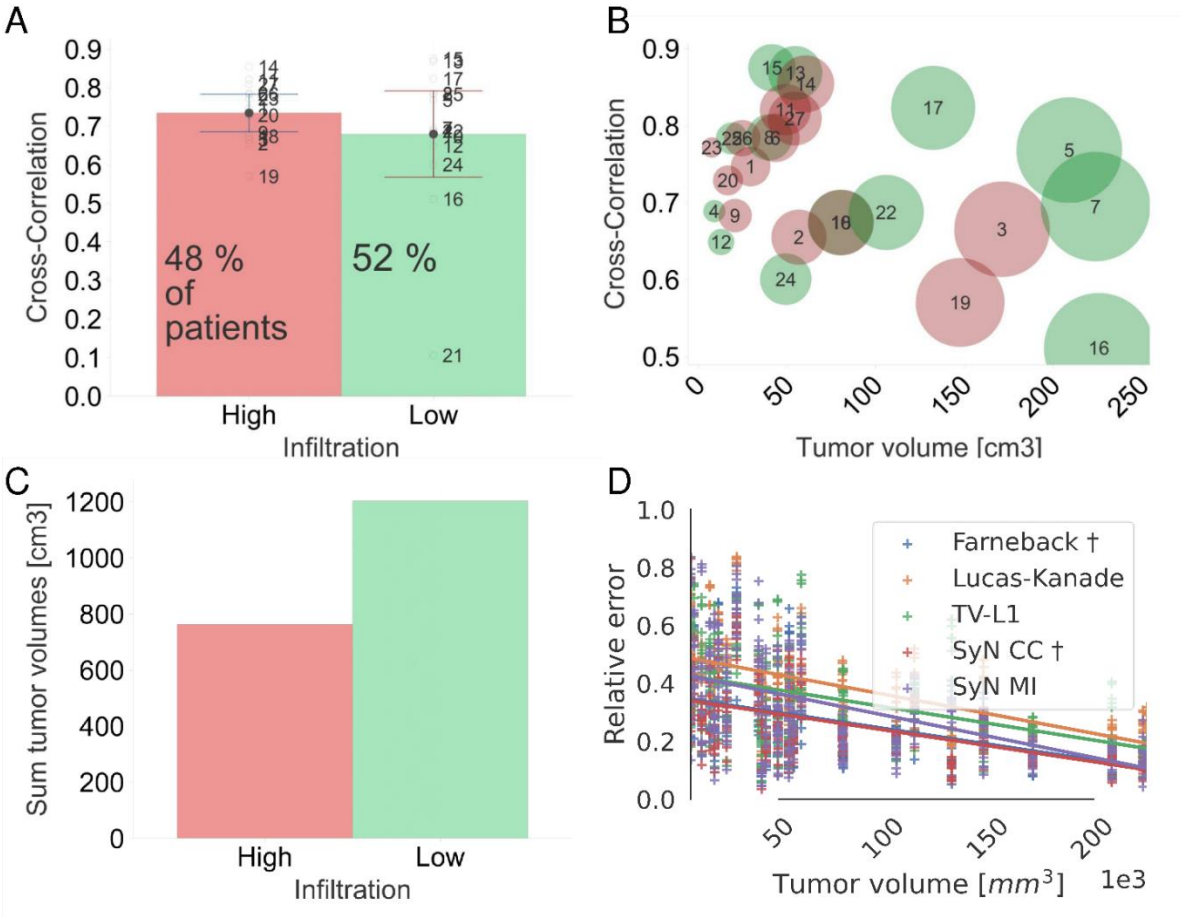

Figure 6: Results from ad-hoc grid search. A)-B) Distribution of low and infiltration growth projections and true tumor volume as measured by cross-correlation between best fit growth projections with true second time-point MRI. Higher cross-correlation is better fit. C) Sum of tumor volumes stratified into best fit low and high infiltration growth projections. D) Regression lines of relative registration errors vs. tumor volume for the different methods. Lower error is better.

Discussion

In our work, we assessed the performance of using state-of-the-art registration methods as a tool for estimating voxel-vise tissue displacement of HGG progression and recurrence. GBM, the main disease investigated, compromise a complex type of cancer spanning a wide variety of genetic profiles. The appearance of tumor growth on diagnostic images may take many different forms on longitudinal MRI exams (6,8,31,32). In our study, we simulated tissue expansion growth mimicking what is observed on longitudinal MRIs of patients with

recurrent HGGs, using only the tumor and brain masks as input. Our main finding indicates significant lower registration errors for low simulated mass effect (3 mm maximum tissue displacement) combined with high infiltration. ANTs SyN with cross-correlation metric and Farneback optical flow registration methods showed the overall best tissue displacement quantification performance for tumor growth.

One benefit of using a deformation model, such as the one proposed in our study, is the ability to simulate multiple synthetic tumor growth projections in a controlled fashion with various degrees of radially enlarged necrotic, enhanced, edematous and other surrounding peritumoral tissue. Specifically, we varied the model parameters mass effect (mm), growth infiltration and growth irregularity to create a dataset of real- and synthetic MRI scan pairs. This design allowed for objective and quantitative comparisons of registration algorithms and displacement methods with full control over simulation parameters.

In addition to showing overall best performance by the topology-preserving method from ANTs with cross-correlation metric, as well as the optical flow method by Farneback, our results indicate significantly different overall performances of the registration methods when varying the growth simulation parameters, and when comparing relative to absolute displacement errors. Significant difference in registration performance in terms of *both* absolute and relative errors were found by varying the mass effect parameter. A low simulated maximum tissue displacement of 3 mm significantly improved registration performance compared to the higher simulated maximum tissue displacement of 8 mm.

For the treating physician, assessment of absolute error values may provide the highest clinical relevance because the measured distance to e.g. eloquent areas help shape the clinical decision-making process. Our study suggests a decrease in estimation accuracy is associated with true increase in absolute displacement. These results may also help determine the expected displacement error when estimating HGG progression in individual patients. To this end, our findings suggest an increase in true tissue displacement may also lead to a subsequent increase in the error (in mm) of the DIR methods. Hence, we may conclude that DIR methods can accurately measure displacements in a scenario of HGG progression with small displacements (i.e. low mass effect). This may be accomplished by short longitudinal time intervals between the MRI exams which may be a challenge for routine examinations, but relevant for clinical trials.

The regions associated with highest performance of the DIR methods were edematous and contrast-enhanced tissue. Although maximal resection of contrast-enhanced tumor tissue is the standard practice today, recent literature suggests that peritumoral regions with high intensity value on T2w-FLAIR may be part of infiltrative tumor and that additional resection of these regions is associated with increased survival (33). Accurate displacement estimates from DIR in these regions may further support the use of DIR to derive biomarkers for survival prognosis, such as contralateral mass effect deformation heterogeneity (8) and peritumoral tissue compression (9).

Our ad-hoc grid search for best fit model on patients with ~2-week time interval between exams returned higher correlation with follow-up scans for low mass effect (3 *mm*) when compared to high mass effect (8 *mm*). This indicates that low simulated mass effect tumor growth was realistic according to our longitudinal data and thus well suited for assessing deformable registration accuracy in GBM.

There are several potential applications of our robust deformation model. One such application is data augmentation. Data augmentation is a process in which the amount of training data is artificially increased using simple imaging operations such as scaling, rotation and translation, to create more robust machine learning predictions. Our model could be applied as a special-purpose data augmentation method by artificially deforming structural MRIs and lesion masks to improve accuracy of segmentation by artificial neural networks under a wider variety of clinical conditions. Dose warping, where radiation dose is deformed into later time-point examinations in order to investigate treatment response in specific tissue areas, is a natural application of DIR methods. Our model could similarly be used as a framework for testing the accuracy of dose warping using DIR methods.

Our study has some limitations. In our deformation model, we assumed non-changing voxel intensities during displacement, which is not the case with true infiltrative growth. In a worst-case scenario, no displacement of tissue and only change of image intensity values (e.g. as a result of a result of infiltrative growth or anti–vascular endothelial growth factor (anti-VEGF) therapy) could make growth characterization by displacement fields irrelevant. Our deformation model is by purpose a rough model that uses only tumor and brain masks to model growth based on ellipsoid-shaped radial expansion. Second, we used the sum of all

tissue types of a patient as the input tumor mask to the model, without differentiating between edema, necrosis and enhanced regions.

Conclusion

Deformable image registration methods have demonstrated their capability to quantify voxel-wise displacements of brain tumors from longitudinal MRI studies. Our deformation model enabled us to perform a parametric evaluation of deformable image registration methods under various simulated conditions. Based on our simulations, we conclude that displacement estimations of glioblastoma growth from deformable image registration present lowest errors in the edema and contrast-enhanced tissues for low mass effect and high infiltration rates. SyN with cross-correlation metric and Gunnar-Farneback optical flow exhibited the best performance for the investigated simulation parameters.

References

1. Louis DN, Perry A, Reifenberger G, von Deimling A, Figarella-Branger D, Cavenee WK, et al. The 2016 World Health Organization Classification of Tumors of the Central Nervous System: a summary. Acta Neuropathol. 2016 Jun;131(6):803–20.

2. Stupp R, Mason WP, van den Bent MJ, Weller M, Fisher B, Taphoorn MJB, et al. Radiotherapy plus Concomitant and Adjuvant Temozolomide for Glioblastoma. New England Journal of Medicine. 2005 Mar 10;352(10):987–96.

3. Hanif F, Muzaffar K, Perveen K, Malhi SM, Simjee SU. Glioblastoma Multiforme: A Review of its Epidemiology and Pathogenesis through Clinical Presentation and Treatment. Asian Pac J Cancer Prev. 2017;18(1):3–9.

4. Davis ME. Glioblastoma: Overview of Disease and Treatment. Clin J Oncol Nurs. 2016 Oct 1;20(5):S2–8.

5. Wen PY, Kesari S. Malignant Gliomas in Adults. New England Journal of Medicine. 2008 Jul 31;359(5):492–507.

6. Steed TC, Treiber JM, Brandel MG, Patel KS, Dale AM, Carter BS, et al. Quantification of glioblastoma mass effect by lateral ventricle displacement. Sci Rep. 2018 12;8(1):2827.

7. Gamburg ES, Regine WF, Patchell RA, Strottmann JM, Mohiuddin M, Young AB. The prognostic significance of midline shift at presentation on survival in patients with glioblastoma multiforme. Int J Radiat Oncol Biol Phys. 2000 Dec 1;48(5):1359–62.

8. Prasanna P, Mitra J, Beig N, Nayate A, Patel J, Ghose S, et al. Mass Effect Deformation Heterogeneity (MEDH) on Gadolinium-contrast T1-weighted MRI is associated with decreased survival in patients with right cerebral hemisphere Glioblastoma: A feasibility study. Sci Rep. 2019 04;9(1):1145.

9. Fuster-Garcia E, Thokle Hovden I, Fløgstad Svensson S, Larsson C, Vardal J, Bjørnerud A, et al. Quantification of Tissue Compression Identifies High-Grade Glioma Patients with Reduced Survival. Cancers. 2022 Jan;14(7):1725.

10. Oh S, Kim S. Deformable image registration in radiation therapy. Radiat Oncol J. 2017 Jun;35(2):101–11.

11. Sotiras A, Davatzikos C, Paragios N. Deformable Medical Image Registration: A Survey. IEEE Transactions on Medical Imaging. 2013 Jul;32(7):1153–90.

12. Wang M, Li P. A Review of Deformation Models in Medical Image Registration. J Med Biol Eng. 2019 Feb 1;39(1):1–17.

13. Haskins G, Kruger U, Yan P. Deep learning in medical image registration: a survey. Machine Vision and Applications. 2020 Jan 29;31(1):8.

14. Dalca AV, Balakrishnan G, Guttag J, Sabuncu MR. Unsupervised learning of probabilistic diffeomorphic registration for images and surfaces. Medical Image Analysis. 2019 Oct 1;57:226–36.

15. Balakrishnan G, Zhao A, Sabuncu MR, Guttag J, Dalca AV. VoxelMorph: A Learning Framework for Deformable Medical Image Registration. IEEE Transactions on Medical Imaging. 2019 Aug;38(8):1788–800.

16. Avants BB, Epstein CL, Grossman M, Gee JC. Symmetric diffeomorphic image registration with cross-correlation: Evaluating automated labeling of elderly and neurodegenerative brain. Medical Image Analysis. 2008 Feb 1;12(1):26–41.

17. Avants BB, Tustison NJ, Song G, Cook PA, Klein A, Gee JC. A reproducible evaluation of ANTs similarity metric performance in brain image registration. Neuroimage. 2011 Feb 1;54(3):2033–44.

18. Farnebäck G. Two-Frame Motion Estimation Based on Polynomial Expansion. In: Bigun J, Gustavsson T, editors. Image Analysis. Berlin, Heidelberg: Springer; 2003. p. 363–70. (Lecture Notes in Computer Science).

19. Besnerais GL, Champagnat F. Dense optical flow by iterative local window registration. In: IEEE International Conference on Image Processing 2005. 2005. p. I–137.

20. Wedel A, Pock T, Zach C, Bischof H, Cremers D. An Improved Algorithm for TV-L1 Optical Flow. In: Cremers D, Rosenhahn B, Yuille AL, Schmidt FR, editors. Statistical and Geometrical Approaches to Visual Motion Analysis. Berlin, Heidelberg: Springer; 2009. p. 23–45. (Lecture Notes in Computer Science).

21. Larsson C. Prognostic Value of Optimized Dynamic Contrast-Enhanced Magnetic Resonance Imaging of High-Grade Gliomas. 2018 [cited 2021 Feb 24]; Available from: https://www.duo.uio.no/handle/10852/62008

22. Larsson C, Groote I, Vardal J, Kleppestø M, Odland A, Brandal P, et al. Prediction of survival and progression in glioblastoma patients using temporal perfusion changes during radiochemotherapy. Magnetic Resonance Imaging. 2020 May 1;68:106–12.

23. Juan-Albarracín J, Fuster-Garcia E, García-Ferrando GA, García-Gómez JM. ONCOhabitats: A system for glioblastoma heterogeneity assessment through MRI. Int J Med Inform. 2019 Aug;128:53–61.

24. Fonov VS, Evans AC, McKinstry RC, Almli CR, Collins DL. Unbiased nonlinear average age-appropriate brain templates from birth to adulthood. NeuroImage. 2009;(47):S102.

25. Avants BB, Tustison NJ, Song G, Gee JC. Ants: Open-source tools for normalization and neuroanatomy. HeanetIe. 2009;10:1–11.

26. Wach J, Hamed M, Schuss P, Güresir E, Herrlinger U, Vatter H, et al. Impact of initial midline shift in glioblastoma on survival. Neurosurg Rev. 2021 Jun 1;44(3):1401–9.

27. Tu PH, Liu ZH, Chuang CC, Yang TC, Wu CT, Lee ST. Postoperative midline shift as secondary screening for the long-term outcomes of surgical decompression of malignant middle cerebral artery infarcts. Journal of Clinical Neuroscience. 2012 May 1;19(5):661–4.

28. Ellenbogen RG, Sekhar LN, Kitchen N. Principles of Neurological Surgery E-Book. Elsevier Health Sciences; 2017. 1063 p.

29. Perlin K. An image synthesizer. SIGGRAPH Comput Graph. 1985 Jul 1;19(3):287–96.

30. Jenkinson M, Beckmann CF, Behrens TEJ, Woolrich MW, Smith SM. FSL. NeuroImage. 2012 Aug 15;62(2):782–90.

31. Itakura H, Achrol AS, Mitchell LA, Loya JJ, Liu T, Westbroek EM, et al. Magnetic resonance image features identify glioblastoma phenotypic subtypes with distinct molecular pathway activities. Sci Transl Med. 2015 Sep 2;7(303):303ra138.

32. Gevaert O, Mitchell LA, Achrol AS, Xu J, Echegaray S, Steinberg GK, et al. Glioblastoma multiforme: exploratory radiogenomic analysis by using quantitative image features. Radiology. 2014 Oct;273(1):168–74.

33. Haddad AF, Young JS, Morshed RA, Berger MS. FLAIRectomy: Resecting beyond the Contrast Margin for Glioblastoma. Brain Sciences. 2022 May;12(5):544.

Acknowledgements

We thank the patients and their relatives for involvement in the study, and Michael Osadebey, PhD, at Department of Physics and Computational Radiology at Oslo University

Hospital for useful discussions on the modeling approach. This work received funding from the Research Council of Norway FRIPRO grant 261984 (KEE), the South Eastern Norway Regional Health Authority grants 2017073 (KEE) and 2013069 (KEE), and the European Research Council (ERC) under the European Union's Horizon 2020 Programme (ERC Grant Agreement No. 758657-ImPRESS) (KEE) , and the European Union’s Horizon 2020 research and innovation Programme (EFG) under the Marie Skłodowska-Curie (Grant Agreement No 844646) and the Spanish State Research Agency, Subprogram for Knowledge Generation (PROGRESS, No PID2021-127110OA-I00).

Conflict of Interest Statement

KEE: NordicNeuroLab AS, Bergen, Norway – Intellectual property rights.

AB: NordicNeuroLab AS, Bergen, Norway – Intellectual property rights.

Deformation model

Overview

The procedure for generating synthetic displacements is as follows:

1) Find the bounding box of the tumor mask in the input image reference space. The tumor mask could be of any tissue type, for instance contrast-enhanced tissue.
2) Create a 3D gaussian using the dimensions (width, height, and depth) of the bounding box from step 1. Scale the gaussian to have a maximum value of 1.
3) Invert the gaussian and compute its gradient to create a vector field. Scale the vector field to have maximum absolute value of 1.
4) Find a subset of the vectors on the inflection surface of the gaussian by thresholding the gaussian on the vector field. The vector subset was selected using an iterative approach maximizing the mean distance from the starting positions between each selected vector and the candidate vector, ensuring maximum spread of the selected vectors' directions.
5) For each of the selected vectors, find all other vectors of the vector field having less than a given angle difference from the selected vector. This defines a cone shaped mask. Find the bounding box for each cone.
6) Remove outer parts of the cones according to thresholding the 3D gaussian (< 0.05). Then geometrically extend each cone until it reaches the end of the brain mask. Find the bounding box for each extended cone.
7) Depending on the infiltration parameter, re-map all components of the vector field within an original cone bounding box to its extended cone bounding box to a certain degree using linear interpolation. Similar was done to create an interpolated 3D gaussian for use in later steps.
8) If noise is enabled, add 3-channel Perlin noise attenuated by the interpolated 3D gaussian to the interpolated vector field.
9) Scale the interpolated vector field by the maximum tissue displacement specified as input. This creates the final displacement field. Lastly, create the final interpolated vector field by restricting displacement vectors to not bypass the brain mask barrier, if any.

Technical description

Let w, h, d be the width, height and depth of the bounding box for the outlined tumor segmentation mask M_l registered to 1 mm^3 MNI space.

The algorithm initially takes w, h, d as inputs to compute a three-dimensional gaussian scalar field g consisting of σ standard normal deviations in each dimension, parameterized in equally spaced intervals and with resolution N according to Equations (0.1) and (0.2).

$$g(x, y, z) = -e^{-\frac{x^2+y^2+z^2}{2}} \tag{0.1}$$

$$\begin{bmatrix} x \\ y \\ z \end{bmatrix} \in \begin{bmatrix} [-\sigma, \sigma]_{N(w)} \\ [-\sigma, \sigma]_{N(h)} \\ [-\sigma, \sigma]_{N(d)} \end{bmatrix}, \qquad N(l) = \begin{cases} l+1, & l\ odd \\ l, & l\ even \end{cases} \tag{0.2}$$

$N(l)$ in Equation (0.2) results in an even number of sampling steps along each bounding box dimension of the tissue mask. This negligible simplification is required to be able to access the geometric center of the bounding box by matrix indexing, which makes various indexing operations in the algorithm easier. See Figure 1 for an illustration of the one-dimensional variant of g.

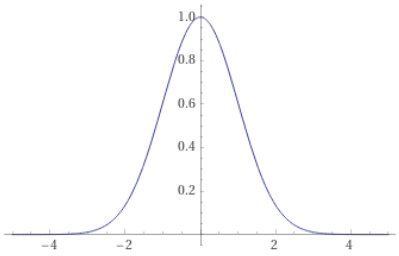

Figure 1: g in one dimension.

An initial model displacement vector field $\boldsymbol{d}(M_l)$ is then computed from the gradient (partial derivatives with respect to x, y and z) of g by $\boldsymbol{d} = \nabla g$. Figure 2 illustrates how $\boldsymbol{d}$ is computed from the tumor mask M_l for various spatial dimensions.

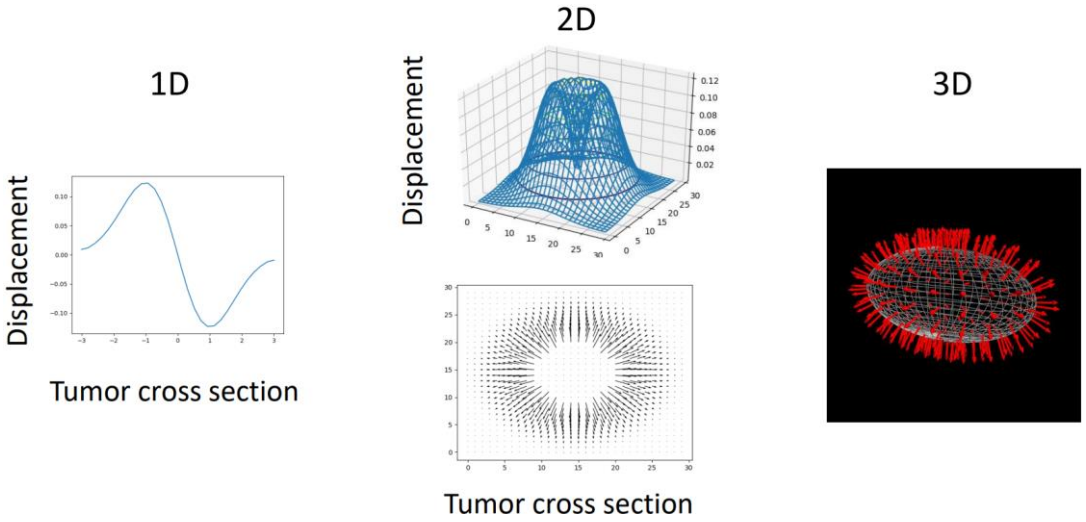

Figure 2: Illustration of computation of initial deformation model $\boldsymbol{d}$ based on 1D, 2D and 3D cross-section of the tumor mask M_l. $\boldsymbol{d}$ is the gradient of g.

Figure 3 (C) displays an ellipsoid and multiple directional cone shapes that are computed from $\boldsymbol{d}$. The purpose of the directional cones is guiding iterative deformation of $\boldsymbol{d}$ in terms of displacing the vector positions in $\boldsymbol{d}$ by $\boldsymbol{d}$ itself by an amount defined by the infiltration parameter β, and then linearly interpolating the displaced $\boldsymbol{d}$ in later computation steps to get a smooth displacement field.

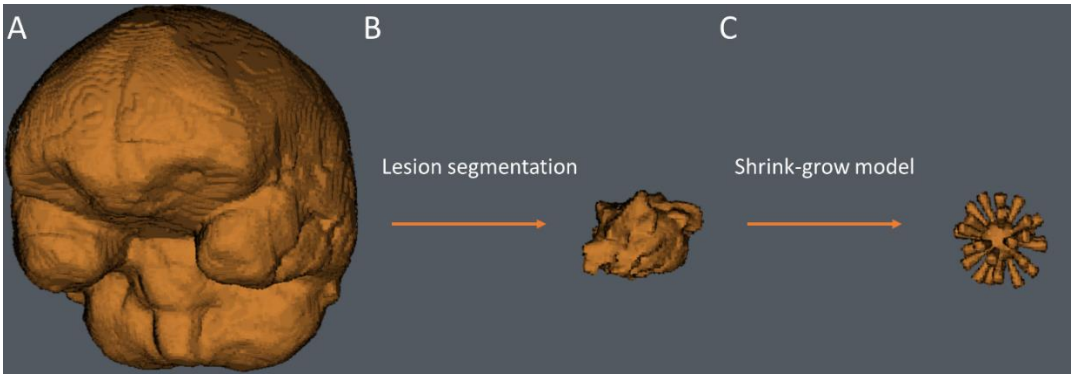

Figure 3: The initial deformation model $\boldsymbol{d}$ is computed from the tissue mask (B). At later steps, the brain mask (A) acts as a boundary for restricting physical displacement when deforming $\boldsymbol{d}$ by extending the "cones" computed from the initial $\boldsymbol{d}$ model (C).

The binary ellipsoid mask M_e in Figure 3 (C) is defined as

$$M_e := g < -e^{\frac{1}{2}} \tag{0.3}$$

The surface of M_e defines the locations with highest spatial intensity change in g, and resultingly the starting positions of the largest gradient magnitudes in $\boldsymbol{d}$. This is the inflection surface of g defined

by $\nabla^2 g = 0$. The algorithm then scales $\boldsymbol{d}$ to have a maximum gradient magnitude of 1 by $\boldsymbol{d} = \frac{\boldsymbol{d}}{|\boldsymbol{d}|}$ and finds the approximate unit normal vectors V for the surface of M_e in MNI voxel-isotropic resolution, by extracting vectors $V \in \mathbb{R}^{N\times 3}$ from $\boldsymbol{d}$ that have starting positions in the center of the voxels in a convex ellipsoid mask M according to Equations (0.4) and (0.5)

$$V = \boldsymbol{d}[M] \tag{0.4}$$

$$M := M_e \; where \;\; \| \; V \; \|_F > 0.99 \tag{0.5}$$

where [] describes tree-dimensional binary mask matrix indexing and $\| \; V \; \|_F \in \mathbb{R}^{N\times 1}$ is the Frobenius norm of V along its second axis dimension, which computes gradient magnitudes. To speed up the algorithm, a fixed subset of N_s maximum spread normal vectors $V_s \in \mathbb{R}^{N_s\times 3}$ is selected from V according to Pseudocode 1.

A gradient magnitude threshold of 0.99 is suitable for realistic glioblastoma bounding box dimensions in $1\ [mm^3]$ voxel-isotropic space, but would possibly need to be lowered with lower isotropic resolutions to ensure extraction of $\geq N_s$ normal vectors. A cone is then computed for each vector in V_s based on a fixed deviation θ in angles between each vector in V_s and $\boldsymbol{d}$ according to Pseudocode 2. 2θ is the resulting top angle in the generated cones as illustrated in Figure 3 (C).

The final mask M displayed in Figure 3 (C) is the conjunction of the ellipsoid mask M_c and all computed s cone masks M_c from Pseudocode 2 according to Equation (0.6)

$$M = M_e \wedge \bigwedge_{i}^{s} M_{c,i} \tag{0.6}$$

Pseudocode 3 describes the next and main part of the algorithm deforming $\boldsymbol{d}$ by an amount β proportional to the maximum distance to the end of the brain (Figure 4), to create the infiltrative displacement field $\boldsymbol{d}_\beta$. An infiltrative gaussian g_β was created similarly.

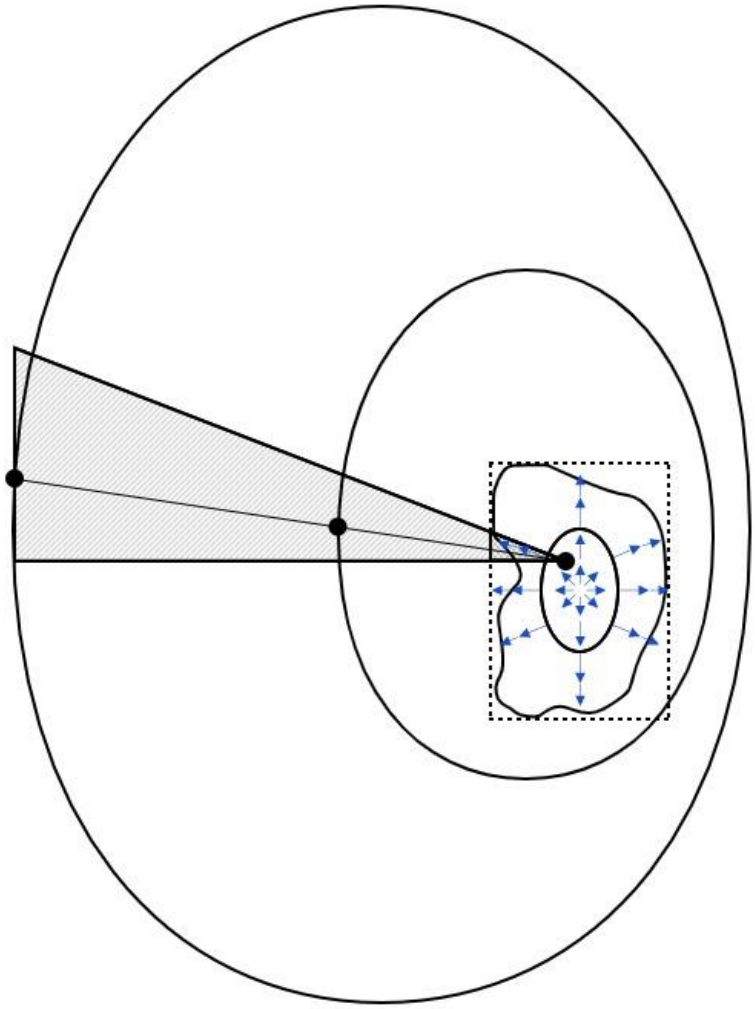

Figure 4: Simplified two-dimensional axial illustration of the infiltration algorithm described in Pseudocode 3. The components of the initial displacement field $\boldsymbol{d}$ (blue arrows) computed from the lesion tissue bounding box is displaced by itself by a fraction $1-\beta$ proportional to the maximum distance to the end of the brain. Here $\beta \sim 0.6$

The final model displacement field is computed according to Equation (0.7)

$$\boldsymbol{d}(M_l, M_b, \alpha, \beta, \gamma) = \left|\alpha \cdot \boldsymbol{d}_\beta(M_l, M_b) + \boldsymbol{p}(\gamma)\right|_{M_b} \tag{0.7}$$

where $\boldsymbol{p}$ is a Perlin noise vector field and $||_{M_b}$ restricts displacement to only occur inside the brain mask. For the latter task, displacements surpassing the brain mask were shortened to end at the brain mask barrier.

Pseudocode

Pseudocode 1: Maximum spread normal vectors by maximizing mean starting distances.

```
algorithm max-spread-vectors is

          input: Normal vectors V

                 Starting positions P of the normal vectors

                 Number of vectors to return N_s

          output: Selection lists containing the subset V_s and P_s of the normal vectors and positions

          1          initialize empty lists for selected vectors and positions

          2          append to the selection lists the first input vector and position

          3          remove the selected vector and position from input lists

          4          for each selected vector 2 to N_s do

          5                    for each selected vector position(s), compute the Euclidean distance to non-selected vector position(s)

          6                    append to the selection lists the input vector and position with the position that makes up the largest mean
          7                    Euclidean distance from the selected vector position(s)

          8                    remove the selected vector and position from the input lists

          9          return V_s and P_s
```

Pseudocode 2: Directional cone masks.

```
algorithm max-spread-cones is

          input: Normal vectors V_s

                 Displacement field d

                 Deviation in degrees θ

          output: Cone masks M_c

          1          initialize empty list M_c for storing cone masks

          2          for each vector v in V_s do

          3                    let ω be the angle difference in degrees between v and all other displacement vectors in d

          4                    let c be the cone mask defined by ω ≤ θ

          5                    append to M_c the cone mask for vector v: c

          6          return M_c
```

Pseudocode 3: Infiltrative deformation of displacement field $\boldsymbol{d}$.

```
algorithm infiltration is
        input: Normal vectors V_s
               Normal vector starting positions P_s
               Displacement field d
               Cone masks M_c
               Brain mask M_b
               Infiltration β
        output: Infiltrative displacement field d_β
        let dnorm be |d|
        let displacements be a list containing one interpolated part of d for each spatial direction in s
        for each spatial direction i in in s do
                let nvd, nvc, bmi be V_s[i], P_s[i], M_c[i] respectively
                let p_max_bmi be the point furthest away nvc along nvd and within bmi
                let disp_max_bmi be the length between nvc and p_max_bmi
                let p_max_brain be the point furthest away nvc along nvd and within M_b
                let disp_max_brain be the length between nvc and p_max_brain
                let dnormcone be dnorm within bmi
                let dxcone, dycone, dzcone be the components of d within bmi
                (the following scales all displacement components to unit norm such that their starting coordinates can be displaced equally far)
                let dxcone, dycone, dzcone be dxcone/dnormcone , dycone/dnormcone , dzcone/dnormcone respectively with element wise fraction
                if β > 0 then
                        let mask_pts be the points within bmi
                        let extension be β*(disp_max_brain - disp_max_bmi)
                        (the following displaces mask_pts according to the extension length)
                        displace the mask_pts x, y, z coordinates extension*dxcone, extension*dxcone, extension*dzcone length respectively
                        let bmi_copy be a copy of bmi
                        add displaced mask_pts to bmi_copy
                        let bm_geom_center and bm_widths be the geometric center coordinates and dimensions of bmi_copy containing displaced
                         points
                else
                        let bm_geom_center and bm_widths be the geometric center coordinates and dimensions of bmi
                let bmi_copy be a copy of bmi
                let mask_pts be the points within bmi
                let extension be disp_max_brain - disp_max_bmi
                displace the mask_pts x, y, z coordinates extension*dxcone, extension*dxcone, extension*dzcone length respectively
                add displaced mask_pts to bmi_copy
                let bm_geom_center_interp and bm_widths_interp be the geometric center coordinates and dimensions of bmi_copy containing displaced
                 points
                deform d by re-mapping components within bm_geom_center and bm_widths to be within bm_geom_center_interp and bm_widths_interp
                 using trilinear interpolation
                append to displacements the deformed components of d for the spatial direction i
        let d_β be the mean of displacements over s for interpolated component data
        return d_β
```

Execution times

Mean execution times for the various methods showed that SyN with cross-correlation metric (red), the method that together with the Farneback optical flow method had highest performance, had the slowest execution time. Oppositely, the Farneback method returned with the fastest execution time being around 29 times faster than SyN CC (blue). The execution speed of running our synthetic deformation model and applying the synthetic deformation field to an image (black), compares with the fastest registration method (Figure 5).

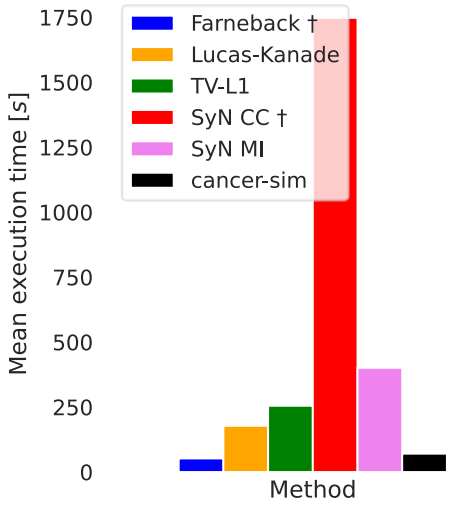

Figure 5: Execution time of a single registration task for the different methods. The total execution time for generating a synthetic displacement field with our model and using it to deform an MRI scan is shown as well (black). †: highest registration accuracy in our work.

The execution times were mean estimated from text logs from custom run scripts, except for the SyN MI and SyN CC methods where the execution times were captured from single runs. All software except the Farneback optical flow was run on a 16-core Intel Xeon E5620, 2.4GHz with 24 GB RAM. The Farneback method was run on a single Nvidia GeForce RTX 2080 Ti GPU with 11 GB VRAM and using CUDA version 11.

Software

The deformation model was written in Python 3.8 and registration performance was assessed using bash scripts and various tools from FSL, ANTs and Convert3D.

Deformation model

https://github.com/ivartz/cancer-sim

The following implementation of 3D Perlin noise in Python was used to simulate growth irregularity:

https://github.com/pvigier/perlin-numpy

Parametric evaluation scripts

https://github.com/ivartz/ants-bcond

https://github.com/ivartz/opticalflow-bcond

Ad-hoc grid search

https://github.com/ivartz/cancer-sim-search

Statistics

All statistical tests were performed in Minitab 19 (Minitab, LLC).